Dissertation

submitted to the

Combined Faculties of the Natural Sciences and Mathematics

of the Ruperto-Carola-University of Heidelberg. Germany

for the degree of

Doctor of Natural Sciences

Put forward by

Julia Anna Haser

born in: Bad Mergentheim

Oral examination: February 4, 2015

Neutron Detection Uncertainties in the θ_{13} Analysis of the Double Chooz Experiment

Kurzfassung

Das Reaktorneutrinoexperiment Double Chooz hat eine präzise Messung des Neutrinomischungswinkels θ_{13} zum Ziel. Die absolute Genauigkeit der Normalisierung und der Form des vorhergesagten Neutrinospektrums bilden die Voraussetzung einer Analyse mit einem einzelnen Detektor. Der größte Beitrag zur Detektionsunsicherheit der Normalisierung des Experiments wird dabei durch die Nachweiseffizienz der Neutronenereignisse verursacht. Letztere sind Teil des durch Antineutrinos erzeugten Koinzidenzsignals. Eine Korrektur der Monte Carlo Normalisierung sowie eine dazugehörige Unsicherheit gewährleisten in der θ_{13} Analyse die Übereinstimmung der Nachweiseffizienz in Daten und Simulation. Kalibrationsmessungen in den inneren zwei Detektorvolumina ermöglichen die Effizienzbestimmung durch ^{252}Cf Spaltneutronen. Neue Verfahren erlauben es die Korrektur der Selektionseffizienz sowie deren Unsicherheit über das gesamte Volumen integriert zu berechnen. Mit diesen verbesserten Methoden gelang es die Unsicherheit der Detektionseffizienz um einen Faktor zwei zu verringern. Welcher Anteil von Neutronen auf einem bestimmten Element eingefangen wird, wird durch das Neutroneneinfangsverhältnis ausgedrückt. Eine Korrektur dieser Größe wurde ermittelt und auf Stabilität überprüft. Ferner wird die Messung der Korrektur durch kosmische Myonen erzeugte Spallationsneutronen diskutiert. Darüber hinaus wurde die Unsicherheit der durch Neutronenmigration erzeugten Randeffekte abgeschätzt. Dies wurde durch die Verwendung unterschiedlicher Monte Carlo Konfigurationen mit variierten Parametern und Modellierungen der Neutronenphysik realisiert.

Abstract

The reactor antineutrino experiment Double Chooz aims to provide a precise measurement of the neutrino mixing angle θ_{13}. In the analysis with one detector, accuracy in the predicted neutrino spectrum from simulation is a necessity with regard to normalization and energy shape. The detection efficiency of neutron events, which are part of the coincidence signal created by neutrinos, introduce the largest uncertainty contribution of the normalization of the experiment related to the signal detection. In order to accomplish a matching of the efficiencies observed in data and simulation, a correction of the Monte Carlo normalization and an associated systematic uncertainty are inputs in the θ_{13} analysis. Calibration source deployments in the inner two detector volumes allow for a measurement of the neutron detection efficiency using ^{252}Cf fission neutrons. New methods enable to compute the correction integrated over the whole volume and the corresponding uncertainty of the selection cut related efficiency. With these revised approaches a factor two improvement in the detection efficiency uncertainty was achieved. The correction of the neutron capture fraction – the capture fraction quantifies the proportion of captures on a particular element – is evaluated and tested for its robustness. Furthermore, a crosscheck of this quantity is discussed using neutrons produced by cosmic muon spallation. Finally, the uncertainty on border effects, emerging from neutron migration at the fiducial volume boundaries, is estimated by means of different Monte Carlo configurations with varying parameters and neutron physics modelings.

für Mimi

In real physics research, mistakes are of course made, and much of the scrutiny given to a surprising result consists of trying to find mistakes in the calculation [...] Scientists digesting reported confidence intervals may in effect modify [them] by adding allowance for "unknown errors" depending on the reputation of the experimenter [...]

– Robert D. Cousins,
"Why isn't every physicist a Bayesian?"

Contents

Introduction

For more than a decade only an upper limit on the mixing angle θ_{13} has been known. The smallness of the parameter complicated the measurement of a non-zero value of θ_{13}, which is a crucial requirement for future projects in the field of neutrino oscillations: The size of θ_{13} predicts the sensitivity of experiments searching for CP violation in the leptonic sector and the determination of the neutrino mass ordering.

The Double Chooz (DC) experiment targets to deliver a precision measurement of the neutrino mixing angle θ_{13} by means of observing electron antineutrino disappearance. It was the first reactor antineutrino experiment reporting a hint of a non-zero θ_{13} at the end of 2011. Located at a nuclear power plant in Chooz, France, it consists of two identical detectors filled with gadolinium-loaded liquid scintillator. A near detector measures the neutrino flux at 400 m distance from the reactor cores, even before three flavor neutrino oscillation takes effect. The far detector, built in a laboratory with 1050 m baseline to the reactors, observes the oscillated neutrino rate and spectral shape distortion. The DC experiment searches then for an energy dependent deficit in the relative comparison of the two measured antineutrino spectra. The DC detector design is optimized for the detection of reactor antineutrinos via inverse beta decay reaction on hydrogen nuclei. Resulting decay products of the neutrino interaction create a coincidence signal consisting of a prompt positron event and a delayed radiative neutron capture on either hydrogen or gadolinium nuclei.

As the experiment is operated with one detector at the far laboratory until the end of 2014, the estimation of θ_{13} relies on the comparison of the observed neutrino flux and energy shape to a Monte Carlo prediction. Thus, the accuracy of the simulated neutrino spectrum and normalization constitutes a crucial requirement in the data analysis.

Discrepancies between data and simulation in the signal selection efficiencies can be handled by implementation of corrections on the Monte Carlo normalization and an associated uncertainty in the θ_{13} fit. The dominant contribution to this systematic uncertainty is introduced by the detection efficiency of the delayed neutron capture. Previous efficiency studies offered potential to improve the approaches utilized for the systematic uncertainty computation. Approaching the two detector phase, one focus of the DC analysis was the development of elaborate techniques for efficiency calculation and detailed studies of systematic influences, as provided in this thesis.

With neutrons from spontaneous fission of ^{252}Cf the two inner detector volumes were sampled along the central symmetry axis and a rigid looped tube in several calibration campaigns, allowing for measurements of neutron related parameters. Careful studies of the ^{252}Cf data as presented in Chapter 4 enables the reduction of background contributions and improve the accuracy of these measurements.

As shown in Chapter 5 it is possible to distinguish different contributions to the total neutron detection efficiency. Whereas one efficiency component depends on the neutron

selection criteria, the other one is an intrinsic characteristic determined by the liquid scintillator composition. Several efficiency definitions will be proposed which allow to test for possible correlations between the Monte Carlo corrections of the neutron efficiency associated with each individual cut.

A global Monte Carlo correction of the neutron detection is desired by the θ_{13} analysis. The ^{252}Cf deployments, however, correspond to point-like measurements of the efficiency. Hence the geometrical condition of the fiducial volume needs to be taken into account by the correction and systematic uncertainty calculation. In Chapter 5 a method to compute the global efficiency correction of the gadolinium-based neutrino analysis from volume-integrated efficiency estimates is developed. The presented technique has to be able to estimate the full volume efficiency from a limited set of calibration positions. Monte Carlo studies offer the possibility to validate the volume-integration approach and evaluate its systematic uncertainty. The robustness of the correction is of particular importance for the systematic uncertainty estimation and requires various tests with respect to modifications in the computational procedures, the efficiency definitions or the datasets. Furthermore, the computed value of the Monte Carlo correction will be a measure of the agreement in the neutron detection efficiency found in data and simulation. Moreover, Chapter 5 deals with the intrinsic efficiency component obtained from measurements with ^{252}Cf data, which exhibits a discrepancy to the predicted value from simulation code. In addition, crosschecks of this deviation are summarized along with the discussion of values gained from a neutron sample produced by muon spallation processes.

The global Monte Carlo correction of the neutron detection efficiency for the neutrino selection via neutron captures on hydrogen is discussed in Chapter 6. In this analysis the volume-integration technique has to be extended to the enhanced fiducial volume size compared to the analysis based on gadolinium.

Neutron migration at the fiducial volume boundaries can enhance the detected neutrino flux and is known as "spill-in/out effect". Also present in the Monte Carlo simulation it could deviate from reality in its strength, thus over- or underestimating the predicted neutrino flux. Since the effect cannot be measured with detector data, a strategy based on Monte Carlo to estimate the systematic influence is put forward in Chapter 7.

About one year after the two detector measurement will have commenced, the detection systematic uncertainty might constitute the largest uncertainty contribution to the θ_{13} analysis. Prospects on the future two detector systematic uncertainty of the neutron detection efficiency will be given based on the studies presented in this thesis.

Chapter 1

Neutrino oscillation and mixing angle θ_{13}

This chapter will start with a short introduction to the neutrino oscillations and the current knowledge on the parameters describing this phenomenon. In Section 1.2 further details on the neutrino mixing parameter θ_{13} will be given, the mixing angle which was measured just recently. The last section, Section 1.3, focuses on the experimental concepts behind a measurement of θ_{13} at nuclear power stations.

1.1 Neutrino oscillation

The history of the neutrino has been accompanied by intriguing peculiarities ever since the first discussions about it as hypothetical particle. It starts with the "desperate remedy" [177] that brought W. Pauli in 1930 to postulate it in order to rescue the conservation of energy and momentum in β-decays. It took more than 26 years to prove the existence of the "poltergeist", which was accomplished by Reines and Cowan in 1956 [85]. Furthermore it was shown that neutrinos are created in a state that is predominantly of left helicity (left-handed) and antineutrinos of right helicity [211, 116], thus attesting the parity violating nature of the weak interaction. In fact a massless particle in the Standard Model, the experiments solving the "solar neutrino problem" established the concept of *neutrino oscillations*[1]. This phenomenon, later proven to exist by atmospheric neutrino measurements of Super-Kamiokande in 1998, revealed the neutrino to be a massive particle.

Today, it is an acknowledged fact that the neutrinos ν_α and their corresponding antiparticles $\bar{\nu}_\alpha$, which participate in weak interactions, occur with three[2] flavors $\alpha = e, \mu, \tau$ [32]. They are considered to be elementary particles and each of the neutrinos is linked to a corresponding charged lepton. Along with this charged lepton of the same flavor, the neutrino can be produced in a charged current weak interaction (e.g. an $\bar{\nu}_e$ is produced together with an e^-). Experiments measuring neutrinos produced in solar or atmospheric processes as well as man-made neutrinos from accelerators or nuclear reactors have provided in the last decades compelling results which demonstrate the

---

[1]The idea of neutrino oscillations was already suggested by B. Pontecorvo in 1957, proposing $\nu \leftrightarrow \bar{\nu}$ conversions, inspired by the $K^0 \leftrightarrow \bar{K}^0$ meson transitions [180].

[2]Actually for neutrinos with $m_\nu < M_Z/2$, where M_Z is the mass of the Z boson.

occurrence of transitions $\nu_\alpha \to \nu_\beta$ ($\alpha, \beta = e, \mu, \tau$) of one type of neutrino to another. The existence of these flavor oscillations imply a non-zero neutrino mass and is a prove that there has to exist physics beyond the Standard Model. At the same time, neutrino oscillations require the occurrence of neutrino mixing, which has its origin in the inequality of the weakly interacting flavor eigenstates $|\nu_\alpha\rangle$ ($\alpha = e, \mu, \tau$) and the (at least) three neutrino mass eigenstates $|\nu_i\rangle$ ($i = 1, 2, 3$). Instead, the flavor eigenstates can be described as coherent linear combinations of the mass eigenstates:

$$|\nu_\alpha\rangle = \sum_i U_{\alpha i}^* |\nu_i\rangle. \tag{1.1}$$

Assuming there are only three flavors participating in the mixing, the conversion between the bases can be expressed by the 3×3 unitary matrix U [180, 154] (also U_{PMNS}, named after Pontecorvo, Maki, Nakagawa and Sakata). Besides an additional factor, that is only relevant if neutrinos are of Majorana nature (i.e. that neutrinos are their own antiparticles), the U_{PMNS} mixing matrix can be parametrized in an analogous form as the CKM matrix known from the quark sector [47]:

$$U_{\text{PMNS}} = \begin{pmatrix} 1 & 0 & 0 \\ 0 & c_{23} & s_{23} \\ 0 & -s_{23} & c_{23} \end{pmatrix} \times \begin{pmatrix} c_{13} & 0 & s_{13}e^{-i\delta_{\text{CP}}} \\ 0 & 1 & 0 \\ -s_{13}e^{i\delta_{\text{CP}}} & 0 & c_{13} \end{pmatrix} \times \begin{pmatrix} c_{12} & s_{12} & 0 \\ -s_{12} & c_{12} & 0 \\ 0 & 0 & 1 \end{pmatrix}$$
$$\times \quad \text{diag}(1, e^{i\alpha_1/2}, e^{i\alpha_2/2}). \tag{1.2}$$

where $s_{ij} \equiv \sin\theta_{ij}$, $c_{ij} \equiv \cos\theta_{ij}$ and the mixing angles θ_{ij}. A non-zero Dirac phase δ_{CP} could lead to a CP non-conservation in neutrino oscillations, the two parameters α_1 and α_2 are the additional Majorana phases. The latter do not influence the oscillation probabilities.

It is possible to distinguish between two types of neutrino oscillation experiments. An *appearance* experiment measures the probability $P(\nu_\alpha \to \nu_\beta)$ and thus searches for an excess of neutrinos with flavor β in a flux of neutrinos ν_α. In contrast to this, *disappearance* experiments seek to measure a deficit in a neutrino flux of certain flavor, either relative to a predicted flux or a second measurement at a different distance to the source. This deficit is characterized by the survival probability of the particular flavor α via $P(\nu_\alpha \to \nu_\alpha)$.

Each of the first three rotation matrices in Eq. (1.2) is associated with a certain neutrino "sector", probed by different oscillation experiments. The (12) "solar" sector is related to the mixing angle θ_{12}, which is measured by solar neutrino experiments, such as SNO and Borexino or the reactor experiment KamLAND. Tested by both, $\nu_\mu \to \nu_e$ appearance and $\nu_e \to \nu_e$ disappearance experiments, the (13) sector contains the mixing angle θ_{13}, which was unknown for a long time. The "atmospheric" sector (23) is probed by experiments measuring $P(\nu_\mu \to \nu_\mu)$ ($P(\bar{\nu}_\mu \to \bar{\nu}_\mu)$) with an atmospheric or accelerator-based neutrino source as done by Super-Kamiokande, K2K, MINOS or T2K.

The probability of a neutrino which is produced as ν_α to be detected in flavor β after traveling a distance L is given by

$$P(\nu_\alpha \to \nu_\beta) = |A(\nu_\alpha \to \nu_\beta)|^2 = |\sum_i U_{\beta i} D(\nu_i) U_{\alpha i}^*|^2. \tag{1.3}$$

In Eq. (1.3), A describes the amplitude of the flavor transition, $U_{\alpha i}^*$ is the amplitude to observe the mass eigenstate ν_i in the initial flavor eigenstate ν_α and $U_{\beta i}$ to find ν_β in a ν_i initial state. The propagation of relativistic ν_i in vacuum[3] is given by $D(\nu_i)$, which can be described by $D(\nu_i) = \exp(-im_i^2 L/2E)$ [45] with the neutrino energy E, the mass of the eigenstate ν_i given by m_i and the distance traveled between source and detector L. For the probability of a neutrino to change flavor we then obtain

$$
\begin{aligned}
P(\nu_\alpha \to \nu_\beta) &= \left| \sum_i U_{\beta i}\, e^{-im_i^2 L/2E}\, U_{\alpha i}^* \right|^2 \\
&= \delta_{\alpha\beta} - 4 \sum_{i>j} \mathrm{Re}(U_{\alpha i}^* U_{\beta i} U_{\alpha j} U_{\beta j}^*) \sin^2(\Delta m_{ij}^2 L/4E) \\
&\quad + 2 \sum_{i>j} \mathrm{Im}(U_{\alpha i}^* U_{\beta i} U_{\alpha j} U_{\beta j}^*) \sin(\Delta m_{ij}^2 L/2E)\,, \qquad (1.4)
\end{aligned}
$$

with the mass squared differences $\Delta m_{ij}^2 \equiv m_i^2 - m_j^2$. For antineutrinos $P(\bar\nu_\alpha \to \bar\nu_\beta)$ the sign of the last term changes. It is an accepted convention that the small mass squared difference is associated with Δm_{12}^2 and it is known from experimental results that $|\Delta m_{21}^2| \ll |\Delta m_{31}^2|$. However, the sign of Δm_{31}^2 is to date not measured. As a consequence, the constellation of the neutrino masses (the neutrino "mass hierarchy"), which obeys with $m_1 < m_2 < m_3$ either normal ordering or with $m_3 < m_1 < m_2$ inverted ordering, remains an unanswered question. Constraints on the absolute neutrino mass are given by cosmological and astrophysical measurements. The Planck Collaboration [24] released in 2013 with

$$
\sum_i m_i < 0.23\,\mathrm{eV}, \quad \text{at } 95\,\% \text{ C.L.}
$$

an upper limit on the summed neutrino masses from the combination with other independent measurements, assuming three active neutrinos with degenerate masses.

In the 1960's R. Davis discovered with the Homestake experiment [92], using a radiochemical detection technique, a deficit in the flux of solar electron neutrinos compared to theoretical predictions of the standard solar model (SSM). A similar observation was made by the gallium radiochemical experiments GALLEX [36] and SAGE [1] in the early 1990's, and later by GALLEX/GNO [140], as well as the water-Cherenkov experiment Kamiokande [128]. In 2001 the combination of the ν_e flux measurements of the SNO and Super-Kamiokande experiments provided evidence of solar ν_e to change flavor [114, 28]. Subsequent measurements by SNO [27] were able to distinguish between electron neutrinos and the flux of μ and τ-neutrinos. In this way, SNO could demonstrate that the total neutrino flux from ^{8}B is consistent with expectations; the "solar neutrino problem" was finally solved. Recent measurements of the solar neutrino flux are conducted by the Borexino experiment [43]. KamLAND, a reactor $\bar\nu_e$ experiment at $\sim 180\,\mathrm{km}$ flux-weighted baseline, finally attested the theory of solar neutrino oscillation in 2002. It observed a deficit in the reactor neutrino flux and affirmed a large mixing angle of $\tan^2 \theta_{12} \approx 0.45$ [102] as explanation of the solar results[4]. Also,

---

[3]In matter the propagation eigenstates of the neutrinos change, which can also change the mixing angles and hence the oscillation probability. This is known as MSW (Mikheyev, Smirnov, Wolfenstein) effect [209, 160].

[4]In fact, the combination of a large mixing angle and the presence of the MSW effect in the matter of the sun explain the measurements of the solar neutrino flux.
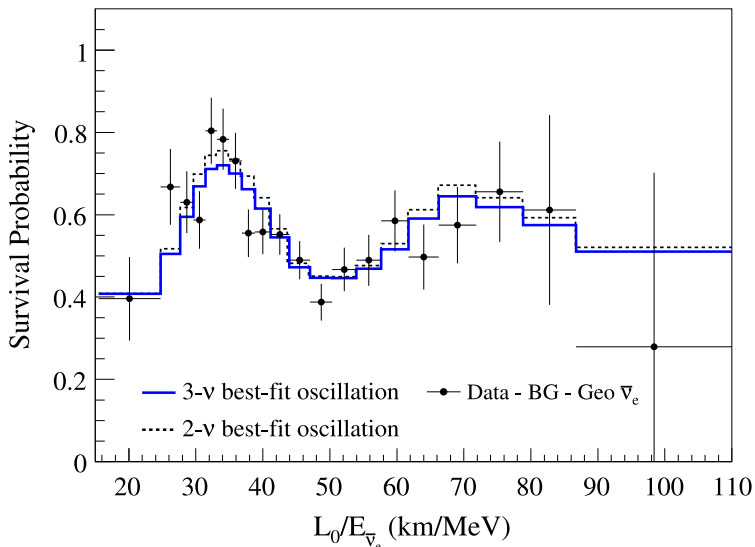
Figure 1.1: Ratio of the KamLAND measured $\bar{\nu}_e$ spectrum to the no-oscillation expectation as a function of L_0/E (black points). The average flux-weighted reactor baseline amounts to $L_0 = 180\,\mathrm{km}$. The blue solid line and the dashed line are the expectations from the unbinned maximum-likelihood analyses with two and three neutrino flavors (from [115]).

KamLAND proved as first experiment the periodic behavior of the survival probability by measuring the spectral shape of the neutrino energy (Fig. 1.1).

It was Super-Kamiokande in 1998 that proved the existence of neutrino oscillations by observing an asymmetry in the upwards and downwards pointing atmospheric μ-neutrino fluxes [113]. Other ν_μ disappearance experiments measure neutrino beams produced at particle accelerators. Long-baseline oscillation experiments probing the disappearance channel are K2K [29], T2K [11] and MINOS [23], the latter two recently still taking data. Due to relative measurements between the far detectors at several hundred kilometers and near neutrino detectors in the vicinity of the beam exit, the precision on the mixing parameters θ_{23} and $|\Delta m_{32}^2|$ was further improved. The first event-by-event evidence of ν_τ appearance in a $\nu_\mu \to \nu_\tau$ measurement was put forward by OPERA with currently 4 ν_τ events for 0.23 ± 0.04 expected background events. The no-oscillation hypothesis is excluded at $4.2\,\sigma$ [144].

Current *global analyses* take into account experimental data accumulated over the past decades and provide combined results on the mass and mixing parameters. Table 1.1 shows the results of the global fit presented in Ref. [111], which is based on neutrino oscillation measurements up to June 2014, including the Double Chooz Gd-III analysis of Ref. [12]. Questions addressed by upcoming oscillation experiments are related to the sign of $\Delta m_{31}^2 (\Delta m_{32}^2)$, whether CP violation is found in the leptonic sector or whether the data implies maximal atmospheric neutrino mixing (i.e. $\sin^2 \theta_{23} = 0.5$). Future experiments trying to solve these issues are amongst others Noνa [40] (running since 2014), PINGU [136], JUNO [151], Hyper-Kamiokande [4], LBNO [25] and LBNE [20].

Table 1.1: Global analysis results [111] for the mass and mixing parameters for 3ν oscillations for normal (NO) and inverted (IO) mass ordering. The upper and lower uncertainties limit the 1σ range of the best fit results. The CP violating phase is taken as defined over the interval $\delta_{\mathrm{CP}} \in [0, 2\pi]$.

Parameter	Best fit	
	NO	IO
$\sin^2 \theta_{12}$ (θ_{12} [°])	0.323 ± 0.016 (34.6 ± 1.0)	
$\sin^2 \theta_{23}$ (θ_{23} [°])	$0.567^{+0.032}_{-0.124}$ ($48.9^{+1.8}_{-7.2}$)	$0.573^{+0.025}_{-0.039}$ ($49.2^{+1.5}_{-2.3}$)
$\sin^2 \theta_{13}$ (θ_{13} [°])	0.0226 ± 0.0012 ($8.6^{+0.3}_{-0.2}$)	0.0229 ± 0.0012 (8.7 ± 0.2)
Δm^2_{21} [10^{-5}eV^2]	$7.60^{+0.19}_{-0.18}$	
Δm^2_{31} [10^{-3}eV^2]	$2.48^{+0.05}_{-0.07}$	$2.38^{+0.05}_{-0.06}$
δ_{CP} [π]	$1.41^{+0.55}_{-0.40}$	1.48 ± 0.31

1.2 The search for non-zero θ_{13}

Owing to the smallness of θ_{13} and the fact that it was the last unknown mixing angle, the possibility to measure the CP violating phase δ_{CP} requires the detection of a non-zero θ_{13}. Moreover, the terms in the appearance probability $P_{\mathrm{matter}}(\nu_\mu \to \nu_e)$ and the disappearance probability $P_{\mathrm{matter}}(\nu_\alpha \to \nu_\alpha)$ for neutrino oscillations in matter, which are sensitive to the neutrino mass ordering, depend both on θ_{13} [200, 174]. As a result, the prospects of future neutrino oscillation experiments on their ability to observe CP violation or solve the mass hierarchy problem is directly linked to the value of θ_{13}.

One of the pioneering experiments attempting to measure antineutrino disappearance started to take data in 1997, even before positive proof for the existence of neutrino oscillations had been provided. The CHOOZ experiment [37, 38], precursor experiment of Double Chooz (see Chapter 2), sought to provide additional insight in the flavor oscillation phenomenon and assist to answer whether the observations with atmospheric neutrinos were caused by $\nu_e \leftrightarrow \nu_\mu$ or $\nu_\mu \leftrightarrow \nu_\tau$ flavor changes. It was the first reactor neutrino experiment able to explore the atmospheric mass regime $|\Delta m^2_{\mathrm{atm}}| \equiv |\Delta m^2_{13}|$ down to 10^{-3} eV^2, as suggested by the atmospheric neutrino experiments. Located at the same laboratory as today's Double Chooz far detector in 1 km distance from the Chooz reactor cores, it consisted of a target vessel filled with 5 t gadolinium-doped liquid scintillator surrounded by 70 cm (17 ton) of undoped scintillator with 192 eight-inch photomultiplier tubes (PMTs) mounted on the walls (Fig. 1.2a). The detection process of electron antineutrinos is common to all experiments of this kind and will be discussed in Section 1.3.2. Limited by the degradation of the scintillator liquid, CHOOZ stopped to take data in summer 1998, finishing after almost a year of live time. More than 40 % of the data were a "background only" measurement with the antineutrino source, two nuclear reactor cores, turned off. Having collected 2991 $\bar{\nu}_e$ candidates the observed-to-predicted ratio of events was estimated to be $R = 1.01 \pm 2.8\,\%\,(\mathrm{stat}) \pm 2.7\,\%\,(\mathrm{syst})$ (Fig. 1.2b). Hence no evidence for $\bar{\nu}_e \to \bar{\nu}_x$ ($x = \mu, \tau$) oscillations was found. It should

(a) CHOOZ detector design (from [37]).

(b) Ratio of the energy-binned CHOOZ data to the expected $\bar{\nu}_e$ spectrum (from [38]), the dashed line corresponds to the no-oscillation prediction. The errors are statistical.
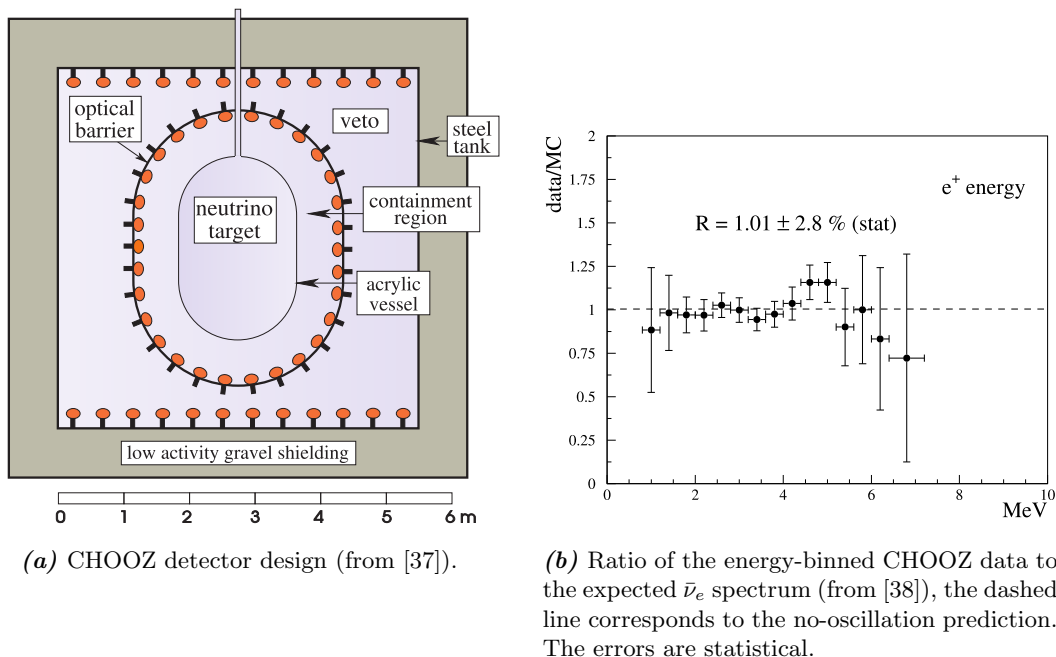
Figure 1.2: The CHOOZ experiment.

take more than a decade to outreach the CHOOZ limit on the mixing angle θ_{13} and to finally prove $|U_{e3}| = \sin\theta_{13} \neq 0$. For $|\Delta m_{13}^2| = 2.4 \times 10^{-3} \text{eV}^2$ CHOOZ could establish $\sin^2 2\theta_{13} \leq 0.15$ at 90 % C.L.

By the end of the CHOOZ runtime, the Palo Verde [52, 53] experiment commenced operation collecting one year of data. The Palo Verde Nuclear Generating Station in Arizona consisted of three reactors, two at 890 m and one at 750 m distance from the segmented neutrino detector. The latter was built up of 6×11 acrylic cells, filled with in total 11 t of Gd-doped scintillator. PMTs were installed at each end of the 9 m long cells to detect the neutrino signal. With an observed-to-predicted ratio in the $\bar{\nu}_e$ candidates of $R = 1.01 \pm 2.4\%$ (stat) $\pm 5.3\%$ (syst) Palo Verde could not outperform the CHOOZ result due to larger systematic uncertainties.

Another possibility to have access to θ_{13} are long-baseline experiments searching for ν_e appearance in a ν_μ beam. The drawback of these experiments is the dependence of a θ_{13} measurement on many oscillation parameters: the appearance channel is not only sensitive to $\pm\Delta m_{13}^2$, θ_{23} and θ_{13}, it also depends on Δm_{21}^2, θ_{12} and the unknown δ_{CP}. Thus the results on the allowed regions of $\sin^2 2\theta_{13}$ are usually visualized for a specific mass hierarchy in bands as a function of $\delta_{\text{CP}} = [0, 2\pi]$. However, by means of a ν_e appearance measurement, a statement on the hypothesis $\theta_{13} = 0$ is possible [174].
The first indication of a non-zero θ_{13} was provided by T2K (Tokai to Kamioka) in July 2011 [3]. The neutrino beam is produced at J-PARC (Tokai, Japan) and directed with 2.5° off-axis to Super-Kamiokande, a water-Cherenkov detector with 22.5 kton fiducial volume in 295 km distance at Kamioka. An off-axis beam alignment narrows the ν_μ energy spectrum and shifts the spectral shape to have the largest intensity at the first oscillation maximum of the ν_e appearance. Two near detectors monitor beam prop-

erties, such as direction, intensity, profile and flavor content. T2K found six events exceeding the expectation and systematic uncertainty of 1.5 ± 0.3 (5.5 ± 1.0) events if $\sin^2 2\theta_{13} = 0$ (0.1), which excluded the no-oscillation hypothesis at $2.5\,\sigma$ statistical significance. In 2014 their result [10] had improved to an observation of 28 events along with an energy distribution consistent with an appearance signal. In total 4.92 ± 0.55 were expected if $\theta_{13} = 0$ or 21.6 for $\theta_{13} = 0.1$ and $\delta_{\mathrm{CP}} = 0$. The significance for a non-zero θ_{13} amounted to $7.3\,\sigma$.

In October 2011 the MINOS (Main Injector Neutrino Oscillation Search) experiment presented results on ν_e appearance [22]. The $3\,\mathrm{GeV}$ neutrino beam is produced by protons on the NuMI target located at Fermilab. It is sent $735\,\mathrm{km}$ downstream to the far detector at the Soudan underground laboratory. The detector consists of alternating layers made of $2.54\,\mathrm{cm}$ thick steel and $1\,\mathrm{cm}$ plastic scintillator with a total mass of $5.4\,\mathrm{kton}$ read out by optical fibers and multianode PMTs. A toroidal magnetic field is applied to focus particles with negative charge. In total 62 events were counted for an expectation of $49.6 \pm 7\,(\mathrm{stat}) \pm 2.7\,(\mathrm{syst})$ events if $\theta_{13} = 0$, disfavoring the hypothesis of $\theta_{13} = 0$ at $89\,\%$ C.L.

The same year, end of 2011, the reactor antineutrino experiment Double Chooz reported an indication of $\bar{\nu}_e$ disappearance [94, 5]. After 101 days of runtime 4121 neutrino candidates were found at the far detector at $1\,\mathrm{km}$ distance from the neutrino source. The ratio of observed events to the prediction was $R = 0.944 \pm 0.016\,(\mathrm{stat}) \pm 0.040\,(\mathrm{syst})$. An analysis of the energy-binned event rate and spectral shape resulted in $\sin^2 2\theta_{13} = 0.086 \pm 0.041\,(\mathrm{stat}) \pm 0.030\,(\mathrm{syst})$ and excluded the $\theta_{13} = 0$ hypothesis at $94.6\,\%$ C.L. In combination with T2K and MINOS the Double Chooz result yields constraint of $0.003 < \sin^2 2\theta_{13} < 0.219$ at $3\,\sigma$. The Double Chooz analysis and results are further discussed in Chapter 3.

The Daya Bay (cf. next section) experiment announced in April 2012 the discovery of θ_{13} [34]: from the analysis of 55 days live-time exposure a value of $\sin^2 2\theta_{13} = 0.092 \pm 0.016\,(\mathrm{stat}) \pm 0.005\,(\mathrm{syst})$ was found with a rate-only fit with a significance of $5.2\,\sigma$ for $\theta_{13} \neq 0$. Shortly after, the RENO (details in the next section) experiment [30] claimed after 229 days of data taking to have measured $\sin^2 2\theta_{13} = 0.113 \pm 0.013\,(\mathrm{stat}) \pm 0.019\,(\mathrm{syst})$, excluding a zero value of θ_{13} at $4.9\,\sigma$ significance.

1.3 Recent reactor antineutrino experiments and θ_{13}

A measurement of specific oscillation parameters of Eq. (1.2) has to be designed so that it is sensitive to a particular mass regime Δm^2 (cf. Eq. (1.4)). The oscillation pattern intended to be measured has to be developed before or at the detector location, i.e. the neutrinos need to have the possibility to oscillate before their detection. The survival probability of a reactor antineutrino can be computed from Eq. (1.2) and (1.4):

$$P(\bar{\nu}_e \to \bar{\nu}_e) = 1 - 4\cos^2\theta_{12}\cos^2\theta_{13}\sin^2\theta_{12}\cos^2\theta_{13}\sin^2\frac{\Delta m_{21}^2 L}{4E}$$

$$- 4\cos^2\theta_{12}\cos^2\theta_{13}\sin^2\theta_{13}\sin^2\frac{\Delta m_{31}^2 L}{4E}$$

$$- 4\sin^2\theta_{12}\cos^2\theta_{13}\sin^2\theta_{13}\sin^2\frac{\Delta m_{32}^2 L}{4E}\,, \tag{1.5}$$
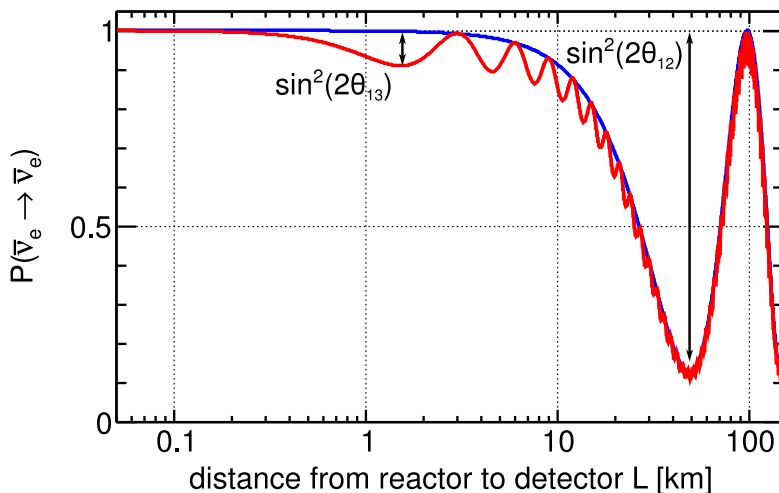
Figure 1.3: Survival probability of electron antineutrinos (Eq. (1.5)) of a fixed energy $E = 3\,\text{MeV}$ as a function of the distance L from the neutrino source to the detector. The red line was computed with the global mixing parameters from Table 1.1. For the blue dashed line the value $\theta_{13} = 0$ was adopted, which isolates the neutrino oscillation in the solar mass regime of Δm_{21}^2. The amplitude of first minimum of the survival probability is given by $\sin^2 2\theta_{13}$ (see red line), while the amplitude of the solar mixing (blue line) corresponds to $\sin^2 2\theta_{12}$.

assuming the absence of matter effects. The arguments in the trigonometric functions of Eq. (1.5) can be converted to SI units by

$$\Delta m_{ij}^2 \frac{L}{4E} = 1.27 \Delta m_{ij}^2 (\text{eV}^2) \frac{L(\text{km})}{E(\text{GeV})} \, . \tag{1.6}$$

Fig. 1.3 illustrates Eq. (1.5) as a function of L. The survival probability clearly exhibits an alternating behavior, which visualizes the periodic nature of neutrino *oscillations*. The oscillation frequency is linked to Δm_{ij}^2, whereas the amplitude of the oscillation is modified by the θ_{ij}. Furthermore, it is possible to see that the ratio L/E of the distance of the neutrino source to the detector and the neutrino energy determines the mass range to which the experiment will be sensitive. Hence, a reactor antineutrino experiment which aims to measure θ_{13} should be adapted to satisfy $E/L \approx 3 \cdot 10^2 [\text{km/GeV}] \approx 1/|\Delta m_{\text{atm}}^2|$. As the average neutrino energy is $\overline{E} \approx 3\,\text{MeV}$ a flux deficit caused by θ_{13} can be observed in 1 km distance from the reactor cores. Since the mass-squared difference Δm_{21} is much smaller than Δm_{31} ($|\Delta m_{12}^2|/|\Delta m_{31}^2| \approx 0.03$), Eq. (1.5) can be simplified to

$$P(\bar{\nu}_e \rightarrow \bar{\nu}_e) \simeq 1 - \sin^2 2\theta_{13} \cdot \sin^2 \left(1.27 \, \frac{\Delta m_{13}^2 \, [\text{eV}^2] \, L \, [\text{m}]}{E_\nu \, [\text{MeV}]} \right) , \tag{1.7}$$

in the case the survival probability is measured with reactor antineutrinos at distances of one kilometer and less. This allows a clean θ_{13} measurement, independent of unknown mixing parameters.
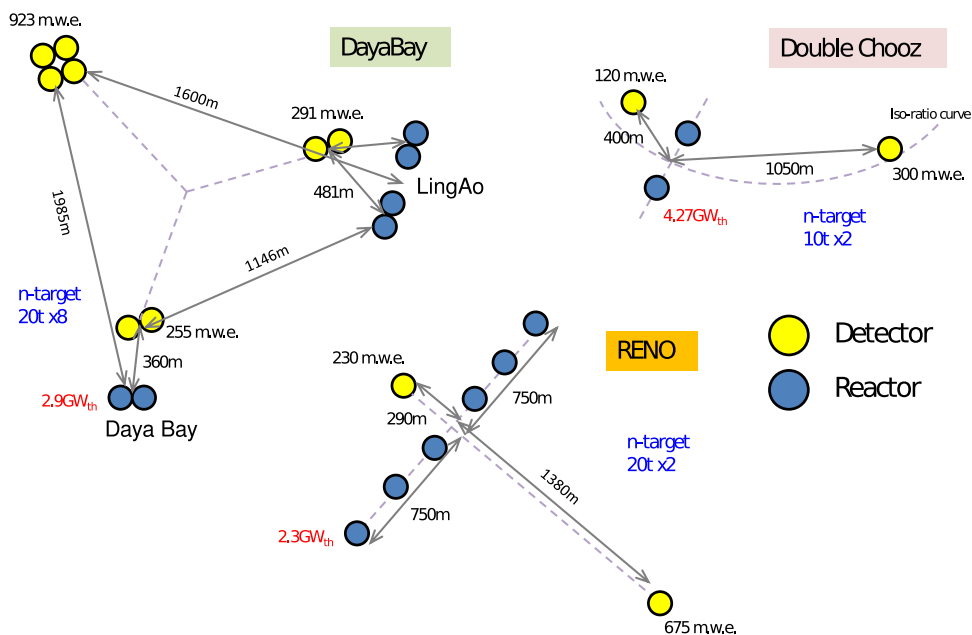
Figure 1.4: *Reactor-detector configurations of the three current reactor antineutrino experiments measuring θ_{13}: Daya Bay, Double Chooz and RENO (from [145]).*

The CHOOZ and Palo Verde experiments had to face systematic uncertainties on the reactor flux normalization of a few percent. In oder to reduce these, the most precise flux measurement to date, provided by the Bugey Collaboration [93], was used to "anchor" the flux prediction. Future reactor experiments were therefore planned to exploit the multi detector principle: identical detectors measure both the unoscillated and the oscillated neutrino flux, thus reducing the systematic uncertainties related to neutrino production and detection. A larger target volume or an increased reactor flux can enhance the statistics of measured neutrino events. However, a simple experimental configuration with e.g. two reactors and two detectors enables to achieve an isoflux condition, for which the ratio of fluxes from the reactors seen by each detector is the same. This allows for a maximal correlation and cancellation of the near-far reactor flux systematics. In addition should a better background reduction with an improved shielding and low radioactivity materials enhance the sensitivity. Therefore the Buffer volume (see also Section 2.1.1) was added to the former CHOOZ detector design.

Current reactor $\bar{\nu}_e$ experiments offer a detector design which is similar to the Double Chooz detector layout (cf. Section 2.1). The main detector is formed by four cylindrical volumes. The innermost volume, the neutrino target, is filled with liquid scintillator (LS) doped with 0.1% gadolinium (Gd). It is surrounded by the "Gamma Catcher", an undoped LS layer, supposed to contain the energy of gammas which are produced by neutrino interactions and escape the target volume. These two volumes are enclosed by the Buffer, a vessel filled with oil and with PMTs installed at the walls. A fourth detector layer is formed by an active veto, which is optically separated from the other volumes. It is either realized in form of a LS detector (Double Chooz) or water-Cherenkov detector (Daya Bay and RENO).
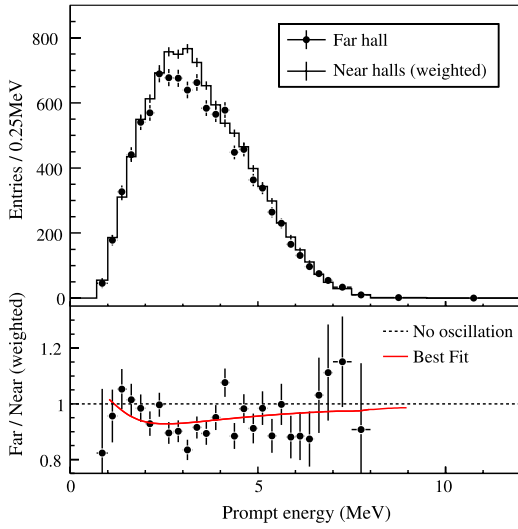
(a) Top: Prompt energy spectrum measured at the far hall (black points) and the no-oscillation prediction (black line) derived from the measurements of the two near halls. The spectra were background subtracted and the uncertainties are statistical only. Bottom: Ratio of the measured spectrum and the no-oscillation prediction, the red solid line corresponds to the best fit. The figure is from [34].
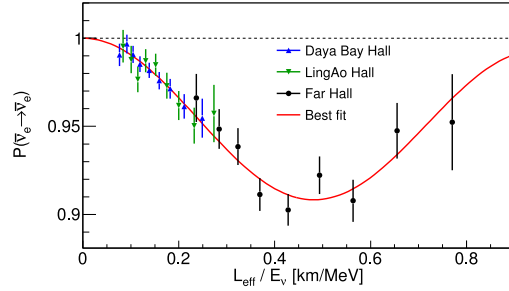
(b) Ratio of the prompt energy spectra measured at the three detector halls and a no-oscillation prediction as a function of $L_{\rm eff}/E_\nu$. The neutrino flux seen in each hall was converted in an effective flux by computation of effective distances $L_{\rm eff}$ between the reactors and the detectors (legend modified, originally from [35]). The error bars are statistical only. The red solid line shows the survival probability using the best fit results of Ref. [35].

Figure 1.5: Daya Bay antineutrino spectrum.
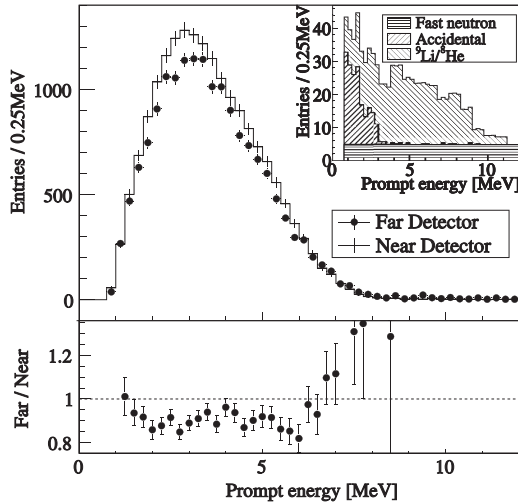
(a) Top: Prompt energy spectrum at the far detector (black points) and the no-oscillation prediction retrieved from the near detector measurement (solid line). Bottom: Ratio of the far detector spectrum and the no-oscillation prediction.
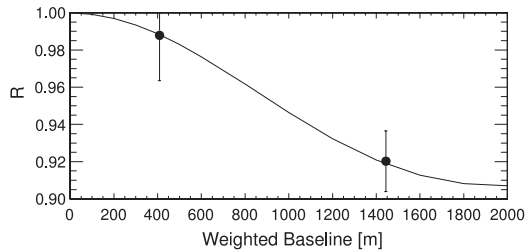
(b) Ratio of the $\bar{\nu}_e$ events and the expectation for $\theta_{13} = 0$. The solid line represents the best fit of the survival probability as a function of the flux-weighted baselines.

Figure 1.6: RENO antineutrino spectrum (from [30]).

The experimental configuration of the Daya Bay project [34] features six reactor cores, each of $2.9\,\mathrm{GW_{th}}$, and six detectors with $20\,\mathrm{t}$ Gd-doped LS targets. Four of the cores are placed at the LingAo reactor site, while two are located at the Daya Bay site. The six detectors are housed in three experimental halls, two with $260\,\mathrm{m.w.e.}$ (meter water equivalent) overburden in the vicinity of the power stations (Fig. 1.4): one $480\,\mathrm{m}$ close to LingAo reactors and the other one $360\,\mathrm{m}$ from the Daya Bay reactors. A far hall with three detectors is located at $1.65\,\mathrm{km}$ flux weighted baseline and is shielded by $860\,\mathrm{m.w.e.}$ rock overburden, which lowers the muon rate by a factor 17 compared to the near halls. Daya Bay provides the best result on θ_{13} at present. In 2014, after 217 days of running, the experiment determined $\sin^2 2\theta_{13} = 0.090^{+0.008}_{-0.009}$ in a neutrino rate and spectral shape analysis, fitting mixing angle and the squared mass difference at the same time [35]. A result consistent with the MINOS and T2K $\nu_\mu \rightarrow \nu_\mu$ measurements was found for the mass splitting. The spectra and the observed-to-predicted ratio measured by the Daya Bay experiment are given in Fig. 1.5.

RENO [30] (Reactor Experiment for Neutrino Oscillation) observes the $\bar{\nu}_e$ flux of six reactor cores (each of $2.8\,\mathrm{GW_{th}}$) with two neutrino detectors, each filled with $16\,\mathrm{t}$ of Gd-loaded LS. The reactors are aligned in a row and the detectors are placed at $294\,\mathrm{m}$ and $1383\,\mathrm{m}$ perpendicular distance from the center of the reactor array (Fig. 1.4). At the far detector site the experiment is shielded by $450\,\mathrm{m.w.e.}$ and at the near by $120\,\mathrm{m.w.e.}$ overburden. The RENO measurements are shown in Fig. 1.6.

1.3.1 Antineutrino source

The origin of the antineutrinos measured by reactor experiments is related to the fissions and associated processes in the nearby nuclear reactor cores. The fuel components contributing to the neutrino production consist mainly of the four isotopes ^{235}U, ^{239}Pu, ^{238}U and ^{241}Pu. Fission reactions of the fuel isotopes are induced by thermal neutrons (except for ^{238}U). A fission releases energy carried away by lighter isotopes and neutrons, the latter maintain the chain reaction running (Fig. 1.7). The produced light isotopes, also called fission fragments, are often neutron-rich and unstable. This induces them to undergo β-decay which creates ~ 6 $\bar{\nu}_e$ per fission[5] [45]. For the detection with a LS detector, however, only those with $E_\nu > 1.8\,\mathrm{MeV}$ are of importance (cf. Eq. (1.9)). Table 1.2 summarizes the number of emitted $\bar{\nu}_e$ with energies above $1.8\,\mathrm{MeV}$ and the released energy per fission for the four fuel isotopes. Nuclear reactors represent a neutrino source of pure electron flavor with large fluxes. In the case of Double Chooz $\sim 10^{21}$ neutrinos are emitted per second.

Detailed knowledge about the thermal power, fissions per second, energy released per fission, the core composition, the neutrinos produced per fission and their energy spectrum is important, especially in a θ_{13} measurement with a far detector solely. With the goal to reduce the $\sim 3\,\%$ uncertainty on the flux normalization, the Double Chooz analysis utilizes the precise Bugey-4 flux measurement (further details in Section 3.1.1) to bypass the absence of a near detector in the first years of the experiment in the same way as CHOOZ and Palo Verde.

---

[5]Another neutrino producing process is the capture of a fast neutron on ^{238}U, resulting in two β-decays to ^{239}Pu.
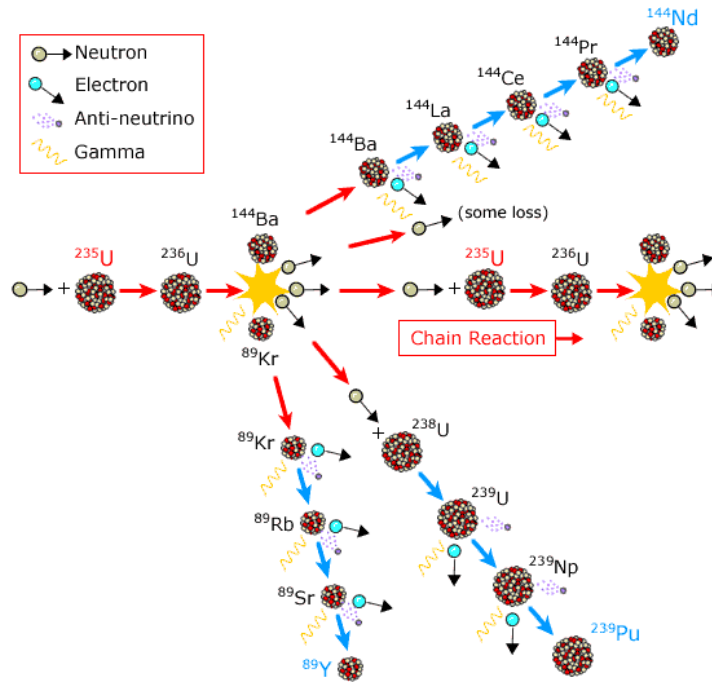
Figure 1.7: Fission in a nuclear reactor (from [137]): Induced fission of a ^{235}U atom produces neutrons and lighter neutron-rich isotopes (fission fragments). The emitted neutrons keep the chain reaction alive. Electron antineutrinos are created in the β-decays of the fission fragments.

The electron spectra emitted by the fission products of ^{235}U, ^{239}Pu and ^{241}Pu were measured at the Institut Laue-Langevin (ILL) in Grenoble [190, 108, 121]. Thermal neutrons from a research reactor were used to cause fissions of the three isotopes which were evaporated on thin nickel foils inside a beta spectrometer.

Since β-decays are mostly three body decays in which the recoil energy of the daughter nucleus can be neglected, the conversion from a measured beta-spectrum to the neutrino spectrum is possible due to energy conservation. For a single β-branch with endpoint energy Q_β this is simply given by $E_{\bar{\nu}_e} = Q_\beta - E_e$. However, thousands of β-branches need to be taken into account in the spectra conversion as well as energy-dependent corrections. New approaches for the calculation of the $\bar{\nu}_e$ spectra have been presented in Ref. [161] and [134]. The first approach constructed the spectra *ab initio* using known β-branches from databases, the missing part to completely reproduce the ILL measurements, was fitted by virtual branches. After all, a 3 % increase of the flux normalization was observed for the new flux prediction [161]. This rise in flux normalization was confirmed by the second approach, a calculation based on virtual branches solely, fitted to the ILL electron spectra [134]. Both computations applied corrections on the β-branch level. Based on the new flux normalizations, a reanalysis using the results of short-baseline reactor experiments with baselines of few tens to several hundred meters revealed a deficit of ~ 6 % in the measured fluxes with 98.6 % C.L. significance [158]. As a consequence, speculations about a fourth mass eigenstate revived. This fourth eigenstate could induce mixing into a "sterile" neutrino (e.g. a right-handed neutrino) which does not interact weakly. The analysis of the past reactor measurements suggest $|\Delta m^2_{\text{new}}| > 1.5\,\text{eV}^2$ and a mixing angle of $\sin^2 2\theta_{\text{new}} = 0.14 \pm 0.08$ at 95 % C.L. [158].

Table 1.2: Total number of emitted $\bar{\nu}_e$ [133] with energies above 1.8 MeV and released energy per fission [153].

isotope	$\bar{\nu}_e$ per fission	released energy per fission [MeV]
^{235}U	1.92 ± 0.037	202.36 ± 0.26
^{238}U	2.38 ± 0.048	205.99 ± 0.52
^{239}Pu	1.45 ± 0.031	211.12 ± 0.34
^{241}Pu	1.83 ± 0.035	214.26 ± 0.33

Recent and future experiments at nuclear reactors searching for neutrino oscillations into sterile eigenstates are STEREO [46], DANSS [91], Neutrino-4 [192] and SoLiδ [215]. Also, the SOX [44] experiment will look for sterile neutrinos with strong β-decay sources.

1.3.2 Neutrino detection

Electron antineutrinos produced in nuclear reactors have energies $E_\nu < 10$ MeV. Since neutrinos interact weakly, the detection rates are – owing to the $\mathcal{O}(10^{-19}\,\mathrm{b})$ cross sections – small, even at strong sources as nuclear power plants. The inverse beta decay (IBD) reaction is a CC (charged current) interaction and was the reaction used to detect neutrinos for the first time back in 1956 [85]. An electron antineutrino interacts with a proton creating a positron and a free neutron (Fig. 1.8a):

$$\bar{\nu}_e + p \rightarrow e^+ + n\,. \tag{1.8}$$

This type of interaction is a practicable detection method in hydrogen-rich targets, such as organic liquid scintillators, as the energy dependence of IBD reactions on hydrogen nuclei can be considered to be the same as on free protons at rest. Due to energy and momentum conservation is the energy threshold given by

$$E_\nu^{\mathrm{th}} = \frac{(m_e + M_p)^2 - M_p^2}{2M_p} = 1.806\,\mathrm{MeV}\,. \tag{1.9}$$

Since the threshold for other antineutrino flavors is too high to produce a μ^+ or τ^+ in a neutrino-proton reaction, this detection channel is sensitive to electron flavor exclusively. The cross-section of $\bar{\nu}_e$ IBD interactions on hydrogen is analytically well-known. In its simplified form, it can be expressed by [204]

$$\sigma_{\mathrm{IBD}}(E_\nu) = K \cdot (E_\nu - \Delta)\sqrt{(E_\nu - \Delta)^2 - m_e^2}\,, \tag{1.10}$$

with the difference in rest mass between a neutron and a proton $\Delta = M_n - M_p = 1.293$ MeV and $K = 0.961 \times 10^{-43}\,\mathrm{cm}^2/\mathrm{MeV}^2$, which includes the neutron lifetime from the MAMBO-II measurement [179]. The reaction products of IBD interactions create a distinct coincidence signal in the detector, which enables to discriminate between a neutrino event and background. This twofold coincidence, consisting of a prompt and a delayed energy deposition, is explained further in the following paragraphs.
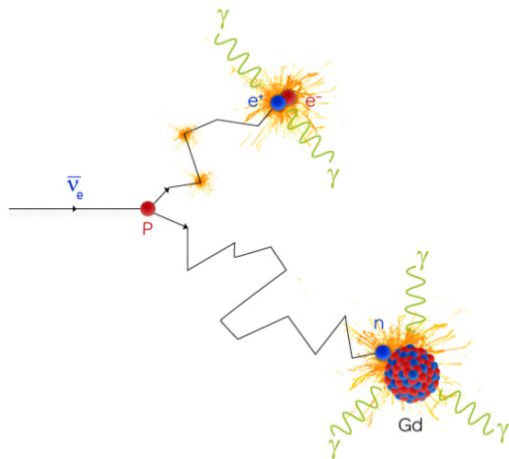
(a) Neutrino detection via IBD reaction with subsequent neutron capture on gadolinium.
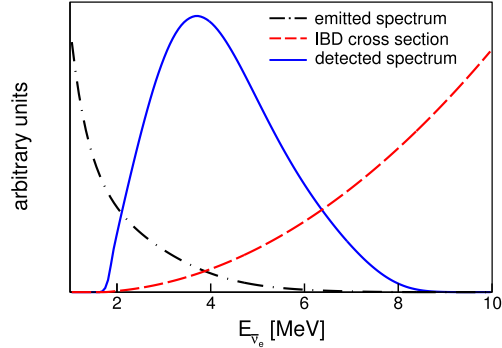
(b) Neutrino spectrum detected via IBD reactions (blue line): It is the product of the emitted reactor spectrum (black dash-dotted line) and the IBD cross section (red dashed line) (by courtesy of A. Collin).

Figure 1.8: The inverse beta decay (IBD) reaction.

Prompt event

The positron produced in the IBD reaction loses its kinetic energy within picoseconds in ionizations and annihilates with an electron. This energy deposition forms the prompt event of the IBD coincidence signal. Since recoil energy of the neutron – which is created along with the positron – is small compared to the neutrino energy, the kinetic energy of the positron is directly linked to the neutrino energy. Actually, the visible energy E_{vis} is measured with the neutrino detector. This quantity is a calorimetric estimate of the absolute energy deposited in the detector. Expressed in terms of visible energy, the prompt signal will result in a signal of

$$E_{\mathrm{vis},e^+} \simeq E_{\mathrm{kin},e^+} + 2m_e \simeq E_\nu - \Delta + m_e = E_\nu - 0.728\,\mathrm{MeV}\,. \qquad (1.11)$$

The minimum energy observable in the detector is, according to Eq. (1.9), given by $E_{\mathrm{vis}}^{\mathrm{th}} \approx 1\,\mathrm{MeV}$. Hence, the measured prompt spectrum is related to the neutrino spectrum: it is formed by the product of the neutrino energy spectrum and the cross section of the IBD reaction (Fig. 1.8b), shifted by $0.8\,\mathrm{MeV}$ and smeared by the energy resolution of the detector.

Delayed event

The neutron originating from the IBD reaction loses energy in scatterings on hydrogen atoms until it is captured - in most of the cases - on Gd or hydrogen (H) nuclei. Owing to the large abundance of hydrogen and the size of the scattering cross section, the probability of an elastic scattering exceeds the neutron capture probability by at least an order of magnitude. Therefore a large fraction of neutrons, which are created with $\sim 15\,\mathrm{keV}$ kinetic energy in the IBD process, reach the thermal energy regime ($E_{\mathrm{kin}} \approx 0.025\,\mathrm{eV}$) before they are caught on a nucleus. As a result of the large

Table 1.3: Natural abundances, thermal neutron capture cross sections and total gamma energies of radiative neutron captures on gadolinium [135]. The uncertainties on the gamma energies are less than 0.01 %.

^{x}Gd isotope	abundance	$\sigma_{\text{n-cap}}$ [b]	total gamma energy [keV]
152	0.2 %	735 ± 20	6247
154	2.2 %	85 ± 12	6435
155	14.8 %	$(6.09 \pm 0.05) \cdot 10^4$	8536
156	20.5 %	1.8 ± 0.7	6360
157	15.7 %	$(2.540 \pm 0.008) \cdot 10^5$	7937
158	24.8 %	2.2 ± 0.2	5943
160	21.9 %	1.4 ± 0.3	5635

scattering cross section, the neutron capture event happens with an average time delay relative to the prompt energy deposition, allowing to identify neutrino interactions by this coincidence pattern.

The neutron capture excites the nucleus (e.g. Gd), which leaves the short-lived excited state by the release of excessive energy in form of a gamma cascade:

$$_{Z}^{A}\text{Gd} + n \rightarrow {}_{Z}^{A+1}\text{Gd}^* \rightarrow {}_{Z}^{A+1}\text{Gd} + \sum_i \gamma_i \,. \tag{1.12}$$
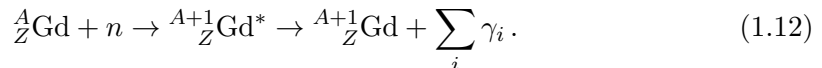
For a neutron capture on Gd the sum of gammas amounts to $\sum_i E_{\gamma,i} \approx 8\,\text{MeV}$. Neutron capture on H yields a single gamma with $2.224\,\text{MeV}$. The isotopes of the rare earth element Gd possess high cross sections for radiative neutron capture, as given in Table 1.3. Therefore the mean capture time in LS doped with 1 % Gd decreases to $\tau_{\text{cap}} \sim 30\,\mu\text{s}$ compared to the unloaded liquids in which the mean capture time is about $\tau_{\text{cap}} \sim 200\,\mu\text{s}$ and dominated by H-captures.

The Gd-loading thus brings along two major advantages which help to reduce backgrounds:

- the high gamma energies of $\sim 8\,\text{MeV}$ yield a delayed energy deposition above the detected energies of natural radioactivity,

- the shortened τ_{cap} allows to shorten the window in which the coincidence is searched.

Two detection channels of the neutrino interaction via IBD reactions are accessible in Gd-doped organic LS. The standard detection channel is based on delayed neutron captures on Gd nuclei. Besides this, neutrino candidates can be selected by the $2.2\,\text{MeV}$ neutron captures on H. Depending on the detection channel, the actual target volume is either formed by the Gd-loaded target or both the target and the Gamma Catcher volume. The H-channel analysis therefore incorporates a larger fiducial volume, the increase in neutrino rate is for the Double Chooz experiment given by a factor of two. However, the background contribution also increases and the signal-to-background ratio drops. Although this analysis approach is more challenging, the Double Chooz Collaboration provided the first H-based θ_{13} measurement in history with a LS detector in 2013 [8].

Chapter 2

The Double Chooz experiment

In this chapter, the experimental concept of the Double Chooz (DC) experiment and the layout of the two detectors is described. Furthermore, the Double Chooz data sets, on which the different DC θ_{13} analyses are based, will be discussed. Details of the data analysis are given in chapter 3, including the neutrino candidate and background extraction as well as the different approaches to determine the oscillation parameter θ_{13}.

The DC experiment is located at the Électricité de France (EDF) nuclear power plant in Chooz (France) featuring two N4 reactor cores, each of 4.25 GW thermal power (Fig. 2.1). According to Eq. (1.7), the mixing angle θ_{13} is directly linked to the oscillation probability at ~ 1 km distance to the reactor cores and can be extracted from a measurement of the neutrino rate deficit and spectral shape distortion. In order to eliminate systematic uncertainties related to the predicted reactor flux and neutrino detection, the DC experiment makes use of a two detector principle. Two identical detectors are built, a near detector (ND) measures the unoscillated neutrino flux at 400 m distance, while a far detector (FD) is placed near the first minimum of Eq. (1.7) at 1050 m distance from the reactor cores. In the relative measurement of the event rate and energy distribution any uncertainty correlated between the two detectors will then cancel out. The FD commenced operation in April 2011, the ND construction was completed end of 2014. Both detectors are located underground, the FD was built in the experimental hall of the preceding CHOOZ experiment, covered by 300 meter water equivalent (m.w.e.) rock shielding, whereas the ND is at a depth of 120 m.w.e. As the DC experiment started data taking with a single detector, the oscillation analysis was performed by the comparison of the measured neutrino candidate rate and spectral shape to a prediction. Further information on the experimental setup, concept and analysis can be found in several DC publications, e.g. [5, 6, 12].

2.1 Detector description

Double Chooz is a liquid scintillator experiment, for which each of the two detectors (illustrated in Fig. 2.2) consists of four nested concentric cylinders. These are filled with different liquids, depending on the purpose of the particular sub-volume. The three innermost sub-volumes form the *inner detector (ID)*, which is surrounded by the *inner veto (IV)* volume. All four cylindrical volumes constitute the *main detector* and are accessible via a *chimney*, which is placed at the detector top and aligned to the vertical detector symmetry axis.
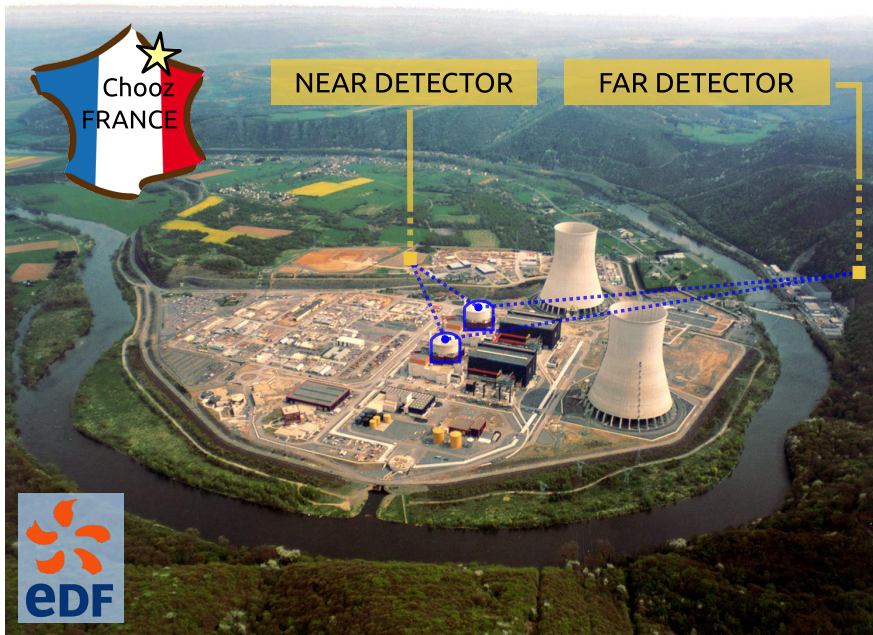
Figure 2.1: Chooz nuclear power station: location of the reactors and detectors.

A 15 cm thick steel shield is installed around and on top of the detector, protecting the ID and IV from external gamma rays. An *outer veto (OV)* system covers the main detector volumes. The detector subsystems as well as the calibration devices are described in the following.

2.1.1   Inner detector

The inner detector represents the neutrino detector as such (Fig. 2.3). The heart of the ID is the *ν-target*, a 8 mm thick acrylic cylinder filled with $10.3\,\mathrm{m}^3$ gadolinium-loaded liquid scintillator. It is surrounded by the *Gamma Catcher* volume, which contains gadolinium-free scintillator liquid of $22.5\,\mathrm{m}^3$, forming a 55 cm thick scintillator layer. The Gamma Catcher vessel consists of a 12 mm thick second acrylic cylinder and is itself surrounded by the *Buffer*, a 105 cm layer of non-scintillating mineral oil. In total 390 Hamamatsu R7081 photomultiplier tubes (PMTs) [157, 41] of 10 inch diameter are mounted to the Buffer walls, collecting the scintillation light produced by interactions in the ID liquids. As the Buffer tank is made of stainless steel, the inner detector volume is optically separated from the rest of the DC detector.

The densities of the inner detector liquids as well as the IV scintillator were optimized to match $0.804 \pm 0.001\,\mathrm{g/cm}^3$ at 15°C, in order to ensure mechanical safety of the detector vessels. Both the *ν*-target and the Gamma Catcher scintillator light yields were optimized with respect to each other to guarantee a homogeneous energy response [16]. In general, the detector liquids had to fulfill the requirements of high stability and radiopurity, as well as optical transparency and material compatibility with the acrylic vessels. Especially the long term stability of the Gd-loaded liquid scintillator was a major improvement compared to the CHOOZ experiment, which was limited in runtime and sensitivity due to the optical instability of their scintillator [37, 38].
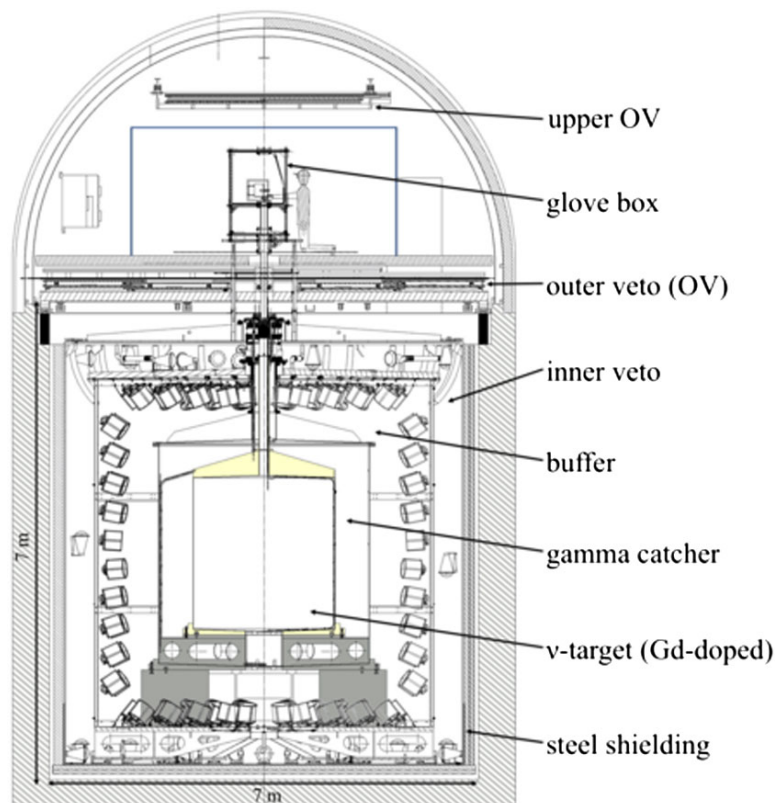
Figure 2.2: Double Chooz detector layout (from [5]).

The ν-target

Incident neutrinos are detected via IBD reactions with the hydrogen nuclei of the ID materials, creating a positron and a neutron. Gammas produced by the positron annihilation and radiative neutron capture are then detected in the ν-target and the Gamma Catcher liquids. The DC ν-target scintillator is an admixture of about 80 % dodecane ($C_{12}H_{26}$) and 20 % PXE (C_6H_{18}) [19]. The PXE and dodecane molecules are then excited by particles interacting in the liquid, whereas the molecules of PPO and bis-MSB shift the wavelength of the scintillation light to regions with higher transparency. Moreover, the scintillator emission spectrum matches the interval of high quantum efficiency of the PMTs. The acrylic material of the ν-target and the Gamma Catcher vessels are transparent to visible light, the attenuation lengths of the wavelength-shifted light in the different liquids are larger than the dimensions of the particular sub-volume.

The rare earth element gadolinium (Gd) possesses with 6.09×10^4 b for ^{155}Gd and 2.54×10^5 b for ^{157}Gd very high cross-sections for the radiative capture of thermal neutrons [135]. Upon neutron capture, gammas with a total energy of 8.54 MeV and 7.94 MeV are produced respectively [135]. These energies are notably larger than the typical energies released in radioactive decays occurring in nature, which makes it possible to suppress the detection of accidental false coincidences. As the metallic Gd atoms are not easy to dissolve in the organic scintillator, the Gd was bound in a β-diketone based metalorganic complex [19]. This complex allowed to dissolve the desired amount of 0.123 % by weight, corresponding to 1 g/L.
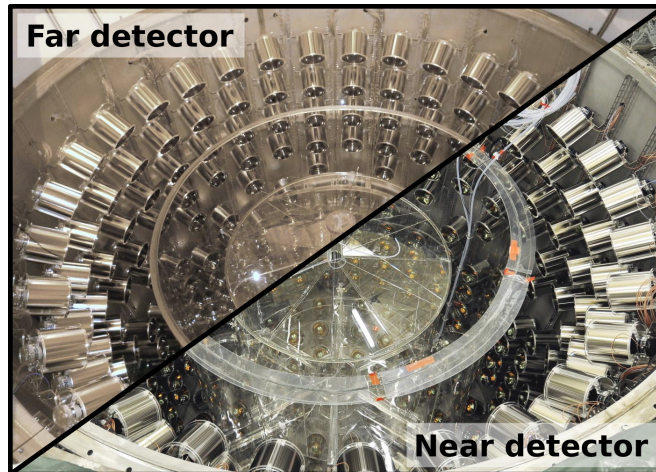
Figure 2.3: The Double Chooz near and far inner detectors. The two innermost vessels built out of acrylics are the ν-target and the Gamma Catcher vessels. Both volumes are surrounded by the Buffer, which is equipped with photomultiplier tubes (from [72]).

The Gamma Catcher

The purpose of the Gamma Catcher is to enhance the detection efficiency of gammas which escape the ν-target volume. In order to match the light yield and density of the Gamma Catcher liquid to the ν-target scintillator, medicinal white oil (Shell Ondina909) was added, constituting the main component of the liquid. The fractions of the other solvents, consisting of dodecane and 4% PXE, are different from the ν-target admixture [19].

The Buffer

The Buffer is filled with $100\,\mathrm{m}^3$ of liquid, consisting of Ondina917 and an n-alkane mixture in the case of the FD [6]. As the liquid is an admixture of non-scintillating components, the Buffer creates a passive shield to keep radioactivity from the PMTs and the surrounding rock from entering the active detector volumes. Including the Buffer as additional sub-volume in the DC detector layout was one of the improvements over the CHOOZ detector design described in Ref. [38]. Along with the purchase of PMTs containing lower amounts of radioimpurities from ^{238}U, ^{232}Th and ^{40}K inside the PMT glass, the accidental rate was reduced to less than $0.5\,\mathrm{d}^{-1}$, almost a factor two compared to the design goal [6]. The angular orientation of each PMT was adjusted to optimize the light collection with respect to uniformity, in addition each PMT was equipped with a cylindrical shaped mu-metal in order to suppress the influence of the earth magnetic field on the photoelectron detection [67].
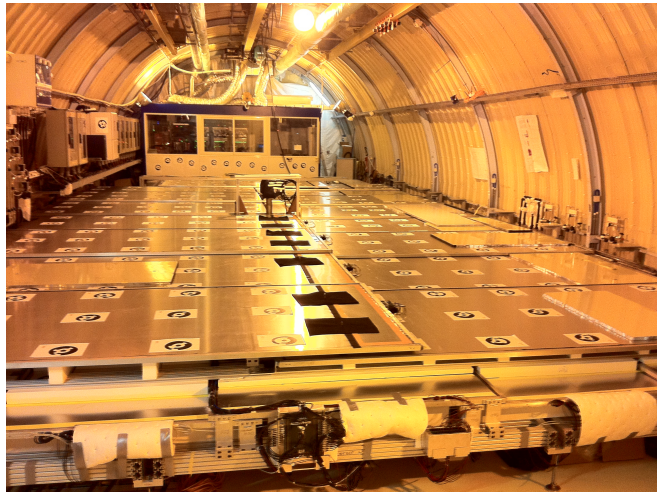
Figure 2.4: Lower outer veto in the laboratory of the far detector (from [51]). The chimney is seen in the middle of the outer veto modules, while the glovebox was not yet installed. In the back of the laboratory the entire DC electronics is stored, on the left hand side the HV splitter boxes are mounted to the side walls.

2.1.2 Veto systems

The DC detector possesses two active muon vetoes, described in the following.

The inner veto

The inner veto contains $90\,m^3$ of liquid scintillator, consisting of LAB and n-alkanes together with the wavelength shifting fluors PPO and bis-MSB [178]. Its boundary is a stainless steel vessel, measuring $6.8\,m$ in height and with a diameter of $6.6\,m$. In total 78 Hamamatsu R 1408 PMTs of 8-inch diameter are mounted to the IV walls. Their configuration was determined using MC simulations, so the light collection as well as the muon and muon-induced background rejection was maximized [95]. As a result, 24 PMTs are mounted to the top, 12 PMTs at the side and 42 PMTs on the bottom of the IV vessel. Reflective white paint covers the inner walls of the far detector IV vessel, furthermore reflective foil (VM 2000, 3M) was attached to the Buffer vessel at the outer side walls in order to maximize the collection efficiency of the scintillation light [6].
The IV acts as an active veto to muon events crossing the sensitive volume. It is also used to identify and reject muon-induced spallation products, such as fast neutrons, and it shields the ID from external radioactivity.

The outer veto

On top of the detector tank a muon tracking detector, the OV is installed [50]. It comprises a lower veto system covering an area of $13 \times 7\,m$ around the chimney (the chimney region is left free) in the FD laboratory (see Fig. 2.4) and an upper system mounted to the ceiling right above the chimney. Each system is built out of sub-modules containing plastic scintillator strips placed side by side and read out by Hamamatsu H8804 MAPMTs. Two sub-modules are then assembled with their strips aligned or-
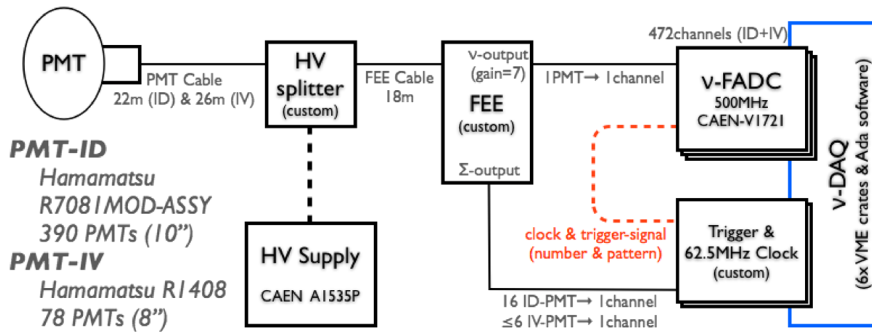
Figure 2.5: Block diagram of the Double Chooz DAQ system (from [6]). Explanations are given in the text.

thogonally for (x, y)-coordinate reconstruction. The upper and the lower OV layer are separated by a distance of about 3.9 m, making it possible to reconstruct the track of muons passing both systems. Both OV systems were available for 27.6 % of the DC-III data set (cf. Section 2.2) published in [12]. Only the lower OV system was present for 56.7 % of the runtime, while 15.7 % of the data was recorded with no OV information available.

2.1.3   Data acquisition

The DC electronics and data acquisition (DAQ) system of the IV and ID is given in Fig. 2.5. Its duty is the digitalization of all signals of the 468 ID and IV PMTs and their storage upon a trigger. Each PMT is connected via one single cable to the readout system, carrying both the high voltage (HV) and the PMT signal. Custom-made HV splitter boxes decouple both components and supply the PMTs with a high voltage of ~ 1.3 kV. From the splitter boxes each PMT signal is passed on to the front-end electronic (FEE) modules, which amplifies the signals. The digitalization is performed by the flash-analog-to-digital converter (FADC) electronics [31] sampled at 500 kHz, with each PMT signal transmitted to a corresponding channel recording a 256 ns waveform. The FEE modules also provide sum signals of groups of either 16 ID PMT or more than 6 IV PMT signals, which are fed into the trigger system [42]. The sum signal amplitudes are proportional to the integrated charge, a trigger is released if the trigger threshold is passed by a minimum number of sum signals. The ID PMTs are divided in two subgroups of sum signals, which can cause a trigger independently. An ID trigger corresponds to energies larger than 350 keV; an IV trigger is released at about 10 MeV energy, which would be released by a minimum ionizing muon traveling at least 8 cm in the IV [6]. Both the ID and IV channels are read out in case any of the two sub-detectors create a trigger. This enables to tag background events entering the ID from outside, as they often also deposit energy in the IV (cf. Section 3.3.4). The DAQ system is operated dead-time free.

The OV information is stored independently from the IV and ID data; utilizing a different DAQ system Signal exchange between the OV and the ID/IV trigger system allows to merge the data sets later [50].

2.1.4 Calibration devices

The Double Chooz detector response and related systematics can be studied by means of different calibration devices, either using light sources or decay products of radioactive isotopes. A regular calibration of the DC readout system is performed with the light injection system:

Light injection system: The time offset and gain of the DC electronics is calibrated on a regular basis using a light injection system [101, 110]. Via optical fibers connected to the support structure of the PMTs, a multi-wavelength LED system is used to illuminate both the ID and IV volumes. In the ID, data are taken at wavelengths of 385, 425 and 470 nm. The IV LEDs are operated at 365 and 475 nm. Furthermore, the LED light intensity, pulse width and flashing frequency can be varied, which is done remotely. Calibration with the ID and IV light injection is part of the normal data taking routine, which allows to monitor the stability of the electronic gains and timing offsets.

Besides the light injection system, a laser ball [117] has been deployed in the ν-target scintillator to perform measurements of the PMT timing, the speed of light inside the detector liquids as well as parameters needed as input for the vertex reconstruction algorithms.

The ID possesses different calibration systems which allow for a deployment of radioactive sources. Dedicated calibration campaigns have been conducted annually. The sources are inserted into the detector volumes from a *glovebox* installed on top of the chimney. The sources are prepared and mounted under a steady nitrogen blanket, maintaining the detector liquid integrity.

Z-axis system: Inside the glovebox a pulley-and-weight system [90] can be operated to lower the sources into the ν-target liquid. The ν-target volume can be calibrated along the cylindrical symmetry axis (in the following referred to as "z-axis") with this system. With a lowest deployment position located 1 cm above the ν-target bottom wall, the sources can be positioned with 1 mm relative precision [6].

Guide-Tube system: The GC volume can be sampled along a rigid looped deployment tube (called Guide-Tube) [175], which is mounted in the y-z-plane of the far detector coordinate system (Fig. 2.6). The sources are pulled through the deployment loop by means of a motor-driven wire. Only the upper half of the GC volume is reached by the Guide-Tube, calibration data can be taken in the radial direction at $z = 0$ and in the GC top volume as well as at various positions close to the ν-target and GC acrylic walls. The deployment locations along the loop are known with a precision of 1 cm [6], whereas the perpendicular distance to the Guide-Tube in the ν-target near region is known within 2 mm [6].

Articulated Arm: The Articulated Arm will allow to scan the ν-target volume using radioactive sources for various positions (z, ρ). Currently in the final development phase, it is planned to be operational for a calibration campaign at a later stage of the data taking with two detectors running.
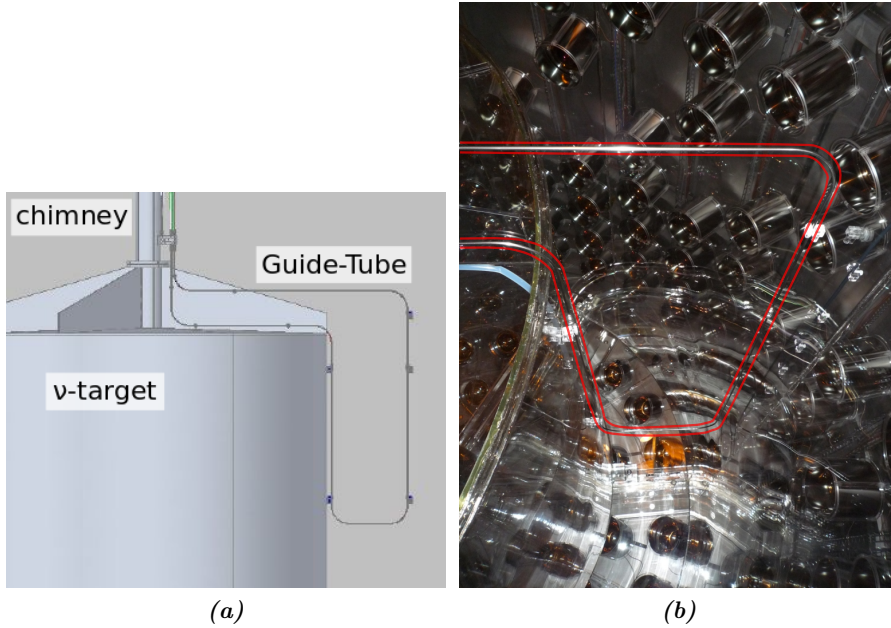
Figure 2.6: Guide-Tube system (modified, from [175]). **a)** Deployment tube orientation relative to the ν-target vessel. **b)** View inside the Gamma Catcher acrylics vessel of the far detector. The deployment tube is located between the red lines.

Pointlike sources of the following encapsulated isotopes can be inserted in the ν-target and GC volume using the deployment systems described above:

- ^{137}Cs releases after β^--decay in $85.1\,\%$ of the cases one $0.662\,\mathrm{MeV}$ gamma [166].

- ^{68}Ge decays via electron capture to ^{68}Ga. The two annihilation gammas of $0.511\,\mathrm{MeV}$ from the subsequent β^+-decay of ^{68}Ga are seen in the detector, offering a calibration signal close to the visible energy threshold of the prompt event in IBD reaction.

- ^{60}Co decays via β^--decay to ^{60}Ni, having a Q-value of $2.82\,\mathrm{MeV}$ [166]. The decay is in $99.88\,\%$ of the time followed by the emission of two gammas of 1.173 and $1.333\,\mathrm{MeV}$, which are used for calibration purposes.

- ^{252}Cf releases neutrons upon spontaneous fission (see chapter 4 for details). The $2.223\,\mathrm{MeV}$ gammas emitted by the radiative neutron capture on H are used to calibrate the energy uniformity. Moreover are the capture characteristics of ^{252}Cf neutrons studied to estimate the detection systematic uncertainties.

Furthermore neutrons produced by cosmic ray spallation can be used to calibrate the detector response as further described in Section 3.2.4 and 5.5, as well as Bi-Po events from the thorium series (cf. Eq. (4.7) and (4.8) in Section 4.3.2).

2.2 Datasets and oscillation analysis publications

Different oscillation analyses have been put forward by the DC collaboration in the past. In addition to modifications in the enhanced analysis techniques, such as energy scale

Table 2.1: Datasets of the different DC oscillation analysis publications. The H-III analysis is in preparation.

Analysis configuration	Detection channel	Live time [days]	Reference
DC-I	Gd-I	96.8	[5]
DC-II	Gd-II	227.93	[6, 14]
	H-II	240.1	[8, 14]
DC-III	Gd-III	460.67	[12]
	H-III	460.67	–

calibration or methods for background rejection, they also differ in the dataset and the detection channel used by the neutrino search. In this section abbreviations labeling the oscillation analyses are introduced as given in Table 2.1. The labels summarize analyses according to the following two attributes:

Analysis configuration: The different analysis configurations are labeled DC-I, DC-II and DC-III. Similarities in analyses with the same DC label exist in the energy scale calibration, the reconstruction algorithms, the calibration campaigns corresponding to the datasets as well as the reactor normalization uncertainty.

Neutrino detection channel: The oscillation analyses depend on the neutron detection channel utilized by the neutrino selection and are therefore labeled Gd (for neutron captures on gadolinium) or H (neutron captures on hydrogen). Differences existing between the Gd and H labeled analyses of the same DC analysis configuration are present in the neutrino selection and related efficiency uncertainties, the background studies, the background veto cuts and the energy scale systematics.

Chapter 3

Data analysis in Double Chooz

As the DC experiment started in the first phase of the data taking with a single detector, the oscillation parameter θ_{13} explaining a deficit in the measured data was extracted from comparison to a Monte Carlo (MC) based prediction. The expected number of events and energy distribution is computed in several steps, simulating the neutrino flux from production in the reactor cores, physical interaction in the DC detector to triggered readout and event reconstruction. The background estimations were obtained from dedicated analyses of detector data; depending on the publication, part of the background spectral shape was based on MC. Calibration data was used to measure the visible energy response and signal detection efficiency (further details in Chapter 4) as well as related systematic uncertainties. Simulation of each calibration source allowed to quantify data to MC discrepancies and ensure the accuracy of the prediction inputs to the θ_{13} fit. Details on the DC data analysis are explained in the following.

3.1 Neutrino prediction

In the absence of a near detector, the MC model becomes a crucial input to the θ_{13} analysis. The absolute normalization of the MC prediction will decide on the experiment's accuracy and the normalization uncertainty will be dominated by how well the MC is expected to reproduce the data or, in case calibration data exists, how well data to MC discrepancies are understood. The expected rate of reactor antineutrinos originating from the two reactors ($R = 1, 2$) observed through IBD reaction inside the DC far detector can be parametrized as

$$\frac{dN^{\nu,\exp}(t)}{dt} = \sum_{R=1,2} \frac{N_{\mathrm{p}}\,\varepsilon_{\det}}{4\pi L_R^2} \times \frac{P_{\mathrm{th},R}(t)}{\langle E_f \rangle_R(t)} \langle \sigma_f \rangle_R(t)\,. \tag{3.1}$$

Here, N_{p} denotes the number of protons present in the fiducial volume, $\varepsilon_{\det}$ the detection efficiency, L_R the baseline between reactor R and the detector, P_{th} the thermal power, $\langle E_f \rangle$ the mean energy released per fission (f for "fission") and the mean interaction cross-section $\langle \sigma_f \rangle$. The last three terms depend on the composition of the reactor core R in which the neutrino is produced and change with respect to time.

The simulated DC expectation is given by Eq. (3.1), its conceptual realization consists of two parts: a reactor model related part corresponding to the second factor of Eq. (3.1), and a detector model related part, which corresponds to the first factor. The reactor model receives information on the thermal power and fuel compositions

as input. Together with predictions of the antineutrino spectra and information about the IBD cross-section, normalized spectra of antineutrinos interacting via IBD in the detector are calculated. These spectra are fed into the detector MC framework, which forms the second part of the neutrino prediction computation. Once the information about the neutrino momentum and interaction location is drawn, secondary particles produced in the IBD reaction are propagated in the detector simulation. This full detector MC includes the simulation of detector response and readout effects, which yields variables such as the digitized waveforms and trigger timing information as output. These variables are used by the same analysis algorithms applied to real detector data, introducing similar inefficiencies due to selection cuts. Details on both steps of the prediction computation are discussed in the next subsections.

3.1.1 Reactor Model

Antineutrinos are produced in the Chooz reactor cores B1 and B2 by the β-decays of fission fragments of the four main fission isotopes ^{235}U, ^{239}Pu, ^{238}U and ^{241}Pu. The two Chooz cores are N4 type pressurized water reactor cores, which consist of a primary loop, heated by the nuclear fissions, and a secondary loop. Heated up by the primary loop, steam is created in the secondary loop, driving the turbines for electricity generation. Data characterizing the thermal power $P_{\mathrm{th},R}$ is recorded approximately every minute by EDF, including parameters such as the temperature of the water circulated in the primary loop (Fig. 3.1a). The in-core measurement devices are tested by heat balance measurements in the secondary loop on a weekly basis and are recalibrated if necessary. The 1-σ uncertainty of $P_{\mathrm{th},R}$ measured at full nominal power amounts to 0.5 % [6].

In order to deduce the expected neutrino flux from the thermal power information, the number of fissions is computed from the ratio $P_{\mathrm{th}}/\langle E_f \rangle$, where $\langle E_f \rangle$ denotes the mean energy released per nuclear fission with about 200 MeV/fission (see Table 1.2). The latter is computed from the mean fission energy per isotope $\langle E_f \rangle_k$ ($k = {}^{235}$U, ^{239}Pu, ^{238}U, ^{241}Pu) and weighted with the fractional fission rates α_k:

$$\langle E_f \rangle = \sum_k \alpha_k \langle E_f \rangle_k \,. \tag{3.2}$$

The parameters α_k represent the relative number of fissions originating from the k-th isotope at a specific point in time (Fig. 3.1b). Using a combination of the simulation codes MURE [159, 163] and DRAGON [155, 139], the evolution in time is computed for the α_k in steps of 0.5 to 2 days, taking into account the detailed geometry and material composition of the Chooz cores (Fig. 3.1b). Furthermore, the fuel assemblies' initial composition, their positions and replacements are considered in the MC modelings. A systematic uncertainty of 0.8 % on the α_k is estimated from variations of input variables, such as density of the moderator material and positions of the control rods as well as from intercomparison of different simulation codes [6].

The last factor required to complete the reactor model description is the expected neutrino energy spectrum, comprising not only shape but also absolute normalization information per fission. Instead of a pure neutrino spectrum, the mean spectrum averaged cross-section per fission $\langle \sigma_f \rangle = \sum_k \alpha_k \langle \sigma_f \rangle_k$ is included in the flux prediction.

(a) Thermal power measured in the two reactor cores B1 and B2 (from [150]).

(b) Evolution of the fission fractions α_k upon fuel burnup (^{235}U depletion and ^{239}Pu and ^{241}Pu built-up) (from [107]).
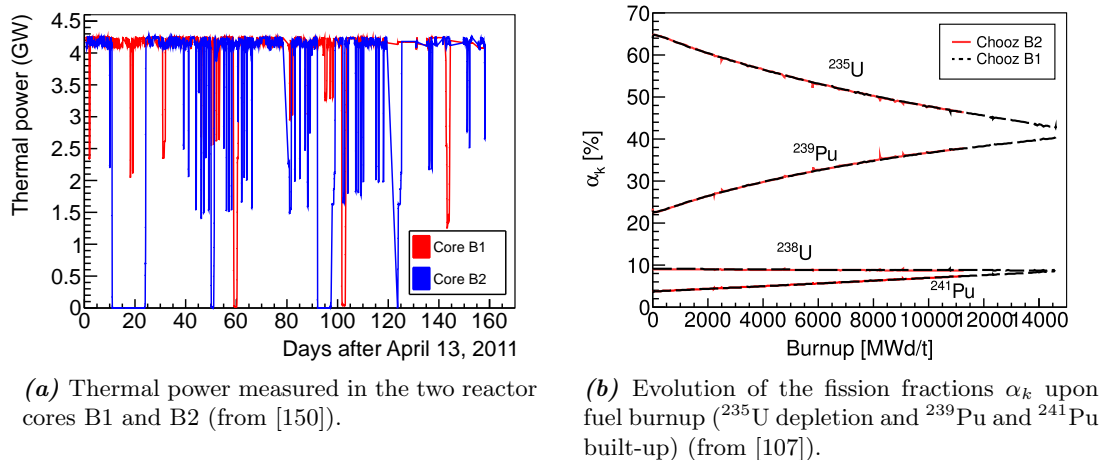
Figure 3.1: Thermal power and fission fractions. The thermal power is given along with other parameters to the reactor simulation as input. The fission fraction and its time evolution is retrieved from the reactor simulation code.

The mean cross-section per isotope and fission [6]

$$\langle \sigma_f \rangle_k = \int dE \, S_k(E) \, \sigma_{\text{IBD}}(E) \tag{3.3}$$

contains the neutrino spectra $S_k(E)$ of the k-th isotope and the inverse beta decay cross-section $\sigma_{\text{IBD}}(E)$, which is known analytically and taken from Ref. [204] in its simplified form (see also Section 1.3.2). Further input is given by the ^{235}U, ^{239}Pu and ^{241}Pu spectra, which are retrieved from the ILL (Institut Laue-Langevin) measurements of the β-spectra [190, 108, 121]. These are converted to antineutrino spectra following Ref. [134] and corrections discussed in Ref. [158] (Fig. 3.2a). The reference spectra $S_k(E)$ are normalized to one fission and contain information on the absolute normalization. The uncertainty of the $S_k(E)$ is energy dependent and amounts to $\sim 3\,\%$ [6]. Whereas the spectrum of ^{238}U had to be derived from a calculation [161] for DC-I and DC-II, it is taken from a measurement in the DC-III analyses [119], which is extrapolated below $3\,\text{MeV}$ and above $7.5\,\text{MeV}$ [12].

In the absence of a near detector, the large normalization uncertainty of the reference spectra can be overcome by inputs from other reactor experiments' results: The Bugey-4 rate measurement executed at $15\,\text{m}$ distance from the Bugey reactor core [93], serves as a substitute for a near detector measurement. As a consequence, the DC θ_{13} measurement is not affected by possible short-baseline oscillations e.g. introduced by sterile neutrinos with $\Delta m^2 \sim 1\,\text{eV}^2$ [158]. The mean cross-section per fission is then given by [6]

$$\langle \sigma_f \rangle_R = \langle \sigma_f \rangle^{\text{Bugey}} + \sum_k (\alpha_k^R - \alpha_k^{\text{Bugey}}) \langle \sigma_f \rangle_k \,, \tag{3.4}$$

which includes a correction due to discrepancies in the fuel composition between Bugey-4 and each of the Chooz reactor cores. Due to the $1.4\,\%$ precision of $\langle \sigma_f \rangle^{\text{Bugey}}$ and since the discrepancies $(\alpha_k^R - \alpha_k^{\text{Bugey}})$ are small, the normalization uncertainty introduced by the reference spectra $S_k(E)$ is reduced to $0.2\,\%$ [6], lowering the overall reactor related
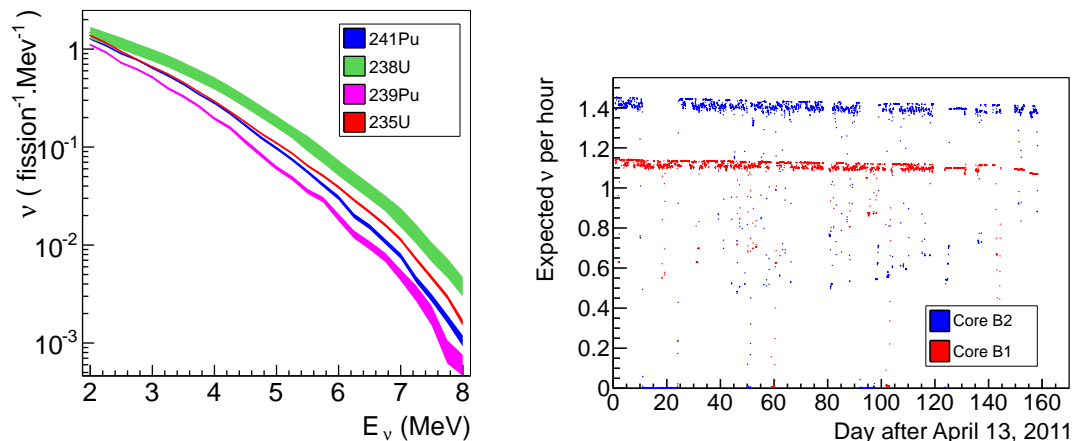
(a) Reference antineutrino spectra used to compute the expected neutrino flux. Note: from DC-III onwards, the ^{238}U spectrum is retrieved from a measurement, not shown in this plot.

(b) Expected neutrinos per hour at the DC far detector. The distance between the detector and the reactor core B1 is larger than the distance to B2, as seen by the lower neutrino rate.

Figure 3.2: Reference spectra and expected neutrinos per hour (from [150]).

uncertainties on the antineutrino prediction from 2.8 % to 1.7 % [12]. The overall normalization uncertainty is dominated by the uncertainties on the Bugey-4 cross-section, the α_k and the thermal power. The reactor flux related uncertainties are propagated to the θ_{13} fit in form of a covariance matrix (cf. Section 3.4.3). Further information can be found in Ref. [6, 112].

The binned expected neutrino flux in the absence of oscillations is then (integrated over time and taking into account the detector related factor) given by [6]

$$N_i^{\nu,\exp} = \sum_{R=1,2} \frac{N_{\mathrm{p}} \, \varepsilon_{\mathrm{det}}}{4\pi L_R^2} \times \frac{P_{\mathrm{th},R}}{\langle E_f \rangle_R} \times \left(\sum_k \alpha_k^R \langle \sigma_f \rangle_k^i \right) \times \left(\frac{\langle \sigma_f \rangle_R}{\sum_k \alpha_k^R \langle \sigma_f \rangle_k} \right), \qquad (3.5)$$

where the sum has to be taken over both reactors R. The last term in Eq. (3.5) normalizes the flux with respect to $\langle \sigma_f \rangle_R$ (see Eq. (3.4)), which includes the Bugey-4 "anchor" of the cross-section normalization. The expected neutrino rate computed by the simulation for each of the cores B1 and B2 is shown in Fig. 3.2b.

3.1.2 Detector Model

The DC detector was modeled using the Geant4 (Geant4.9.2.p02 [26, 33]) based simulation package DCGLG4sim [130]. Enhancements of the code are related to scintillation process, PMT cathode, neutron scattering and gamma cascade modeling. The full detector geometry was implemented to great detail, including the vessels and tanks, PMTs, mu-metal shieldings, support structures and materials. Dimensions and orientation of the components are known from photographic surveys. The optical properties of the scintillator liquids were evaluated from laboratory measurements and used as input to the MC: parameters describing the ionization quenching [17, 18] following Birk's law [48, 49], light yield, light attenuation as well as scintillation timing [19] and emission spectra were implemented in the DC simulation. From the DC-II analyses onwards, a custom patch NeutronTh, affecting neutron physics at energies below 4 eV,

was implemented to improve the elastic scattering modeling. Moreover, NeutronTh modifies the gamma emission spectra of radiative neutron captures on Gd with energies $E_\mathrm{n} < 300\,\mathrm{keV}$ (further details on NeutronTh can be found in Section 7.3).

The Readout System Simulation (RoSS [196]) allows to simulate the event readout, modeling the full DAQ with PMTs, front-end electronics, trigger system and FADCs. Channel-wise variations in the gains, baseline fluctuations and noise are taken into account, incorporating resolution effects into the MC.

3.2 Event reconstruction

The detector data is initially given in form of binary files. After conversion into a data format based on ROOT (an object-oriented data analysis framework, developed by CERN [58]), each file contains information about the waveforms, trigger, run and data taking conditions. These "RAW" data files possess the structure required by the *Double Chooz Offline Group Software* (DOGS [171]), which is used for further data manipulation. The event reconstruction algorithms applied to the RAW files create and fill variables used for high level analysis. The set of algorithms for pulse, muon track, vertex, and energy reconstruction are combined in the *Common Trunk* (CT), having CT files as output.

In case of the MC production of the neutrino prediction or calibration simulations, information on each simulated event is provided in RAW file format after utilization of RoSS (cf. Section 3.1.2). The CT configuration subsequently applied to the MC RAW files contains only slight modifications compared to the one used on detector data. After CT processing, the MC simulation files additionally include "truth" information, e.g. on energy, position and particle type. A simplified overview on the data processing is illustrated in Fig. 3.3.
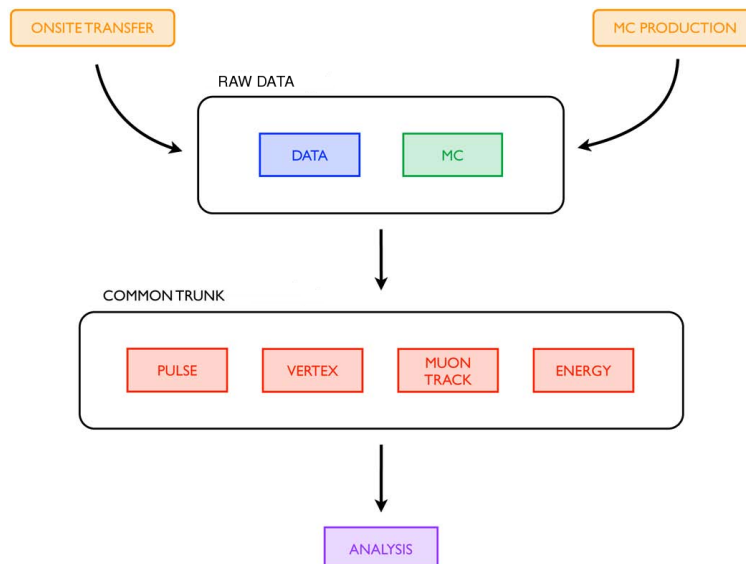
Figure 3.3: Schematic overview of the data flow in the Double Chooz data processing (modified, from [186]).

33

3.2.1   Pulse reconstruction

The number of photons detected by each PMT is contained in the FADC waveforms and can be read out by pulse integration in form of a charge q. The algorithm DCRecoPulse [170] is applied to reconstruct charge and timing detected in each channel. A fixed trigger of $1\,\mathrm{kHz}$ enables to measure the mean baseline B_{mean} and baseline fluctuation as RMS B_{rms} for each DAQ channel. The charge q seen by a channel is gained from integration of the waveform over a $112\,\mathrm{ns}$ wide window after subtraction of the baseline B_{mean}. The starting point of the integration is chosen so that the integrated charge becomes maximal. For energy depositions generated by the neutrino signal, about one photoelectron is detected per PMT, corresponding to a pulse amplitude of about six ADC counts[1]. In order to prevent that a reconstructed baseline fluctuations is misidentified as signal, a minimum pulse amplitude of $2\,\mathrm{ADC}$ counts and $q > B_{\mathrm{rms}} \cdot \sqrt{N}$ are required, where N ($N = 56$ for a $112\,\mathrm{ns}$ integration interval) represents the number of samples integrated by the algorithm. The pulse start time is determined by the time when $20\,\%$ of the pulse maximum amplitude is exceeded by the waveform.

3.2.2   Muon reconstruction

Two algorithms for muon track reconstruction have been used in the data analysis. The first one, available since the first DC publication [5], is based on the spatial pattern of the ID PMT hit times [212]. Information from the ID, IV and OV are used by the second algorithm, described in Ref. [15]. A likelihood analysis (see Section 3.3.4) enables to identify the decays of β-n emitters (such as ^{9}Li and ^{8}He), which are produced by cosmic muons and constitute the main source of background in the oscillation analysis. While the former algorithm is used to estimate the ^{9}Li and ^{8}He background rate, the latter one is utilized to reduce this background via likelihood cut [83] and to extract its energy spectrum.

3.2.3   Position reconstruction

The vertex reconstruction algorithm RecoBAMA[2] is based on the charge and pulse hit time information of each PMT. Assuming the light was emitted isotropically by a point-like source, the hit time and charge observed by a PMT will be given by the relative distance to the source location and the light intensity. Vice versa, the characteristics $\mathbf{X}$ of a source can be determined by means of a charge and time maximum likelihood algorithm having both the hit and non-hit PMT information as input [6]. Here, the set $\mathbf{X} = (x_0, y_0, z_0, t_0, \Phi)$ includes the event position and time as well as the emitted light intensity per unit solid angle Φ given in photons/sr. For each set $\mathbf{X}$, the hit time of the i-th PMT [6]

$$\tau_i = t_0 + \frac{r_i}{c_n} \tag{3.6}$$

is given by the event time t_0, the relative distance between the event location and the PMT and the speed of light in the medium c_n. Furthermore, the amount of charge detected by the i-th PMT [6]

$$\mu_i = \Phi \epsilon_i A_i \Omega_i \,, \tag{3.7}$$

---

[1]One ADC count corresponds to about $4\,\mathrm{mV}$ signal amplitude.
[2]Named after Alabama, where the institution of the code developers is located.
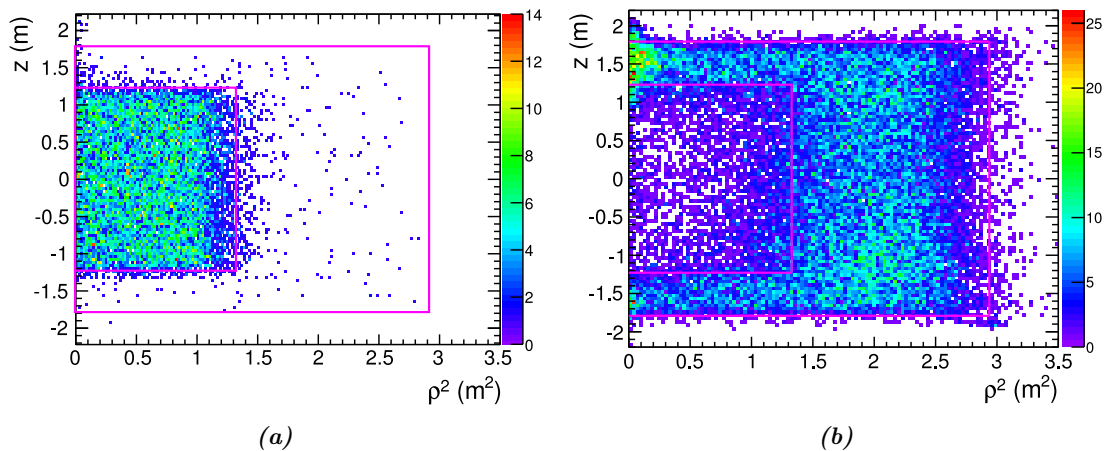
Figure 3.4: Prompt event reconstructed vertices plotted in the (ρ^2, z) plane. The inner magenta lines mark the ν-target acrylic vessel, the outer lines the GC boundaries. **a)** Prompt vertices of the Gd-III candidate sample (from [172]). **b)** Prompt vertices of the H-II candidate sample (from [199]).

is the product of the intensity Φ with the quantum efficiency ϵ_i, the light transmission amplitude A_i and the solid angle Ω_i observed by the PMT. The likelihood of the event is then given by [6]

$$\mathcal{L}(\mathbf{X}) = \prod_{q_i=0} f_q(0; \mu_i) \prod_{q_i>0} f_q(q_i; \mu_i)\, f_t(t_i; \tau_i, \mu_i)\,, \tag{3.8}$$

where q_i and t_i are the charge and hit time of the i-th PMT, f_q and f_t the probabilities to measure these for a given $\mathbf{X}$. The first product of Eq. (3.8) takes into account all PMTs which have not been hit. Using the information from all PMTs as well as input from both charge and time enhances the performance of the likelihood algorithm. The set $\mathbf{X}$ maximizing the likelihood is then found by minimizing

$$F_{\mathrm{V}} = -\ln \mathcal{L}(\mathbf{X})\,. \tag{3.9}$$

The charge and time probability densities used to be extracted from MC simulations in the Gd-I and Gd-II analyses. For the Gd-III analysis laser calibration data was analyzed to measure the charge and time probability densities, which improved the data to MC agreement of the vertex reconstruction [12]. Other parameters are obtained from source calibration data. From ^{68}Ge source analysis the spatial resolution of the reconstruction was found to be 22 cm, while it was 24 cm for ^{60}Co gammas [6].

While the reconstructed vertices have been used in the Gd-II analysis only as input to the energy uniformity calibration, a cut on the relative distance of coincident events is applied by the H-channel and Gd-III analysis to reject accidental background. In Fig. 3.4 the reconstructed prompt event positions are shown for the candidate samples of the Gd-III and H-II analyses.

3.2.4   Energy reconstruction

The Double Chooz experiment uses calorimetric scintillator detectors to measure the visible energy E_{vis}, which is an estimate for the absolute energy deposited in the detector per trigger. As the θ_{13} analysis relies on a data to MC comparison of the prompt energy spectrum, the accuracy of the simulated energy scale is a critical aspect. Therefore a detailed understanding of the energy response is essential, especially the dependence on time, position and energy non-linearities.

The energy reconstruction of the first published DC result based on the Gd-channel utilized a parametric function correcting the MC simulation [5]. After initial computation of the total charge Q_{tot} observed by the PMTs and the correction for gain fluctuations, Q_{tot} was multiplied by a scaling factor converting charge into MeV. The subsequently applied correction function was gained from data to MC comparison of calibration deployments and incorporated an energy dependent and position dependent term [112].

After the first DC publication the energy calibration was improved in many aspects. From the DC-II analyses [6] onwards, the energy of both data and MC was calibrated with respect to readout effects, spatial uniformity, time stability and non-linearity step by step. The different calibration stages from charge to visible energy in MeV are:

1. Linearized Charge to PE conversion

2. Uniformity calibration

3. Absolute energy scale calibration

4. Stability calibration

5. Energy non-linearity calibration

Expressed in terms of formulae, the visible energy of detector data is given by [12]

$$E_{\text{vis}} = N_{\text{pe}} \times f_{\text{u}}^{\text{data}}(\rho, z) \times f_{\text{MeV}}^{\text{data}} \times f_{\text{s}}(E_{\text{vis}}^0, t) \,, \tag{3.10}$$

while for the MC it is defined as [12]

$$E_{\text{vis}} = N_{\text{pe}} \times f_{\text{u}}^{\text{MC}}(\rho, z) \times f_{\text{MeV}}^{\text{MC}} \times f_{\text{nl}}(E_{\text{vis}}^0) \,. \tag{3.11}$$

Here, z and ρ represent the event position in cylindrical coordinates, while t is the time of the event in elapsed days. N_{pe} represents the measured charge in photoelectrons (PE), the correction factors f_{u}, f_{MeV}, f_{s} and f_{nl} refer to the spatial uniformity, absolute energy scale, time stability and non-linearity correction, respectively. The uniformity corrected energy is given by E_{vis}^0, which is in the final reconstruction step either stability corrected (for data) or corrected for non-linearities (in MC). The last term in Eq. (3.11), the energy non-linearity correction, was introduced in the Gd-III analysis [12], whereas previous analyses accounted for non-linearities by a systematic uncertainty. Each term in Eq. (3.10) and (3.11) is further explained in the next paragraphs.
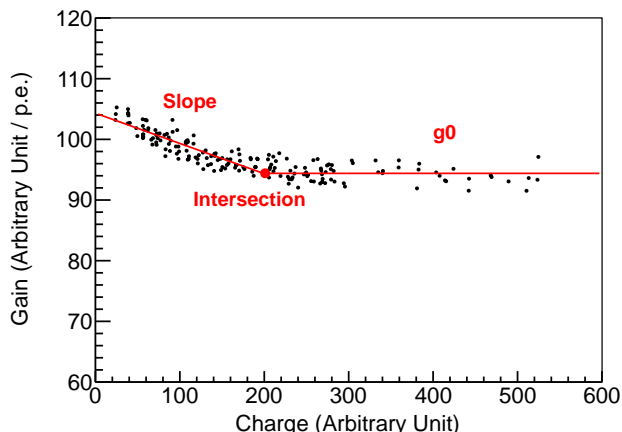
Figure 3.5: Measured gain as a function of the integrated charge for one readout channel. The data points represent the measurements, the red line corresponds to the gain function described in the text (from [185]).

1) Linearized Charge to PE conversion

The conversion from measured charge to PE is carried out by the *linearized PE calibration*. The total number of photoelectrons

$$N_{\text{pe}} = \sum_i q_i/g_i^m(q_i, t) \tag{3.12}$$

is built from the sum over the charges q_i divided by the conversion factor g_i^m (also called gain) of all accepted channels i, with the index m representing either data or MC. An accepted channel is characterized by a well behaved waveform and only very few channels happen to not pass the requirements. Owing to baseline estimation biases arising from the binned waveform measurement with the smallest unit of 1 ADC count, gain non-linearities are observed [6, 7]. The magnitude of the non-linearity depends on the measured charge, especially low energy depositions in the few PE region are affected. This effect is handled by taking into account both charge and time dependence of g_i^m, which is parametrized with respect to charge by a constant component for large charges, a slope at low charges and a transition point between the two regions (Fig. 3.5). Light injection calibration data of different intensities is used to measure the gain of each channel. As the gain and its functional form change after the readout electronics is power cycled, it is recalibrated on the occasion of a new power-cycle.

2) Uniformity calibration

To correct for position dependencies of the PE response observed in data and MC, 2D maps $f_u^m(\rho, z)$ were extracted using the 2.223 MeV gamma from neutron captures on hydrogen. After the calibration maps were applied, the PE of each event reconstructed at any position (ρ, z) will be corrected for discrepancies of the response relative to the one at the ν-target center. The event should then possess a PE response as if it were measured at $(\rho = 0, z = 0)$ [6]:

$$PE^m(0,0) = PE^m(\rho, z) \times f_u^m(\rho, z), \tag{3.13}$$
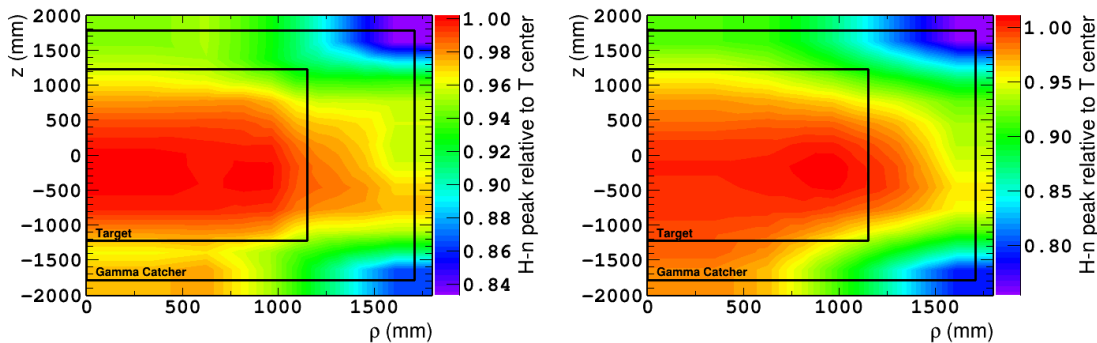
(a) Uniformity correction map applied to detector data.

(b) Uniformity correction map applied to the MC simulation.

Figure 3.6: Uniformity correction maps for data and MC, obtained from fits of the energy peak from neutron captures on hydrogen (from [185]).

with m for data or MC. Spallation neutron captures on hydrogen occur in both the ν-target and Gamma Catcher volume, being a suitable source to construct the data response map (Fig.3.6a). For data, the spatial non-uniformity can reach up to 5 % in the ν-target volume [6]. IBD neutrons were simulated in the full detector volume to create a similar map for the MC (Fig.3.6b). A correction factor for any position (ρ, z) is found by a 2D-interpolation algorithm having the uniformity maps as input.

The systematic uncertainty was estimated from position dependent data to MC discrepancies after uniformity calibration of spallation neutron captures on Gd.

3) Absolute energy scale calibration

In the absolute energy scale calibration the conversion factor f_{MeV} from PE to MeV is determined using the H-capture peak of 2.223 MeV from ^{252}Cf deployed at the ν-target center (Fig. 3.7). For data the value of $1/f_{\mathrm{MeV}}$ was measured to be 186.2 PE/MeV and for the MC simulation it amounts to 186.6 PE/MeV in the Gd-III analysis [12]. While for the Gd-III calibration the data of the second calibration campaign (May 2012) was used, the preceding DC analyses were calibrated with respect to the first campaign (August 2011).

4) Stability calibration

The uniformity corrected visible energy of the data is observed to vary with respect to time mainly due to gain fluctuations during a power cycle period. A time stability correction f_{s} is therefore introduced, which is estimated using spallation neutron captures on H and Gd as well as ^{212}Bi-^{212}Po coincidences[3] from radioimpurities (see also Section 4.3.2 for details on Bi-Po decays). The Gd and H captures offer visible energies of about 2.22 and 8 MeV, whereas the α particle from ^{212}Po decay has a visible energy of ~ 1 MeV after quenching. Gain variations are corrected assuming the discrepancies to depend linearly on energy [12]. The remaining increase of the response of $+0.3$ %/year found in the analysis of neutron captures on hydrogen are expected to be related to

---

[3]The ^{212}Bi-^{212}Po data has only been used by the Gd-III analysis.
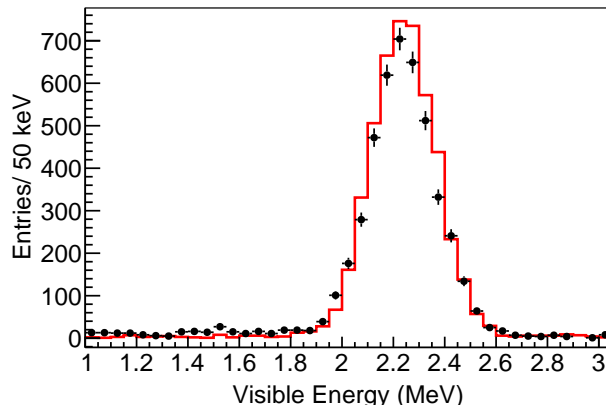
Figure 3.7: Absolute energy scale calibration by means of the ^{252}Cf neutron capture peak on hydrogen at the ν-target center (from [185]). The black points show the peak induced by ^{252}Cf fission neutrons, the red line corresponds to the MC simulation. The energy spectra shown include the calibration steps 1) – 3).

changes in the readout or scintillator response and were calibrated as well [12].

In Fig. 3.8 the relative stability of the peak energies for the two neutron capture energies and the alpha particle is shown as evaluated by the Gd-III analysis. The systematic uncertainty of the time stability correction was estimated from the residual variations after correction to be 0.61 % for the Gd-II and 0.5 % for the Gd-III analysis [6, 12]. Moreover, the uncertainty estimation accounts for the conversion from calibration sources to the full prompt energy range.

5) Energy non-linearity calibration

After the preceding steps of energy calibration were conducted, a remaining non-linear discrepancy of the energy scales between data and MC is found. While in the DC-II analyses (Gd-II and H-II) the energy non-linearity was studied using z-axis calibration data and a 0.85 % uncertainty on the energy scale assigned [6], the Gd-III analysis utilizes a function to correct the MC for non-linearities. This non-linearity correction function is given by [12]

$$f_{\mathrm{nl}}(E_{\mathrm{vis}}^0) = (0.0023 \cdot E_{\mathrm{vis}}^0 + 0.9949) \times (-0.027/E_{\mathrm{vis}}^0 + 1.008) \tag{3.14}$$

with E_{vis}^0 in MeV. Just as the correction function is the non-linearity composed of two factors: the charge non-linearity, corresponding to the first factor in Eq. (3.14) and the light non-linearity, represented by the second factor.

Charge non-linearity (QNL): This contribution is expected to be introduced by data to MC discrepancies in the readout and charge integration and therefore affects any event. It is studied from the comparison of the reconstructed visible energies of gammas from neutron captures on H and Gd. Since multiple gammas in the energy range of about 2 MeV are released upon Gd-captures, discrepancies to the energy response of the 2.22 MeV single gamma from H-captures are thought to be readout and reconstruction algorithm related.

39
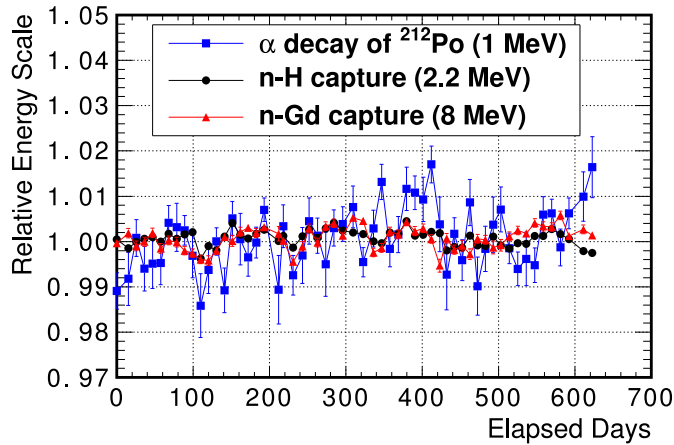
Figure 3.8: Variation of the peak energies after stability calibration as a function of time (from [185]). The data points show the ratios of the peak energies of neutron captures on Gd (black) and H (red) and from the α-decay of ^{212}Po (blue) to their nominal values. The error bars represent the statistical uncertainties on the peak energies.

Light non-linearity (LNL): Since this non-linearity is particle dependent, the LNL correction is only applied to the visible energy of positron candidates (prompt events). The LNL is represented by the remaining non-linearity after QNL correction and most likely related to the modeling of the scintillator. The correction is evaluated by matching the MC to calibration data. This is done by variation of the optical scintillator properties in the simulation within their uncertainties, which are taken from laboratory measurements. Based on the optical parameters giving the best agreement to the data, the LNL correction is extracted from MC.

Systematic energy scale uncertainty

The systematic uncertainties on the energy scale of the Gd-II and Gd-III analyses are shown in Table 3.1. These uncertainties enter the θ_{13} fit as uncertainties on the parameters of a parametric function, which is allowed to shift the energy scale. In the Gd-II fit a linear variation is tolerated corresponding to a parameter α_E with 1.13 % uncertainty [6]. The Gd-III analysis utilizes a second-order polynomial with three energy scale parameters in total [12]. The fluctuation of the parameters is in both fits included in form of additional terms in the χ^2 (Section 3.4). Bin-to-bin correlations in the rate and shape fit (Section 3.4.3) are covered by a covariance matrix in the case of Gd-II, while in Gd-III the correlations are assigned to the three energy scale parameters.

A plot of the Gd-III energy resolution is given in Fig. 3.9.

The H-II energy scale systematic uncertainties are identical to the Gd-II uncertainties except for a larger contribution from non-uniformity (1.33 %) [198]. As no Gd-complex is present in the Gamma Catcher liquid, ^{252}Cf source data is used to estimate the non-uniformity uncertainty in the Gamma Catcher volume. The total normalization uncertainty in the H-II analysis is therefore 1.7 % [8].

The Gd-I analysis handled the energy scale uncertainty by means of a covariance matrix with a normalization uncertainty of 1.7 % [5, 112]. The normalization uncertainty is

Table 3.1: Systematic uncertainties of the energy scale calibration evaluated as weighted averages over the prompt energy spectrum [6, 12, 70]. The last column represents the remaining fraction of the uncertainties in Gd-III relative to Gd-II.

	Gd-II [%]	Gd-III [%]	Gd-III/Gd-II
Relative non-uniformity	0.43	0.36	0.84
Relative instability	0.61	0.50	0.72
Relative non-linearity	0.85	0.35	0.41
Total	1.13	0.74	0.65
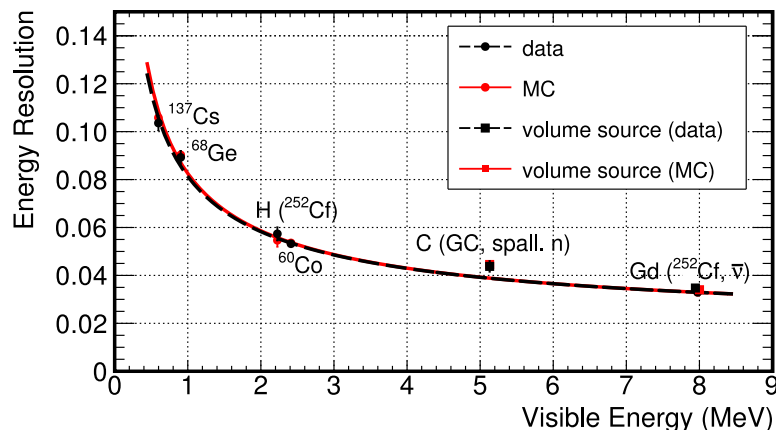
Figure 3.9: Energy resolution of various energy peaks observed in data (black) and MC (red) after energy scale calibration as a function of the peak visible energy (from [185]). The bullets correspond to measurements performed with point-like deployment sources at the ν-target center, the squares are obtained from event samples distributed over the ν-target (for neutron captures on Gd) and GC (mainly for neutron captures on carbon) volume. The values are fitted with $\sigma/E_{\mathrm{vis}} = \sqrt{a^2/E_{\mathrm{vis}} + b^2 + c^2/E_{\mathrm{vis}}^2}$ for data (dashed black line) and MC simulation (red line).

the fraction of energy scale uncertainty propagated in the rate-only (Section 3.4.4) θ_{13} analysis. It amounts to 0.32% in the DC-II fits and is negligible in the Gd-III analysis [70].

3.3 Neutrino data analysis

With the far DC detector ~ 200 trigger events are recorded per second, whereas only ~ 50 antineutrino interactions are expected per day. The goal of the neutrino selection algorithm is to filter out the relatively rare neutrino events from the large amount of other data. Properly chosen selection criteria manage to reduce the contribution from background events at acceptable loss of signal and with small systematic uncertainties. A large fraction of the recorded events is caused by cosmic muons, sporadic light emission from the PMT bases (also referred to as *light noise* [6]) and natural radioactivity. The first two are mostly removed from the data samples by means of veto information and rejection cuts described in the next paragraph. The latter is strongly suppressed

by the search for a coincidence signal (cf. Section 1.3.2). Newly developed background vetoes on the data analysis level succeed to suppress backgrounds further. Remaining background contributions are studied thoroughly and information on the expected rate and energy distributions are input to the θ_{13} fit framework.

Valid trigger

In order to improve the data handling and processing times of the high level analyses, preselected data sets were prepared, containing a reduced amount of data. The preselection is passed by events which come into consideration for further analysis, classified as *valid triggers*. A valid trigger

- has an energy larger than 0.4 MeV,

- is not a muon (a muon is identified as such in case $E_{vis} > 20$ MeV or if the energy deposited in the IV $E_{IV} > 16$ MeV),

- does not occur within less than 1 ms time difference to the last preceding muon, and

- is not a light noise event.

Light noise events show different characteristics than usual physics events which makes it possible to isolate this type of background. In the majority of cases a flash of light is produced by only one PMT base. The light is detected after reflections by the surrounding PMTs and thus creates a relatively localized hit pattern in the detector, while the PMT pulses are spread in time. In the DC-I and DC-II analyses, light noise events were rejected by requiring the ratio q_{max}/q_{tot} of the largest amount of charge seen by a single PMT and the total observed charge to be smaller than a threshold value [6, 12]. This cut guaranteed the spatial homogeneity of a physics signal. A cut on the standard deviation of the pulse arrival times σ_t removed events in case this variable was larger than 40 ns [6, 12]. The cut threshold on q_{max}/q_{tot} was relaxed in the Gd-III analysis, since additional light noise rejection criteria were developed [12]: 1) $\sigma_t > 36$ ns and $\sigma_q > (464 - 8\sigma_t)$ CU (charge unit), where σ_q corresponds to the standard deviation of the PMT charges; 2) $Q_{dev} > 3 \cdot 10^4$ CU. The variable in 2) is here defined as $Q_{dev} = 1/N \cdot \sum_i^N (q_{max} - q_i)^2/q_i$ and the sum is performed over all PMTs with maximal distance of 1 m to the PMT with largest charge q_{max}. The change of the cut thresholds and the introduction of new cuts allowed to enhance the IBD signal efficiency, at the same time the background rejection capability was improved, especially at high energies (≥ 8 MeV) [12].

3.3.1 Neutrino candidate selection

The IBD candidate selection comprises cuts on energy, relative timing and relative distance of the prompt and delayed events (as illustrated for the Gd-III analysis in Fig. 3.10). Depending on the detection channel, the corresponding neutron captures are selected by a cut on the delayed energy. Hence, neutron captures on Gd can be discriminated from H-captures without ambiguity by requiring the visible energy to be around 8 MeV. The cut on the prompt to delayed correlation time ($\Delta t_{p\text{-}d} = t_d - t_p$) is determined based on the mean neutron capture time of ~ 30 μs in the ν-target scintillator liquid. No additional correlation distance cut (cut on ΔR, the absolute distance

(a) Prompt visible energy.

(b) Delayed visible energy.

(c) Prompt to delayed correlation time.

(d) Prompt to delayed correlation distance.
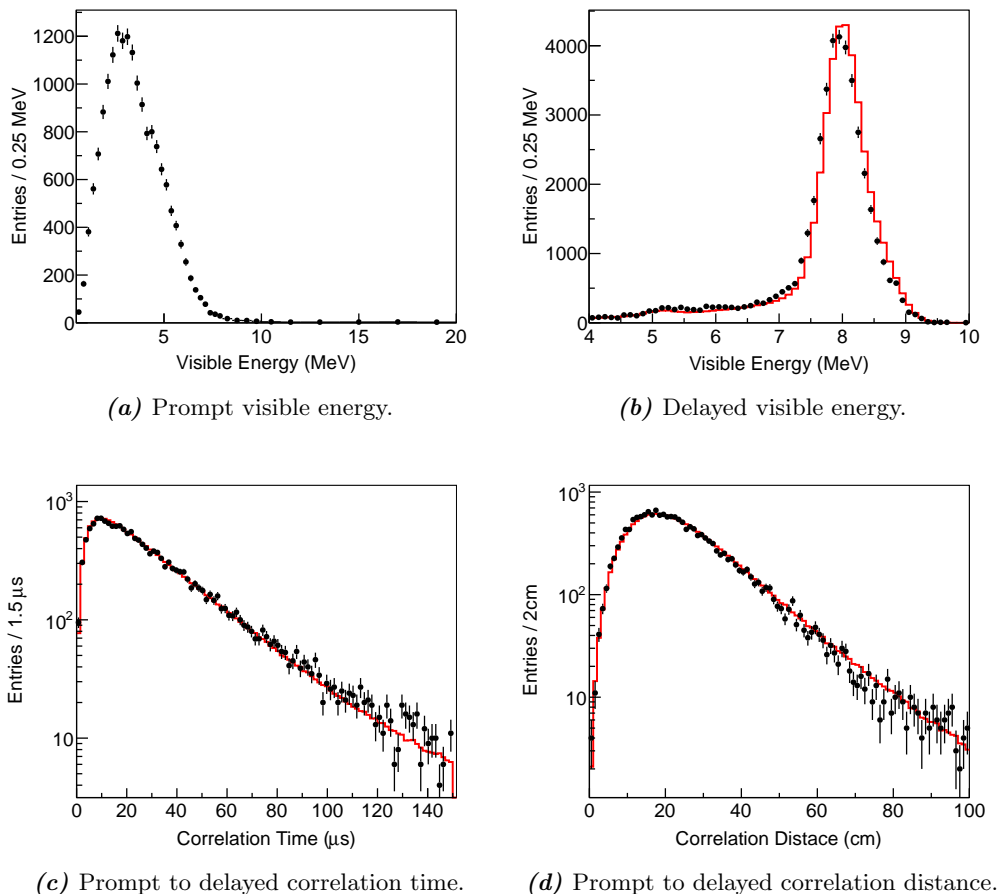
Figure 3.10: Energy, timing and correlation distance spectra of the 17358 neutrino candidates selected during reactor-on and -off phases in the Gd-III analysis (from [172]).

between reconstructed prompt and delayed position) is applied in the Gd-I and Gd-II analyses. Requiring that no other trigger besides the delayed event occurs in Gd-I+II (Gd-III) 100 µs (200 µs) before and 400 µs (600 µs) after the prompt event, reduces the selection of muon-induced correlated backgrounds, which are often accompanied by multiple neutrons.

The selection criteria for the H-channel analysis is adjusted to the different energy, timing and background properties of the neutron captures on hydrogen. Therefore the required energy interval of the delayed event is chosen based on the H-capture 2.2 MeV gamma. As most of the contributions (about 95 % [8]) to the IBD signal are expected to occur in the gamma catcher volume where no Gd nuclei are present, the upper correlation time cut is enlarged to 600 µs to account for the ∼ 200 µs lifetime of the neutron captures in the gamma catcher liquid. The lower correlation time cut of 10 µs efficiently rejects correlated backgrounds such as stopping muon events and correlated light noise (see Section 3.3.4). Accidental coincidences (cf. Section 3.3.3) which are the main source of background in an H-channel based analysis are suppressed by the 90 cm cut on the correlation distance.

43

Table 3.2: Criteria of the neutrino candidate selection [5, 6, 12, 8].

	Gd-I and Gd-II	Gd-III	H-II
Prompt energy	$0.7 < E_{\text{p}} < 12.2\,\text{MeV}$	$0.5 < E_{\text{p}} < 20\,\text{MeV}$	$0.7 < E_{\text{p}} < 12.2\,\text{MeV}$
Delayed energy	$6 < E_{\text{d}} < 12\,\text{MeV}$	$4 < E_{\text{d}} < 10\,\text{MeV}$	$1.5 < E_{\text{d}} < 3\,\text{MeV}$
Corr. time	$2 < \Delta t_{\text{p-d}} < 100\,\text{µs}$	$0.5 < \Delta t_{\text{p-d}} < 150\,\text{µs}$	$10 < \Delta t_{\text{p-d}} < 600\,\text{µs}$
Corr. distance	-	$\Delta R < 100\,\text{cm}$	$\Delta R < 90\,\text{cm}$
Event isolation	$[-100\,\text{µs}, +400\,\text{µs}]$	$[-200\,\text{µs}, +600\,\text{µs}]$	$[-600\,\text{µs}, +1000\,\text{µs}]$

In Table 3.2 the selection cuts of the three Gd-channel and the H-channel analyses are summarized. The Gd-II analysis included an additional high energy muon cut: the event veto after a muon was extended to $0.5\,\text{s}$ in the analysis in case the muon energy in the ID exceeded $600\,\text{MeV}^*$ (The energy unit MeV^* is not corrected for non-linearities at high energies.) and is also referred to as *showering muon veto*. This cut increased the dead time from $4.5\,\%$ to $9.2\,\%$ [5, 6] and could be abandoned in the Gd-III analysis due to improved background rejection techniques. As from the Gd-II data set on the OV information became available, a prompt trigger is rejected if it occurs simultaneously (within $224\,\text{ns}$ [12]) with an OV trigger in the Gd-II and Gd-III selection. The dead time introduced by the OV is with less than $0.1\,\%$ negligibly small [80, 81].

Upon the DC-III Gd-channel analysis, several changes on the candidate selection were made: only few positron events from IBD reactions are expected for visible energies smaller than $\sim 1\,\text{MeV}$ and larger than $8\,\text{MeV}$. Still the prompt selection window was increased, as the extension of the prompt energy range to background dominated regions adds additional constraints on the backgrounds in the spectral shape related fit. The delayed energy and correlation time criteria were loosened, thus increasing the neutron detection efficiency. The lower correlation time cut of $0.5\,\text{µs}$ was introduced, as the stopping muon background (details in Section 3.3.4) was suppressed by new veto cuts. In addition a selection criterion on the correlation distance was added, leading to a reduction in the selection of false coincidences (*accidental background*, described in Section 3.3.3), which in turn enabled to extend the delayed energy and correlation time cuts.

Using MC simulation, the Gd-III selection efficiency[4] was found to have increased to $98.4\,\%$ compared to the Gd-II efficiency of $91.2\,\%$, where the efficiency was estimated relative to a loosened selection of $3.5 < E_{\text{delayed}} < 12\,\text{MeV}$, $0.25 < \Delta t < 1000\,\text{µs}$ and no constraint on the correlation distance. The Gd-III analysis additionally rejects events satisfying the following veto cuts [12] (descriptions of the vetoes are given in Section 3.3.4):

- If along with a prompt event more than $400\,\text{CU}$ (charge units, where $400\,\text{CU}$ is equivalent to $0.2\,\text{MeV}$) is deposited in the IV, hitting more than ≥ 2 PMTs and the ID and IV events are less than $3.7\,\text{m}$ spatial and $50\,\text{ns}$ in time close to each other, the candidate is rejected. This veto, called *IV veto*, loses $(0.058 \pm 0.001)\,\%$ of the IBD signals [12].

---

[4]The event isolation cut is not included in this estimation.
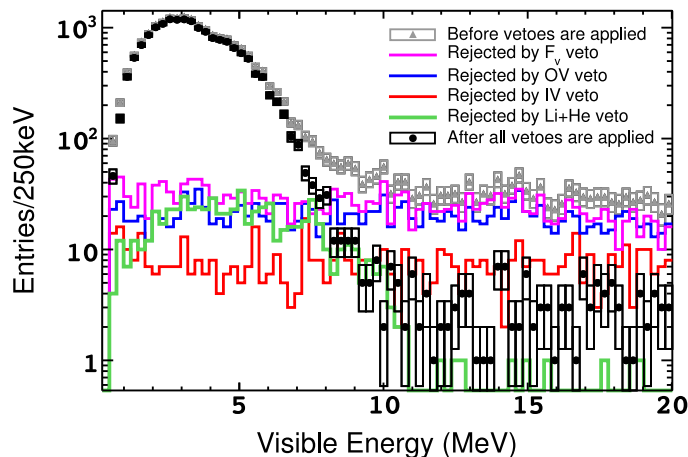
Figure 3.11: Visible energy of the signal prompt events kept or rejected by the background vetoes. The data points represent the measured spectra and their statistical uncertainties before (gray, triangle) and after (black, circle) the F_V, OV, IV and ^{9}Li+^{8}He likelihood veto were applied in combination. The colored lines show the candidates rejected by each individual veto: F_V veto (magenta), OV veto (blue), IV veto (red) and ^{9}Li+^{8}He likelihood veto (green) (from [66]).

- The F_V *veto* excludes events from the candidate selection, if the delayed event visible energy is $E_{\mathrm{vis}} < 0.068 \cdot \exp(F_V/1.23)$. This cut not only rejects stopping muon background (cf. Section 3.3.4) but also light noise events with a loss of $(0.06 \pm 0.11)\,\%$ of the IBD signals [12].

- In case the maximum ^{9}Li+^{8}He likelihood $\mathcal{L}_{\mathrm{Li}}$ of the candidate in combination with all preceding muons within $700\,\mathrm{ms}$ is larger than a threshold value, it is rejected. About $55\,\%$ of the cosmogenic background is removed by this veto, while $(0.504 \pm 0.018)\,\%$ of the the IBD signals are lost [12].

In total 5.4 events per day are vetoed by a combination of OV, IV and F_V veto [83]. Above $12\,\mathrm{MeV}$ $90\,\%$ of the events passing the IBD selection cuts without vetoes are removed by a combination of the three vetoes [12] (see also Fig. 3.11). The overlap in vetoed events is illustrated in Fig. 3.12.

3.3.2 Signal detection efficiency

Most of the selection criteria determining the collection of the neutrino candidate sample as well as background rejection veto aim at maximizing the signal to background ratio, however in many cases at the cost of signal detection efficiency. As the DC experiment targets the measurement of a deficit in the detected neutrino flux in comparison to a MC prediction or between two measured neutrino spectra, accurate knowledge of the relevant detection efficiencies and related uncertainties is of crucial importance in the oscillation analysis.

We can split the signal detection efficiency into different contributions coming from 1) the active background vetoes, 2) the number of hydrogen nuclei in the ν-target liquid and the candidate extraction consisting of 3) the prompt event selection and 4) the
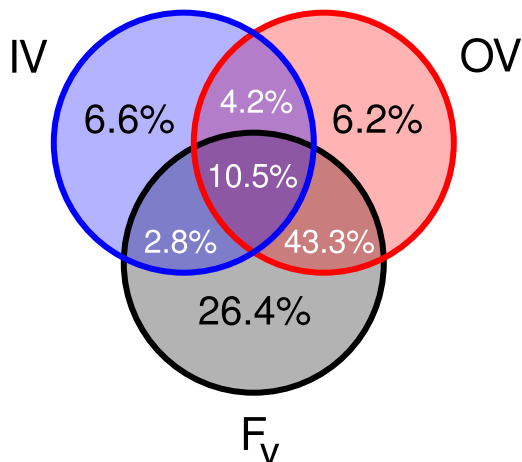
Figure 3.12: Venn diagram illustrating the overlap in vetoed events removed by the OV, IV and F_V vetoes. The fractions are computed relatively to the total number of vetoed IBD candidates. Results and idea from [83].

delayed event selection. Throughout the past DC analyses, the main contribution to the veto inefficiency of $\sim 4.5\,\%$ (in Gd-I and Gd-III) to $9.2\,\%$ (in Gd-II) but negligible uncertainty has been introduced by the veto applied after a muon event. The additional background veto techniques discussed in the past two sections impose a reduction of $(0.60 \pm 0.11)\,\%$ on the signal detection in the Gd-III analysis. The MC normalization is diminished by the same relative amount as the detection efficiency of the data is reduced by the application of a veto.

Since protons in form of hydrogen nuclei represent the target for antineutrinos undergoing the IBD reaction and recalling Eq. (3.1), the absolute number of hydrogen atoms present in the liquid scintillators is a critical input. This quantity, the "proton number" N_p, is $(6.747 \pm 0.020) \times 10^{29}$ in the ν-target [5] and $(1.582 \pm 0.016) \times 10^{30}$ in the GC liquid of the far detector [8]. For the ν-target proton number a $0.3\,\%$ relative uncertainty coming from the knowledge of the hydrogen ratio in the scintillator and the with $0.04\,\%$ precision weighted mass of the ν-target liquid filled into the detector. The $1\,\%$ relative uncertainty on the GC value is deduced from survey data of the acrylic vessels' geometry together with laboratory measurements of the hydrogen content in the GC scintillator liquid [60].

A reduction of the prompt event selection efficiency can be introduced by trigger inefficiencies and the event isolation cut. The latter omits about $1\,\%$ or less of the neutrino candidates due to accidental coincidences hindering the candidate identification. This reduction in efficiency, however, can be precisely measured knowing the single event rate, and is hence an irrelevant source of detection uncertainty [13]. The trigger efficiency at the analysis thresholds of the different DC analyses has been in all cases almost $100\,\%$, for Gd-I an uncertainty of $0.4\,\%$ was assigned, for the other analyses the uncertainty was found to be negligible ($< 0.1\,\%$).

A component having a large impact on the signal detection efficiency is given by the choice of the delayed event selection criteria, and is hence related to neutron detection. To which level of accuracy the neutron detection efficiencies observed in detector

data can be reproduced by the DC simulation code is studied by means of a ^{252}Cf calibration source (Gd-I to Gd-III) or a IBD neutron sample (Gd-III). The fraction of neutrons captured on Gd was found to be $\sim 2\,\%$ lower in the data compared to the fraction estimated by MC simulation code. To accommodate the predicted neutrino flux from MC to this discrepancy, a correction factor is applied lowering the number of expected neutrinos. Border effects at the ν-target acrylic walls due to neutron mobility are observed to slightly change the fiducial volume boundaries, both in data and MC simulation. Different simulation configurations and neutron modelings are used to study this "spill-in/out" effect and to quantify the systematic uncertainty on the neutrino prediction. Further details on the signal detection efficiency and in particular the DC-III neutron detection efficiency are addressed in Chapter 5 and Chapter 6. The spill-in/out effect in the Gd-channel analyses and its contribution to the detection systematic uncertainty is discussed in Chapter 7.

The total signal detection uncertainties including all mentioned contributions amount to $1.4\,\%$, $1\,\%$ and $0.6\,\%$ in the three Gd-channel analyses and $1.6\,\%$ in the H-channel analysis (see also Table 3.6 and Table 5.1).

3.3.3 Accidental background

The neutrino selection focuses on filtering out correlated events, however false coincidences can be among the selected set of candidates. These false coincidences consist of two uncorrelated events *accidentally* passing the cuts, featuring a flat distribution in the correlation time spectrum. In Fig. 3.13 the visible energy spectrum of valid triggers is shown. The main contribution to the *singles spectrum* is located below 3 MeV. For energies larger than the 2.64 MeV gamma radiation from ^{206}Tl decay [166], the spectrum drops off steeply, while the only noteworthy decays contributing at higher energies[5] are from β-decay of ^{214}Bi (Q-value of 3.27 MeV [166]) and ^{208}Tl (Q-value of 5.0 MeV [166]). In this context the purpose of the Gd-loading becomes evident: with a visible energy of roughly 8 MeV the delayed neutron capture deposits a considerably higher amount of energy compared to the single events. In addition, the neutron capture time is lowered to $\sim 30\,\mu s$ on average, whereas it would be $\sim 200\,\mu s$ without loading. Both properties of Gd lead to a significant reduction of the accidental background for a Gd-based analysis. In the Gd-III analysis a cut on the correlation distance was introduced to suppress the selection of accidental coincidences further. In the case of the H-channel analyses a correlation distance cut represents an essential selection criterion to reject accidental background, which constitutes by far the largest background contribution.

The remaining accidental background contribution can be measured by means of an *off-time window* method, selecting delayed candidates with 1 s offset to a prompt. The statistics can be further increased by adding successive windows to the background measurement. Dead times originating from the standard neutrino selection are accounted for by application of correction factors. In the Gd-III analysis the influence of the Li+He veto cut had to be taken into consideration. This also explains why the uncertainty of the Gd-III accidental background slightly increased with respect to the other publications [12]. The measured rates are summarized in Table 3.3 in Section 3.4.

---

[5]At higher energies other sources, such as the decay of ^{12}B (Q-value of 13.37 MeV [166]), neutron captures on iron (7.65 MeV and 9.30 MeV [135]) and Gd are present, but with considerably lower rate than the decays with energies $E < 5$ MeV. Furthermore the possibility of events from bremsstrahlung photons originating from cosmic muons is discussed in Ref. [39].
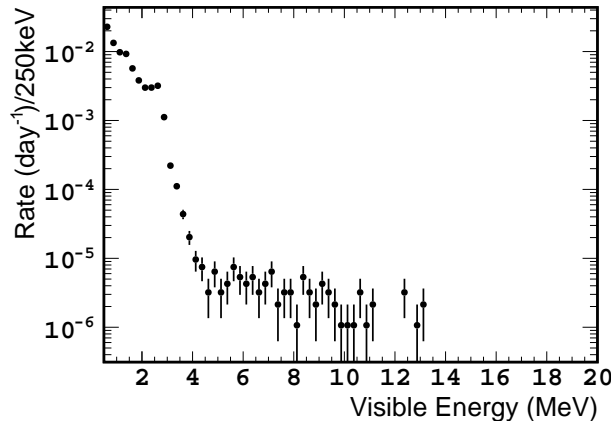
Figure 3.13: Prompt visible energy of the accidental background, measured using the off-time window technique (from [152]).

3.3.4 Correlated background

Unlike the accidental coincidences, the correlated background prompt and delayed events originate from a common physical process. The prompt and delayed visible energies coincide with the IBD selection criteria and the correlation time is determined by the underlying production mechanism. Most of the correlated backgrounds relevant for the DC analyses are muon-induced. Their correlation to the parent muon can therefore either be used to study rate and shape of the backgrounds or reduce their contribution further by means of vetoes on the analysis level, newly developed in the Gd-III analysis.

Three relevant classes of correlated backgrounds are considered in the fit of the Gd-channel θ_{13} analysis: the β-n decays of the cosmogenic isotopes ^{9}Li and ^{8}He, fast neutrons and stopping muon decays. Each type of background, their rate and energy shape estimation as well as reduction vetoes are discussed in the following.
A fourth background contribution has been observed in the H-II analysis. Correlated light noise events of $\Delta T \approx 14\,\mu$s were found to pass both the light noise rejection and the candidate selection cuts [164, 8]. Dedicated studies to measure the spectral shape and rate of these background events were performed, making use of the observation that the reconstructed background vertices accumulate at the ν-target center [198].
The correlated background rates are given in Table 3.3 in Section 3.4.

Cosmogenic isotopes

Long-lived *radio-isotopes* like ^9Li and ^8He are produced by cosmic muon spallation on ^{12}C [120, 2], abundant in the organic compounds of the liquid scintillators and the vessel acrylics. These isotopes are β-n emitters, whereas the β-decay of ^{9}Li is in 50.8 % of the cases accompanied by two α-particles and a neutron [166]. The β-n-decay of ^{8}He, occurring with a branching ratio of 16 %, can either create an additional neutron or a neutron, an α-particle and a triton [166]. Both decays can include an intermediate state of ^{5}He, which is included in the MC simulation of the cosmic isotope spectra [103]. The energy deposition of the β-particle, the α-particle, the triton and the kinetic energy

loss of the neutron is hence identified as prompt event[6], while the neutron capture on H or Gd creates the delayed energy deposition. As the delayed particle is given by a neutron produced along with the β-particle, the event topology will be in space and time the same as for an IBD interaction. The cosmogenic isotopes decay with lifetimes of $\tau = 257\,\mathrm{ms}$ (^{9}Li) and $\tau = 172\,\mathrm{ms}$ (^{8}He), too long to be effectively removed by a veto after muons without a tremendous increase of the detector dead time. The correlation to the parent muon can, however, be used to extract the rate and shape of this type of background. In particular produced by highly energetic muons ("showering muons"), for $E_{\mathrm{vis},\mu} > 600\,\mathrm{MeV}^*$ the correlation time between the muon and any subsequent IBD candidate is fitted with

$$f(\Delta t_{\mu\text{-IBD}}) = (A/\tau_{\mathrm{Li}}) \cdot e^{-\Delta t_{\mu\text{-IBD}}/\tau_{\mathrm{Li}}} + B \,, \qquad (3.15)$$

with $\Delta t_{\mu\text{-IBD}} = t_{\mathrm{IBD}} - t_\mu$ (see Fig. 3.14b). The ^{8}He content was neglected by the DC-I and DC-II analyses, as it is known to be far less abundant [6] and was later included in the Gd-III systematic uncertainty [13]. In order to take into account the ^{9}Li+^{8}He production by muons with energies below $600\,\mathrm{MeV}^*$, only IBD candidates with a distance $d_{\mu\text{-IBD}} < 80\,\mathrm{cm}$ ($75\,\mathrm{cm}$ in the Gd-III analysis) perpendicular to the muon track are included in the $\Delta t_{\mu\text{-IBD}}$ fit, to reduce the contribution of accidental coincidences. This analysis is performed for sub-samples divided with respect to the muon energy; the selection inefficiency introduced by the cut on $d_{\mu\text{-IBD}}$ is studied using the lateral distance profile of the ^{9}Li+^{8}He production at high muon energies [12].
In the Gd-III analysis a lower limit on the ^{9}Li+^{8}He rate was imposed, gained from the analysis of a Li-enriched sample. The energy and lateral distance cuts were refined so that the signal (^{9}Li+^{8}He) to background (accidental muon-IBD coincidences) ratio was increased, which results in a reduction of the fit uncertainties [12, 213].

In the course of the Gd-III analysis, a ^{9}Li+^{8}He likelihood veto was developed, allowing to either select cosmogenic decay candidates for further investigations or reject them in the IBD candidate search.

^{9}**Li+^{8}He likelihood:** The likelihood makes use of information about the lateral distance $d_{\mu\text{-IBD}}$ to the parent muon and the number of neutrons created along with the ^{9}Li+^{8}He candidate. The probability density functions (PDFs) used by this method are extracted from ^{12}B events, which are proven to generate the same PDFs as ^{9}Li and are available with higher statistics [83, 79].

The rates estimated by a Li-candidate selection using the ^{9}Li+^{8}He likelihood agrees with the results from the correlation time method described above [13].
In Fig. 3.14a the spectrum of ^{9}Li+^{8}He prompt events is given and was measured using the ^{9}Li+^{8}He likelihood cut. While in the DC-I and DC-II θ_{13} rate and shape fits a MC simulated spectrum was used as input [5, 6], the Gd-III analysis retrieved the cosmogenic background spectrum from data for the first time.
Details on the cosmogenic isotope studies can be found in Ref. [6, 12, 83].

---

[6]The visible energy will be dominated by the β-particle's energy deposition as the other decay products, especially the α-particle, will lose a large fraction of their energy non-radiatively due to quenching effects.
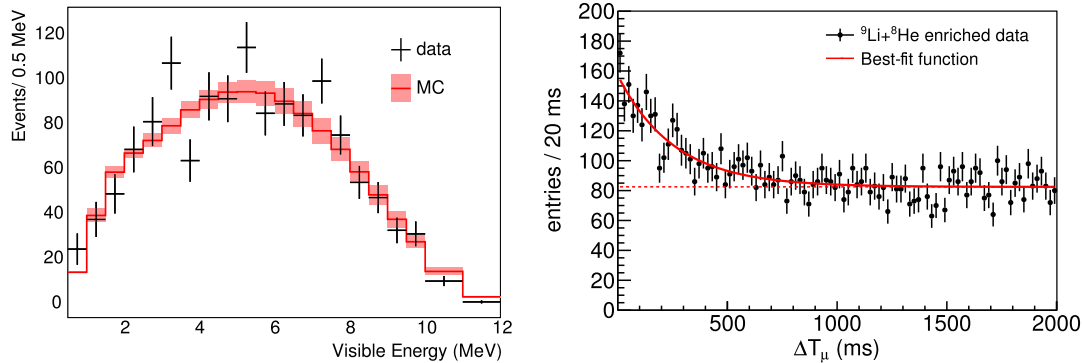
(a) Prompt energy spectrum of the cosmogenic isotopes (from [82]). The Li-candidates (black points, with statistical uncertainty) were selected by means of the ^{9}Li+^{8}He likelihood. The red line corresponds to the MC prediction including only ^{9}Li.

(b) Time to last muon ΔT_μ of events in the Li-enriched sample (from [214]). The red line corresponds to the fit of Eq. (3.15) to data, including accidental coincidences (dashed line) and the ^{9}Li-decays (solid line).

Figure 3.14: Cosmogenic isotopes prompt energy and correlation time spectrum.

Fast neutrons and stopping muons

Another class of correlated backgrounds can be created by muons which do not pass the active detector regions or deposit only little energy in the muon vetoes and are therefore missed. *Fast neutrons* (fast-n) can be produced by cosmic muon spallation in the surrounding rock and penetrate the detector [206]. The neutrons will moderate mostly by elastic scattering with the protons present in the scintillator liquids. In case the neutrons are energetic enough, the proton recoil will deposit a visible amount of energy, creating a flat spectrum in the full prompt energy range. The radiative capture of the recoiling or any other neutron will constitute the delayed event, thus mimicing the IBD signal. As the neutrons on their way to the ID often deposit energy in the IV scintillator, they can be identified by tagging techniques [186].

Muons entering the detector through the chimney can stop inside the ν-target and decay into a Michel electron (or positron) and a muon-neutrino and are therefore referred to as *stopping muons* (stopping-μ). The electron deposits up to $52.8\,\text{MeV}$ and is detected as delayed event, while the prompt energy deposition is created by the muon track. Prompt and delayed event are separated in time by the muon live-time, which is on average $2.2\,\mu\text{s}$.

While the fast-n and stopping-μ background was largely suppressed upon the OV commissioning ($53\,\%$ reduction according to Ref. [9]), stopping muon events can additionally be removed by a veto on the likelihood value judging the success of the vertex reconstruction:

$F_{\mathbf{V}}$ **veto:** Stopping-μ and light noise events can create PMT hit patterns different from common physics events. The latter are rather point-like leading to a successful vertex reconstruction, whereas for stopping muon and light noise events the negative log-likelihood of RecoBAMA in Eq. (3.9) becomes large [12]. Stopping-μ mainly enter the detector through the chimney and thus cause vertex reconstruction to be difficult.
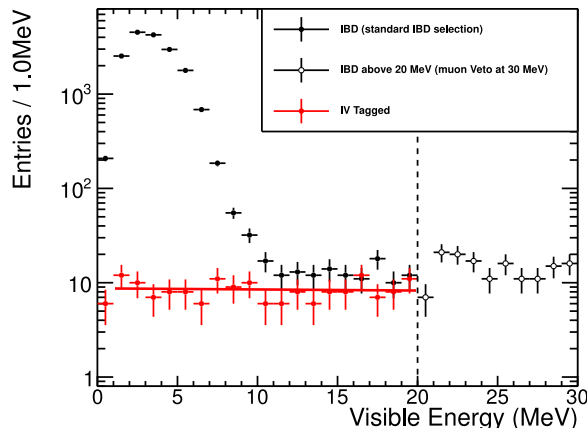
Figure 3.15: The prompt energy spectra for three different datasets (from [143]): standard IBD candidate selection (black filled points), IBD candidate selection above 20 MeV (black empty circles) and the IV tagged events (red points) fitted by a linear function with (-0.02 ± 0.11) events/MeV^2.

While the fast-n and stopping-μ shape was estimated from IBD candidates in the 12.2 to 30 MeV interval in the DC-I analysis and extrapolated to the prompt energy range (featuring a flat spectrum), the DC-II and DC-III analyses made use of the IV tagging:

IV veto: The IV veto criteria described in Section 3.3.1 aim at the detection of fast-n and stopping-μ events, entering the sensitive detector volumes from outside. As the IV data is read out after every ID trigger, IV information below the muon trigger threshold is available. Requiring the distance between the ID and IV reconstructed vertices to not exceed 3.7 m, reduces the rejection of accidental IV and ID coincidences.

With the IV tagged events which also pass the IBD selection criteria, the fast-n and stopping-μ spectra were measured in the full prompt energy range. A spectral shape consistent with a flat spectrum was found and confirmed using different selection criteria and combinations with the OV vetoed events [6, 12, 13]. Moreover, it is in agreement with the IBD candidate spectrum for $E_{\mathrm{vis}} > 12$ MeV, the region in which the correlated background contribution becomes dominant (Fig. 3.15). Hence, a flat spectral shape was used by all three Gd-channel analyses as input to the θ_{13} rate and shape fit.

The fast-n and stopping-μ rate was estimated by all three Gd analyses in the higher prompt energy regions, where no IBD candidate is expected. The background rate was computed from the events in the energy window $E_{\mathrm{w}} < E_{\mathrm{vis,p}} < 30$ MeV, with $E_{\mathrm{w}} = 12.2, 12, 20$ MeV (Gd-I, Gd-II and Gd-III analysis[7]), and extrapolated to the full prompt energy region [5, 12]. In the Gd-II analysis the final result on the fast-n and stopping-μ rate was calculated using the IV tagged events [6]. Whereas the fast-n and stopping-μ contributions were of comparable size in the Gd-II analysis [6], the Gd-III rate is, because of the F_{V} veto cut, predominantly given by fast-n events [12].

---

[7]For this analysis the ID energy threshold of the muon veto had to be changed from 20 MeV to 30 MeV, having negligible impact [142].

In the H-channel analysis the stopping-μ background contribution to the candidate selection was largely suppressed by the minimum correlation time cut of $10\,\mu s$. The remaining fast-n background was studied using the IV tagging technique [198]. As the fast-n shape was found to deviate from flatness and rather resembles an exponential spectrum rising towards lower energies, the rate was estimated from an integral of the measured spectrum taking into account the IV tagging efficiency.

3.4 Oscillation analysis: Fitting θ_{13}

The deficit in measured IBD candidates compared to the reactor prediction (Table 3.4) observed by the DC experiment can be understood as result of the neutrino oscillation phenomenon. Different analysis frameworks were developed to extract the oscillation parameter θ_{13} using Eq. (1.7), nonetheless all of them are based on the minimization of a χ^2 statistics. A direct measurement of θ_{13} is achieved, with the current best result of $\Delta m_{31}^2 = 2.44^{+0.09}_{-0.10} \times 10^{-3}\,\text{eV}^2$ [23] ($\Delta m_{31}^2 = (2.32 \pm 0.12) \times 10^{-3}\,\text{eV}^2$ [21] in DC-I and DC-II) as only additional input.
The *Rate+shape (R+S) analysis* (Section 3.4.3), the *Rate-only (RO) fit* (Section 3.4.4) and the *Reactor Rate Modulation (RRM) analysis* (Section 3.4.5) as well as the corresponding results are presented in the upcoming sections.

Prior to the θ_{13} fit frameworks and results, the oscillation analysis backgrounds, observed and predicted rates will be summarized and discussed in this paragraph. In Table 3.3 the rates of all relevant background contaminations are given along with their total uncertainties. From comparison of the different DC analyses, the impact of the muon detectors and analysis vetoes become evident. The Gd-II fast-n and stopping-μ rates are reduced compared to Gd-I due to the availability of OV data. The application of the showering muon veto[8] lowered the cosmic isotope background by $40\,\%$ and as well affected the accidental rate, which decreased by $26\,\%$ [9]. Lower background rates are observed in the Gd-III analysis, which instead of the showering muon veto utilized newly developed background vetoes. The rate of accidental coincidences is significantly reduced by the correlation distance cut; the systematic uncertainty, however, is increased due to the ^{9}Li+^{8}He likelihood veto [12]. The uncertainties in the correlated backgrounds are further reduced. Besides this, the actual reduction in the fast-n background is roughly $50\,\%$, as the Gd-II background has to be scaled for a direct comparison to the Gd-III value due to the wider selection windows in the Gd-III analysis, especially the prompt energy range [12].
In the Gd-III analysis the impact of correlated events among ^{12}B decays (with a lifetime of $29.1\,\text{ms}$ [166]) or ^{12}B together with spallation neutrons were studied. Moreover, the contribution from ^{13}C(α,n)^{16}O reactions was investigated. Both possible sources of background were found to be negligible [12].
Table 3.4 summarizes the number of candidates, backgrounds and the reactor prediction for each DC dataset. The size of the datasets increases from Gd-I to Gd-III, while the dataset of the previous analysis is contained in the successive one. The H-II dataset is with $240.1\,\text{days}$ live-time slightly larger than the Gd-II dataset, which is caused by a difference in the veto cuts.

---

[8]The relative reduction was evaluated using the Gd-II data set with Gd-I and Gd-II selection cuts [9]. Therefore the numbers might differ from the ones given in Table 3.3.

Table 3.3: Background rate estimations of the four DC analyses [5, 6, 8, 12], the systematic uncertainties are included.

Background (d^{-1})	Gd-I	Gd-II	H-II	Gd-III
^{9}Li+^{8}He	2.3 ± 1.2	1.25 ± 0.54	2.8 ± 1.2	$0.97^{+0.41}_{-0.16}$
Fast-n, Stopping-μ	0.83 ± 0.38	0.67 ± 0.20	2.50 ± 0.47	0.604 ± 0.051
Accidental	0.33 ± 0.03	0.261 ± 0.002	73.45 ± 0.16	0.070 ± 0.003
^{13}C(α,n)^{16}O	–	–	–	< 0.1
^{12}B	–	–	–	< 0.03
Correlated Light Noise	–	–	0.32 ± 0.07	–

Table 3.4: Measured IBD candidates and unoscillated reactor prediction of the four DC analyses [5, 6, 8, 12]. The Gd-III numbers are for the reactor-on phase. The number of observed IBD candidates and the total prediction are highlighted in bold.

	Gd-I	Gd-II	H-II	Gd-III
Live-time (days)	96.8	227.93	240.1	460.67
IBD candidates	**4121**	**8249**	**36284**	**17351**
Reactor $\bar{\nu}_e$	4009	8439.6	17690	17530
^{9}Li+^{8}He	222.6	284.9	680	447
Fast-n, Stopping-μ	80.3	152.7	600	278
Accidental BG	31.9	59.5	17630	32.3
Correlate Light Noise	–	–	80	–
Total prediction	**4344**	**8937**	**36680**	**18290**

3.4.1 Reactor off measurements

Owing to the simple experimental configuration with only two reactor cores, the DC experiment experiences data taking phases with both reactors turned off. This special condition allows for a background measurement with only a small residual signal contribution, unique to the DC experiment. In total 7.53 days of reactor-off data were collected in 2011 and 2012 [9], the corresponding number of live-days depends on the selection cuts and vetoes imposed on the data, as given in Table 3.4. The estimated number of detected residual $\bar{\nu}_e$, the total expected number of events and observed IBD candidates is summarized in Table 3.4. The expected number of events is obtained from the background rate estimates and the number of residual neutrinos. The showering muon veto reduces the number of life-days and detected candidates in the Gd-II analysis, whereas the OV information is only used by the Gd-II and Gd-III results. In the Gd-III analysis a new set of veto cuts was introduced, which decreases the number of predicted events while the live-time is enhanced. In case of the Gd-III analysis the number of observed and predicted events are compatible at 9.0% ($1.7\,\sigma$) [12].

Whereas the reactor-off data has been used as crosscheck of the background measurement in the Gd-I and Gd-II R+S analyses, the accumulated amount of data was large enough upon the Gd-II RRM analysis [14] to use it as input to the oscillation fit (cf. Section 3.4.3 and Section 3.4.5).

Table 3.5: Reactor off predicted and observed number of IBD candidates for the three different Gd-channel based selections. [9, 12].

	live-days	residual $\bar{\nu}_e$	expected	observed
Gd-I	7.19	1.49 ± 0.60	25.8 ± 4.4	21
Gd-II	6.84	1.42 ± 0.57	15.1 ± 4.1	8
Gd-III	7.24	1.57 ± 0.47	$12.9^{+3.1}_{-1.4}$	7

3.4.2 Systematic uncertainty budget

A summary of the normalization uncertainties of signal and background relative to the signal prediction is given in Table 3.6. Due to improved data analysis, calibration techniques and accumulated statistics, the uncertainties on the backgrounds, energy response and detection efficiency could be further reduced with each Gd-channel analysis. The reactor related uncertainty remains the dominant systematic uncertainty in an oscillation analysis with a single detector. The projected sensitivity with one detector and both, ND and FD, is addressed in Section 3.4.6.

Table 3.6: Signal and background normalization uncertainties of the DC analyses, relative to the signal prediction [5, 6, 8, 12]. Note that the uncertainties are given relative to the signal prediction (not total prediction) and can hence differ from the values presented in the cited references.

Uncertainty (%)	Gd-I	Gd-II	H-II	Gd-III
Reactor flux	1.8	1.8	1.8	1.7
Detection Efficiency	1.4	1.0	1.6	0.6
Detector Response	1.7	0.3	0.3	–
^{9}Li+^{8}He BG	2.9	1.5	1.6	$+1.1$ / -0.4
Fast-n, Stopping-μ BG	0.9	0.5	0.6	0.1
Accidental BG	0.07	0.01	0.2	0.01
Light Noise	–	–	0.1	–
Statistics	1.6	1.1	1.1	0.8
Total	4.4	2.8	3.1	$+2.3$ / -2.0

3.4.3 Combined rate and spectral shape fit

The *Rate+shape (R+S) analysis* exploits the energy dependence of the neutrino oscillation deficit and constitutes the standard analysis framework for the four DC publications on θ_{13}. The comparison of the measured IBD candidate rate to the predicted rate is hence done within different energy regions of the prompt visible energy. In addition, further constraint on the background rates is added to the fit, as the expected signal to background proportions vary over the energy spectrum. To optimize the event statistics measured at different energies, the prompt spectrum is separated in energy bins of variable sizes.

The signal and background prediction consists of the expected number of antineutrinos from the two reactors $N_i^{\mathrm{exp},R}$ (as in Eq. (3.5)), the survival probability $P_{\bar{\nu}_e \to \bar{\nu}_e}$ including θ_{13} and the three backgrounds N_i^b (accidental, cosmogenic isotopes and correlated fast-n and stopping-μ events) [6]:

$$N_i^{\mathrm{pred}} = \sum_{R=1,2}^{\mathrm{Reactors}} P_{\bar{\nu}_e \to \bar{\nu}_e}(\theta_{13}) \cdot N_i^{\mathrm{exp},R} + \sum_b^{\mathrm{Bkgnds}} N_i^b \, . \tag{3.16}$$

Estimates for the background rates and energy distributions are taken from the measurements described in Section 3.3.1, except for the $^9\mathrm{Li}+^8\mathrm{He}$ spectral shape, which was retrieved from MC simulations in DC-I and DC-II. In the Gd-III analysis every background input of the fit was extracted from detector data for the first time.

Statistical and systematic uncertainties are propagated by means of covariance matrices of size ($n_{\mathrm{bins}} \times n_{\mathrm{bins}}$) with the number of bins n_{bins}, which account for correlations in the uncertainties between the energy bins. The covariance matrix [6]

$$M_{ij} = \sum_A^{\mathrm{Uncert}} M_{ij}^A + \sum_b^{\mathrm{Bkgnds}} M_{ij}^b \tag{3.17}$$

includes the covariances $M_{ij}^A = \mathrm{cov}(N_i^{\mathrm{pred}}, N_j^{\mathrm{pred}})$ related to the uncertainties of source A and the different backgrounds b. Depending on the other terms added to the χ^2 definition of the different DC analyses, the covariance matrix comprised contributions from reactor, energy response, efficiency, backgrounds and statistical uncertainties.

The binned rate and spectral shape χ^2 definition is in a general form given by

$$\chi_{\mathrm{R+S}}^2 = \sum_{i,j}^{\mathrm{Bins}} (N_i - N_i^{\mathrm{pred}})(M_{ij})^{-1}(N_j - N_j^{\mathrm{pred}})^T + \chi_{\mathrm{Pulls}}^2 + \chi_{\mathrm{off}}^2 \, , \tag{3.18}$$

where the last term χ_{off}^2 corresponds to a Poisson likelihood term for the reactor-off data, which was only used in the Gd-III fit. Besides the oscillation parameter θ_{13}, other parameters p_k which can modify the prediction N_i^{pred} – such as correlated background rates, Δm_{31}^2 or energy scale parameters – were allowed to vary in the fit. These parameters were constraint by their uncertainty by adding "pulled terms" [197] to the χ^2, which was done in the DC-II and any successive analysis [112]:

$$\chi_{\mathrm{Pulls}}^2 = \sum_{k=1}^{\mathrm{Pulls}} \frac{(p_k - p_k^{\mathrm{cv}})^2}{(\sigma_k^p)^2} \, , \tag{3.19}$$

with their central values p_k^{cv} and uncertainties σ_k^p as input values. This procedure does not increase the degrees of freedom of the fit, as each pull term adds a "data point" to the χ^2 statistics. The pulled parameters preferentially cover those systematic normalization uncertainties which are fully correlated between the energy bins, while shape and remaining normalization uncertainties are absorbed in the covariance matrices. The exact form of the $\chi_{\mathrm{R+S}}^2$ used by the different analyses and the decomposition of uncertainties in covariances and pulled terms can be found in Ref. [6, 8, 12].

In order to obtain the best fit value of θ_{13}, the χ^2 of Eq. (3.18) is then scanned in $\sin^2 2\theta_{13}$, minimizing over the pulled parameters.

Table 3.7: Rate+Shape results of the four DC publications Ref. [5, 6, 12, 68].

	$\sin^2 2\theta_{13}$	$\chi^2_{\min}/\text{NDF}$	null-oscillation excluded at
Gd-I	$0.086 \pm 0.041\,(\text{stat}) \pm 0.030\,(\text{syst})$	23.7/17	94.6 % C.L.
Gd-II	$0.109 \pm 0.030\,(\text{stat}) \pm 0.025\,(\text{syst})$	42.1/35	99.8 % C.L. $(2.9\,\sigma)$
Gd-III	$0.090^{+0.032}_{-0.029}\,(\text{stat+syst})$	52.2/40	99.9 % C.L. $(3.2\,\sigma)$
H-II	$0.097 \pm 0.034\,(\text{stat}) \pm 0.034\,(\text{syst})$	38.9/30	97.4 % C.L. $(2.0\,\sigma)$

In the Gd-II analysis the data set was additionally subdivided in two periods of high and low thermal power, duplicating the number of energy bins. In this way, additional information is retrieved from the changing signal to background ratio in the two phases.

Since additional spectral shape information can be obtained from background dominated regions, the prompt energy window was increased in the Gd-III fit, ranging from 0.5 to 20 MeV. The Gd-III best fit result of $\sin^2 2\theta_{13}$ is computed assuming normal mass hierarchy[9] of the neutrinos using an effective $\Delta m^2_{13} \equiv \Delta m^2_{ee}$ [195] , instead of averaging over the two hierarchies as done for the DC-I and DC-II results [13].

Table 3.7 summarizes the best fit values of the three Gd-channel analyses published in Ref. [5, 6, 12], showing consistent results of $\sin^2 2\theta_{13}$. The best result obtained by the DC experiment is currently represented by the Gd-channel based R+S analysis. A frequentist approach [109] was used to exclude the no-oscillation hypothesis at a certain C.L., given in the last column. The background rate and uncertainties of all three analyses are further constrained by the fits. Moreover, the output parameters agree with the inputs of the pulled terms. After fitting, a background rate of $(1.38 \pm 0.14)\,\text{d}^{-1}$ is found in the DC-III analysis, which is in agreement with the background estimations. The uncertainty on the background rate reduces due to the energy shape information. The energy dependence of the neutrino oscillation is clearly visible in the bottom panel of Fig. 3.16. There, the ratio of the background subtracted data to the unoscillated prediction is shown as a function of the prompt visible energy. The deficit between 0.75–4 MeV is interpreted as observation of electron antineutrino disappearance. The spectrum distortion above 4 MeV does not affect the θ_{13} measurement and is not further discussed in this thesis. Details can be found in Ref. [12].

3.4.4 Rate only fit

In the *Rate-only (RO) fit* the χ^2 statistics consists of the comparison of the total measured and the predicted rate, without talking into account spectral shape information. Other terms, like constraints on pulled parameters χ^2_{Pulls} or reactor off information can be added, as for the case of the Gd-III RO fit:

$$\chi^2_{\text{RO}} = \frac{N^2}{\sum_{i,j} M_{ij}} + \chi^2_{\text{Pulls}} + \chi^2_{\text{off}} , \qquad (3.20)$$

---

[9]The fit is also evaluated assuming inverted hierarchy in Ref. [12], giving a similar result on $\sin^2 2\theta_{13}$.
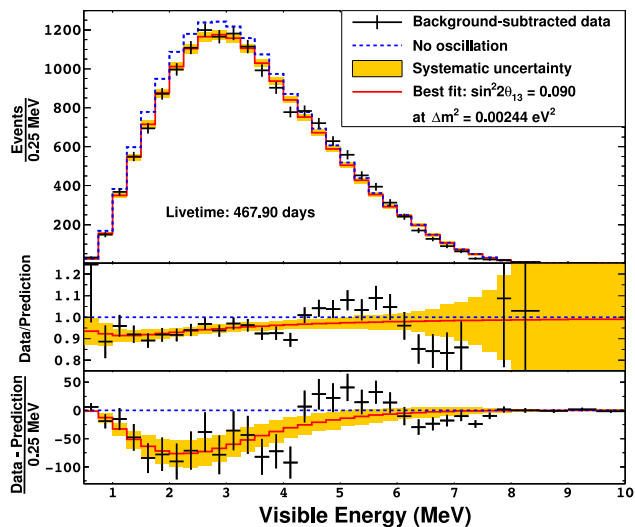
Figure 3.16: Observed IBD candidate spectrum (black points), the backgrounds were subtracted using the R+S fit outputs for normalization (from [68]). The no-oscillation prediction (blue dashed line) and the predicted oscillated spectrum (red line) at the R+S best fit value of θ_{13} are superimposed. Bottom panels: differences between the data and the no-oscillation prediction (data points), and differences between the best-fit prediction and the no-oscillation prediction (red curve). The orange band corresponds to the systematic uncertainties on the best-fit prediction.
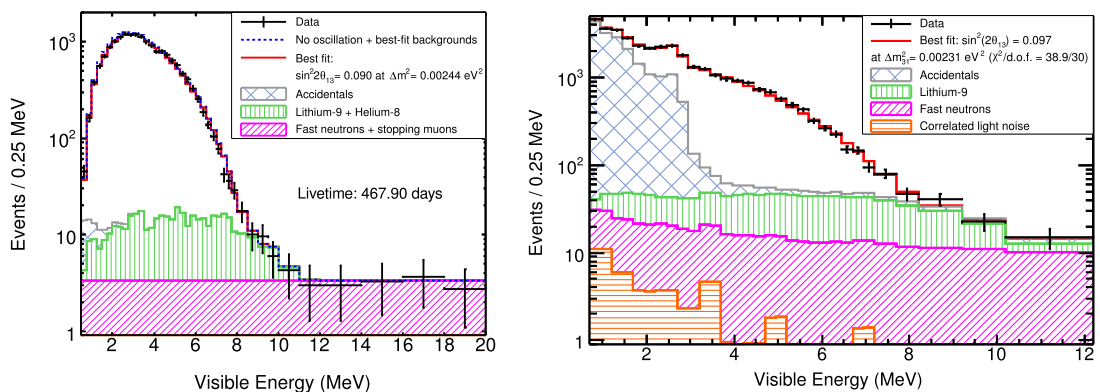
(a) Prompt candidate energy spectrum of the Gd-III dataset (black points) (from [68]). The predicted spectrum in the absence of neutrino oscillations (blue dashed line) as well as the best-fit spectrum at $\sin^2 2\theta_{13} = 0.09$ (red line) were superimposed.

(b) Prompt candidate energy spectrum of the H-II dataset (black points) (from [199]). The best-fit spectrum at $\sin^2 2\theta_{13} = 0.097$ (red line) was superimposed.

Figure 3.17: Prompt candidate energy spectra of the Gd-III (left) and H-II (right) analyses, superimposed with the corresponding best-fit spectrum. Background contributions after the fit are shown as stacked histograms: Fast neutrons and stopping muons (magenta, slant-hatched), cosmogenic isotopes (green, vertical-hatched), accidental background (gray, cross-hatched) and correlated light noise (orange, horizontal-hatched).

57

with $N = \sum_i (N_i - N_i^{\text{pred}})$.

The Gd-III result was evaluated to be $\sin^2 2\theta_{13} = 0.090^{+0.036}_{-0.037}$ (stat+syst) [12]. The RO fit yields a result consistent with the R+S value, yet with larger uncertainty as no shape information is used.

3.4.5 Background model independent fit

The DC experimental configuration features only two reactors, therefore large relative variations in the total thermal power can be observed. Taking advantage of this fact, the *Reactor Rate Modulation (RRM) analysis* [14] separates the data sample with respect to the reactor power conditions into seven data points. These data points are related to three different power states: full power with both reactors turned on (yielding three data points), intermediate power while one reactor is off (giving three data points), or background-only measurement while both reactors are off (adding one data point). The observed daily candidate rate of each data point is then plotted as a function of the expected daily neutrino rate (Fig. 3.18a). The linear dependence between these two quantities can be parametrized by a straight line, since the background contribution in the observation was found to remain stable. Hence, the mixing angle θ_{13} (corresponding to the slope of the line) and the daily background rate (related to the intercept) can be measured at the same time. Moreover, the possibility of a background model independent θ_{13} analysis is given by the RRM fit.

The results presented in the following can be found in Ref. [12]. The χ^2 statistics of the RRM analysis is defined as [12]

$$\chi^2_{\text{RRM}} = \sum_{i=1}^{6} \frac{(R_i^{\text{obs}} - R_i^{\text{exp}}(\theta_{13}) - B)^2}{(\sigma_i^{\text{stat}})^2} + \chi^2_{\text{off}} + \frac{(B - B^{\text{exp}})^2}{\sigma_{\text{BG}}^2} + \chi^2_{\text{Pulls}}. \qquad (3.21)$$

Here, the expected daily rate R_i^{exp} includes the neutrino oscillation parameter θ_{13}. The measured daily candidate rate is represented by R_i^{obs}. The last term in Eq. (3.21) comprises pulled terms on three parameters, which are allowed to correct R_i^{exp} in the fit for systematic effects: the detection efficiency with an uncertainty of 0.6 %, the number of residual neutrinos with $\sigma_{\text{res}} = 0.3\%$ and the reactor power uncertainty of the reactor-on data. The latter depends on the reactor power and therefore ranges from 1.73 % (at full power) to 1.91 %. Additional constraint is added by a pulled term on the background expectation, with input value $B^{\text{exp}} = 1.64^{+0.41}_{-0.17}\,\text{d}^{-1}$ (cf. Table 3.3). The term χ^2_{off} represents the reactor-off data point, which is expressed in terms of Poisson likelihood due to low statistics. The possibility to add this reactor-off point is an aspect unique to the DC experiment.

The Gd-III analysis yields $\sin^2 2\theta_{13} = 0.090^{+0.034}_{-0.035}$ as result of the RRM analysis, in excellent agreement with the R+S and the RO result. The background rate after the fit is given by $B = 1.56^{+0.18}_{-0.16}\,\text{d}^{-1}$, consistent with the background estimation. In addition, the RRM fit is performed treating the background rate B as free parameter by removing the background constraint (the third term in Eq. (3.21)). This background unconstraint fit yields $\sin^2 2\theta_{13} = 0.060 \pm 0.039$ with a background rate of $B = 0.93^{+0.43}_{-0.36}\,\text{d}^{-1}$. A third fit removing both the background constraint and the reactor-off data point is carried out giving $\sin^2 2\theta_{13} = 0.089 \pm 0.052$ and a background rate of $B = (1.56 \pm 0.86)\,\text{d}^{-1}$. These tests demonstrate the significant impact of the
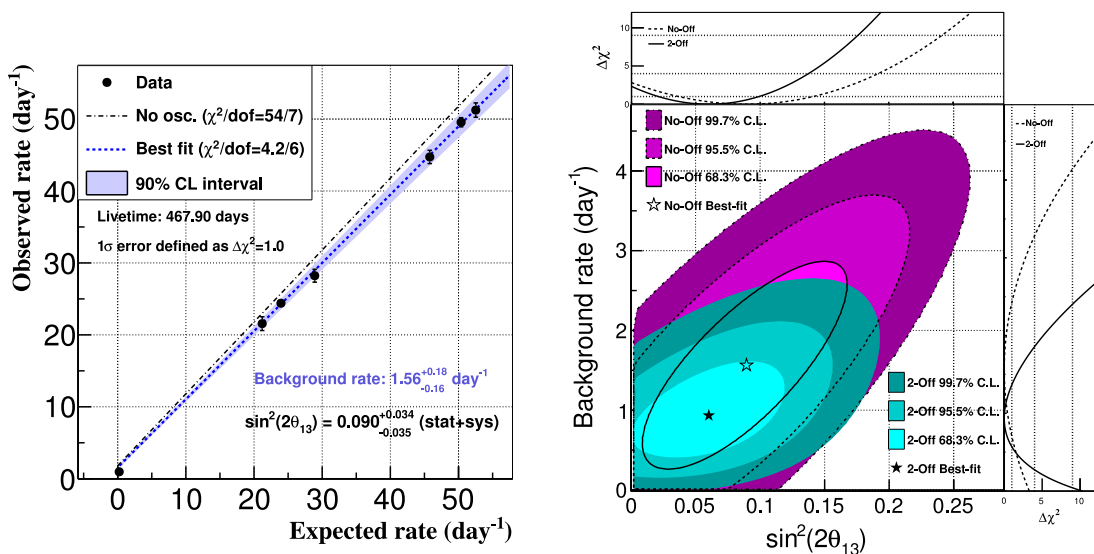
(a) Correlation of the measured daily candidate rate and the expected daily neutrino rate. The blue line corresponds to the best RRM fit. In this analysis the reactor-off point (first data point) and the background estimates were included.

(b) Contours on $(\sin^2 2\theta_{13}, B)$ of the RRM fit with (cyan) and without (magenta) reactor-off data.

Figure 3.18: RRM analysis for three different configurations (from [173]): **a)** with reactor-off point and background rate constraint. **b)** θ_{13} analysis without constraint on the background rate, either with or without reactor-off data.

reactor-off measurement on the θ_{13} precision, besides this, the different results are all in good agreement. In Fig. 3.18b the 68.3, 95.5 and 99.7 % C.L. allowed regions of the parameters $(\sin^2 2\theta_{13}, B)$ obtained from the background unconstraint fits are shown for the two cases, having the reactor-off data point excluded and included.

3.4.6 Conclusion

The current best result of the DC experiment is given by the R+S fit of the Gd-channel analysis with $\sin^2 2\theta_{13} = 0.090^{+0.032}_{-0.029}$ (stat+syst). Analyses of other fit frameworks evaluating the same data set, but using different approaches to extract θ_{13}, yield consistent results. Furthermore, the θ_{13} values of the three Gd-channel based DC publications are in good agreement.

Only running with the far detector (FD), the precision of the DC result is limited by the reactor flux uncertainty. With the near detector (ND) those systematic uncertainties which are correlated between the two detectors will cancel, such as large fractions of the flux and parts of the detection systematic uncertainties. As the background uncertainties are expected to dominate the total error, increased statistics and further improvements on the analysis techniques will reduce the background systematic uncertainties and thus enhance the DC sensitivity.

The projected sensitivity of the Gd-channel analysis with either FD or both FD+ND is shown in Fig. 3.19. The sensitivity curves are given with respect to the Gd-II (black) and Gd-III (blue) analysis, depicting the improvement achieved by the Gd-III analysis.
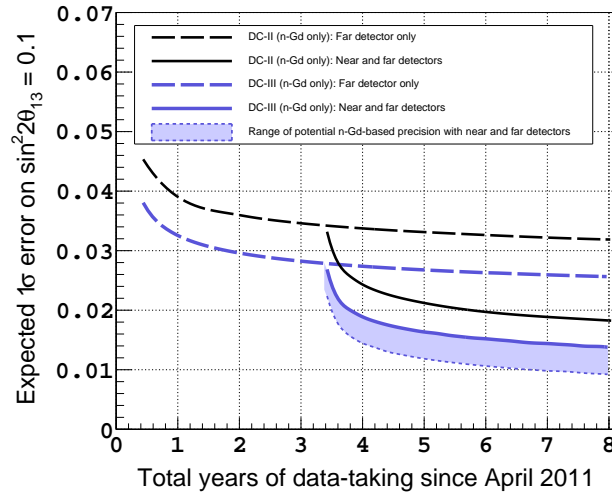
Figure 3.19: The projected sensitivity of Double Chooz for an analysis using the neutron detection channel on Gd (from [69]).

For the FD+ND case a 0.2% uncertainty on the detection efficiency, 0.1% remaining uncorrelated[10] flux uncertainty and background uncertainties scaled from the FD to ND are used as input. Below the blue FD+ND sensitivity curve, the range of possible improvement is illustrated by the shaded area, while the lowest sensitivity would be reached in case the reactor flux was the only systematic uncertainty.

After three years of running with two detectors, $\sigma(\sin^2 2\theta_{13}) = 0.015$ is reached . The sensitivity can be further improved to 0.010, depending on the improvements made on the analysis [12].

---

[10]Here, uncorrelated corresponds to uncorrelated between the FD and ND, due to slight deviations in the flux ratio from the two reactors observed by each detector.

Chapter 4

^{252}Cf calibration source analysis

Since the element's accidental discovery in a nuclear bomb's debris in 1952 [156], ^{252}Cf has become one of the most common portable neutron sources, owing to its 3.816 a lifetime combined with a relatively high probability of spontaneous fission. The sources emit neutrons with comparatively soft energy spectra, produce little heat and are in general of small size. Only 1 g of the isotope can emit 2.3×10^{12} neutrons per second [141].

This chapter will discuss the use of ^{252}Cf deployment data to test the detector stability with respect to the neutron capture fraction on Gadolinium. The second part will deal with the improved understanding of the ^{252}Cf source data by introduction of an accidental background subtraction technique and correlated background studies. The knowledge gained will be used and further discussed in Chapter 5 and Chapter 6, which will present the systematic uncertainty estimation of the IBD neutron detection.

4.1 ^{252}Cf source data

The ^{252}Cf sources are custom-made at the University of Alabama [182]. They are double-sealed in an inner and outer cylindrical capsule, both made of stainless steel (SS304). With an outer radius of only 2 mm, the completed and certified source is of standard size. It can then be placed inside a source rod which has a diameter of 4 mm at its end. The source rod itself is attached to a spool-wire-weight consisting of transparent acrylics, building the interface to the wire of the z-axis calibration system (described in Section 2.1.4).
During Guide-Tube deployment (see also Section 2.1.4) the source is screwed into a connector which is attached with a hook to the guide wire. The hook guarantees the source to flexibly follow the tube's bends during deployment. All source capsule and calibration system elements are considered by the full detector MC simulation.

Three calibration campaigns have been realized so far using these two deployment systems. The first two campaigns are enclosed by the DC-III data sample runs and are consequently used for energy scale calibration. Therefore these source deployment runs are calibrated in energy themselves. The third calibration campaign data is not part of the DC-III data taking period, but will be used in the following with its provisional

(a) Outer source encapsulation.

(b) Guide-Tube deployment hook.
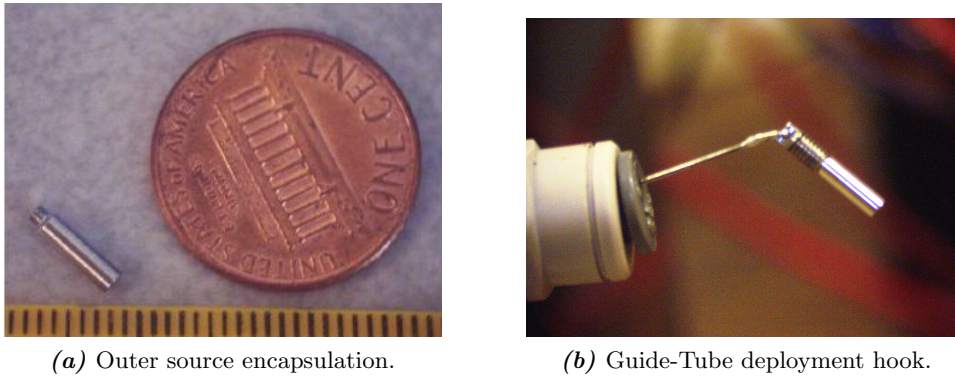
Figure 4.1: Calibration source design (from [63]).
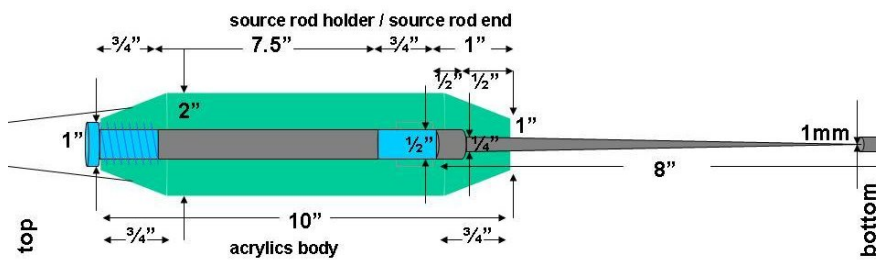
Figure 4.2: Calibration source rod with acrylic weight interface (from [90]).

energy scale for preliminary stability cross-checks. Each of the deployment campaigns was carried out by Double Chooz collaborators of the DC Calibration Expert Group.

The tables of the different ^{252}Cf calibration campaigns with run numbers, deployment position, date and run length can be found in Appendix B.

4.1.1 ^{252}Cf fission products

The actinide element californium (Cf) with atomic number $A = 98$ consists solely of radioactive isotopes. Most of them decay via alpha decay, with ^{251}Cf being the isotope with the longest half-live of 898 years [166]. Some of the Cf isotopes can undergo spontaneous fission accompanied by neutron emission, while ^{252}Cf, the most stable among these with a life-time of $\tau = 3.816\,\mathrm{yr}$ [166], is widely used as portable neutron source. In 97% of the cases it undergoes alpha decay, whereas 3.1% of the time it decays via spontaneous fission [166]. Upon spontaneous fission the fission fragment nuclei can emit the following particles [147, 148]:

- prompt neutrons with a time constant $\tau < 10^{-13}\,\mathrm{s}$

- delayed neutrons within a time of 10^{-1}–$10^{2}\,\mathrm{s}$

- prompt gamma radiation with a time constant τ of 10^{-11}–$10^{-9}\,\mathrm{s}$

- delayed gamma radiation with a time constant τ of 10^{-9}–$10^{-3}\,\mathrm{s}$

- electrons and gammas from β-decay of the fission fragments
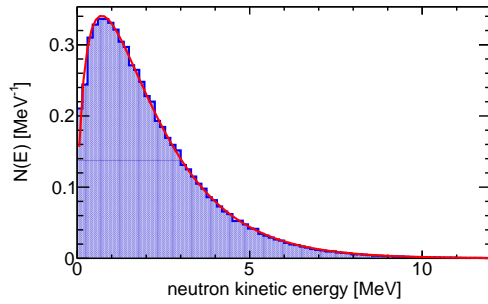
Figure 4.3: Prompt neutron kinetic energy spectrum. Maxwellian distribution of Eq. (4.1) with $T_M = 1.42\,\text{MeV}$ in red, Double Chooz MC simulation spectrum shown by the blue filled histogram.

The prompt neutrons are emitted from the excited fission fragments with a mean number of $\bar{n} = 3.757 \pm 0.005$ neutrons per fission [147]. Their kinetic energy spectrum can be described by either the Watt distribution [207] or the Maxwellian distribution [87]

$$N(E) = \frac{2}{\sqrt{\pi T_M}} \cdot \sqrt{E} \cdot e^{-\frac{E}{T_M}} \, , \tag{4.1}$$

with the effective nuclear temperature parameter $T_M = 1.42 \pm 0.01\,\text{MeV}$ [147]. The mean neutron energy is linked to this parameter via $\bar{E} = \frac{3}{2}T_M$, while the experimental result for the average kinetic energy amounts to $(2.13 \pm 0.01)\,\text{MeV}$ [147]. From the graph of Eq. (4.1) in Fig. 4.3 it is possible to see that the most probable kinetic energy is at $0.7\,\text{MeV}$.

Delayed neutron emission can occur immediately after β-decays of fission fragments into daughter nuclei with an excess of neutrons, constituting $\sim 1\,\%$ of the total neutron yield [147]. Various articles can be found about the prompt gamma characteristics [203, 193, 194, 165], while the experimental values depend on the energy thresholds and measurement ranges of the experiments. For an energy window of $0.14 > E > 10\,\text{MeV}$ and $\Delta t < 10\,\text{ns}$ the mean gamma multiplicity is measured to be $N_\gamma = (7.8 \pm 0.4)$, with a total energy of $\bar{E}_\gamma = (6.84 \pm 0.30)\,\text{MeV}$ and $(0.88 \pm 0.04)\,\text{MeV}$ on average per gamma quantum [203]. A different measurement with an energy threshold of $E > 0.114\,\text{MeV}$ and $\Delta t < 12\,\text{ns}$ obtained $N_\gamma = (9.7 \pm 0.4)$ as mean number of gamma quanta, a total gamma energy of $\bar{E}_\gamma = (7.0 \pm 0.3)\,\text{MeV}$ and a mean single gamma energy of $0.72\,\text{MeV}$ [193]. Most of the gamma radiation will be detected as a single event in the Double Chooz detector with a measurement window width of $256\,\text{ns}$. The delayed gamma radiation has for the time range of $15\text{-}100\,\text{ns}$ a relative intensity of $6\,\%$ [138] compared to the prompt gamma emission and the intensity continues to drop for $t > 100\,\text{ns}$.

Gamma ray and neutron emission can be competitive processes, sharing the excitation energy of the fission fragments according to rules of angular momentum conservation [208]. This also explains why the average total gamma energy exceeds the mean neutron binding energy of about $5\,\text{MeV}$, even though gamma emission occurs with a lower probability and mainly after the neutrons were released [148]. A linear correlation exists between the total gamma ray energy and prompt neutron multiplicity [169], which can be described by

$$\bar{E}_\gamma = (0.75 \cdot \bar{n} + 4)\,\text{MeV} \, . \tag{4.2}$$

An increase in fission fragment excitation energy is consequently linked to an increase in both the gamma energy as well as the number of emitted neutrons. The mean energy of a single photon, however, seems not sensitive to a change in excitation energy [169], while the average neutron kinetic energy does slightly depend on it [55]. It is therefore not possible to conclude that the kinetic energy of individual neutrons is independent of the total gamma energy or neutron multiplicity. Dedicated crosschecks of the neutron capture fraction[1] with respect to prompt energy or neutron multiplicity cuts are performed at the end of this chapter.

In the Double Chooz Monte Carlo simulation a ^{252}Cf fission event generator written by M. Worchester has been utilized [210]. After a neutron multiplicity is picked following Ref. [54], each neutron is provided with a momentum according to Eq. (4.1). The gamma radiation is simulated based on a probability density distribution of the gamma multiplicity with mean value $N_\gamma = 7.8$ measured by Brunson [57] along with the single gamma spectrum from Verbinsky et al. [203]. No correlation condition between the neutron multiplicity and total gamma energy or single gamma energy and gamma multiplicity is implemented. Consequently a larger total gamma energy is observed on average in the MC simulation compared to data [210] (see also Fig. 4.10b), while the impact of this discrepancy on the results presented in this thesis are considered to be negligible.

4.1.2 ^{252}Cf fission event selection

Fission events of the ^{252}Cf source during the first campaign occur with a rate $\sim$ 4.16 Bq [182], which corresponds to $3.76 \times 4.16 \approx 15.6$ neutrons per second in case of 100 % detection efficiency. For the second campaign we expect 12.9 neutrons per second. The actual activity of the source is indeed higher, but the by far more often emitted alpha particles will not succeed in leaving the source capsule material, while the fission gammas and neutrons will pass it almost unhindered. Although gamma emission will not start until the neutrons have evaporated off the fission fragments, the gammas will induce in nearly all cases the first event seen in the detector upon ^{252}Cf fission. This happens not only due to the very short time constant of gamma emission of less than a nanosecond, but also because of the energy dependence of the neutron capture cross sections, especially in the ν-target liquid where the radiative neutron capture cross section of gadolinium does not become significant until the neutron has lost a large fraction of its kinetic energy (further description can be found in Section 7.3). The detection of the gamma energy deposition hence enables to tag with negligible uncertainty the point in time when the fission has occurred. We will therefore refer to the fission gamma event as *prompt event*. Note that the prompt event will not only contain the energy deposited by the fission gammas, but also includes the visible fraction of the neutrons' kinetic energy lost via proton recoil in the first hundreds of nanoseconds after neutron emission. The subsequent neutron captures are detected in coincidence with the prompt gamma event. The neutron capture rate as a function of the prompt-neutron correlation time $\Delta T = T_{\text{delayed}} - T_{\text{prompt}}$ follows for $\Delta T > 10\,\mu$s in the Gd-doped scintillator an exponential law with capture time constant τ_{cap}, just as the inverse beta decay neutrons. Every event succeeding the prompt trigger within a

---

[1]The neutron capture fraction on particular nuclei are known to be neutron energy dependent, for more details see Section 7.3.

certain period of time will be considered as fission neutron or *delayed event.*

Upon radiative neutron capture of the fission neutrons, we will expect to measure a visible energy spectrum ranging from 0 to 20 MeV as illustrated in Fig. 4.4. The dominant structures are the single gamma peak at 2.2 MeV from the neutron capture on hydrogen, the ~ 8 MeV peak plus Compton tail from neutron capture on Gd nuclei and the ~ 16 MeV bump from two neutron captures on Gd seen within one measurement window of 256 ns. Also visible but much less distinct is the simultaneous capture of one neutron on H and another on Gd with a total visible energy of roughly 10 MeV.

Since the visible energies of the prompt fission gammas and the delayed neutron capture gammas are in the same energy range, an event will be identified as such in case there was no other trigger preceding the potential prompt signal. Requesting a time difference of at least 1.5 ms between a prompt fission candidate and the last preceding trigger makes sure that a delayed candidate in the 1 ms measurement window after a prompt is not classified as prompt itself. An additionally set low energy threshold $E_{th,p}$ on the prompt event energy will reduce the probability of measuring accidental coincidences of the background detector radioactivity. Altogether, the ^{252}Cf will be selected as follows:

1. **Selection of valid triggers:**

   - not a random trigger
   - not a muon (a muon trigger is defined as either total charge in IV > 30000 DUQ or total charge in ID > 20 MeV)
   - time difference to last muon > 1 ms
   - visible energy larger than 0.4 MeV
   - not a light noise trigger (see Section 3.3)

2. **Prompt event selection**:

   - time difference to last valid trigger > 1.5 ms
   - visible energy: $E_{th,p} < E_{prompt} < 30$ MeV

3. **Delayed event selection**:

   - time difference to last prompt event (*prompt identification veto*): $0 < \Delta T < 1000 \, \mu$s
   - visible energy: $0.5 < E_{delayed} < 25$ MeV

Further cuts are applied to the prompt and delayed selection, depending on the purpose of the study. Any additional cut will be mentioned in each of the paragraphs separately.

4.2 Neutron detection stability measurements

Two calibration campaigns in both the ν-target (Target) and Gamma Catcher volume have been conducted in the time period covered by the DC-III data set. In order to test the neutron detection stability, the Gd-fraction of ^{252}Cf fission neutrons in the Target cylinder and the H-fraction in the Gamma Catcher volume will be computed.

This particular study was performed before the DC-III energy scale *ESv5* was finalized and uses therefore the DC-II energy scale *ESv2*. Besides this the DC-II valid trigger, muon reduction and light-noise cuts were used to select the ^{252}Cf fission events:

- visible energy larger than 0.5 MeV

- reject events with $F_V < 0$ (unsatisfactory vertex reconstruction)

- not a muon (total charge in IV should be < 10000 DUQ)

- light-noise rejection, while a light-noise event features

  - RMS(T_{start}) > 40 ns
  - prompt: $q_{max}/q_{total} > 0.09$
  - delayed: $q_{max}/q_{total} > 0.06$

- prompt visible energy: $4 < E_{prompt} < 30$ MeV

- delayed visible energy: $0.7 < E_{delayed} < 25$ MeV

All other cuts are consistent with those of Section 4.1.2, no background subtraction is applied.

4.2.1 ν-target Gd-fraction stability

The Gd-fraction f_{Gd} describes which fraction of neutron captures occurred on gadolinium nuclei, while the rest of the captures in the Target volume happen mostly on hydrogen and carbon. Depending mainly on the relative Gd to H abundance, it offers information about the Gd concentration in the liquid. For a homogeneously admixed liquid the Gd-fraction is constant all-over the full volume. In reality, however, it is difficult to measure and verify this statement since f_{Gd} is estimated by measuring the number of delayed events in the Gd peak area, defined by an energy interval (see Eq. 4.3). Due to energy leakage if an event occurs close to the acrylic wall, a decrease of about 2 % in the Gd-fraction estimate is expected from analysis of MC simulation data. Apart from that, when the ^{252}Cf source approaches the Target wall, an increasing number of neutrons will undergo radiative neutron capture outside the Target volume, mainly on hydrogen (cf. "spill-out" events, Chapter 7). These events will enhance the relative amount of energy depositions in the hydrogen window compared to neutron captures on Gd and therefore lead to a significant reduction of the Gd-fraction.

The Gd-fraction will be computed via the DC-II definition, which is slightly different compared to the one used in the DC-III efficiency systematics analysis (cf. Eq. (4.15) in Section 4.3.2 and Chapter 5.3):

$$f_{Gd}^{DC\text{-}II} = \frac{N(4 < E_d < 11\,\text{MeV})}{N(0.7 < E_d < 11\,\text{MeV})}\,. \tag{4.3}$$

A Gd-capture energy window ranging from 4 to 11 MeV is used in order to also include the events in the Gd Compton tail, as the capture peak to Compton tail ratio changes with deployment position due to larger energy losses when the source is moved towards the Target acrylic wall as shown in Fig. 4.4. This definition will also include neutron
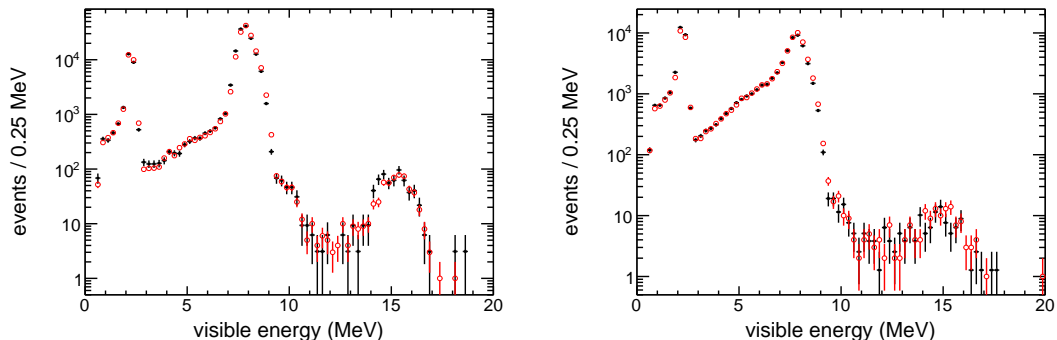
(a) Calibration source deployed at Target center $(x,y,z) = (0,0,12)$ mm.

(b) Calibration source deployed at Target bottom $(x,y,z) = (0,0,-1238)$ mm.

Figure 4.4: Visible energy spectra of the delayed ^{252}Cf fission events. The black bullets show the first campaign data, the red empty circles correspond to the second campaign.

captures on ^{12}C, as these emit one or two gammas with in total $5\,\text{MeV}$ energy, but they will contribute only with a negligible amount of $< 0.1\,\%$.

The Gd-fraction uncertainty is calculated as

$$\Delta f_{\text{Gd}} = \sqrt{\frac{f_{\text{Gd}} \cdot (1 - f_{\text{Gd}})}{N(0.7 < E_{\text{d}} < 11\,\text{MeV})}} \,, \tag{4.4}$$

following binomial statistics (for more details see Chapter 5.2).

Other variables used in the following sections are the deployment position z_{calib} along the Target symmetry axis, the discrepancy in the mean reconstructed z and ρ position and the distance to the Target wall d. In case the reconstructed vertex locations are studied, the prompt vertex will be used, since the prompt event is not affected by the neutron capture displacement from the source and consists in general of multiple gammas, unlike the delayed neutron capture on hydrogen. To suppress background contamination contribution, the mean vertex position is calculated after limiting the range according to the distribution's standard deviation σ to $[\text{mean} - 4\sigma; \text{mean} + 4\sigma]$. A fit of a normal distribution to the data via minimization of a χ^2 statistics has also been tested, yielding the same results. The mean reconstructed ρ position is computed using the mean reconstructed x and y positions via $\bar{\rho}^2 = \bar{x}^2 + \bar{y}^2$. The detector geometry including the slope in top and bottom lid is considered when the distance d is calculated, which corresponds to the perpendicular distance to the nearest Target wall. The Target chimney is not taken into account.

The calibration runs used for this analysis are listed in Appendix C, while only runs inside the Target volume with $z_{\text{calib}} < 1.2\,\text{m}$ have been used, excluding the deployment runs in the chimney. Runs which have not been available for this analysis are 25083, 25076 and 45701. The data of runs taken at the same position are merged if not stated differently. For the direct comparison of the two campaigns, only runs with the same z_{calib} source location are considered.
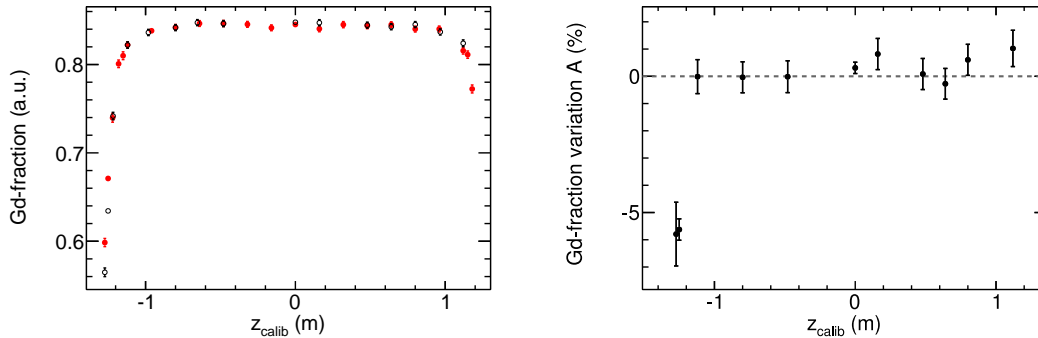
(a) Gd-fraction: the black empty circles show the first calibration campaign data, the red filled boxes correspond to the second campaign data.

(b) Gd-fraction variation A as a function of the deployed z position.

Figure 4.5: Gd-fraction and Gd-fraction variation as a function of the deployed z position. The Gd-fraction variation A describes the relative discrepancy between the Gd-fractions of the first and second calibration campaign.

Results

Concerning the energy scale stability a good performance is given, even though the energy stability calibration was not yet extended to the time period of the second calibration. The Gd-capture energy peak discrepancy between the first and the second campaign, analyzed at the different z deployment positions, was shown to be less than 1 % [184]. The energy reconstruction uncertainty should have little impact on Δf_{Gd}, since the energy window thresholds for the Gd-fraction computation are placed at energy regions of low counting rate.

In Fig. 4.5a the Gd-fraction of both campaigns are given with respect to the theoretical calibration position z_{calib}. In the Target center region from $z = -1$ to $+1$ m, the values for f_{Gd} are stable and vary within 1 %. Close to the Target borders, the graph exhibits the expected decrease in the Gd-fraction. The shape of the Gd-fraction behavior appears to be symmetric around $z = 0$, which supports the assumption that no spatial inhomogeneity in the Gd-concentration is present.

The local variations are studied using the asymmetry in Gd-fraction defined by

$$A = 2 \cdot \frac{f_{\mathrm{Gd}}^{\mathrm{1st}} - f_{\mathrm{Gd}}^{\mathrm{2nd}}}{f_{\mathrm{Gd}}^{\mathrm{1st}} + f_{\mathrm{Gd}}^{\mathrm{2nd}}}, \tag{4.5}$$

with the Gd-fraction values of the first campaign $f_{\mathrm{Gd}}^{\mathrm{1st}}$ and the second campaign $f_{\mathrm{Gd}}^{\mathrm{2nd}}$. The results for A are plotted in Fig. 4.5b as a function of the deployed z position, with a mean value of $\bar{A}(|z| < 1\,\mathrm{m}) = (0.21 \pm 0.15)\,\%$.

For z values below $-1.2\,\mathrm{m}$ a local deviation of more than 5 % is observed. Assuming that the detector properties – such as the Target vessel position relative to the glovebox or scintillator optics – did not change between the two calibration campaigns, a systematic shift in the deployment positions could cause this discrepancy. It was found that a shift of the second campaign data upwards in z by 7 mm brings both campaigns' data in good agreement as illustrated by the upper plots of Fig. 4.6. A relative crosscheck of the reconstructed positions of the first and second campaign revealed that a systematic

(a) Data points not shifted.

(b) Data points of the second calibration campaign shifted by 7 mm upwards.

(c) Discrepancy in reconstructed z position. Dashed line represents the arithmetic mean.

(d) Discrepancy in reconstructed ρ position. Dashed line represents the arithmetic mean.
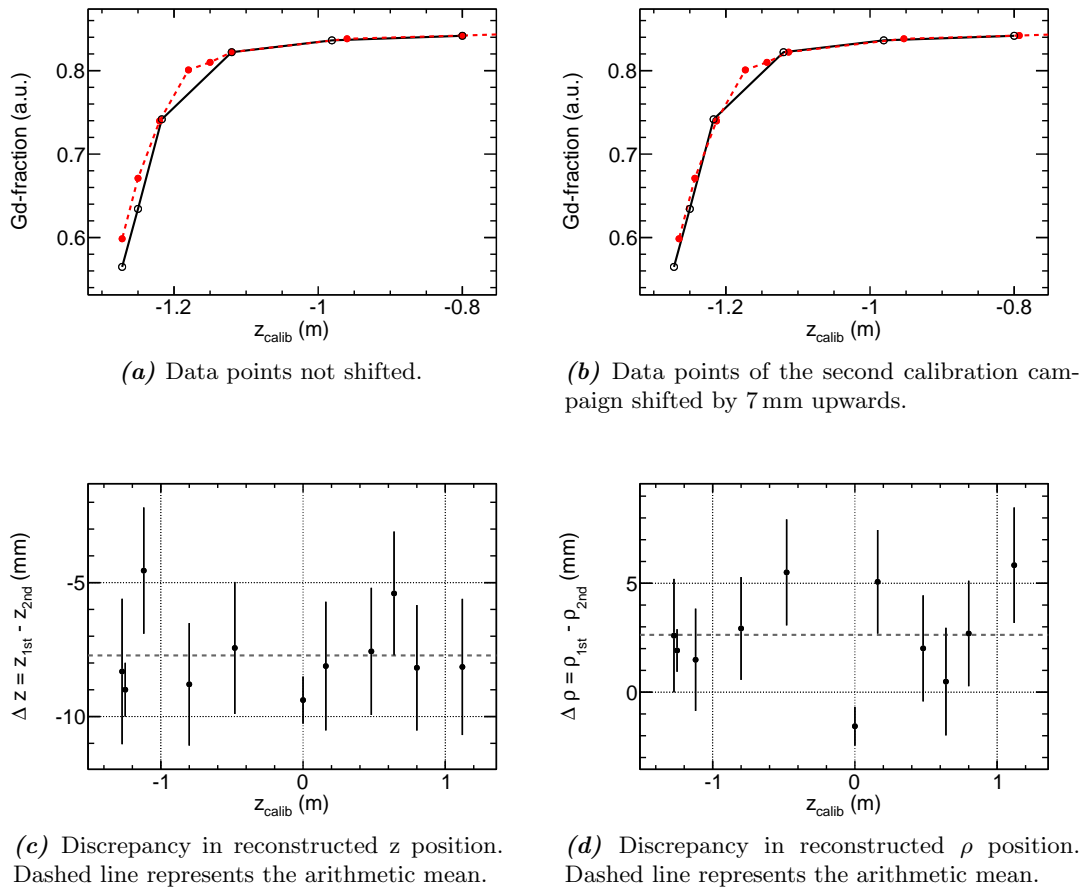
Figure 4.6: **Top**: Gd-fraction as a function of the deployed z position. The black empty circles show the first calibration campaign data, the red filled boxes correspond to the second campaign data. **Bottom**: Discrepancy of the reconstructed position of the prompt fission events between first and second campaign.

shift in all reconstructed z positions is present. The discrepancy in z between the two campaigns is computed at each deployment position via $\Delta z = \bar{z}_{1st} - \bar{z}_{2nd}$ (Fig. 4.6c), while the mean discrepancy amounts to $\langle \Delta z \rangle = (-7.7 \pm 0.5)$ mm. This is consistent with the statement that the second calibration campaign data might have been taken at deployment positions higher than the theoretical ones. The mean discrepancy of the reconstructed ρ positions (Fig. 4.6d) was $\Delta \rho = (2.6 \pm 0.7)$ mm. The systematic shift between the deployment locations of both campaigns is of significant size, as the relative precision of the deployment location along the z-axis is quoted to be 1 mm [6]. An explanation would be a misadjustment of the calibration device during source deployment at the very bottom of the Target or that the lowest point in the Target was missed due to the conical shape of the bottom lid. The deployment position at the bottom is used as reference point during calibration and a systematic offset would be transferred to any other calibration position as well.

It is hence possible to exclude an accumulation over time of the Gd carrying molecules at the Target bottom as possible origin of a Gd-fraction asymmetry between first and second calibration campaign data.

Table 4.1: ^{252}Cf calibration campaign runs at the Target center and Target bottom with deployment position $(x,y,z) = (0,0,z_{\text{calib}})$.

(a) $z_{\text{calib}} = 0\,\text{mm}$

data point	campaign	date [yy-mm-dd]	length [s]	run number
1	1$^{\text{st}}$	2011-08-18	3600	23981
2	1$^{\text{st}}$	2011-08-23	900	24408
3	2$^{\text{nd}}$	2012-05-15	3600	43075
4	2$^{\text{nd}}$	2012-05-22	3600	44236
5	2$^{\text{nd}}$	2012-05-28	3600	44656
6	2$^{\text{nd}}$	2012-06-06	3600	45042
7	2$^{\text{nd}}$	2012-06-15	3600	45700

(b) $z_{\text{calib}} = -1238\,\text{mm}$

data point	campaign	date [yy-mm-dd]	length [s]	run number
1	1$^{\text{st}}$	2011-08-18	3600	23986
2	1$^{\text{st}}$	2011-08-23	900	24411
3	1$^{\text{st}}$	2011-09-02	900	25082
4	2$^{\text{nd}}$	2012-05-15	1200	43706
5	2$^{\text{nd}}$	2012-05-28	3600	44657
6	2$^{\text{nd}}$	2012-06-06	3600	45044

In addition, the Gd-fraction stability was tested at two particular deployment positions, at which more than one run was taken during both calibration campaigns. A period of several days separates most of the runs within the same campaign, as summarized by Table 4.1. The run-wise values for f_{Gd} as a function of either the run number or the distance of reconstructed position to Target wall d are plotted for $z_{\text{calib}} = 0\,\text{mm}$ in Fig. 4.7a and b. In Fig. 4.7c and d the graphs for $z_{\text{calib}} = -1238\,\text{mm}$ are given. From the deployment at the center of the detector, we can see that the Gd-fraction is very stable, not only within a single campaign but also after almost a year in time. The slight variation of about 0.5 cm in the source location relative to the Target side walls has no effect on the results. In the lower part of the Target, roughly 4 cm above the bottom, the single Gd-fraction values vary within 6 %. From the strong correlation between the Gd-fraction decrease and the source distance close to the acrylic wall, we can see once again how sensitive this observable becomes once the Target borders are reached: a difference in d of 0.5 cm changes f_{Gd} by about 3 %.

The results presented suggest that the Gd-fraction is stable throughout the Target volume with respect to time, although differences between the two calibrations have been found at the borders. Clearly a strong correlation between source position and Gd-fraction value has been proven for the source deployments at the boundary. Together with an offset in the actual deployment positions the discrepancies between first and second campaign can be explained.
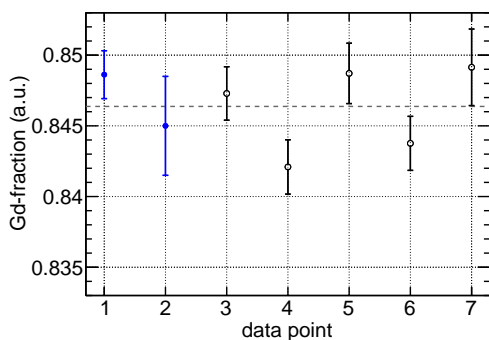
(a) Gd-fraction vs. deployment run at Target center $(x,y,z) = (0,0,12)$ mm. Dashed line shows the arithmetic mean.
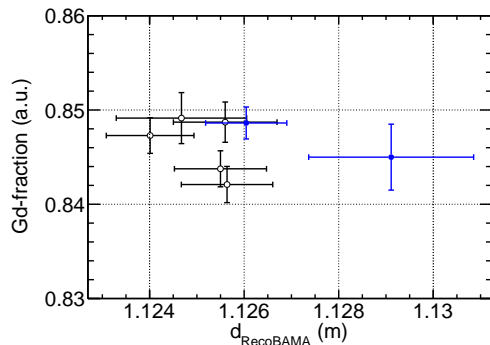
(b) Gd-fraction vs. prompt reconstructed distance to Target acrylic wall at Target center $(x,y,z) = (0,0,12)$ mm.
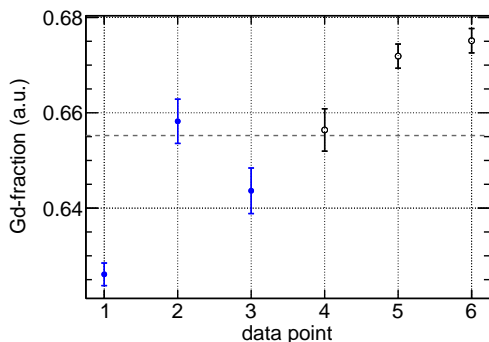
(c) Gd-fraction vs. deployment run at Target bottom $(x,y,z) = (0,0,-1238)$ mm. Dashed line shows the arithmetic mean.
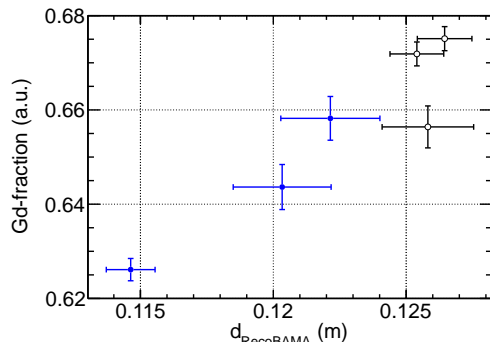
(d) Gd-fraction vs. prompt reconstructed distance to Target acrylic wall at Target bottom $(x,y,z) = (0,0,-1238)$ mm.

Figure 4.7: Gd-fraction stability with respect to run and reconstructed position. The blue filled bullets represent the first campaign, the black empty circles show the second campaign.

4.2.2 Gamma-catcher H-fraction stability

Since the Gamma Catcher (GC) is not Gd-doped, most of the neutrons are caught on hydrogen nuclei and a remaining small fraction on carbon. Therefore the H-fraction is studied inside the GC volume, using the DC-II definition

$$f_{\mathrm{H}}^{\mathrm{DC\text{-}II}} = \frac{N(0.7 < E_{\mathrm{d}} < 3\,\mathrm{MeV})}{N(0.7 < E_{\mathrm{d}} < 11\,\mathrm{MeV})}\,, \tag{4.6}$$

and the binomial uncertainty as in Eq. 4.4. For very large H-fraction values, close to $100\,\%$, the uncertainty could be slightly underestimated (see Section 5.2.4). This, however, will not constitute a problem for the stability checks performed in this section.

Calibration runs with the same deployment position and campaign are merged. The run lists are given in Appendix C. As the first and second campaign deployment locations $(x,y,z)_{\mathrm{calib}}$ are not exactly the same, nearby source positions are used to compare both calibrations. The data selection cuts are the same as for the Target $^{252}\mathrm{Cf}$ analysis given above.
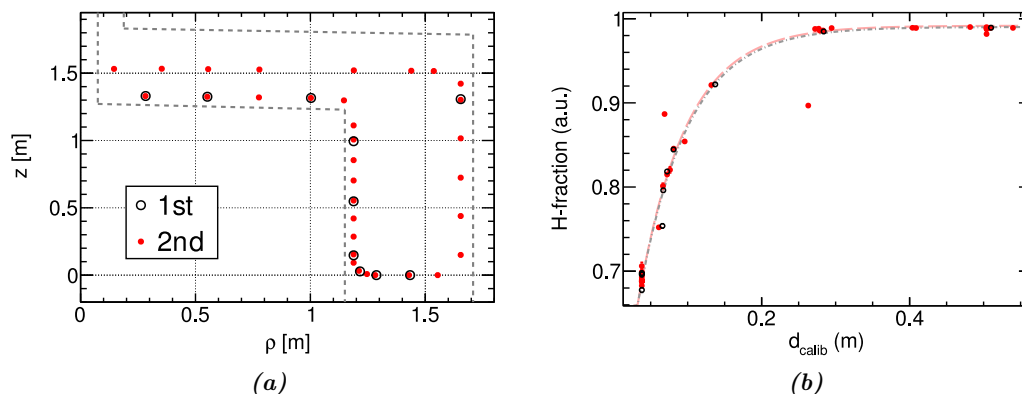
Figure 4.8: First and second campaign Guide-Tube ^{252}Cf source calibration. The first calibration positions are marked by the black circles, the second campaign source locations are given by the red data points. **a)** Deployment positions in the (z, ρ) plane. The inner (outer) gray dashed line represents the Target (Gamma Catcher) wall. **b)** H-fraction as a function of the deployed distance to Target acrylic wall d_{calib}. A function $f(d) = p_1 \cdot exp(-p_2 \cdot d) + p_3$ with three parameters p_i ($i = 1, 2, 3$) was fitted to the first calibration campaign data points (dash-dotted gray line) and the second campaign's data points (light red dashed line).

Results

The Guide-Tube deployment locations are shown in Fig. 4.8a. Determining a meaningful parametrization of the GC geometry is apparently harder than for the cylindrical Target volume. But also here the distance to wall variable d is a reasonable choice in terms of neutron physics dominated observables. As the neutron mean free path is of $\mathcal{O}(10\,\text{mm})$, the measurement should not depend on the difference in GC top or side geometry or the curvature of the acrylic vessels' mantle. In Fig. 4.8b the H-fraction is plotted vs. the deployed distance to Target acrylic wall d_{calib}. Except for two data points of the second campaign, the values follow the same trend. The larger the variable d, the farther is the source from the Target wall and thus the H-fraction higher, up to almost 99 %, while the remaining 1 % of neutron captures mainly occur on carbon. The two outliers are for $d = 26.3\,\text{cm}$ the measurement close to the Target chimney (which contains Gd-loaded liquid) and for $d = 6.9\,\text{cm}$ the data point next to the Target edge at $(z, \rho) \approx (1.3, 1.15)\,\text{m}$. For these locations the H-fractions deviate from the expected curve since the relative volume of GC liquid to Target scintillator is compared to the other data points at similar d much smaller or larger, respectively.

For the data points close to the Target side wall ($d < 5\,\text{cm}$), no correlation to the height z is found. The values of f_H vary within 2 %, but are in agreement within uncertainties. The direct comparison of the first and second campaign are shown in Fig. 4.9a, where the H-fraction variation is plotted computed via equation (4.5). The variation demonstrates the good agreement with an arithmetic mean of (-0.055 ± 0.129) % and a standard deviation of 0.41 %. For $d > 20\,\text{cm}$ the H-fraction asymptotically approaches the value of the pure Gamma Catcher liquid of about 99 %, as the neutron travel distance is that short that only few neutrons will reach the Target volume to be caught on Gd instead of H. The mean values of the H-fraction for $d > 20\,\text{cm}$ are computed to be (98.71 ± 0.22) for the first and (98.79 ± 0.06) for the second campaign (see Fig. 4.9b). No H-fraction deviation exceeding the statistical uncertainties has been observed.

(a) H-fraction variation as a function of the deployed d position.

(b) H-fraction for $d_{\mathrm{calib}} > 0.25\,\mathrm{m}$ as a function of the deployed d position.
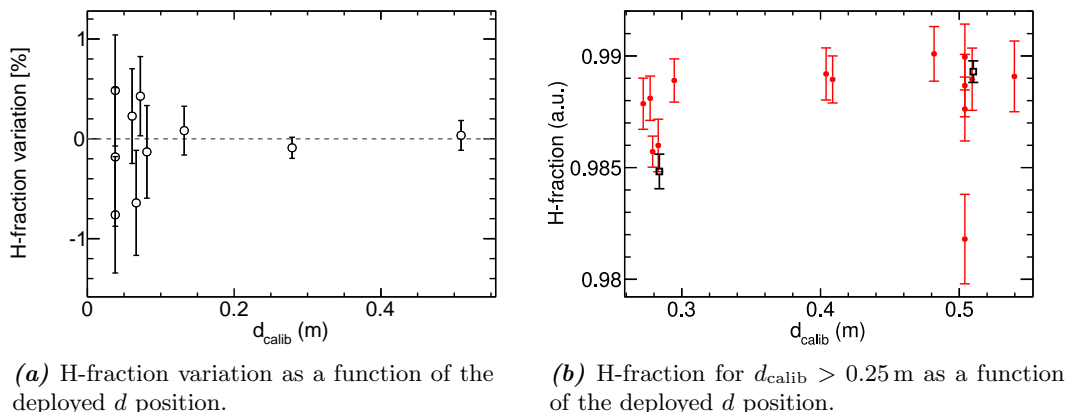
Figure 4.9: H-fraction and H-fraction variation as a function of the deployed distance to Target acrylic wall d_{calib}. The H-fraction variation describes the relative discrepancy between the H-fractions of the first and second calibration campaign.

4.3 Background reduced fission neutron data

When we compare the spectra of the selected ^{252}Cf delayed events in deployment data to the selection obtained from MC simulation runs (see Fig. 4.10), we will notice discrepancies in several regions of the visible energy spectra, for large correlation times and large correlation distances. Once the prompt energy threshold $E_{\mathrm{th,p}}$ is lowered, the discrepancies between data and MC rise in all observables. For the delayed energy spectra especially at low energies $< 2\,\mathrm{MeV}$ and at around 12–15 MeV difference become evident. The overall discrepancy in hydrogen to gadolinium capture peak height will be discussed in Chapter 5 Section 5.4.

No question about it, any other energy deposition than the ones originating from the desired fission products can contribute as background, either in random coincidence with another background event or with the fission events. Furthermore, any correlated background signal matching the ^{252}Cf signature will be selected, too. In order to obtain as clean as possible source spectra to reduce any background bias when comparing data to Monte Carlo, the different backgrounds and their reduction are studied in the following, separated in accidental and correlated contributions.

4.3.1 Accidental background subtraction

There are many different possibilities to accidentally measure false coincidences. They are formed in case either an event not representing a fission prompt is misidentified as such or when any uncorrelated event is selected as delayed. Not every kind of accidental event represents necessarily a background event. An uncorrelated neutron capture is for example not a background if one is interested in the capture gamma energy. However, it contributes to the uncorrelated part in the prompt to delayed coincidence time spectrum, while it is not a background event with respect to the prompt-delayed correlation distance if the neutron is originating from the ^{252}Cf source. The main different accidental background combinations are:

73

(a) Delayed visible energy.

(b) Prompt visible energy.

(c) Prompt-delayed correlation time.

(d) Prompt-delayed correlation distance.

Figure 4.10: Merged data and simulation spectra of the six ^{252}Cf second calibration campaign deployment runs at the Target center $(x,y,z) = (0,0,12)$ mm. Prompt energy cut $E_{\mathrm{prompt}} > 0.5$ MeV and a maximal selected prompt-delayed correlation time of 1 ms. The red line shows the MC simulation spectra, the black points are from data. The discrepancy in the prompt visible energy is caused by an imperfect gamma spectrum modeling in the MC, but is expected to have no effect on the neutron analyses.

Single event + fission events: A single event is by mistake considered as prompt fission event. In case it is followed by a ^{252}Cf fission, all the fission sub-events passing the energy, timing and spacial cuts, will be taken as delayed. Therefore also the prompt sub-event energy spectrum can be recognized in the delayed energy spectral shape. A higher threshold $E_{\mathrm{th,p}}$ reduces this contribution, since most of the single event energies are below 3.5 MeV.

Fission events + single event: In this case the single event is wrongly detected as delayed sub-event and will mainly contribute to the low energy discrepancy at $E_{\mathrm{delayed}} < 2$ MeV.

Single + single: Two single events form a false coincidence. Due to a radioactivity rate of $8.2\,\mathrm{s}^{-1}$ – almost twice as large as the fission rate of the ^{252}Cf source – in the energy range from 0.7 to 12.2 MeV [6], this is the largest contribution to the accidental backgrounds of the ^{252}Cf selection. This contribution is also suppressed by an increased threshold $E_{\mathrm{th,p}}$.

Fission + fission: If two fission events due to their rate of about $\sim 4\,\mathrm{Bq}$ occur too close in time, it can happen that all of the second fission's sub-events are treated as delayed coincidences. Again, the prompt fission energy shape will appear in the delayed spectrum.

To be more precise: actually any type of event which is not related to the source's fissions can realize an uncorrelated false coincidence, while single gammas constitute the largest contribution.

All these types of background can be measured by a *off-time window* measurement. This technique is also used in other parts of the Double Chooz analysis, e.g. by the accidental background measurement of the neutrino candidates or in the context of the cosmogenic spallation neutron selection for energy scale calibration.

The underlying principle of this method is quite simple: an additional delayed event search is performed following every prompt event with such a large offset in time, that no correlated event is expected anymore. The correlation time of the off-time events is measured with respect to the prompt time plus time-offset Δt_{vp} (vp for "virtual prompt"). At the same time this off-time measurement has to be performed under similar conditions as the actual "on-time" measurement, i.e. by application of the same vetoes and cuts. To increase the statistics of the background measurement, more than one off-time window related to the same prompt event can be used by carrying out additional delayed event searches with respect to $t_n = (t_{\mathrm{prompt}} + n \cdot \Delta t_{\mathrm{vp}})$, as illustrated by Fig. 4.11.
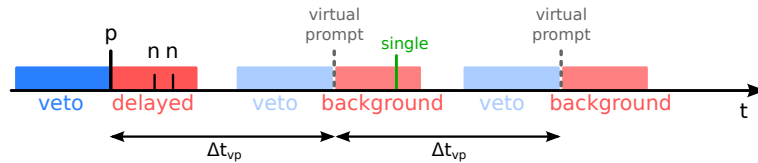
Figure 4.11: Concept of the off-time window method: The accidental background events are measured after an offset in time Δt_{vp} (vp for "virtual prompt"). The blue boxes represent the prompt identification vetoes, the red boxes the delayed event measurement ranges.

The different plots of Fig. 4.12 show the on- and off-time delayed event spectra for the ^{252}Cf source and simulation data. For the delayed energy spectra of the ^{252}Cf data in Fig. 4.12a, we can see that the background consists of 3 components, as explained above: singles for roughly $E < 5\,\mathrm{MeV}$, a broad distribution coming from the fission prompt gammas and the neutron captures of an uncorrelated fission event, clearly cognizable by the neutron capture peaks at $2.2\,\mathrm{MeV}$ and around $8\,\mathrm{MeV}$. This also explains the off-time correlation distance ΔR spectrum in Fig. 4.12g; the events at larger distances $\Delta R > 1\,\mathrm{m}$ are mainly caused by single events, whereas the short distance events with $\Delta R < 1\,\mathrm{m}$ are source-related false coincidences. The accidental backgrounds follow a flat distribution in the correlation time ΔT (see Fig. 4.12e and 4.12f), while the drop-off at short ΔT is caused by the fact that especially uncorrelated fission events can due to the prompt identification veto (cf. Section 4.1.2) only occur after a prompt. We can see that the simulation data as well contains source related background events which are uncorrelated in time, just like the deployment data, except for singles.
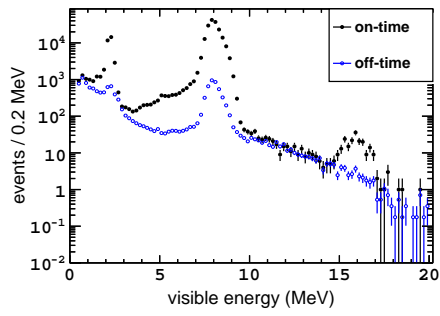
(a) Data delayed visible energy.
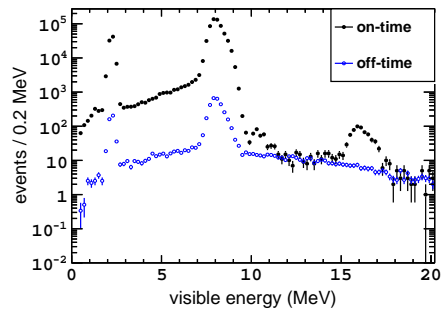
(b) MC delayed visible energy.
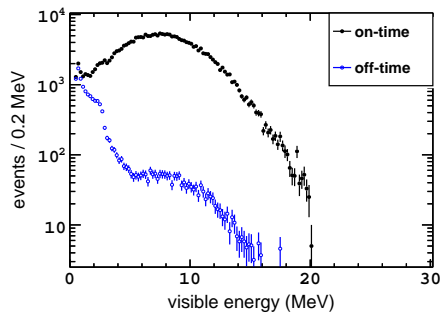
(c) Data prompt visible energy.
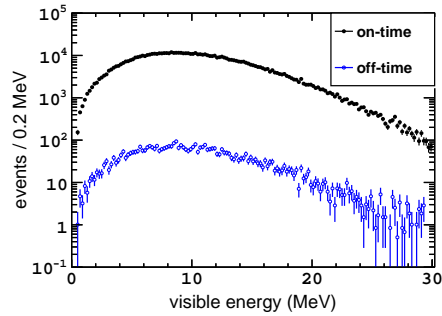
(d) MC prompt visible energy.
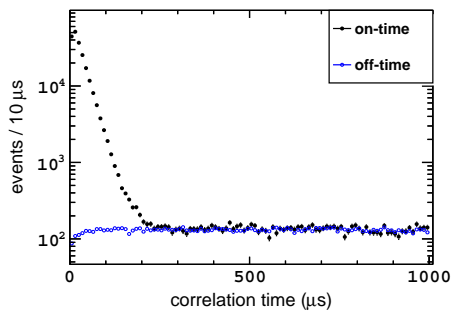
(e) Data prompt-delayed correlation time.
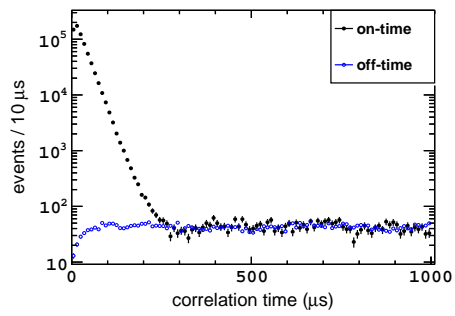
(f) MC prompt-delayed correlation time.
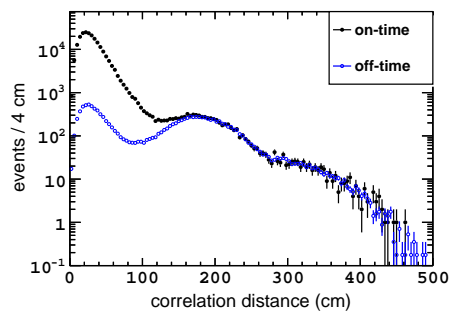
(g) Data prompt-delayed correlation distance.
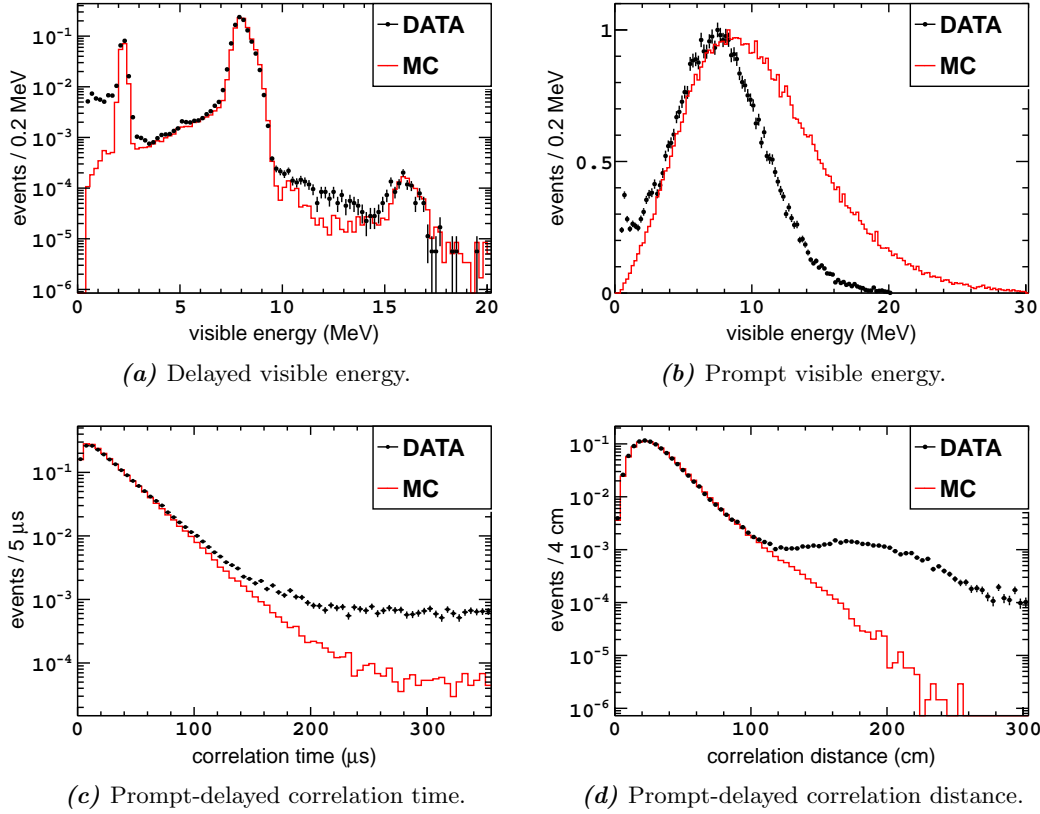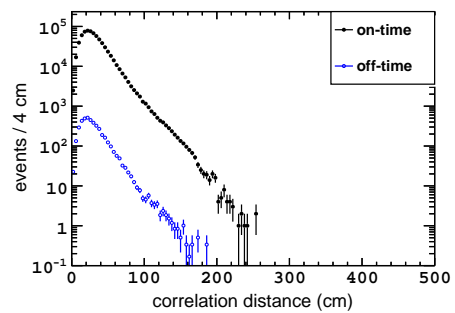
(h) MC prompt-delayed correlation distance.

Figure 4.12: Merged data and MC simulation spectra of the six ^{252}Cf second calibration campaign deployment runs at the Target center $(x,y,z) = (0,0,12)$ mm. Prompt energy cut $E_{\text{prompt}} > 0.5$ MeV and a maximal selected prompt-delayed correlation time of 1 ms. The black points show the on-time delayed events, the blue points the off-time (accidental background) delayed events.

4.3.2 Correlated background: neutron multiplicity separation

After the accidental background was subtracted, the ^{252}Cf data and MC delayed energy spectra still show discrepancies at energies below 2 MeV and for the region of 3–4 MeV, as shown in Fig. 4.13. There is the possibility to detect along with the signal a correlated form of background, which cannot be removed by the off-time window accidental subtraction. All processes not implemented in the MC simulation (such as delayed ^{252}Cf radiation) could introduce a data to MC discrepancy, while any other energy deposition than a fission neutron capture could compromise the detection efficiency measurements in general. Different processes can lead to a correlated background event, they could originate from the source itself or from detector material, cosmic rays can interact with atoms in the detector or surrounding rock and create events with correlated signature. We will now discuss each of these options one after another and show that most of them are negligible.

Any contamination of the source material or on the source capsule surface which produces a coincidence signal will be part of the correlated background. As it is not possible to identify these events, it will be hard to separate them from the signal in case of a high rate or high delayed event multiplicity. Known by-products of the ^{252}Cf source are the isotopes ^{249}Cf, ^{250}Cf, ^{246}Cm and ^{248}Cm [64]. All of them would create correlated events via fission, with either very low fission fractions is or extremely long half lives (e.g. 3.48×10^5 a for ^{248}Cm). In case a neutron multiplicity measurement is not pursued, fissions of other isotopes than ^{252}Cf will not constitute a background but rather another contribution to the neutron signal. The influence of these isotopes can therefore be neglected. A subsequent radioactive decay of a fission fragment, however, cannot be ruled out.

Another possible source-related form of background triggers could be created when a fission neutron, while being slowed down, transfers a large amount of its kinetic energy to a proton. For energy transfers larger than roughly 1 MeV the proton recoil could induce a trigger, as the proton quenching factor is around 2-3 in the Target scintillator liquid [216]. As the timescale in which a neutron loses energies of $\Delta E > 1$ MeV is too close to the prompt event to create an own trigger, proton recoils will not create background events.
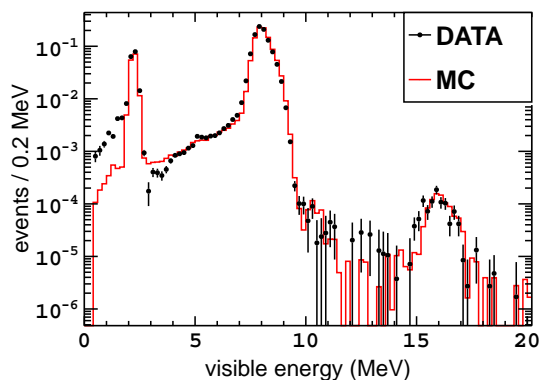
Figure 4.13: Merged data and MC simulation delayed energy spectra of the six ^{252}Cf second calibration campaign deployment runs at the Target center $(x,y,z) = (0,0,12)$ mm. The plot shows the same data set as Fig. 4.10. In addition, the accidental background was subtracted as described in Section 4.3.1.

Also, the possibility of detecting correlated gamma-gamma coincidences of the ^{252}Cf fission exists, since the delayed gamma emission occurs with a time constant of up to 10^{-3} s after the prompt. Likewise could a delayed neutron induce background triggers due to proton recoil at visible energies, in case the neutron is released > 128 ns after the prompt event[2]. However, the probability for these two events to happen is presumably small.

One more class of events which would distort the prompt energy spectrum, the short ΔT part of the correlation time spectrum as well as the tail of the correlation distance distribution are cases, in which the prompt event is not detected. This kind of events are expected to be rare, as the mean of the total gamma energy amounts to more than 6 MeV. On average ~ 7 prompt gammas are released, and the case of no gamma is with about 0.09 % very low if we would assume the multiplicity to follow Poissonian statistics. Only one gamma will be observed in roughly 0.5 % of the fissions according to Ref. [57], while the probability to miss it is, regarding the mean energy of individual photons being around 1 MeV, surely lower. In case of a missed prompt event, the first neutron will be misidentified as such. This would mainly be seen as ~ 8 MeV peak in the prompt spectrum, which is not observed. In the GC, however, fission events with missed prompt energy depositions are detected, as the detection efficiency in the GC decreases. Since most of the neutrons are caught on hydrogen with an energy of 2.2 MeV and less, this contribution is removed by the prompt energy cut[3] of 4 MeV. There is no need to consider missed fission neutron events, as long as one is not interested in a quantitative measurement of the neutron multiplicity.

Correlated background events can as well originate from natural radioactivity or cosmic ray spallation with sufficiently high rate in the detector. In order to study this detector-related contribution, 100 hours of neutrino data runs were analyzed (taken on days close to the first ^{252}Cf calibration campaign), following the ^{252}Cf selection and accidental background subtraction as described in Section 4.3.1 and 4.3.1.
The contribution of spallation neutrons is strongly reduced in the data by application of a 1 ms veto after a muon and the remaining fast neutron events occur with very low rates. As product of natural radioactivity within the ^{232}Th and ^{238}U chains, the BiPo β-α coincidences need to be considered, where the prompt event is given by electrons and gammas from bismuth decay followed by the alpha decay of polonium, which produces the delayed event [166]:

$$^{212}\text{Bi} \xrightarrow[2.254\,\text{MeV}]{\beta\,(64.06\,\%)} {}^{212}\text{Po}\,(\tau = 431\,\text{ns}) \xrightarrow[8.954\,\text{MeV}]{\alpha} {}^{208}\text{Pb}\,, \qquad (4.7)$$

$$^{214}\text{Bi} \xrightarrow[3.27\,\text{MeV}]{\beta\,(99.98\,\%)} {}^{214}\text{Po}\,(\tau = 237\,\text{μs}) \xrightarrow[7.833\,\text{MeV}]{\alpha} {}^{210}\text{Pb}\,. \qquad (4.8)$$
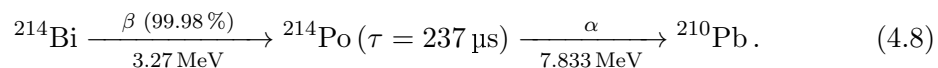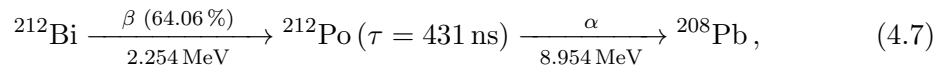
Figure 4.14 shows the prompt and delayed energy spectra of the correlated events found in 100 hours of neutrino data. Besides IBD events with delayed peaks at 2.2 MeV and 8 MeV, coincidences with prompt events around 1 and 2 MeV and delayed events with energies smaller than 1.5 MeV are observed. ^{214}Bi prompt decays have been measured

---

[2]This is the minimum time difference needed between two events to create another trigger.

[3]Spill-in events into the Target being caught on Gd make up a insignificant fraction and are neglected.

(a) Prompt visible energy.

(b) Delayed visible energy.
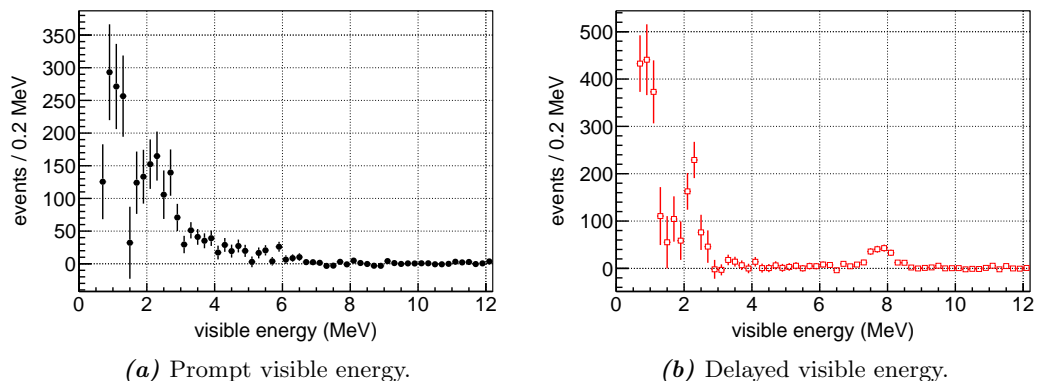
Figure 4.14: Energy spectra of the correlated events in 100 hours of neutrino data runs. The energy threshold was 0.7 MeV in this analysis, the accidental background was subtracted.

to peak at 2 MeV , ^{212}Bi prompt events below 1 MeV [129]. The delayed event alpha energies are quenched by a factor on the order of 10 [17] to values between 0.3 and 1 MeV [129]. It can be shown that the observed events are BiPo coincidences by focusing on the ^{212}Bi-^{212}Po signature, as the short time constant allows to distinguish them from IBD neutron captures. A binned likelihood fit using the parametrization $(a \cdot \exp^{-t/\tau} + b)$ of the correlation time spectrum (see Fig. 4.15a) from 0.33 to 10 µs yields $\tau = (449.5 \pm 26.1)$ ns, which is in good agreement with the literature value of (431 ± 3) ns [166]. The plot in Fig. 4.15b shows the correlation between delayed visible energies smaller than 2 MeV and a short prompt to delayed coincidence time ΔT. For the selection cuts of $E_{\text{delayed}} < 2$ MeV and $\Delta T < 1$ µs the delayed event reconstructed vertices are plotted in Fig. 4.15c and 4.15d, confirming the expectation to find ^{212}Bi-^{212}Po mainly in the Target volume, as the Target liquid contains more ^{232}Th [62].

In the delayed energy region of 0.7 to 2 MeV we can count (15.3 ± 0.5) ^{212}Bi-^{212}Po and ^{214}Bi-^{214}Po coincidences per hour[4], which is in reasonable agreement with the 23 events/hour observed in Ref. [129] with a lower energy threshold. A rate of 23 events per hour would correspond to less than 0.06 % of the ^{252}Cf delayed event data sample. Since the number of events with energies $E < 1.5$ MeV makes up 1 % of the ^{252}Cf delayed events, a detector contamination related source of the data to MC discrepancy can be excluded. The daily rate of the events in the region of 4 to 10 MeV is computed to be (64 ± 8) d^{-1}, which which is in agreement with the about (50 ± 4) expected neutrino events[5] per day in this particular data taking period [172].

Other correlated backgrounds known from the neutrino candidate selection, like fast neutrons, stopping muons or cosmogenic ^{9}Li decays can be neglected due to their low daily rates, even with the loose ^{252}Cf selection criteria.

---

[4]While this cross-check analysis has been performed with the DC-II valid trigger selection and background reduction cuts.

[5]The number of expected neutrinos is a rough estimate, using the measured neutrino events from Gd-III selection at the same days as the runs used in this analysis, corrected for the loss in signal efficiency due to tighter selection cuts. A systematic uncertainty of 1.5 events per day is included, as the Gd-III selection applies additional background veto cuts.
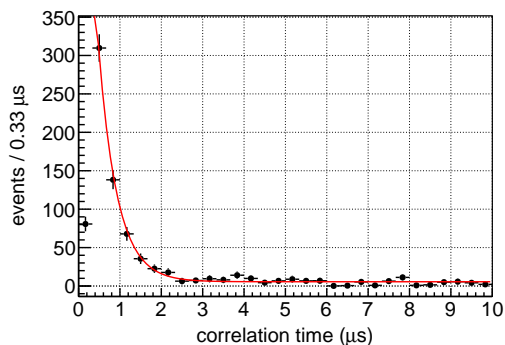
(a) Fit of the short component of the correlation time spectrum.
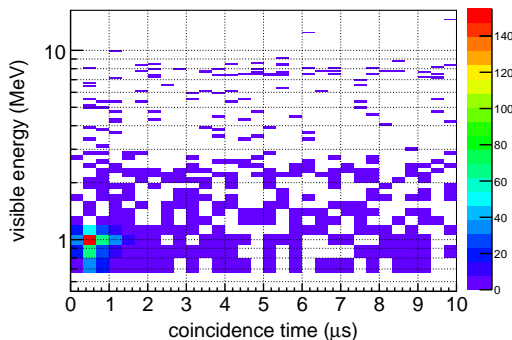
(b) Delayed visible energies vs. prompt-delayed correlation time.
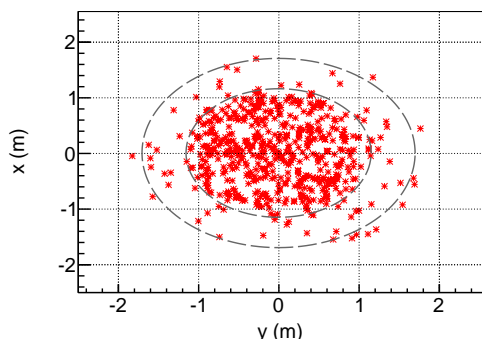
(c) Delayed event reconstructed vertex in the x-y plane for $E_{\mathrm{delayed}} < 2\,\mathrm{MeV}$ and $\Delta T < 1\,\mathrm{\mu s}$.
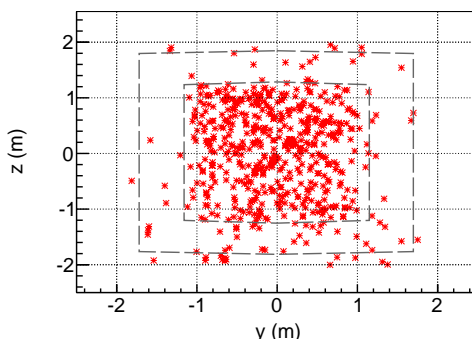
(d) Delayed event reconstructed vertex in the y-z plane for $E_{\mathrm{delayed}} < 2\,\mathrm{MeV}$ and $\Delta T < 1\,\mathrm{\mu s}$.

Figure 4.15: ^{212}Bi-^{212}Po events: (a) Fit of the short component of the correlation time spectrum from 0.33 to 10 MeV with a binned likelihood fit using the parametrization $(a \cdot \exp^{-t/\tau} + b)$. The black bullets are data points, the red line is the fit result. (b) Correlation between delayed visible energy and prompt to delayed coincidence time. (c) and (d) Delayed event reconstructed vertices, the inner dashed line marks the Target volume border, the outer dashed line represents the Gamma Catcher vessel.

We have seen that many of the possible correlated background contributions are expected to be negligible. In the next section we will show that a correlated background contribution was found and how it can be handled by a cut on the prompt visible energy or neutron multiplicity. The same two cuts can furthermore be used to suppress accidental backgrounds in the ^{252}Cf analysis further. Remaining background contributions at low energies and their influence on the detection efficiency results are discussed again in the next to last paragraph of Section 5.4.

Multiplicity analysis

In order to gain knowledge about the quantity and the features of possible correlated background, we proceed with the analysis of a breakdown into different delayed event multiplicities, as suggested by other studies [183, 99]. In the ideal case, i.e. in the absence of backgrounds, the delayed event multiplicity would correspond to the neutron
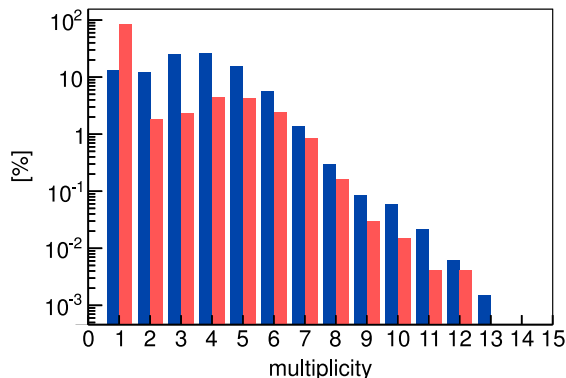
Figure 4.16: Merged on-time and off-time delayed event multiplicity spectra of the six ^{252}Cf second calibration campaign deployment runs at the Target center $(x,y,z) = (0,0,12)$ mm. The blue histogram shows the on-time multiplicity spectrum, the red histogram is the off-time multiplicity spectrum.

multiplicity of ^{252}Cf fissions. The ^{252}Cf delayed event multiplicity is given in Fig. 4.16. The off-time multiplicity distribution shows that $(83.6 \pm 0.2)\,\%$ of the accidental background events have multiplicity $m = 1$, whereas $(13.4 \pm 0.2)\,\%$ of the measured on-time events occur with $m = 1$. As the fission and single rates are quite low $(< 10\,\mathrm{Bq})$, most of the uncorrelated background events are expected to be single radioactive events, contributing largely to the $m = 1$ on-time content via single-single coincidences. Also, we might not be too surprised if any correlated background component were of low multiplicity. The bulk of larger multiplicities is shifted by to the right for the off-time spectrum. This happens because fission prompt gammas are counted themselves as accidental delayed in an off-time window, raising the multiplicity by one count.

When splitting into different multiplicities, the accidental background has to be scaled and subtracted accordingly. The corresponding background spectrum "compositions" of a certain on-time multiplicity result from the following underlying logic: An uncorrelated background event with multiplicity b only contributes to measured on-time multiplicities $m \geq b$. Therefore an on-time spectrum with $m = 1$ is subtracted by a background spectrum of $b = 1$, while a measured $m = 2$ spectrum contains background with $b = 1$ and $b = 2$.

The background spectra for a measured on-time multiplicity m at energy bin i are composed of the measured background spectra β_b with off-time multiplicity b:

$$B_m(i) = \sum_{b=1}^{m} s_{m,b} \cdot \beta_b(i) \,, \tag{4.9}$$

with scaling factors $s_{m,b}$. The scaling factors are computed based on the assumption of actually measuring uncorrelated events in the off-time windows. For a given true fission multiplicity n the probability to measure an on-time multiplicity m is given by the product of the true signal probability $P_\mathrm{s}(n)$ and the probability to accidentally obtain b uncorrelated events $P_\mathrm{off}(b)$:

$$P_\mathrm{on}(m \,|\, n) = P_\mathrm{on}(n + b \,|\, n) = P_\mathrm{s}(n) \cdot P_\mathrm{off}(b) \,, \tag{4.10}$$

while $m = n + b$. For the sake of simplicity multiple events in an off-time window with $b \geq 2$ are treated as statistical entity. The total probability to measure m on-time events is then given by

$$P_\mathrm{on}(m) = \sum_{n=0}^{m} P_\mathrm{on}(m \,|\, n) = \sum_{n=0}^{m} P_\mathrm{s}(n) \cdot P_\mathrm{off}(m - n) \,. \tag{4.11}$$
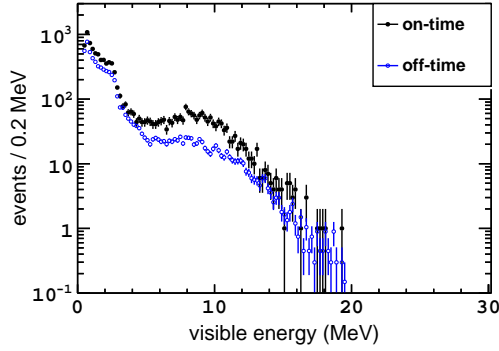
(a) Data prompt visible energy.
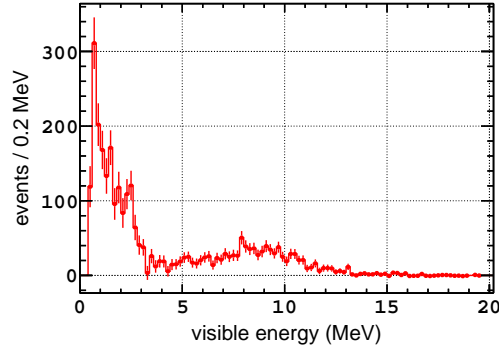
(b) Accidental background subtracted data prompt visible energy.
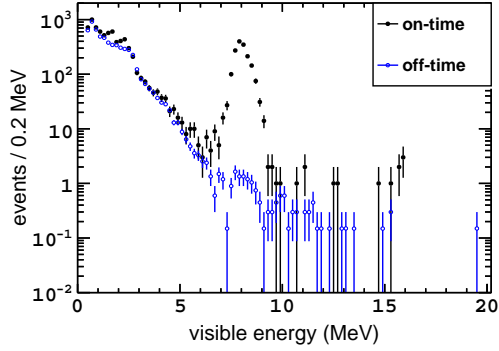
(c) Data delayed visible energy.
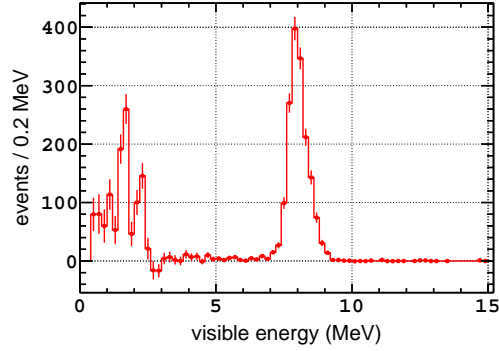
(d) Accidental background subtracted data delayed visible energy.

Figure 4.17: Merged data spectra for multiplicity $m = 1$ of the six ^{252}Cf second calibration campaign deployment runs at the Target center $(x,y,z) = (0,0,12)$ mm. Prompt energy cut $E_{\text{prompt}} > 0.5$ MeV and a maximal selected prompt-delayed correlation time of 1 ms. The black points show the on-time delayed events, the blue points the off-time (accidental background) delayed events. The red data points are the accidental background subtracted spectra.

The probabilities $P_s(n)$ can be calculated successively, since the $P_{\text{on}}(m)$ and $P_{\text{off}}(b)$ are known from the on- and off-time window measurements. As shown by Eq. (4.12) and (4.13), we start with the calculation of $P_s(0)$ by

$$P_{\text{on}}(0) = P_s(0) \cdot P_{\text{off}}(0) \quad \Rightarrow \quad P_s(0) = P_{\text{on}}(0)/P_{\text{off}}(0), \tag{4.12}$$

and proceed with $P_s(1)$ via

$$P_s(1) = \frac{P_{\text{on}}(1) - P_s(0) \cdot P_{\text{off}}(1)}{P_{\text{off}}(0)}. \tag{4.13}$$

Every other $P_s(n)$ is then computed likewise. The scaling factors $s_{m,b}$ used in Eq. (4.10) then consist of the ratio of all on-time measurement windows N_{on} (equals the total number of prompt events) and all off-time windows N_{off} multiplied by the $P_s(n = m-b)$:

$$s_{m,b} = \frac{N_{\text{on}}}{N_{\text{off}}} \cdot P_s(m - b). \tag{4.14}$$

(a) Data prompt-delayed correlation time.

(b) Accidental background subtracted data prompt-delayed correlation time.

(c) Data prompt-delayed correlation distance.

(d) Accidental background subtracted data prompt-delayed corr. distance.
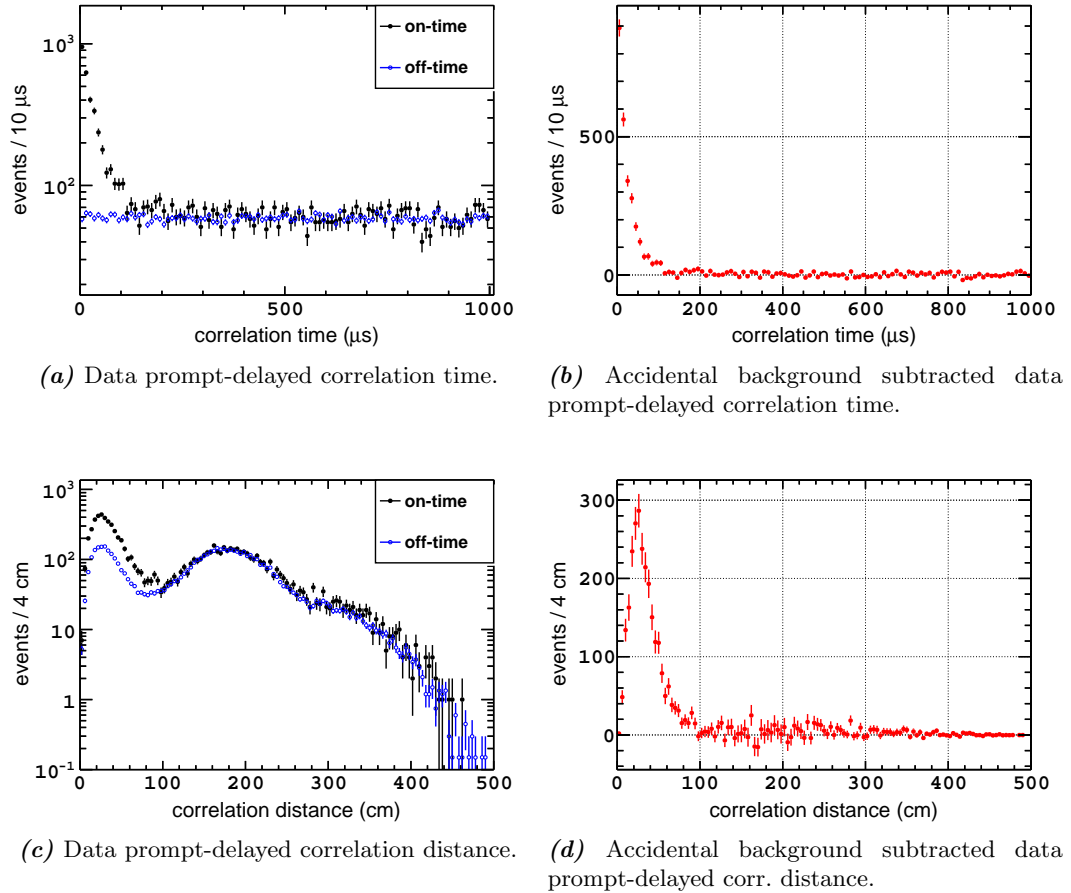
Figure 4.18: Merged data spectra for multiplicity $m = 1$ of the six ^{252}Cf second calibration campaign deployment runs at the Target center $(x,y,z) = (0,0,12)$ mm. Prompt energy cut $E_{prompt} > 0.5$ MeV and a maximal selected prompt-delayed correlation time of 1 ms. The black points show the on-time delayed events, the blue points the off-time (accidental background) delayed events. The red data points are the accidental background subtracted spectra.

It can occur that either an event is both on-time as well as background event or that it is counted as background event more than once. The first case is given for 30-40 %, the latter for less than 5 % of the events, depending on the prompt energy cut. For these events the same energy information is counted multiple times, either in both the signal and background spectra or several times in the background spectrum. The correlation distance and time will be different, as they are relative quantities computed with respect to the prompt's or virtual prompt's observable. We will not account for any correlations due to this double counting in the following analyses, since these events will either not make up the dominant fraction of the off-time spectra (they will be scaled down, as they are almost never of $b = 1$) or the total off-time spectrum will be low due to additional cuts improving the signal to background ratio.

The plots in Fig. 4.17 and 4.18 show the on-time and background spectra as well as the background subtracted spectra for the multiplicity $m = 1$. Further plots of $m = 2$ and $m = 3$ can be found in Appendix C. From intercomparison of the off-time spectra

(a) Prompt visible energy.

(b) Delayed visible energy.
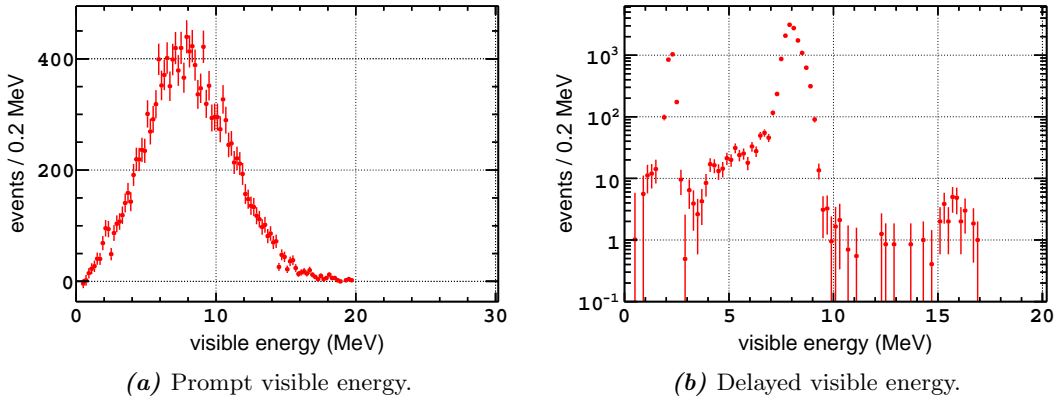
Figure 4.19: Merged accidental background subtracted data spectra for multiplicity $m = 2$ of the six ^{252}Cf second calibration campaign deployment runs at the Target center $(x,y,z) = (0,0,12)$ mm. Prompt energy cut $E_{\mathrm{prompt}} > 0.5$ MeV and a maximal selected prompt-delayed correlation time of 1 ms.
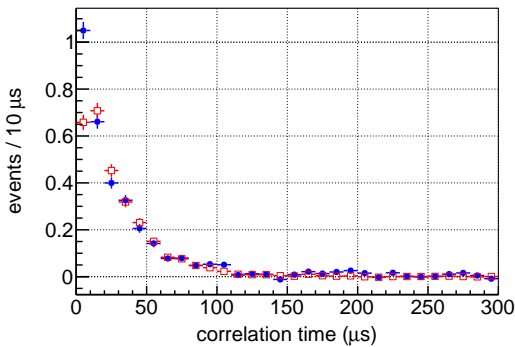
Figure 4.20: Accidental background subtracted correlation time spectra for the multiplicity $m = 1$. The data in blue are selected with a prompt energy cut > 0.5 MeV, the red data points correspond to $E_{\mathrm{prompt}} > 4$ MeV, normalized in the region from 40-150 µs.

for different m we can see that for $m = 1$ indeed a large fraction of the measured accidental background are single-single coincidences: the energy spectra for $m = 1$ both possess a dominant exponential contribution for $E < 4$ MeV, the flat component in the correlation time spectrum is one order of magnitude higher than for the multiplicities 2 or 3, and there is a significant number of events with correlation distances of $\Delta R > 1$ m. For the prompt and delayed energy spectra of $m = 1$ unexpected events with energies below 2 MeV are observed. These events feature a 1.6 MeV peak on top of other low energy events in the delayed energy spectrum and are not seen in the spectra of $m = 2$ (cf. Fig. 4.19). The only events observed in this range in physics data haven been the BiPo coincidences given in Fig. 4.14. With maximal (115 ± 25) anticipated BiPo events in 5 hours of calibration data taking coming from the detector materials, the observed excess cannot be explained. It was therefore assumed that a source-related effect caused this correlated background.

Since we can see from the prompt spectrum in Fig. 4.17b that the correlated background mainly has $E_{\mathrm{prompt}} < 4$ MeV, we can remove it by increasing the lower selection threshold of the prompt energy. The effect of this cut on the selection can be seen in Fig. 4.20: With a low energy threshold of 0.5 MeV, the correlated background component is measured, adding a contribution with short time constant to the correlation time spectrum.

Once a prompt cut of $E_{\mathrm{prompt}} > 4\,\mathrm{MeV}$ is applied, these short ΔT events disappear. Due to the large contribution of single-single uncorrelated coincidences to the spectra, the best signal to background ratio is achieved with a prompt cut. At the same time the correlated background seen in the spectra for $m = 1$ is removed. Another possibility to remove the correlated background component is a multiplicity cut requesting $m \geq 2$. The stability of the observed neutron physics with respect to these cuts will be discussed in the next paragraph.

Robustness of the Gd-fraction for different multiplicities and prompt cuts

Upon the proposal of new delayed event selection cuts for the future ^{252}Cf analyses, the robustness of the results with respect to changing selection criteria needs to be proven. As test observable the Gd-fraction will be used, as its sensitivity to a relevant change in neutron kinetic energy is straight forward to measure. Here we will compute the Gd-fraction via the definition which is used in the Gd-III efficiency systematics analysis (cf. Section 5.3):

$$f_{\mathrm{Gd}} = \frac{N(3.5 < E_{\mathrm{d}} < 10\,\mathrm{MeV})}{N(0.5 < E_{\mathrm{d}} < 10\,\mathrm{MeV})}. \tag{4.15}$$

The results are presented in Table 4.2a for data and Table 4.2b for the MC simulation of the six ^{252}Cf deployment runs of the second calibration campaign at the Target center $(x,y,z) = (0,0,12)\,\mathrm{mm}$. The Gd-fraction f_{Gd} has been computed for different delayed event multiplicities as well as the two different energy thresholds of 0.5 and 4 MeV for prompt event selection. All results are corrected for accidental background.
For the ^{252}Cf data with $E_{\mathrm{prompt}} > 4\,\mathrm{MeV}$ we find the f_{Gd} in good agreement within statistical uncertainties for all six configurations: split up in multiplicities $m = [1, 2, 3, 4]$, for $m > 1$ and if all multiplicities are included. The value for $m > 3$ is $(0.18 \pm 0.03)\,\%$ lower than for $m > 1$, only by removing events of the two multiplicities $m = 2$ and $m = 3$. Since each of the low multiplicities $m = [1, 2, 3]$ exhibit higher f_{Gd} values than the combined sample of all neutron multiplicities, the value for a sample with $m > 3$ is caused to have a lower Gd-fraction. Although the statistical uncertainty of this discrepancy might be underestimated by the assumption of the full data set with all multiplicities to be fully correlated to the sample with $m > 3$, this systematic shift hints at a dependence of f_{Gd} on the neutron multiplicity (and hence a probable dependence on neutron energy) or suggests remaining correlated background.
Similar results are found for the prompt cut $E > 0.5\,\mathrm{MeV}$, except for a clear deviation of f_{Gd} for the case of $m = 1$, induced by correlated background events. This confirms the statement that the impact of correlated background can either be reduced by a prompt energy cut or removing events with multiplicity $m = 1$.
The f_{Gd} values of simulated ^{252}Cf fission events are as expected all in good agreement within their statistical uncertainties. The prompt energy cut of 4 MeV increases the statistical uncertainty by an acceptable amount.
The results of $E_{\mathrm{prompt}} > 4\,\mathrm{MeV}$ show that fission events with multiplicity $m = 1$ can be removed without introducing a systematic shift of the Gd-fraction. Moreover do only few fissions occur with neutron multiplicity $m = 1$ and mainly accidental and correlated backgrounds are removed by requesting $m > 1$. In order to account for possible biases due to potential remaining background, different f_{Gd} definitions and sample selections will be used when the detection systematics is studied (see Chapter 5.3).

Table 4.2: ^{252}Cf data and MC simulation Gd-fraction f_{Gd} results for different delayed event multiplicities and the two different prompt energy cuts $E > 4\,\mathrm{MeV}$ and $E > 0.5\,\mathrm{MeV}$. The absolute discrepancy Δf is computed with respect to the Gd-fraction for all multiplicities and $E > 4\,\mathrm{MeV}$, while the uncertainties (statistical only) for $m > 1$ and $m > 3$ are taken to be fully correlated to $m = \mathrm{all}$.

(a) Data: ^{252}Cf Gd-fraction f_{Gd}

multiplicity	$E_{\mathbf{prompt}} > 4\,\mathrm{MeV}$		$E_{\mathbf{prompt}} > 0.5\,\mathrm{MeV}$	
	$f_{\mathbf{Gd}}$	Δf	$f_{\mathbf{Gd}}$	Δf
all	0.8530 ± 0.0009	–	0.8494 ± 0.0009	-0.0036 ± 0.0001
1	0.843 ± 0.011	-0.010 ± 0.011	0.6041 ± 0.0195	-0.25 ± 0.02
2	0.8580 ± 0.0029	0.0050 ± 0.0031	0.8590 ± 0.0030	0.0060 ± 0.0032
3	0.8556 ± 0.0018	0.0026 ± 0.0021	0.8563 ± 0.0016	0.0033 ± 0.0019
4	0.8563 ± 0.0015	0.0033 ± 0.0018	0.8555 ± 0.0014	0.0025 ± 0.0017
$m > 1$	0.8531 ± 0.0009	0.0001 ± 0.0001	0.8528 ± 0.0009	-0.0002 ± 0.0001
$m > 3$	0.8516 ± 0.0011	-0.0013 ± 0.0002	0.8510 ± 0.0010	-0.0020 ± 0.0001

(b) MC simulation: ^{252}Cf Gd-fraction f_{Gd}

multiplicity	$E_{\mathbf{prompt}} > 4\,\mathrm{MeV}$		$E_{\mathbf{prompt}} > 0.5\,\mathrm{MeV}$	
	$f_{\mathbf{Gd}}$	Δf	$f_{\mathbf{Gd}}$	Δf
all	0.8749 ± 0.0005	–	0.8749 ± 0.0004	< 0.0001
1	0.8676 ± 0.0046	-0.0072 ± 0.0047	0.8681 ± 0.0042	-0.0068 ± 0.0043
2	0.8771 ± 0.0015	0.0022 ± 0.0016	0.8764 ± 0.0014	0.0016 ± 0.0015
3	0.8755 ± 0.0009	0.0007 ± 0.0011	0.8758 ± 0.0009	0.0009 ± 0.0011
4	0.8747 ± 0.0008	-0.0002 ± 0.0010	0.8745 ± 0.0007	-0.0003 ± 0.0009
$m > 1$	0.8749 ± 0.0005	< 0.0001	0.8749 ± 0.0004	< 0.0001
$m > 3$	0.8745 ± 0.0005	-0.0004 ± 0.0001	0.8745 ± 0.0005	-0.0004 ± 0.0001

Finally we will focus on the Gd-fraction stability with respect to changing prompt cuts. Table 4.3 summarizes the results given earlier for $m > 1$ and additionally contains the values for $E > 7\,\mathrm{MeV}$. It is shown that the f_{Gd} are in agreement for data and MC respectively. Also the ratio of data to MC appears to be independent of individual prompt cut combinations in data and MC. The difference for high energies in the prompt spectrum as shown in Fig. 4.10b is therefore considered to be negligible for the type of studies presented in this thesis.

From the comparison of the MC simulation results for f_{Gd} to the ones obtained with data, we find a discrepancy of roughly 2.5 %. This data to simulation mismatch is in Chapter 5 also observed with antineutrino data, when analyzing a cosmic spallation neutron sample and in the comparison of simulation codes using different neutron scattering models. In the course of the signal detection efficiency calibration, Monte Carlo normalization correction factors are introduced, removing data to MC inconsistencies. The calculation of the Gd-fraction related MC normalization correction along with the systematic uncertainty estimation will be discussed in Chapter 5.3.

Table 4.3: ^{252}Cf data and MC simulation Gd-fraction f_{Gd} results of multiplicity $m > 1$ for different prompt energy cuts. The absolute discrepancy Δf is computed with respect to the Gd-fraction for $E > 4\,\text{MeV}$, while the uncertainties (statistical only) are taken to be fully correlated.

E_{prompt} cut	DATA		MC	
	f_{Gd}	Δf	f_{Gd}	Δf
0.5 MeV	0.8528 ± 0.0009	0.0002 ± 0.0003	0.8749 ± 0.0004	0.0001 ± 0.0001
4 MeV	0.8531 ± 0.0009	–	0.8749 ± 0.0005	–
7 MeV	0.8528 ± 0.0011	0.0002 ± 0.0002	0.8749 ± 0.0005	< 0.0001

Default background reduction

The previous paragraph has shown that consistent results of the Gd-fraction can be found for different delayed event multiplicities, except for the multiplicity $m = 1$ selected with a low prompt energy threshold $E > 0.5\,\text{MeV}$. Furthermore we could conclude that a rejection of fission neutron data with $m = 1$ does not change f_{Gd}, in case the correlated background was already removed e.g. by a prompt energy cut. Also, the Gd-fraction is proven to be independent of the prompt energy cut, while this cut has to be chosen such that the correlated background is rejected without removing too much signal from the sample.

The default background reduction cuts for the subsequent analyses will therefore include

- a prompt event selection criterion with $E_{\text{prompt}} > 4\,\text{MeV}$,

- a delayed multiplicity selection cut with $m > 1$.

The prompt cut was chosen such that the signal to background ratio is improved from 16.6 to 80. Besides removing the correlated background, also a large fraction of the single-single accidental coincidences are eliminated. The comparison between the results with a 0.5 and 4 MeV prompt cut will later be used to study systematic effects, since the amount of accidental background differs greatly for the two selections. In addition the multiplicity cut is applied, which excludes only a small amount of events, but can have a significant impact on the background rejection.

In total a high selection efficiency is achieved with the selection criteria presented in this chapter. For a prompt cut of 0.5 MeV (4 MeV) and $m > 1$ plus accidental background subtraction 11.57 ± 0.03 (10.34 ± 0.03) neutrons per second are detected at the Target center in the second campaign, when 12.9 are expected.

Chapter 5

Neutron detection efficiency in the Gd-channel analysis

This chapter will discuss the neutron detection efficiency estimation in data and MC simulation as well as the neutron detection related MC correction factor estimation along with its systematic uncertainty in the context of the DC-III Gd-channel analysis [12]. First, a general introduction to the signal detection uncertainty and MC normalization corrections in the DC experiment will be given, followed by details on the neutron detection efficiency in particular, which is separated in selection cut dependent and detector intrinsic terms. The different neutron efficiency definitions, statistical uncertainty treatment and the computation of a corresponding MC correction will be explained in Section 5.2–5.2.4. Various neutron sources were used by the Gd-III analysis to estimate and crosscheck the neutron efficiency corrections, as briefly described in Section 5.2.1.

The terms *volume-wide efficiency* and *volume-wide* or *global MC correction* is introduced in Section 5.3, both in relation to the cut dependent efficiency. Section 5.3.1 describes the Monte Carlo studies performed to validate the concept of a volume-wide efficiency computation. Results with the ^{252}Cf are given in Section 5.3.2, whereas the systematic uncertainty estimation is addressed in Section 5.3.3. The ^{252}Cf values are then compared to the results of a study based on IBD neutrons (Section 5.3.4).

The estimation of the detector intrinsic efficiency, the Gd-fraction, and its MC normalization correction using ^{252}Cf is described in Section 5.4. Muon spallation as possible source of neutrons for efficiency analyses is addressed in Section 5.5; a crosscheck value of the Gd-fraction correction is also given and discussed.

The chapter closes with the discussion on the combination of the efficiency results computed for the Gd-III oscillation analysis. The conclusions are given along with an outlook on the neutron detection efficiency in the near and far detector phase.

5.1   Signal detection uncertainty in Double Chooz

The predicted number of neutrino events in the Double Chooz analysis of each reactor (R = 1, 2) in the absence of neutrino oscillation is given by Eq. (3.1) in Chapter 3. Many of the terms in Eq. (3.1) are reactor related, such as: the mean IBD cross sec-

tion per fission[1] $\langle \sigma_f \rangle$, the thermal power P_{th} and the mean energy released per fission $\langle E_f \rangle$. Two factors, however, are solely detector related and their uncertainties form the detection systematic uncertainty of the Double Chooz experiment. N_p is the number of protons, which are the target for electron antineutrinos undergoing IBD, the factor ε_{det} represents the signal detection efficiency. The product of $\langle \sigma_f \rangle$ and N_p provides the number of IBD reactions per nuclear fission, while ε_{det} expresses the percentage of successfully recorded and identified IBD reactions in the Double Chooz detector.

The Double Chooz DAQ system features a dead-timeless data acquisition. The energy threshold of the trigger system is set to 0.4 MeV with a detection efficiency of 100 % and negligible uncertainty [196]. Hence any arising detection inefficiencies will depend on the signal selection as well as the background reduction criteria.

The IBD signature consists of two energy depositions correlated in time: the prompt positron energy deposition, which is directly linked to the neutrino kinetic energy, and the delayed radiative neutron capture (see Section 1.3.2). Owing to the IBD energy threshold of 1.8 MeV and the connection between incident neutrino energy and prompt signal energy given by Eq. (1.11), the lowest detectable energy deposition caused by IBD reaction will be with 1.08 MeV well above the analysis threshold of 0.5 MeV. Hence the prompt signal alone is detectable with close to 100 % efficiency[2]. In order to pass the selection, the delayed IBD neutron event needs to satisfy various criteria, making it the dominant contributor to the signal detection efficiency. Its selection efficiency will not only depend on the cuts imposed on the event characteristics but has also a component intrinsic to the detector liquid composition (the *Gd-fraction*, see Section 5.2). Although the delayed IBD neutron detectability is not only determined by the characteristics of the neutron captures but also the detection of resulting gammas, we will speak simply of "neutron detection efficiency" in the upcoming chapters.

Further contributions to the selection efficiencies arise due to background vetoes as well as the IBD isolation cut (cf. Section 3.3.1). The largest inefficiencies among these contributions are caused by the 1 ms veto after a muon and the IBD isolation cut.

Monte Carlo correction factors

As the Double Chooz oscillation analysis relies on MC simulation data to retrieve the predicted neutrino rate and spectrum, a good data to MC accuracy is essential. In order to correct for any differences between data and MC simulation due to discrepancies in the detection efficiencies, *MC correction factors* and corresponding uncertainties are introduced. The MC correction factors and their relative uncertainties for each contribution are summarized in Table 5.1.

The simulated IBD data contain no background events and shows a slightly different performance with respect to background veto cuts. Hence it is needed to correct the MC neutrino flux for inefficiencies or discrepancies in the inefficiencies due to the event veto after a muon, the isolation cut of the IBD candidates and other background reduction cuts such as OV, IV, FV and Li+He vetoes as well as Light Noise cuts. Due to the high trigger efficiency, the DAQ and trigger related correction component is 1

---

[1]The cross section per fission contains the inverse beta decay cross section, but also information about the fission spectra. Further details can be found in Section 3.1.1.

[2]The energy resolution at 1 MeV is roughly 8 % [12] and a shift in the energy scale introduces negligible uncertainty in the Gd-III analysis (see Section 3.2.4).

Table 5.1: Signal MC correction factors and uncertainties of the Gd-III analysis [68].

Correction source	MC correction factor	Relative uncertainty [%]
Muon veto of $1\,\mathrm{ms}$	0.955	< 0.1
Other vetoes[3]	0.994	0.11
DAQ and trigger	1.000	< 0.1
IBD isolation	0.989	< 0.1
N_{p}	1.000	0.30
IBD selection	1.000	0.20
Gd-fraction	0.975	0.43
Spill-in/out	1.000	0.27
Total	0.915	0.63

(i.e. no correction) and has a negligible uncertainty. The ν-target proton number N_{p} is known with a precision of $0.3\,\%$ [60].

The last three contributions in Table 5.1 mainly represent the neutron detection corrections. The IBD selection efficiency does not need to be corrected, while its uncertainty is formed by the neutron detection uncertainty. Discrepancies in the detector intrinsic neutron detection have been found between data and simulation, expressed by the Gd-fraction correction. Mismatch in the neutron migration between detector sub-volumes resulting in flux discrepancies are covered by the spill-in/out uncertainty. More details can be found in Section 5.2.2 and 5.2.3.

Detection systematic uncertainty in the oscillation analysis

In the θ_{13} fit the MC correction factor c_{MC} will modify the predicted neutrino flux in each energy bin i via

$$N_{\mathrm{pred},i}^{\mathrm{corr}} = N_{\mathrm{pred},i} \cdot c_{\mathrm{MC}} \,. \tag{5.1}$$

The detection systematic uncertainty enters the fit in the form of the relative uncertainty $\sigma_{\mathrm{det}} = (\Delta c_{\mathrm{MC}}/c_{\mathrm{MC}})$, which corresponds to a relative uncertainty on the neutrino rate. It is included in the RRM χ^2 definition (Eq. (3.21) in Section 3.4.5) as "pulled parameter". The Rate+Shape fit incorporates the detection systematics fully correlated between the energy bins i, j of the prompt spectrum in terms of a covariance matrix (Eq. (3.17) and (3.18) in Section 3.4.3)

$$M_{i,j}^{\mathrm{det}} = N_{\mathrm{pred},i}^{\mathrm{corr}} \cdot N_{\mathrm{pred},j}^{\mathrm{corr}} \cdot \sigma_{\mathrm{det}}^2 \,. \tag{5.2}$$

5.2 Neutron detection efficiency and Monte Carlo normalization correction

With the IBD prompt event detection being $100\,\%$ efficient along with negligible uncertainty and the background reduction cuts adding insignificant contribution to the detection systematics, the dominant part of the detection uncertainty is delayed event related or, more precisely, connected to the IBD neutron detection.

---

[3]Outer Veto cut, Inner Veto cut, FV veto, Light Noise cut and Li+He veto.

The magnitude of the IBD neutron detection efficiency and its uncertainty depend on
three main contributions:

- The **Gd-fraction** $f_{\mathbf{Gd}}$, which represents the fraction of neutron captures occur-
  ring on Gd nuclei. It is in general controlled by the relative abundance of neutron
  capturing isotopes and their capture cross sections.

- The **selection efficiency** $\varepsilon_{\mathbf{cut}}$ which is mainly determined by the selection cri-
  teria an IBD neutron candidate needs to satisfy.

- Border effects increasing the fiducial volume to regions outside the ν-target (Tar-
  get) due to neutron mobility are summarized as **"Spill-in/out effect"**.

A mismatch between data and MC in any of these quantities can be compensated by the
introduction of a MC correction factor. The robustness of this correction or remaining
discrepancies are covered by the systematic uncertainty on each contribution. Hence
the absolute value of ε_{cut} as well as the uncertainty of its MC correction can be modified
with respect to the choice of selection cuts. The Gd-fraction f_{Gd}, however, is inherent
to the scintillator composition.

5.2.1 Neutron sources

The detection correction factors and systematic uncertainties are estimated by means
of different neutron sources. Furthermore neutron simulation code on the basis of dif-
ferent neutron modelings are used in case it is not possible to extract the systematic
effect from existing detector data.
Neutrons of three sources are available in the DC experiment: neutrons from calibration
source deployments of ^{252}Cf, neutrons from the IBD reaction of reactor antineutrinos
and - usually background in the search of the oscillation signal - neutrons from cosmic
ray spallation. Originating from different production processes their kinetic energies
therefore span different energy ranges. This allows to test whether an energy depen-
dence of the neutron detection efficiency correction is observed. Some of the sources
have been taken to compute the correction inputs to the θ_{13} fit, others were analyzed
to obtain cross-check results. Moreover, the volumes tested by the sources are not the
same, making it possible to cross-check the Target-wide efficiency estimation methods
(see Section 5.3). The three neutron sources will be discussed briefly in the following.

^{252}Cf fission neutrons

The spontaneous fission of the DC ^{252}Cf source provides in the second calibration
campaign with ~ 15.6 neutrons per second a high rate in neutron events. Due to
a preceding prompt gamma signal, the neutron events can be extracted efficiently,
offering a large signal to background ratio. The mean kinetic energy is roughly $2\,\text{MeV}$,
the most probable energy amounts to $0.7\,\text{MeV}$. The ^{252}Cf calibration source is deployed
at various positions along the central symmetry axis (Fig. 5.4 in Section 5.3), probing
the spherical sub-volume around the deployment location. More details on the ^{252}Cf
source can be found in Section 4.1.

IBD neutrons

The IBD neutrons are the most natural source to use for efficiency studies, as they are part of the neutrino signal. The candidate selection, however, contains various backgrounds and possesses low statistics compared to the ^{252}Cf source. The mean kinetic energy of IBD neutrons is about 15 keV. In contrast to ^{252}Cf source neutrons, the IBD neutrons can test the full detector volume. Though the knowledge about their spatial origin is limited to the precision of the position reconstruction.

Cosmic ray spallation neutrons

Neutrons can be produced upon cosmic ray spallation. In general background to the IBD signal, they can be used for calibration purposes. These neutron events can be observed after high energy depositions in the detector, caused by cosmic muons. The full detector volume is reached by spallation neutrons, but their production location is not known. Their average kinetic energy right after production is expected to be ~ 20 MeV [39] and depends mainly on the muon energy [206].

5.2.2 Efficiency definitions

The selection efficiencies are in general defined as the ratio of the number of events in two sub-samples of the data set. The efficiency ε_x of a certain selection x is then described as

$$\varepsilon_x = \frac{N(\text{selection with cuts } x)}{N(\text{wide selection cuts})} \,, \tag{5.3}$$

where the sample in the enumerator will be always a sub-sample of the sample selected by the denominator, as the latter is selected with wider cuts. Hence the value of ε_x is a real number between 0 and 1.

Intrinsic efficiency: the Gd-fraction

Neutron capture on a nucleus is a competitive process among the different isotopes' nuclei present in the scintillator liquid. The probability of a neutron to be finally caught on a certain type of isotope mainly depends on the neutron capture cross-sections and abundances of the isotopes present in the medium. The capture cross-sections are energy dependent and increase if the neutron kinetic energy decreases (cf. Fig 7.5). In case a neutron is moderated in the detector, the capture probabilities will change with respect to time, until the neutron has reached the thermal energy regime.
The fraction of neutron captures occurring on Gd nuclei is represented by the Gd-fraction f_{Gd}. An estimate for f_{Gd} is retrieved from the energy spectrum of the de-excitation gammas emitted upon neutron capture on a negligibly short time scale. More than 99 % of the neutrons are caught on H and Gd nuclei in the Target scintillator. After neutron capture on H, a 2.2 MeV gamma is released, whereas neutron capture on Gd triggers the emission of a gamma cascade with a total energy of about 8 MeV. The Gd-fraction is then defined as the ratio of events in the energy region from 3.5 to 10 MeV with respect to all neutron captures depositing energy between 0.5 and 10 MeV. The visible energy of neutron capture E_{delayed} is called *delayed energy*, as the neutron events studied in efficiency analysis are always part of a coincidence signal and
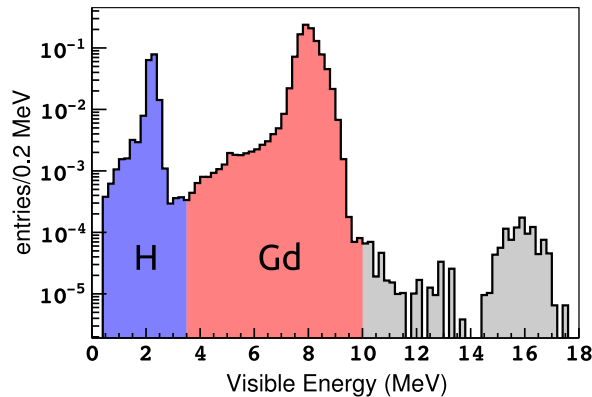
Figure 5.1: The neutron capture energy spectrum is used to estimate the Gd-fraction.

Table 5.2: Selection cuts of the DC-III Gd-channel analysis affecting the delayed event extraction [12].

Cut variable	Selection range
Delayed energy	$4 < E_{\text{delayed}} < 10\,\text{MeV}$
Correlation time	$0.5 < \Delta T < 150\,\mu\text{s}$
Correlation distance	$\Delta R < 1\,\text{m}$

therefore occur associated with a preceding *prompt event*. The Gd-fraction can then
be expressed as

$$f_{\text{Gd}} = \frac{N(3.5 < E_{\text{delayed}} < 10\,\text{MeV})}{N(0.5 < E_{\text{delayed}} < 10\,\text{MeV})}\,. \tag{5.4}$$

Doing so, the energy spectrum is effectively split in a hydrogen and a gadolinium
capture part, as shown in Fig. 5.3. The small fraction of neutron captures on carbon[4]
is mostly included in the Gd energy window in this definition, as these captures take
part in the IBD candidate selection in the Gd-channel analysis. The Gd-H double
captures at $\sim 10.2\,\text{MeV}$ and the Gd-Gd double captures at $\sim 16\,\text{MeV}$ are excluded from
the analysis, having negligible effect on the result.

Cut dependent efficiency

In case of the cut dependent efficiency, the enumerator in Eq. (5.3) is determined by
the neutrino selection criteria involving the delayed event. These three cuts on energy,
timing and spatial separation are in the DC-III Gd-channel analysis given in Table 5.2.
The previous Gd- and H-channel analyses [5, 6, 8] defined the cut dependent efficiency
as product of the efficiencies ε_i for each individual selection cut i. The combined cut
dependent efficiency was therefore computed in an *exclusive* way, via

$$\varepsilon_{\text{exc}} = \Pi_i\, \varepsilon_i\,. \tag{5.5}$$

---

[4]The fraction of neutron captures on ^{12}C is estimated from MC simulation to make up $< 0.1\%$ of
all neutron captures.

(a) Isolated efficiency parameter space.

(b) Nested efficiency parameter space.
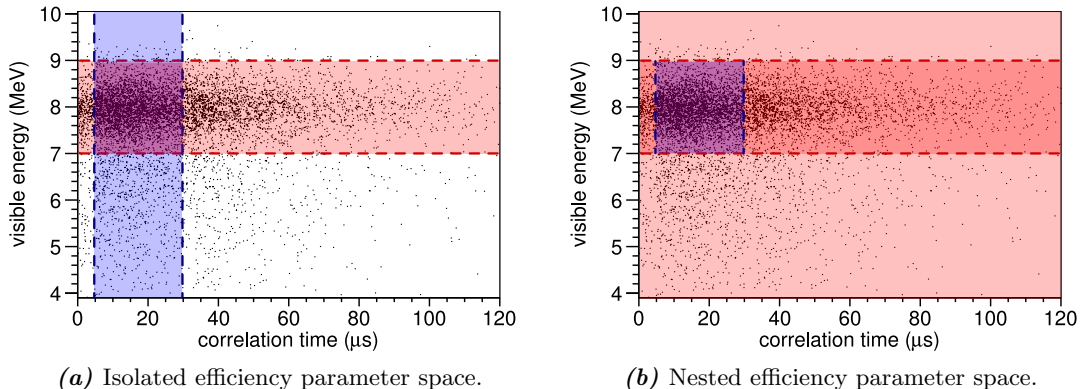
Figure 5.2: The parameter space exploited in the isolated and nested efficiency computation
for the case of two cuts on the delayed visible energy and the correlation time. The isolated
efficiency definition computes the cut efficiencies separately using one colored band for each
cut. In contrast to that the nested efficiency estimates the cut efficiencies step by step, moving
from the full parameter space to the darker red band and from there to the selection shown in
blue. The cuts presented are not used by the official analysis and were used for visualization
only.

For the Gd-III analysis the *exclusive efficiency* would hence be given by

$$\varepsilon_{\text{exc}} = \varepsilon_{E_{\text{d}}} \cdot \varepsilon_{\Delta T} \cdot \varepsilon_{\Delta R} \,, \tag{5.6}$$

where $\varepsilon_{E_{\text{d}}}$ denotes the delayed energy cut efficiency, $\varepsilon_{\Delta T}$ the efficiency on the correla-
tion time cut and $\varepsilon_{\Delta R}$ the cut efficiency on the correlation distance.

In the following, two different ways to compute the individual cut efficiencies are dis-
cussed. The first one is the *isolated efficiency* definition, used in former DC analyses.
In this definition, the wide selection of the denominator in Eq. (5.3) is always given
by the neutrino selection cuts of the enumerator, while only the selection cut, whose
efficiency is studied, is relaxed. The isolated efficiency for the delayed energy cut would
therefore be given by

$$\varepsilon_{E_{\text{d}}}^{\text{iso}} = \frac{N(4 < E_{\text{delayed}} < 10\,\text{MeV} \ \cap \ \Delta R < 1\,\text{m} \ \cap \ 0.5 < \Delta T < 150\,\text{μs})}{N(3.5 < E_{\text{delayed}} < 10\,\text{MeV} \ \cap \ \Delta R < 1\,\text{m} \ \cap \ 0.5 < \Delta T < 150\,\text{μs})} \,. \tag{5.7}$$

Figure 5.2a illustrates the isolated efficiency definition for the case of only two example
cuts, which are used for visualization only and are not part of the official analysis. The
delayed visible energy cut limits from 7 to 9 MeV are given by the red dashed lines, the
correlation time between prompt and delayed event limits from 5 to 30 μs by the blue
dashed lines. The events in the rectangular shaped area where both selection bands
meet correspond to the combined event selection. Computation of the isolated effi-
ciency $\varepsilon_{E_{\text{d}}}^{\text{iso}}$ therefore exploits only the parameter space marked by the colored red area.
Likewise, the blue colored region is used when the isolated efficiency $\varepsilon_{\Delta T}^{\text{iso}}$ is calculated.
In case of correlations between the selection cuts which could affect the efficiency com-
putation, the combined exclusive efficiency and the actual cut efficiency will not give
the same result.
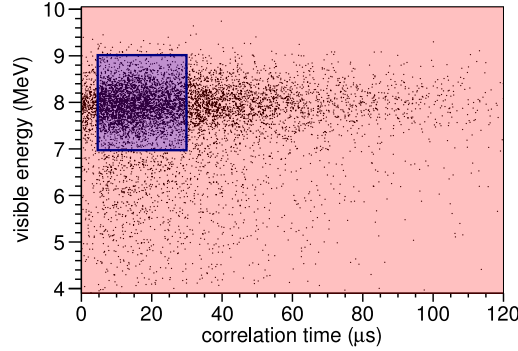
Figure 5.3: The semi-inclusive efficiency computation in case of two cuts. The events in the blue box represent the selected sample, the red colored area is the sample selected with wide cuts, which includes the blue colored region. This plot illustrates an arbitrary set of cuts, which is not used by the official DC analysis.

In the *nested efficiency* computation, however, one efficiency definition is built on the other, guaranteeing to yield the same result as the actual cut efficiency. As shown in Fig. 5.2b the efficiency ε_{E_d} is computed using the full parameter space, while $\varepsilon_{\Delta T}$ is calculated after the delayed energy selection cut was applied.

From Fig. 5.2a we have seen that the isolated efficiency computation uses only the colored regions in the E_{delayed}-ΔT parameter plane. Provided that there are no correlations between the selection cuts this definition can be of advantage as it reduces the influence of backgrounds on the efficiency estimation.

Going back to the DC-III selection, the nested efficiency definitions for the delayed cut is expressed by

$$\varepsilon_{E_d} = \frac{N(4 < E_{\text{delayed}} < 10\,\text{MeV})}{N(3.5 < E_{\text{delayed}} < 10\,\text{MeV})}\,. \tag{5.8}$$

Hence the correlation distance efficiency will be defined as

$$\varepsilon_{\Delta R} = \frac{N(4 < E_{\text{delayed}} < 10\,\text{MeV}\ \cap\ \Delta R < 1\,\text{m})}{N(4 < E_{\text{delayed}} < 10\,\text{MeV})}\,, \tag{5.9}$$

leaving for the correlation time cut efficiency to be given by the ratio

$$\varepsilon_{\Delta T} = \frac{N(4 < E_{\text{delayed}} < 10\,\text{MeV}\ \cap\ \Delta R < 1\,\text{m}\ \cap\ 0.5 < \Delta T < 150\,\mu\text{s})}{N(4 < E_{\text{delayed}} < 10\,\text{MeV}\ \cap\ \Delta R < 1\,\text{m})}\,. \tag{5.10}$$

Even if the exclusive efficiency ε_{exc} will yield the same result as the actual cut efficiency, discrepancies in the systematic or statistical uncertainties can arise e.g. due to double counting of error contributions. While for ε_{exc} the contribution of each selection cut is computed separately, the efficiency representation below in Eq. (5.11) applies all selection cuts simultaneously:

$$\varepsilon_{\text{semi}} = \frac{N(4 < E_{\text{delayed}} < 10\,\text{MeV}\ \cap\ \Delta R < 1\,\text{m}\ \cap\ 0.5 < \Delta T < 150\,\mu\text{s})}{N(3.5 < E_{\text{delayed}} < 10\,\text{MeV})}\,. \tag{5.11}$$

This definition makes use of the full parameter space, as visualized in Fig. 5.3, accounts for all correlations between different cuts and should ensure that no double counting in the uncertainty estimation due to correlations will occur. It is called *semi-inclusive efficiency*, as it includes all selection efficiencies at the same time, except for the Gd-fraction.

Total neutron detection efficiency

The total neutron detection efficiency is defined as the ratio of the number of events selected by the full set of cuts (given in Table 5.2) and all detectable neutron captures. In contrast to the semi-inclusive efficiency the *inclusive efficiency* [65, 124] takes the Gd-fraction into account, as the energy window in the denominator ranges from 0.5 to 10 MeV:

$$\varepsilon_{\text{inc}} = \frac{N(4 < E_{\text{delayed}} < 10\,\text{MeV} \ \cap \ \Delta R < 1\,\text{m} \ \cap \ 0.5 < \Delta T < 150\,\text{μs})}{N(0.5 < E_{\text{delayed}} < 10\,\text{MeV})}. \tag{5.12}$$

This definition is the most complete one, but will include neutrons captured outside the neutrino Target (in $> 99\,\%$ of the cases on hydrogen) in the wide sample of the denominator. In this way border effects can be introduced to the efficiency measurement, which is not always desired.

Another possible way to compute the total efficiency is defined as product of the semi-inclusive efficiency from Eq. (5.11) (or exclusive efficiency given in Eq. (5.6)) with the Gd-fraction f_{gd} (cf. Eq. (5.4)):

$$\varepsilon_{\text{total}} = \varepsilon_{\text{semi}} \cdot f_{\text{Gd}}. \tag{5.13}$$

We will in the following make use of the different efficiency definitions presented above, depending on the detector region investigated or the effect studied.

5.2.3   Monte Carlo normalization correction

In order to correct for discrepancies in the selected data and MC simulated neutrino flux, the correction factor c_{MC} is introduced, which is applied to the MC predicted rate as given in Eq. (5.1). Regarding the neutron detection efficiency, the correction factor $c_{\text{MC,det}}$ is determined via

$$c_{\text{MC,det}} = \frac{\varepsilon_{\text{det}}^{\text{Data}}}{\varepsilon_{\text{det}}^{\text{MC}}}, \tag{5.14}$$

with the neutron detection efficiencies $\varepsilon_{\text{det}}^{\text{Data}}$ and $\varepsilon_{\text{det}}^{\text{MC}}$ estimated using neutron data and MC simulation, respectively. As efficiency definition in Eq. (5.14) either the inclusive or the total efficiency can be applied to yield the full neutron related MC correction. If the total efficiency from Eq. (5.13) is used, the MC correction can be split into two factors

$$c_{\text{MC,det}} = \frac{(\varepsilon_{\text{semi}} \cdot f_{\text{Gd}})^{\text{Data}}}{(\varepsilon_{\text{semi}} \cdot f_{\text{Gd}})^{\text{MC}}} = c_{\text{cut}} \cdot c_{\text{Gd}}. \tag{5.15}$$

The MC correction $c_{\text{MC,det}}$ is then the product of the cut dependent efficiency correction c_{cut} and the Gd-fraction correction c_{Gd}. In Section 5.3 we will see that this separated definition is the preferred choice to estimate a Target-wide correction factor.

5.2.4 Efficiency statistical uncertainty

This section will discuss the statistical uncertainty estimation of the efficiencies. In our measurements we will always obtain two numbers: the selected events n with loose cuts and the events k passing the tighter selection cuts. The efficiency estimate of the unknown parameter ε is gained from

$$\hat{\varepsilon} = \frac{k}{n}\,, \tag{5.16}$$

the denominator and enumerator statistically depend on each other, since $n = k + m$ with m being the number of events not passing the tight cuts. Both n and k are related via the binomial law: out of n draws the probability of one success is given by ε, and we find for the discrete probability of k successes

$$p(k|\varepsilon, n) = \binom{n}{k} \varepsilon^k (1 - \varepsilon)^{n-k}\,. \tag{5.17}$$

A solution to compute the uncertainty from the variance $\sqrt{\mathrm{Var}(k)} = \sigma_k = \sqrt{n\varepsilon(1 - \varepsilon)}$ is gained from approximation of the binomial distribution by a normal distribution [176, 202]:

$$\Delta\hat{\varepsilon} = \sqrt{\frac{\hat{\varepsilon}(1 - \hat{\varepsilon})}{n}}\,. \tag{5.18}$$

This uncertainty is often referred to as *binomial uncertainty* or $\hat{\varepsilon} \pm \Delta\hat{\varepsilon}$ as *Wald interval* [56]. Apart from the fact that for the case of $\varepsilon = 1$ or 0 it yields the unphysical value $\Delta\varepsilon = 0$, the binomial uncertainty intervals have the problem to often provide a coverage which is smaller than the desired probability [56, 71].

Clopper-Pearson confidence intervals

Many ways to compute a binomial proportion confidence interval based on frequentist argumentation can be found in the literature, where one of the most popular is the Clopper-Pearson confidence interval [73]. It is constructed following the classical Neyman definition [168] of a central confidence interval (e.g. $\alpha_{\mathrm{low}} = \alpha_{\mathrm{up}} = 1 - \mathrm{CL}$) by requiring the lower bound $\varepsilon_{\mathrm{low}}$ to fulfill

$$P(X \geq k; \varepsilon_{\mathrm{low}}) = \frac{\alpha}{2} \quad \text{or} \quad P(X \leq k - 1; \varepsilon_{\mathrm{low}}) = 1 - \frac{\alpha}{2}\,, \tag{5.19}$$

and the upper bound to satisfy

$$P(X \leq k; \varepsilon_{\mathrm{up}}) = \frac{\alpha}{2}\,. \tag{5.20}$$

where $P(X \leq k)$ denotes the cumulative distribution function. Here k represents the events counted with the tight selection cuts and X a binomial distributed random variable, while the number of events n passing the wide cuts is kept fixed. The lower bound value $\varepsilon_{\mathrm{low}}$ is found by computation of the $\frac{\alpha}{2}$ quantile of the beta distribution [56, 188]

$$\frac{\alpha}{2} = I_{\varepsilon_{\mathrm{low}}}(k, n - k + 1)\,, \tag{5.21}$$

whereas the upper bound $\varepsilon_{\mathrm{up}}$ is gained from calculation of the $1 - \frac{\alpha}{2}$ quantile of the beta distribution

$$1 - \frac{\alpha}{2} = I_{\varepsilon_{\mathrm{up}}}(k + 1, n - k)\,, \tag{5.22}$$

where $I_\varepsilon(a, b)$ denotes the regularized incomplete beta function

$$I_\varepsilon(a, b) = \frac{(a + b - 1)!}{(a - 1)! \cdot (b - 1)!} \cdot \int_0^\varepsilon t^{a-1}(1 - t)^{b-1} \, \mathrm{d}t \,. \tag{5.23}$$

The quantile q of the beta distribution can be computed by means of the function
`ROOT::Math::beta_quantile(q,a,b)` provided by the data analysis framework
`ROOT` [189]. Solving Eq. (5.21) and (5.22) will yield asymmetric uncertainties, as the
estimator $\hat{\varepsilon}$ is computed as given by Eq. (5.16).

For cases in which $\hat{\varepsilon} = 1$ or 0, an upper or lower limit can be computed, respectively.
The classical Neyman construction of a confidence level guarantees that for any value of
ε no undercoverage is observed. Owing to the discreteness of the binomial distribution
this results in turn in over-coverage [84]. Considered as conservative, this property is
widely accepted and the Clopper-Pearson confidence intervals are often used in particle
physics.

Background fluctuation incorporation

As the efficiency values are fluctuated within their uncertainties in order to propagate
their uncertainty when the "sampling method" (cf. Section 5.3) is used, assumptions
about the pdf of the efficiency ε need to be made. In order to obtain $p(\varepsilon|n, k)$, Bayes'
Theorem [47] is applied and the posterior probability density of ε can be expressed by

$$p(\varepsilon|n, k) = \frac{p(k|\varepsilon, n)\pi(\varepsilon)}{\int p(k|\varepsilon, n)\pi(\varepsilon) \, \mathrm{d}\varepsilon} \,. \tag{5.24}$$

Here, $p(k|\varepsilon, n)$ is given by the binomial distribution (as in Eq. (5.17)), while a flat prior

$$\pi(\varepsilon) = \begin{cases} 1 & \text{if } 0 \leq \varepsilon \leq 1 \\ 0 & \text{otherwise} \end{cases} \tag{5.25}$$

is used, which expresses no prior knowledge about ε except that $0 \leq \varepsilon \leq 1$ has to be
satisfied. As a result

$$p(\varepsilon|n, k) = \frac{(n + 1)!}{k!(n - k)!} \cdot \varepsilon^k(1 - \varepsilon)^{n-k} = \binom{n}{k} \cdot (n + 1) \cdot \varepsilon^k(1 - \varepsilon)^{n-k} \tag{5.26}$$

is obtained by solving Eq. (5.24) [176]. Since a flat prior is used, the probability
density of ε is given by a beta distribution, which is the conjugate prior of the bino-
mial distribution. The computation of a central confidence interval is done by solving
$I_{\varepsilon_{\mathrm{low}}}(k + 1, n - k + 1) = \alpha/2$ and $I_{\varepsilon_{\mathrm{up}}}(k + 1, n - k + 1) = 1 - \alpha/2$, which coinciden-
tally yields almost the same result as the Clopper-Pearson construction, but follows a
different interpretation. The mean value of Eq. (5.26) is given by

$$E(\varepsilon) = \frac{k + 1}{n + 2} \,, \tag{5.27}$$

while the most probable value $\mathrm{mode}(\varepsilon) = k/n$ agrees with the previously defined es-
timate $\hat{\varepsilon}$ in Eq. (5.16) [86]. The measured number of events n and k in the following
studies are that large, that the discrepancy between mean value and mode becomes
negligible.

In case of the ^{252}Cf and spallation neutron studies, the measured events $n = (n_{\text{s}} + B)$
and $k = (k_{\text{s}} + b)$ contain signal (represented by n_{s} and k_{s}) as well as the background
contributions B and b. The estimate of the signal efficiency should then be represented
by

$$\hat{\varepsilon}_{\text{sig}} = \frac{k - b}{n - B} \tag{5.28}$$

and for the probability density distribution one might adopt $p(\varepsilon_{\text{sig}}|n - B, k - b)$ as in
Eq. (5.26). In a subsidiary background measurement we have measured the expected
background R in the wide sample and the corresponding background cut efficiency
$\varepsilon_{\text{bg}} = u/R$ (u are the background events in the tight selection cut sample), both with
enlarged statistics due to multiple off-time windows (see Section 4.3.1). The actual
on-time background rates B and b are, however, unknown.

In order to include the knowledge about the on-time background gained from the off-
time measurements as well as their possibility to fluctuate, B and b will be additionally
varied input of $p(\varepsilon_{\text{sig}}|n - B, k - b)$.

We have measured the on-time expectation value μ_{bg} in the wide sample, and draw the
number of events B from the Poissonian distribution

$$p(B) = \frac{(\mu_{\text{bg}})^B}{B!} \cdot e^{-\mu_{\text{bg}}} \, . \tag{5.29}$$

The background events b in the tight cut sample depend on B and the background
efficiency ε_{bg} and are then drawn from the binomial distribution

$$p(b|\varepsilon_{\text{bg}}, B) = \binom{B}{b} \varepsilon_{\text{bg}}^b (1 - \varepsilon_{\text{bg}})^{B-b} \tag{5.30}$$

The background expectation μ_{bg} is measured with the off-time windows and is assumed
to be Erlang distributed [127]:

$$p(\mu_{\text{bg}}) = \omega \cdot \frac{(\omega\, \mu_{\text{bg}})^R}{R!} \cdot e^{-\omega\, \mu_{\text{bg}}} \, , \tag{5.31}$$

which represents a special case of the gamma distribution. Its mean is given by $(R+1)/\omega$
and the variance by $\sqrt{R+1}/\omega$, letting the relative dispersion $1/\sqrt{R+1}$ decrease with
increasing measurement time. The parameter ω is a scaling factor and with multiple
background windows we easily reach $\omega > 1$:

$$\omega = \frac{N(\text{off-time virtual prompts})}{N(\text{on-time prompt events})} \tag{5.32}$$

The background efficiency ε_{bg} is taken to be beta distributed with input R and u from
the subsidiary background measurement:

$$p(\varepsilon_{\text{bg}}|R, u) = \binom{R}{u} \cdot (R + 1) \cdot \varepsilon_{\text{bg}}^u (1 - \varepsilon_{\text{bg}})^{R-u} \, . \tag{5.33}$$

Details on each distribution presented here and the corresponding random number
generation can be found in [205].

In the following the efficiency uncertainties of background free samples are computed using the Clopper-Pearson confidence level construction. In most cases no asymmetric error is quoted if the difference between upper and lower error is too small.

If background is present in the analysis sample, the efficiency values are fluctuated using the upper formulae. The introduction of fluctuating background only slightly increases the uncertainties by $\sim 5\%$ for the volume-wide efficiencies and MC corrections (both quantities are explained below). The change in the mean of the results computed from fluctuation of the efficiencies and inputs compared to the calculation without value fluctuation is of negligible size.

5.3 Volume-wide MC correction and detection systematic estimation

In this section we will discuss the computation of a volume-wide efficiency and detection efficiency related MC correction. To understand the term "volume-wide" and the way this can be achieved using the different types of neutron data, it is first necessary to study the behavior of the detection efficiency at different positions in the fiducial volume. Consistent with the geometrical symmetry of the DC detector are spatial dependencies of the efficiencies described with respect to cylindrical coordinates (z, ρ) in the following. Calibration data with the ^{252}Cf source are available along the Target symmetry axis, also called "z-axis". The ^{252}Cf calibration positions of the first and second campaigns are plotted in Fig. 5.4. In Fig. 5.5 the results of the inclusive efficiency from Eq. (5.12) for $|z| < 1.3$ m (no source deployments in the chimney) are shown. The inclusive efficiency values are stable within $< 0.4\%$ in the Target for deployment positions $|z| < 0.7$ m. This is the case, as 99% of the neutrons are caught within less than 40 cm linear distance[5] from the source position. Hence the capture location is too far from acrylic walls for the neutrons to observe border effects or their capture gammas to suffer energy loss inside the walls.

When the calibration source approaches further the Target acrylic walls, the efficiency decreases, as seen in Fig. 5.5 for $|z| > 0.7$ m. The reduction in the inclusive detection efficiency is caused by a combination of several effects. To begin with the most dominant influence: if the source is deployed close to the walls a portion of the fission neutrons will cross the acrylics and leave the Target. Neutrons entering the gamma catcher or the acrylics are mostly caught on hydrogen and therefore are lost to the Gd-based detection channel (these events are known as *spill-out*). Furthermore, a certain percentage of the events leaves the Target volume but will later return to the Target – due to the notably larger capture time[6] in the gamma catcher – and will be finally caught in it. This crossing of volumes increases the effective capture time for this type of events and hence lowers the detection efficiency. Moreover energy loss due to the acrylics decreases the efficiency.

From the data and concepts discussed above, we conclude that the accuracy of a detection efficiency measurement with calibration data at the Target center should be independent from slight variations of the source position. The precision of such an

---

[5]The linear distance was computed using ^{252}Cf MC simulation at the Target center.

[6]The neutron capture time in the gamma catcher is with 200 μs hydrogen dominated and longer compared to the 30 μs of the Target.
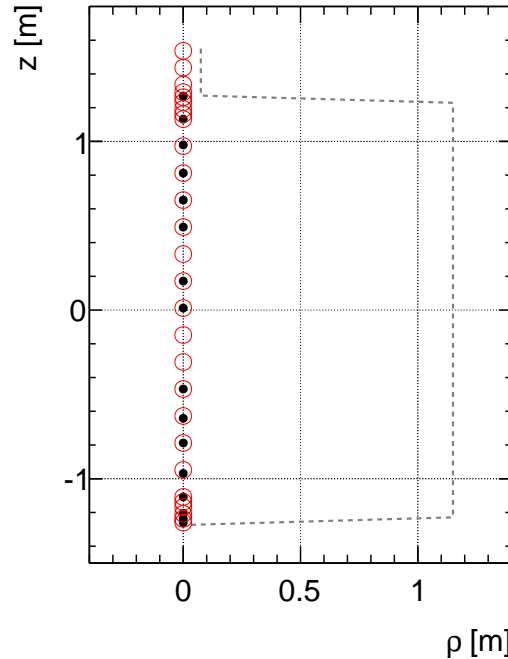
Figure 5.4: ^{252}Cf source calibration positions in the (z, ρ) plane. The black bullets show
the deployment positions for the first, the red open circles for the second campaign. The gray
dashed line represents the Target acrylic wall.

efficiency determination is due to the long run lengths, and thus higher event statistics,
better than the one obtained with IBD or spallation neutrons.

An efficiency calibration at the fiducial volume border is more difficult, in case we want
to rely on a data to MC simulation point-to-point comparison as slight deviations on
the few millimeter scale in the source position changes the neutron detection. However,
it is very important to consider the ^{252}Cf deployment runs close to the Target walls.
Due to the cylindrical shape the Target volume increases proportional to ρ^2. Likewise,
for the number of detected IBD events holds

$$N_\nu^{\mathrm{det}} \propto \iint_{V_{\mathrm{t}}} N_{\mathrm{p}} \cdot \varepsilon(z, \rho) \, \rho \, \mathrm{d}\rho \, \mathrm{d}z \,, \tag{5.34}$$

where the product of the proton number N_{p} and the parametrized efficiency $\varepsilon(z, \rho)$
is integrated over the Target volume V_{t}. Provided that the incoming neutrino flux
is homogeneous throughout the detector, an increasing fraction of events occurs with
increasing distance from the center following Eq. (5.34). Therefore an estimator for the
full volume efficiency ε_{v} is required, which computes the weighted average of the point-
wise efficiency measurements according to their geometrical relevance. The detection
efficiency related MC correction factor c_{v} (v for "volume-wide") will then be computed
globally, rather than point-to-point, via

$$c_{\mathrm{v}} = \frac{\varepsilon_{\mathrm{v}}^{\mathrm{Data}}}{\varepsilon_{\mathrm{v}}^{\mathrm{MC}}} \,. \tag{5.35}$$

In case the efficiency correction c_{v} is calculated using the inclusive efficiencies given
in Fig. 5.5, spill-out related data to MC discrepancies are included in the correction
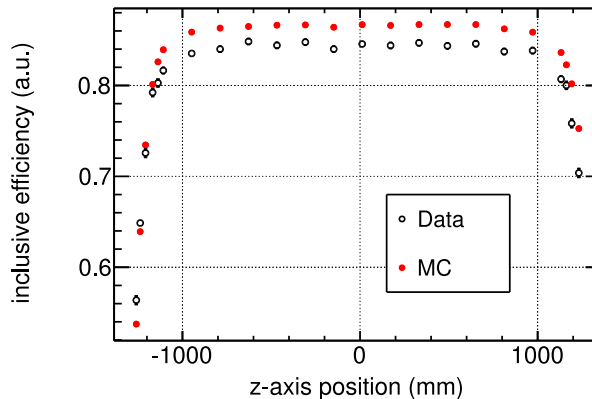
Figure 5.5: Inclusive efficiency of ^{252}Cf source data versus deployed z position. The black open circles show the values for ^{252}Cf data, red bullets represent the results for the ^{252}Cf MC simulation.

factor and uncertainty computation. This source of uncertainty is, however, covered by the spill-in/out error, leading to a double counting of uncertainties. Since the spill-out is only affecting the Gd-fraction component of the total efficiency, the MC correction definition from Eq. (5.15) including the semi-inclusive efficiency will be used in the following way: the volume-wide efficiency correction is estimated by the semi-inclusive efficiency, which is due to the 3.5 to 10 MeV cut in the denominator selective for Gd captures and hence Target events[7]. The Gd-fraction correction will be separately measured at the Target center. The combined neutron detection dependent MC correction can then be expressed as

$$c_{\mathrm{MC,det}} = \frac{\varepsilon_{\mathrm{v,semi}}^{\mathrm{Data}}}{\varepsilon_{\mathrm{v,semi}}^{\mathrm{MC}}} \cdot \frac{(f_{\mathrm{Gd}}^{\mathrm{Data}})|_{(x,y,z)=(0,0,0)}}{(f_{\mathrm{Gd}}^{\mathrm{MC}})|_{(x,y,z)=(0,0,0)}} = c_{\mathrm{v}} \cdot c_{\mathrm{Gd,\odot}} , \qquad (5.36)$$

with the circled dot $\odot$ meaning "Target center".

The computation of $\varepsilon_{\mathrm{v,semi}}$ is for a neutron source which is evenly distributed over the full volume, like the IBD neutrons, rather straightforward. For the ^{252}Cf calibration data an analysis method is needed, which makes use of the different deployment data locations.

The neutron detection response in the DC scintillator liquids exhibits properties which could lead to a z-ρ symmetry in the detection efficiency inside the cylindrical Target volume. The mean free path traveled by the neutrons is of the order $\mathcal{O}(10\,\mathrm{mm})$ and thus notably smaller than the geometrical dimensions of the Target vessel with a height of roughly 2.5 m and a diameter of about 2.3 m. Neutrons detected in the Gd-channel induce per neutron capture on average the emission of about 4-5 gammas of similar energy, smearing geometrically induced discrepancies in the E_{delayed} efficiency and position reconstruction. The absolute gamma peak response is homogeneous in space after uniformity correction with the energy maps [6, 12]. Based on these facts the conclusion is drawn that the efficiency might decrease following the same functional form, no matter whether the neutron source approaches the approximatively flat Target top or the bended side walls. Data to MC discrepancies at the top or bottom of the Target

---

[7]Along with a small fraction of ^{12}C captures from both Target and gamma catcher volume.

are then assumed to be of the same magnitude as in the ρ-direction.

Any detection efficiency inside the Target will be assumed to follow the parametrization

$$\varepsilon(z, \rho) = \varepsilon_\odot \cdot f_1(z) \cdot f_2(\rho). \tag{5.37}$$

The efficiency at any position (z, ρ) in the Target is supposed to be formed by the product of the efficiency at the Target center $\varepsilon_\odot$ with the two efficiency shape functions $f_1(z)$ and $f_2(\rho)$. The term $f_1(z)$ represents the efficiency shape function along the Target symmetry axis ($\rho = 0$) as a function of z. In the same way describes the $f_2(\rho)$ the isolated efficiency shape function for $z = 0$ along ρ. Equation (5.37) postulates therefore independence of $\varepsilon(z, \rho)$ in z and ρ. If Eq. (5.37) holds the volume-wide efficiency ε_v can be computed via

$$\varepsilon_\mathrm{v} = \frac{\iint_{V_\mathrm{t}} \varepsilon(z, \rho) \, \rho \, \mathrm{d}\rho \, \mathrm{d}z}{\iint_{V_\mathrm{t}} \rho \, \mathrm{d}\rho \, \mathrm{d}z} = \varepsilon_\odot \cdot f_z \cdot f_\rho, \tag{5.38}$$

where f_z and f_ρ denote the mean isolated efficiency reduction in z- and ρ-direction, respectively.

The mean efficiency reductions f_z and f_ρ are estimated using the *sampling method*, described in [198]. The sampling method resembles the computation of a mean value, for the space between two deployment runs the linear interpolation of the measured values is used. This method is adapted to fit our needs: the ρ and z-shape curves have to be sampled differently to account for the correct volume weighting. In other words, the efficiency shape function $f_1(z)$ along the Target symmetry axis has to be sampled equidistant when computing the mean. If we define $f_{z,i}$ to be the ith sampling point out of $N+1$ along the z-shape and Δz the constant sampling distance, the mean value f_z is given by

$$f_z = \frac{\int_0^{h_\mathrm{t}} f_1(z') \, \mathrm{d}z'}{\int_0^{h_\mathrm{t}} \mathrm{d}z'} = \frac{1}{N} \sum_{i=0}^{N} f_1(i \cdot \Delta z). \tag{5.39}$$

Similarly will $f_{\rho,i}$ represent the ith sampling point of the ρ-shape and the mean value

$$f_\rho = \frac{\int_0^{\rho_\mathrm{t}} f_2(\rho') \, \rho' \, \mathrm{d}\rho'}{\int_0^{\rho_\mathrm{t}} \rho' \, \mathrm{d}\rho'} = \frac{1}{N \cdot \frac{1}{2}\rho_\mathrm{t}} \sum_{i=0}^{N} \left(i \cdot \Delta\rho \cdot f_2(i \cdot \Delta\rho)\right) \tag{5.40}$$

is computed by weighting the $f_{\rho,i}$ with ρ, where Target radius is given by ρ_t, the constant sampling distance by $\Delta\rho$ and the number of sampling points by $N+1 = (\rho_\mathrm{t}/\Delta\rho) + 1$. The same result can be achieved by sampling of the $f_{\rho,i}$ from 0 to ρ_t in square root like decreasing distances:

$$f_\rho = \int_0^{\rho_\mathrm{t}^2} f_2(\sqrt{x}) \frac{1}{\rho_\mathrm{t}^2} \, \mathrm{d}x = \frac{1}{N} \sum_{i=0}^{N} f_2(\sqrt{i \cdot \Delta x}). \tag{5.41}$$

For a fixed sampling distance Δx then number of sampling points is then computed via $N+1 = (\rho_\mathrm{t}^2/\Delta x) + 1$. Following Eq. (5.40) or Eq. (5.41) the ρ-behavior far from the Target center is weighted stronger, corresponding to the increase in the number of IBD reactions.

Before the upper equations are used to calculate the volume-wide efficiencies and with
those the correction factor in Section 5.3.2, the proposed assumptions will be studied
in Section 5.3.1 using MC simulation data. First, the independence of the efficiency
behavior with respect to z and ρ needs to be proven. If this is the case, it can be
tested whether the ρ-behavior can be derived from the z-behavior according to MC
data. Provided that Eq. (5.37) and (5.38) can be verified, the ^{252}Cf z-axis data can
be used to extrapolate the z-behavior to the full volume, and the border effects in z
and ρ are taken to be fully correlated. The volume-wide efficiency is then estimated
using ^{252}Cf data as input solely, without any further constraints from MC data on the
weighting of the individual deployment runs.

The systematic uncertainties of this method are investigated in Section 5.3.3, while
Section 5.3.4 will briefly summarize the results of a study using IBD neutrons for MC
correction estimation (further described in [89]) and compare them to the ^{252}Cf mea-
surements. The IBD neutron results and the ^{252}Cf values are then combined to a final
result in Section 5.6.

5.3.1 Target-wide MC studies

This subsection will deal with the computation of the volume-wide efficiency by means
of antineutrino MC data, based on information about the efficiency behavior along the
Target symmetry axis. The MC data sample meets the requirements for this study,
the IBD reactions are evenly distributed over the full detector volume and offers high
statistics with 4.37×10^6 events in the Target. Furthermore, true information about
the position of IBD reaction or neutron capture can be retrieved.

In the first step Eq. (5.38) will be tested. Afterwards, the efficiency shapes in z and
ρ will be studied, along with the sampling methods of Eq. (5.39) and (5.41). Finally
the possibility to compute the volume-wide efficiency using z-information solely is in-
vestigated. The analyses presented in the following make use of the semi-inclusive effi-
ciency definition, given in Eq. (5.11). Similar studies using the inclusive, semi-inclusive,
E_{delayed} as well as the ΔT efficiency have been performed with half the MC statistics
and the DC-II cuts [125], drawing the same conclusions as given here. The systematic
uncertainty estimation of this analysis method will be described in Section 5.3.3.
Information on the data labels used can be found in Appendix A.1.

Efficiency factorization in z and ρ

Whether the efficiency can be factorized by means of Eq. (5.38) suggesting independence
in z and ρ is investigated by calculation of the isolated efficiencies ε_z for $\rho \approx 0$ and ε_ρ for
$z \approx 0$. In general, only IBD events consistent with the DC-III selection and occurring in
the Target are taken into account. Further constraints on the semi-inclusive definition
are therefore

- the prompt energy E_{p} has to satisfy $0.5 > E_{\text{p}} > 20\,\text{MeV}$

- the IBD reaction has to occur inside the Target volume

- the neutron capture position has to be inside the Target volume

- the chimney region is not included in the analysis ($z < 1274.54\,\text{mm}$)
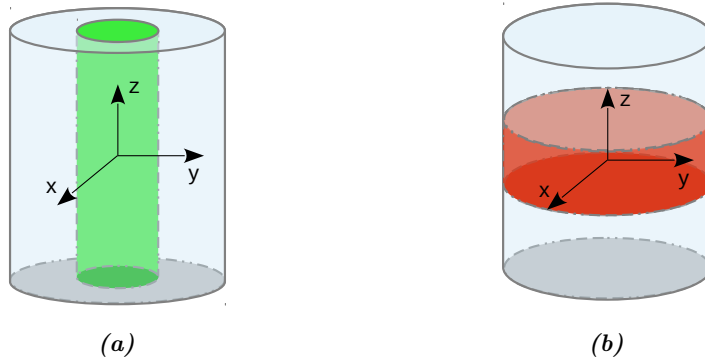
Figure 5.6: Sub-sample selections to compute the isolated efficiencies $\varepsilon_z(\rho_{\mathrm{IBD}} < r_{\mathrm{cylinder}})$ and $\varepsilon_\rho(|z_{\mathrm{IBD}}| < h_{\mathrm{disk}}/2)$. ***a)*** Sub-sample selection in an inner cylinder with radius r_{cylinder} to compute the isolated efficiency ε_z. ***b)*** Sub-sample selection in a disk-shaped sub-volume with height h_{disk} to compute the isolated efficiency ε_ρ.

The z and ρ factorization is now tested by calculation of the detection efficiency at the Target center $\varepsilon_\odot$ and the two efficiency reduction factors f_z and f_ρ. The latter two are computed using the isolated efficiencies in z and ρ-direction via

$$f_z(r_{\mathrm{cylinder}}) = \frac{\varepsilon(\rho_{\mathrm{IBD}} < r_{\mathrm{cylinder}})}{\varepsilon_\odot(\rho_{\mathrm{IBD}} < r_{\mathrm{cylinder}} \,\cap\, |z_{\mathrm{IBD}}| < 300\,\mathrm{mm})} \tag{5.42}$$

and

$$f_\rho(h_{\mathrm{disk}}) = \frac{\varepsilon(|z_{\mathrm{IBD}}| < h_{\mathrm{disk}}/2)}{\varepsilon_\odot(|z_{\mathrm{IBD}}| < h_{\mathrm{disk}}/2 \,\cap\, \rho_{\mathrm{IBD}} < 300\,\mathrm{mm})} \,, \tag{5.43}$$

where z_{IBD} and ρ_{IBD} are the coordinates of the IBD true vertex position, the constraints on them, given by r_{cylinder} and h_{disk}, are described below. From the events inside sub-cylinders as illustrated in Fig. 5.6 the mean efficiency in z-direction is separated from the influence of the efficiency loss in ρ-direction and vice versa. The vertex cuts are only imposed on the IBD true position, e.g. the location of neutron origin. Inner cylinders placed along the symmetry axis like the one in Fig. 5.6a contain the samples for ε_z computation. Disk-shaped cylinders with center at $z = 0$ and a radius of $r_{\mathrm{disk}} = r_{\mathrm{Target}}$ as shown in Fig. 5.6b are used to retrieve the subsample for calculation of ε_ρ. The radii r_{cylinder} of the cylinders for ε_z estimation and half the heights of the disks $h_{\mathrm{disk}}/2$ for ε_ρ calculation are varied in steps of 10 cm. The efficiency at the Target center $\varepsilon_\odot$ is calculated for the vertex cuts of the IBD true position $|z_{\mathrm{IBD}}| < 300\,\mathrm{mm}$ and $\rho_{\mathrm{IBD}} < 300\,\mathrm{mm}$. Table 5.3 summarizes the results of the efficiency reductions f_z and f_ρ and the product of these two factors with $\varepsilon_\odot = (0.9906 \pm 0.0004)$ to yield a volume-wide efficiency estimator ε_{v} for the different sub-volume heights h_{disk} and radii r_{cylinder}. The last column contains the discrepancy of the estimate ε_{v} to the detection efficiency $\varepsilon_{\mathrm{Target}} = (0.9844 \pm 0.0001)$ computed using the full Target sample. The quantities in Eq. (5.42), (5.43) and (5.38) are considered as statistical correlated or uncorrelated depending on the overlap in the respective sub-samples.

From the results in Table 5.3 we can see that the different estimates of ε_{v} and the efficiency $\varepsilon_{\mathrm{Target}}$ of the full Target sample agree within statistical uncertainties. The negligibly small discrepancies between the two quantities suggest that the full Target efficiency can be estimated using the information of inner sub-volumes. Furthermore it can be concluded that the efficiency shows an independent behavior in z and ρ.

Table 5.3: Computation of the efficiency estimate ε_{v} via Eq. (5.38) using sub-sample information in the Target. The last column contains the discrepancy of ε_{v} to the detection efficiency $\varepsilon_{\mathrm{Target}} = (0.9844 \pm 0.0001)$ computed using the full Target sample. h is the half disk height $h_{\mathrm{disk}}/2$, r is the sub-cylinder radius r_{cylinder}. The term "full" in the first column denotes that the full Target was used. The efficiency at Target center is $\varepsilon_{\odot} = (0.9906 \pm 0.0004)$.

h, r	f_z	f_ρ	$\varepsilon_{\mathrm{v}} = f_z \cdot f_\rho \cdot \varepsilon_{\odot}$	discr. [%]
200 mm	0.9983 ± 0.0003	0.9955 ± 0.0005	0.9845 ± 0.0008	0.01 ± 0.08
300 mm	0.9981 ± 0.0005	0.9957 ± 0.0005	0.9844 ± 0.0005	0.002 ± 0.046
400 mm	0.9980 ± 0.0004	0.9953 ± 0.0004	0.9841 ± 0.0003	0.04 ± 0.03
500 mm	0.9981 ± 0.0003	0.9956 ± 0.0004	0.9843 ± 0.0003	0.01 ± 0.03
600 mm	0.9980 ± 0.0003	0.9955 ± 0.0003	0.9842 ± 0.0006	0.02 ± 0.05
full	0.9981 ± 0.0002	0.9957 ± 0.0003	0.9844 ± 0.0005	0.002 ± 0.041

Efficiency estimation using z information

In order to investigate how the lack of calibration data in ρ-direction can be overcome using data in z, the behavior of the efficiency shape is studied as a function of z and ρ. First of all, the efficiency shape in each dimension is isolated from the other. This is achieved by the selection of sub-volumes as shown in Fig. 5.6. The radius of the inner cylinder to separate ε_z as well as the height of the disk for ε_ρ separation were set to $r_{\mathrm{cylinder}} = h_{\mathrm{disk}}/2 = 300$ mm. Then, the two samples are further subdivided in smaller slices and hollow cylinders as illustrated in Fig. 5.7. Each slice height Δh and hollow cylinder thickness is chosen such that most of the sub-volumes are of equal size for the ε_z and ε_ρ sample respectively. The efficiency in each subdivision is then plotted as a function of the relative distance of its center of mass to the Target wall. In z-direction this distance for every point i is basically given by

$$\hat{z}_i = 1 - \frac{|z_{\mathrm{CM},i}|}{\frac{1}{2}h_{\mathrm{Target}}} = 1 - \frac{|z_{\mathrm{CM},i}|}{1274.54\,\mathrm{mm}} , \qquad (5.44)$$

while close to the slightly cone shaped top and bottom walls the shortest distance perpendicular to the acrylic wall d is used, which is converted to $\hat{d} = d/1274.54\,\mathrm{mm}$. In the direction of the coordinate ρ the relative distance to the Target wall is

$$\hat{\rho}_i = 1 - \frac{\rho_{\mathrm{CM},i}}{\rho_{\mathrm{Target}}} = 1 - \frac{\rho_{\mathrm{CM},i}}{1150\,\mathrm{mm}} , \qquad (5.45)$$

where the center of mass position is computed via $\rho_{\mathrm{CM}}^2 = \frac{1}{2}(r_{\mathrm{inner}}^2 + r_{\mathrm{outer}}^2)$ with the inner radius r_{inner}^2 and outer radius r_{outer}^2 of the hollow cylinder. A value of $\hat{z} = 1$ or $\hat{\rho} = 1$ corresponds then to the Target center, whereas $\hat{z} = 0$ or $\hat{\rho} = 0$ is reached at the Target wall. The efficiencies $\varepsilon_z(\hat{z}_i)$ and $\varepsilon_\rho(\hat{\rho}_i)$ are then converted into the efficiency shape functions $f_1(\hat{z}) = \varepsilon_z(\hat{z}_i)/\varepsilon_{\odot}$ and $f_2(\hat{\rho}) = \varepsilon_\rho(\hat{\rho}_i)/\varepsilon_{\odot}$.

The plots in Fig. 5.8 show the isolated efficiency shape functions $f_1(\hat{z})$ for the top and bottom volume of the Target separately and $f_2(\hat{\rho})$. Top and bottom z-information is merged into one z-shape in Fig. 5.9. The agreement of both $f_1(\hat{z})$ and $f_2(\hat{\rho})$ is good within uncertainties. Any discrepancies for $\hat{z} < 0$ or $\hat{\rho} < 0$ is not relevant, as the volume-wide efficiency is estimated using only the range from 0 to 1. Further MC efficiency shapes for the exclusive and inclusive efficiencies can be found in Appendix D.1.

(a)   *(b)*
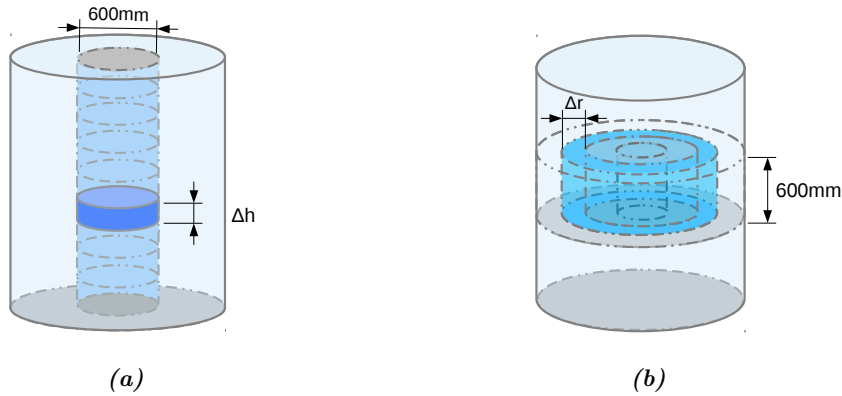
Figure 5.7: Division of the ε_z and ε_ρ samples from Fig. 5.6 in sub-samples. **a)** Subdivision of the inner cylinder in slices of height Δh. **b)** Subdivision of the inner cylinder in hollow cylinders with varying thickness $\Delta \rho$.

Table 5.4: "True" values obtained from the full Target volume or sub-samples. f_z, f_ρ and $\varepsilon_\odot$ are computed for the sub-volume cuts: $r_{\text{cylinder}} = h_{\text{disk}}/2 = 300\,\text{mm}$. The uncertainties are statistical.

parameter	value
f_z	0.9981 ± 0.0005
f_ρ	0.9957 ± 0.0005
$\varepsilon_\odot$	0.9906 ± 0.0004
ε_{v}	0.9844 ± 0.0001

The efficiency curves of Fig. 5.9 are now used to estimate the full Target efficiency. The computation of f_z and f_ρ is effectively the estimation of the mean value of the shape curves $f_1(\hat{z})$ and $f_2(\hat{\rho})$, as described in Eq. (5.39) to (5.41). To do this, the interpolated graphs are sampled at 9000 points. The statistical uncertainty is estimated from variation of the graphs' data points within their statistical uncertainty. In the first step each data point is varied within uncertainties and subsequently the mean value f_z or f_ρ is calculated. This process is repeated 5000 times, yielding a Gaussian shaped distribution for f_z and f_ρ. The mean value of these distributions are used as central value, the standard deviation is taken as the statistical uncertainty.

The results of f_z, f_ρ and the volume-wide efficiency ε_{v} are given in Table 5.5. There, the mean values for f_z and f_ρ from shape integration are presented along with the discrepancy to the "true" values from analysis of the undivided sample (cf. Table 5.4). The value of f_ρ is not only estimated using the ρ shape $f_2(\hat{\rho})$, but also computed from the z efficiency curve $f_1(z)$. We can see that mean value calculation from the efficiency shapes results in slightly lower values. Nevertheless the f_z factor can be reproduced with an accuracy of $\sim 0.1\,\%$. Likewise the value of f_ρ was reproduced within $\sim 0.1\,\%$ using either the ρ or z shape. The volume-wide efficiency estimate agrees within $(0.17 \pm 0.09)\,\%$ with the actual full volume efficiency.

Table 5.5: Efficiency reduction factors f_z and f_ρ as well as the volume-wide efficiency estimates computed from efficiency shape integration (see Eq. (5.39) to (5.41)) using $\varepsilon_\odot = 0.9906 \pm 0.0004$. The last column contains the discrepancy to the "true" values in Table 5.4. The bold numbers are received using z information solely. The uncertainties are statistical, correlations are taken into account.

parameter	value	discrepancy to "true" [%]
f_z	0.9973 ± 0.0006	0.09 ± 0.05
f_ρ from z-shape	0.9948 ± 0.0006	0.09 ± 0.05
$f_z \cdot f_\rho \cdot \varepsilon_\odot$	$\mathbf{0.9827 \pm 0.0007}$	$\mathbf{0.17 \pm 0.07}$
f_ρ from ρ-shape	0.9948 ± 0.0005	0.08 ± 0.02
$f_z \cdot f_\rho \cdot \varepsilon_\odot$	0.9828 ± 0.0006	0.17 ± 0.06

(a) *(b)* Zoom of figure (a).
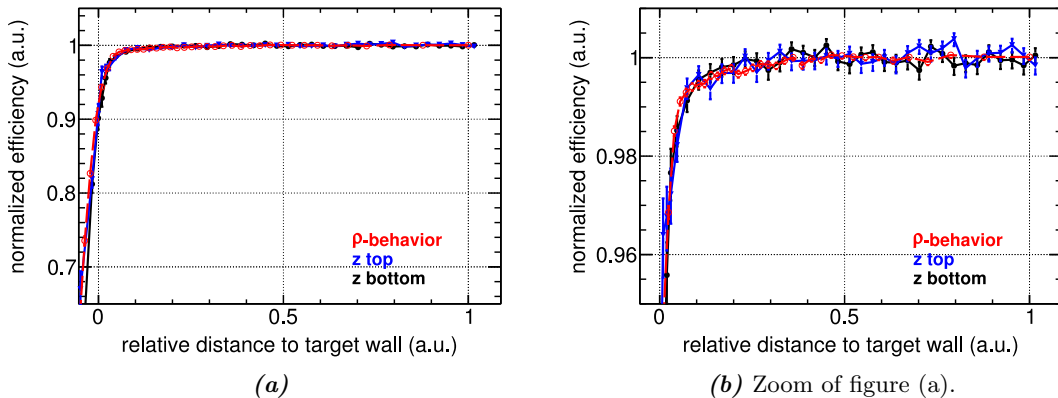
Figure 5.8: Efficiency shape functions of the semi-inclusive efficiency. $f_1(\hat{z})$ is given for the top and bottom volume of the Target separately. The red open circles connected by the dashed red lines represent the ρ-shape $f_2(\hat{\rho})$. The blue triangles show the z-shape $f_1(\hat{z})$ for the Target top data, while the black bullets show the z-shape $f_1(\hat{z})$ for the Target bottom.

(a) *(b)* Zoom of figure (a).
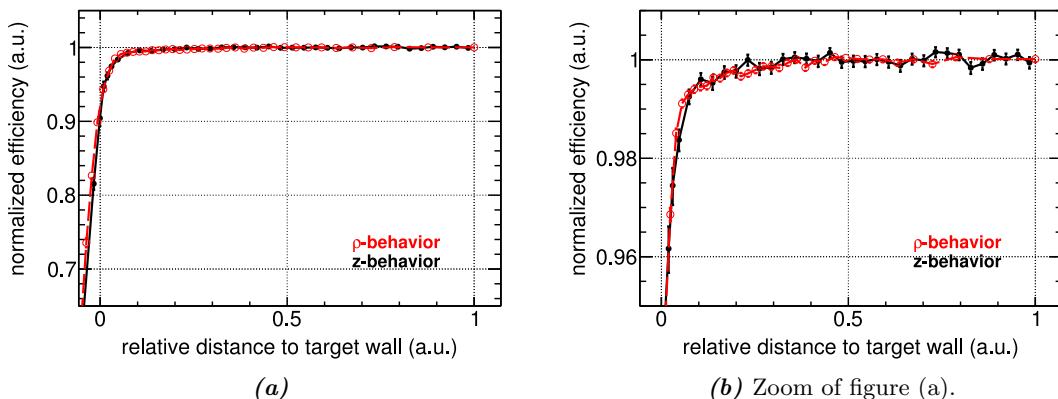
Figure 5.9: Efficiency shape functions $f_1(\hat{z})$ and $f_2(\hat{\rho})$ of the semi-inclusive efficiency. The top and bottom z data was combined in one shape. The red open circles connected by the dashed red lines represent the ρ-shape $f_2(\hat{\rho})$. The black bullets show the z-shape $f_1(\hat{z})$.

Conclusion

The MC data analysis studies demonstrated that the efficiency $\varepsilon(z, \rho)$ exhibits an independent behavior in z and ρ, as shown by the results in Table 5.3. The mean efficiency reduction factors f_z and f_ρ were reproduced from the efficiency shapes using the *sampling method* with an accuracy of $\sim 0.1\,\%$. Using these results, the full volume efficiency estimate agreed with the actual Target-wide efficiency within $(0.17 \pm 0.09)\,\%$. Furthermore it was shown that it is possible to infer an estimate for the ρ-shape from the z-efficiency shape.

5.3.2 ^{252}Cf data analysis

In this subsection the computation of the volume-wide efficiency and its MC correction by means of the ^{252}Cf calibration data is discussed. This is realized using the same techniques as described in Section 5.3.1, based on Eq. (5.38) to (5.41). The used data labels are given in Appendix A.1.

The fission event selection is carried out as explained in Section 4.1.2, background reduction cuts are by default the requirements $E_{\mathrm{prompt}} > 4\,\mathrm{MeV}$ and multiplicity $m > 1$ (cf. Section 4.3.2) and remaining accidental background is subtracted using an off-time window selection (see Section 4.3.1).

Out of three calibration campaigns the first two are considered for calibration purposes, as the third calibration campaign is not part of the official DC-III data set. The second calibration campaign features runs at 28 different deployment positions compared to in total 16 for the first campaign. Although the source activity had decreased in the time period between the first two calibrations, the second campaign offers slightly more statistics, due to extended deployment times. The second calibration campaign runs will therefore be used to compute the MC correction factor of the detection efficiency and its uncertainty, whereas the first campaign results will serve as crosscheck of the time stability. A list of the runs used for the analysis described in the following can be found in Appendix B.

As a first crosscheck, the comparison of the volume-wide efficiency ε_v for both MC simulations of IBD and ^{252}Cf fission neutrons are presented in Table 5.6, together with the parameters used for the ε_v calculation. Details on ε_v computation with ^{252}Cf z-axis data can be found below. For the antineutrino MC data the f_z and f_ρ values of Table 5.3 as well as the shape integration results are given. Despite the large difference in neutron kinetic energy, a good agreement between the IBD and ^{252}Cf neutron results can be discovered in general. The energy loss of the fission neutrons to reach the intermediate energies of IBD neutrons is a fast process and seems to have negligible impact on the detection efficiency, as indicated by the MC simulation. Discrepancies are observed for the ^{252}Cf reconstructed and the neutrino MC full volume ε_v, but these discrepancies are well covered by the systematic uncertainty of the method as we will later see in Section 5.3.3.

The definition of the semi-inclusive efficiency used by the DC-III analysis is given by

$$\varepsilon_{\mathrm{semi}} = \frac{N(4 < E_{\mathrm{delayed}} < 10\,\mathrm{MeV} \ \cap \ \Delta R < 1\,\mathrm{m} \ \cap \ 0.5 < \Delta T < 150\,\mu\mathrm{s})}{N(3.5 < E_{\mathrm{delayed}} < 10\,\mathrm{MeV} \ \cap \ 0.25 < \Delta T < 1000\,\mu\mathrm{s})} \ . \tag{5.46}$$

Table 5.6: Crosscheck of the volume-wide efficiency ε_v and related parameters for MC simulation data of IBD and ^{252}Cf fission neutrons. For the IBD neutrons the sampling results are given as well. The ^{252}Cf values were computed using the z-axis MC simulation runs of the second calibration campaign. The last column shows the discrepancy between the IBD and ^{252}Cf results. Uncertainties are statistical.

parameter	IBD-MC	^{252}Cf-MC	discrepancy [%]
$\varepsilon_\odot$	0.9906 ± 0.0004	0.9908 ± 0.0002	0.02 ± 0.05
f_z	0.9981 ± 0.0005	0.9969 ± 0.0002	0.12 ± 0.06
f_z (sampling)	0.9973 ± 0.0006		0.04 ± 0.07
f_ρ	0.9957 ± 0.0005	0.9947 ± 0.0002	0.10 ± 0.06
f_ρ (sampling)	0.9948 ± 0.0006		0.01 ± 0.07
ε_v	0.9844 ± 0.0001	0.9826 ± 0.0003	0.18 ± 0.04
ε_v (sampling)	0.9828 ± 0.0006		0.02 ± 0.07
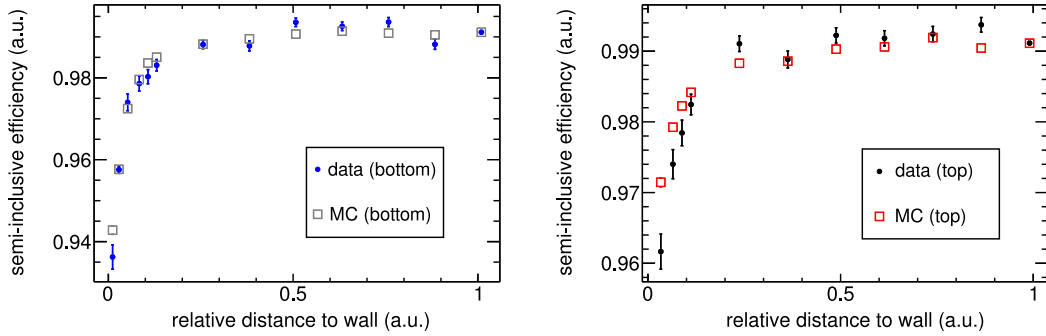
(a) Semi-inclusive bottom ($z_{\text{calib}} \leq 0$) shape. The data results are given by the blue bullets, the MC values by the gray open boxes.

(b) Semi-inclusive top ($z_{\text{calib}} \geq 0$) shape. The data results are given by the black bullets, the MC simulation values by the red open boxes.

Figure 5.10: Semi-inclusive efficiency shapes as a function of the relative distance to wall. The z-axis top ($z_{\text{calib}} \geq 0$) and bottom ($z_{\text{calib}} \leq 0$) data is plotted separately, the MC simulation values are multiplied with the correction c_v from Table 5.9. The uncertainties are statistical, a position dependent uncertainty is not included.

Compared to the definition of Eq. (5.11) a lower ΔT cut in the denominator was included for consistency reasons with other efficiency analysis (e.g. using IBD neutrons, as briefly discussed in Section 5.3.4) and has a negligible effect on the results.

Figure 5.10 shows the semi-inclusive efficiency shapes for the z-axis ^{252}Cf calibration data as a function of the relative distance to the Target wall. The z shapes in the left plot represent the Target top data with deployment positions $z_{\text{calib}} \geq 0$, the right plot shows the Target bottom data with $z_{\text{calib}} \leq 0$. The MC simulated efficiency points were already multiplied with the volume-wide efficiency correction calculated in the following.
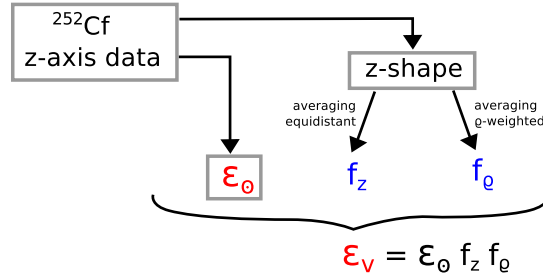
Figure 5.11: Chart of the volume-wide efficiency ε_v computation using the ^{252}Cf z-deployment information only.

The volume-wide efficiency ε_v computation is similar to the one described in the previous section and sketched in Fig. 5.11. The efficiency reduction f_z and f_ρ with respect to the Target center are computed by computation of a weighted mean of the z efficiency shape via Eq. (5.38) and (5.41). The interpolated top and bottom efficiency graphs are each sampled at 9000 points and their mean values are combined afterwards. As for the lowest deployment position the source's center of activity was placed with $z_{\mathrm{calib}} = -1260\,\mathrm{mm}$ roughly $1.4\,\mathrm{mm}$ above the Target bottom lid, the full volume efficiency estimate does not include the outer $1.4\,\mathrm{cm}$ in the z-direction and the outer $1.3\,\mathrm{cm}$ in the ρ-direction. In total $> 98\,\%$ of the Target volume should be covered by the data points and their interpolation. Both reduction factors f_z and f_ρ are extracted from the z efficiency shape and form multiplied with the efficiency at the Target center $\varepsilon_\odot$ the volume-wide efficiency estimate ε_v. The statistical uncertainty is computed by variation of the data points within their uncertainties. Each data point is varied, the volume-wide efficiencies ε_v for data and MC as well as the MC correction c_v recomputed and the values finally filled in histograms. After 5000 repetitions the histograms' mean values are used as central values, the standard deviations are taken as uncertainties. Correlations between the reduction factors f_z and f_ρ and the center efficiency $\varepsilon_\odot$ are taken into account. The volume-wide MC correction for the semi-inclusive or any other efficiency is at the same time calculated as in Eq. (5.35) and (5.36) from the ratio of data and MC:

$$c_v = \frac{(\varepsilon_\odot \cdot f_z \cdot f_\rho)^{\mathrm{Data}}}{(\varepsilon_\odot \cdot f_z \cdot f_\rho)^{\mathrm{MC}}} \,. \tag{5.47}$$

As the calibration measurements at the Target center (with $z_{\mathrm{calib}} = 0$) are the most accurate and possess very high statistics, for comparison the center MC correction $c_\odot$ is computed via

$$c_\odot = \frac{(\varepsilon_\odot)^{\mathrm{Data}}}{(\varepsilon_\odot)^{\mathrm{MC}}} \,. \tag{5.48}$$

Results

As suggested in Section 5.2.2, the exclusive efficiency definitions could be used to see whether correlations between the different selection cuts or missed backgrounds exist. Table 5.7 summarizes the MC correction results for the semi-inclusive, the nested and the isolated exclusive efficiencies. The results for the MC correction at the Target center $c_\odot$ are in excellent agreement, not only for the central value, but also in the statistical uncertainty. In the Target-wide correction slight discrepancies are observed, while the

Table 5.7: Comparison of the center and volume-wide MC corrections using the semi-inclusive and different exclusive efficiency definitions. The uncertainties are statistical.

efficiency definition	$c_\odot$	c_v	discrepancy $(c_\mathrm{v} - c_\odot)$ [%]
semi-inclusive	1.0003 ± 0.0004	1.0003 ± 0.0007	0.003 ± 0.09
exclusive (nested)	1.0003 ± 0.0004	0.9999 ± 0.0007	0.04 ± 0.08
exclusive (isolated)	1.0003 ± 0.0004	1.0000 ± 0.0007	0.03 ± 0.08

Table 5.8: Comparison of the detection efficiency correction $c_\mathrm{MC,det}$ from inclusive, semi-inclusive and exclusive efficiency definition. The semi-inclusive and the exclusive efficiency corrections are multiplied with the Gd-fraction correction $c_\mathrm{Gd,\odot}$ of Table 5.1. The last column contains the discrepancy of the volume-wide and center correction. The uncertainties are statistical.

efficiency definition	$c_\odot$	c_v	discrepancy $(c_\mathrm{v} - c_\odot)$ [%]
inclusive	0.9755 ± 0.0012	0.9722 ± 0.0022	0.33 ± 0.29
semi-inc. $\times\, c_\mathrm{Gd,\odot}$	0.9753 ± 0.0011	0.9753 ± 0.0013	0.003 ± 0.088
exclusive $\times\, c_\mathrm{Gd,\odot}$	0.9753 ± 0.0011	0.9749 ± 0.0013	0.04 ± 0.08

cause for the difference is unclear. One possibility could be the circumstance that correlations become visible on the volume-wide scale. Nonetheless, all three measurements using different efficiency definitions lead to results of c_v consistent with unity, which corresponds to a data to MC agreement in the cut related detection efficiencies.

In the following it is tested whether exclusive, inclusive and semi-inclusive lead to the same results. The exclusive and semi-inclusive are multiplied with the Gd-fraction correction $c_\mathrm{Gd,\odot}$ given in Table 5.1. Good agreement is observed at the Target center, the $0.014\,\%$ discrepancy of the inclusive definition to the semi-inclusive or exclusive result can be explained by slight differences in the lower ΔT in the Gd-fraction calculation. The Volume-wide discrepancies to inclusive definition is not surprising, as this definition includes data to MC discrepancies in the spill-out fraction which can easily be introduced by slight deployment position mismatches.

To sum up, good agreement is found for all the correction factor results using different efficiency definitions. Discrepancies observed are negligible and for most of them the origin is understood. In case correlations in the different cut efficiencies exist, they are of negligible size and had no effect on the final MC correction result or uncertainty in the context of this analysis.
Owing to the improved DC-III candidate selection criteria consistent values were estimated for the center and the volume-wide MC correction. This result indicates that the new neutrino selection provides not only data to MC agreement in the detection efficiency at the Target center, at the same time data to MC efficiency discrepancies at the borders are removed. For the DC-II cuts a center to volume discrepancy of $(0.6 \pm 0.2)\,\%$ was evaluated [126].

(a) Semi-inclusive detection efficiency.

(b) Delayed energy cut detection efficiency.

(c) Correlation distance cut detection efficiency.

(d) Correlation time cut detection efficiency.
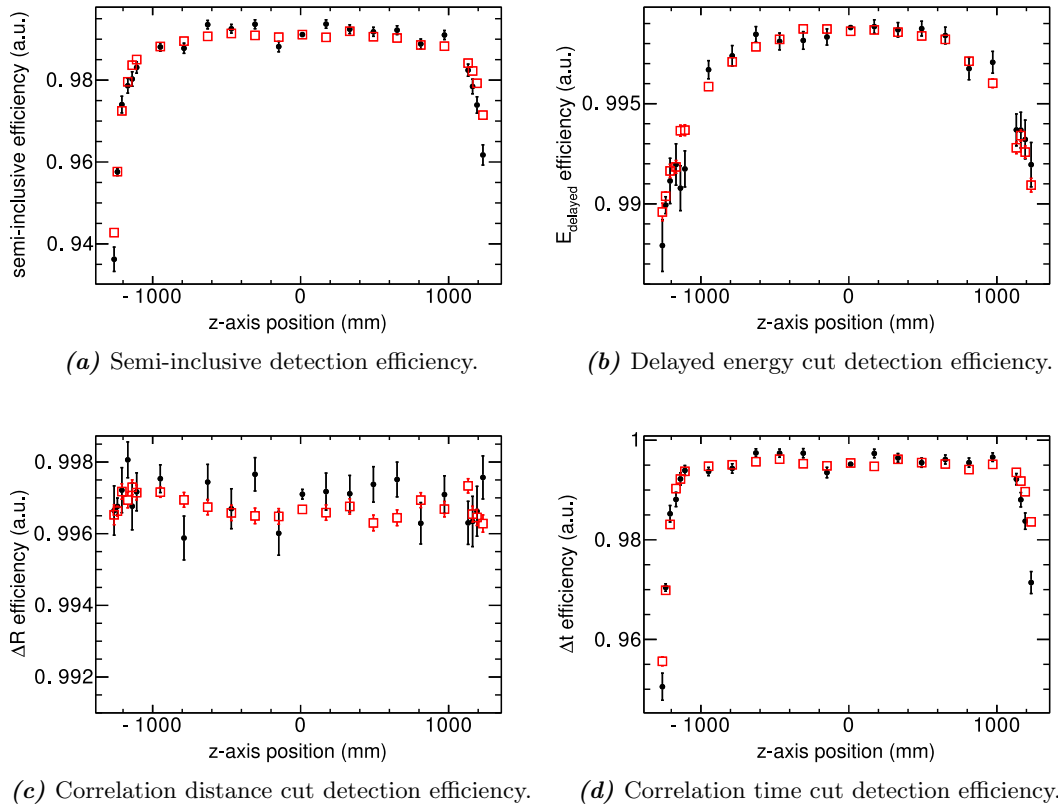
Figure 5.12: Data and MC selection efficiencies from ^{252}Cf calibration as a function of the theoretical deployed z-coordinate z_{calib}. The black bullets show the efficiency results of the ^{252}Cf data runs, the red open boxes the values from ^{252}Cf MC simulation. All uncertainties are statistical, a position dependent uncertainty is not included.

We close this section with the data and MC cut dependent efficiencies from ^{252}Cf calibration plotted as a function of the theoretical deployed z-coordinate z_{calib}. In Fig. 5.12 the semi-inclusive as well as the three cut efficiencies are shown independently. The MC efficiencies were corrected with the c_{v} values summarized in Table 5.9.
Further details on each data and MC efficiency as well as the correction factors can be found in Appendix D.2.

5.3.3 Systematic uncertainty estimation

The neutrino oscillation analysis requires a systematic uncertainty on the expected number of neutrinos as input. This systematic error is expected to cover the uncertainty on the MC correction factor, i.e. the uncertainty on how well the correction succeeds to bring the detection efficiencies of data and MC simulation into agreement. The volume-wide MC correction (cf. Eq. (5.35)) represents a global correction factor, this means that any global data to MC discrepancies are already compensated by it. Local fluctuations in the correction factor are in general not of interest in this context. The application of a global correction factor could, however, introduce a distortion on the prompt energy spectrum. This possible impact is therefore discussed in the end of this section.

Table 5.9: Target-wide MC correction c_v for the semi-inclusive and the different cut efficiencies. The exclusive efficiencies were computed using the nested efficiency definitions. All uncertainties are statistical.

efficiency definition	c_v
semi-inclusive	1.0003 ± 0.0007
E_delayed	1.0005 ± 0.0003
ΔR	1.0009 ± 0.0003
ΔT	0.9986 ± 0.0006

The systematic uncertainty requested in the final fit is rather the uncertainty on how well the global correction factor applied in the θ_{13} fit meets its true value. The approach is therefore to test the robustness of the MC correction c_v in the following. The different influences on the MC correction factor can be introduced by

1.) the MC model and it's parameters,

2.) the difference in ^{252}Cf and IBD neutron kinetic energy,

3.) spatial inhomogeneity and position dependency of the ^{252}Cf calibration,

4.) the ^{252}Cf fission event selection,

5.) time variation,

6.) the efficiency definitions,

7.) the volume-wide efficiency estimation method.

Each of these possible contributions will be studied below. We will see that all of them have negligible impact on the systematic error except for the last point: the volume-wide estimation method uncertainty.

1.) MC model dependent uncertainty

The neutron detection efficiency in the Double Chooz MC simulation can be altered by change of the parameters which have an influence on the neutron physics modeling. This can either be done by changing the neutron scattering model or by variation of the Gd-concentration, which modifies the effective neutron capture probability. The effect of a different neutron scattering model can only be tested indirectly, as discussed below. To test the latter case, the Gd-concentration could be actively altered and additional MC samples were produced: the input Gd-concentration parameter was varied $\pm 3\,\%$, which corresponds to the difference between the calculated value from weight measurement of $0.123\,\mathrm{wt.\,\%}$ and the lowest data point in the 1-sigma C.L. of a laboratory measurement performed at MPIK[8] of $(0.122 \pm 0.002)\,\mathrm{wt.\,\%}$ [61]. Besides the default concentration of $989\,\mathrm{mg/l}$ Gd-concentration [19], two data sets were prepared with $960\,\mathrm{mg/l}$, and $1020\,\mathrm{mg/l}$, respectively. The results for the volume-wide correction factor computed by means of the semi-inclusive efficiency definition are shown in Table 5.10. The discrepancies to the default value are smaller than $0.1\,\%$ and of the size of

---

[8]Max-Planck-Institut für Kernphysik, Heidelberg, Germany

Table 5.10: Volume-wide correction factor for different Gd-concentrations in the MC simulation. The value of 989 mg/l represents the default Gd-concentration from weight measurement [19].

Gd-concentration	c_{v}
960 mg/l	1.0011 ± 0.0008
989 mg/l	1.0003 ± 0.0007
1020 mg/l	0.9995 ± 0.0008

the statistical uncertainty. One might expect that an increase of the Gd-concentration leads to an enhancement of the neutron detection efficiency, mainly caused by a gain of ΔT cut efficiency at the borders. For a reduction of the relative amount of Gd atoms in the scintillator, the observed effect would then change the efficiency in the opposite direction. However, the variations in the semi-inclusive or especially in the ΔT cut efficiency are not significant. Besides that, any offset from the true value of the Gd-concentration, would be calibrated out by the MC correction.

In the context of the spill-in/out studies performed by A. Collin for the DC-III analysis [75], IBD neutron characteristics were studied using another neutron scattering MC simulation model, named **Tripoli-4**. **Tripoli-4** is known to provide a more realistic neutron modeling, better suited to low energy processes (further details can be found in Section 7.3).
In this analysis, the detection efficiencies related to the correction time cut were computed from a Target-wide IBD neutron sample for both, the DC-III and the **Tripoli-4** based MC simulation code. As the scintillator model and position reconstruction of Double Chooz was not implemented in the **Tripoli-4** analysis, only the ΔT efficiencies are compared. Assuming that the **Tripoli-4** code models the neutron scattering more realistically, a correction factor for the Double Chooz MC can be computed using the volume-wide efficiencies $\varepsilon_{\Delta T,\mathrm{v}}$ in the following way:

$$c_{\mathrm{v}}^{\mathrm{T4}} = \frac{(\varepsilon_{\Delta T,\mathrm{v}})^{\mathrm{T4}}}{(\varepsilon_{\Delta T,\mathrm{v}})^{\mathrm{DC\text{-}MC}}} \, . \tag{5.49}$$

In the upper formula DC-MC stands for the Double Chooz MC with **NeutronTh** expansion, while T4 denotes **Tripoli-4**. The evolution of the MC-MC correction given in Eq. (5.49) with respect to changing upper ΔT cuts is plotted in Fig. 5.13, along with the results from ^{252}Cf data analysis. For extended detection windows the correction factors increase, which corresponds to a decrease in the efficiency discrepancy. The same trend is observed in the ^{252}Cf results. Furthermore, the agreement with the MC-MC values is very good. These results constitute therefore a MC-based verification of the ^{252}Cf calibration analysis presented in the previous section.

2.) Neutron kinetic energy

The kinetic energy of the ^{252}Cf fission neutrons is with an average value of 2 MeV considerably higher than the kinetic energy of neutrons created in IBD reaction. Although the IBD neutron energies of tens of keV might be reached quickly by the source neutrons, the detection efficiency could be altered or, more importantly, the data to MC
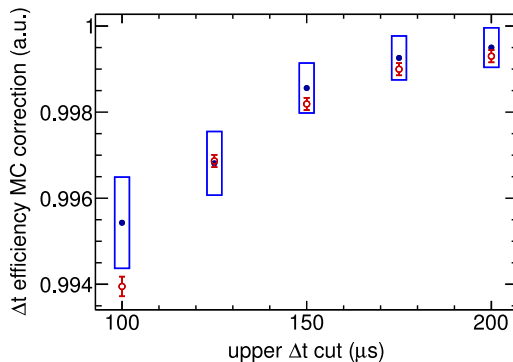
Figure 5.13: Evolution of the volume-wide MC correction factors $\varepsilon_{\Delta T,\mathrm{v}}$ of the correlation time cut efficiency with respect to changing upper time cuts. The red open circles show the Double Chooz MC to Tripoli-4 correction [75], while the blue bullets represent the ^{252}Cf results.

ratio of the detection efficiencies could change.

From the agreement of the efficiency results from official DC-III antineutrino and ^{252}Cf MC simulation given in Table 5.6 we would expect not to observe any energy dependent discrepancies in the detection efficiency for these two sources. Furthermore, the ΔT cut related correction estimated from ^{252}Cf was shown to match the MC-MC correction values based on IBD neutron kinetic energies (see Fig. 5.13). Still it is not possible to exclude the existence of a significant difference in the ^{252}Cf and IBD efficiencies from real detector data. Without a way to determine a plausible uncertainty on this problem, a neutron energy dependent uncertainty is not considered in the overall c_{v} error. However, the possibility exists to compare the ^{252}Cf results to a c_{v} measurement using an IBD neutron sample (see Section 5.3.4), which is an important crosscheck.

3.) Spatial inhomogeneity and position dependency

The volume-wide correction is tested for the existence of a spatial inhomogeneity in the Target volume by comparison of the results gained from the separate analysis of the top and bottom calibration data. The term "top data" refers to the deployment positions with $z_{\mathrm{calib}} > 0$, whereas "bottom data" is associated with the deployments at $z_{\mathrm{calib}} < 0$. Possible discrepancies could emerge as the calibration neutrons close to the Target top can be caught inside the chimney region, which could lead to larger efficiencies and a change in the data to MC agreement. In contrast to this, the detection efficiency at the Target bottom could suffer from the influence of the Target acrylic stilts.

In Section 4.2 it was shown that a systematic shift of roughly $7\,\mathrm{mm}$ was observed by comparison of the first and second calibration campaigns' deployment positions. To study the effect of a position shift on the c_{v} result, all data points were either shifted up or down by $10\,\mathrm{mm}$ simultaneously and the correction factor recomputed.

The results in Table 5.11 show that the discrepancies of the results from analyses with modified or restricted data sets yield variations compatible with the default value of (1.0003 ± 0.0007). The c_{v} value from bottom data analysis agrees with the default measurement using the full z-axis range. Furthermore, the top data result is compatible with the bottom value within statistical uncertainties.

Table 5.11: Volume-wide correction factor from analysis with shifted deployment runs or
using either the top ($z_{\text{calib}} > 0$) or bottom ($z_{\text{calib}} < 0$) data points. The discrepancy to the
default value (1.0003 ± 0.0007) from full z-axis range and no shift is given.

| analysis modification	c_{v}	discrepancy [%]
shift data 10 mm up	1.0003 ± 0.0008	< 0.001
shift data 10 mm down	1.0003 ± 0.0008	0.006
top data only	0.9997 ± 0.0009	0.07
bottom data only	1.0002 ± 0.0009	0.02

4.) ^{252}Cf fission event selection

As the ^{252}Cf data and MC samples contain different types and amounts of backgrounds,
the effectiveness of the background subtraction could have an influence on the MC
correction computation. Including all delayed event multiplicities of the ^{252}Cf selection
in the analysis yields a discrepancy of less than 0.01%, while for $m > 1$ and no
accidental subtraction the result changes only by 0.03%, as the largest fraction of
background consists of natural radioactivity and do not pass the 3.5 MeV energy cut
of the semi-inclusive wide sample selection. A different signal to background ratio in
the analysis sample can be achieved by relaxation of the selection cut on the ^{252}Cf
prompt event energy. With a prompt cut of $E_{\text{prompt}} > 0.5$ MeV the MC correction is
$c_{\text{v}} = (0.9997 \pm 0.0011)$ and changes by $(0.06 \pm 0.03)\%$. Hence the influence of the data
selection on the cut dependent MC correction result is expected to be negligible.

5.) Time stability

As the second calibration campaign data is analyzed to provide the ^{252}Cf reference
measurement of the MC correction, the stability of the results with respect to time
can be checked using the first campaign's data. The second calibration campaign was
conducted one year after the first campaign, right in the middle of the Gd-III data
taking period and features calibration runs with higher statistics. The first calibra-
tion yields a result of $c_{\text{v}} = 0.9984 \pm 0.0011$ which corresponds to a discrepancy of
$(0.19 \pm 0.13)\%$ between the two campaigns' measurements. Both results are in agree-
ment, while the discrepancy might not only be caused by a statistical fluctuation. From
the semi-inclusive efficiency shapes of the first campaign in Fig. 5.14 we can see that
less calibration positions were measured along the z-axis, especially close to the Target
top wall. There, the volume-wide estimation relys on the interpolation between the
two highest deployment points. Separate analyses of the top and bottom data show
that the first and second campaigns' bottom data results agree within $(0.06 \pm 0.15)\%$,
whereas the top volume values are off by $(0.27 \pm 0.15)\%$.

Time dependent fluctuations of the cut efficiency MC correction c_{v} exceeding the sta-
tistical fluctuations has not been observed in case of neither the full volume nor the
top and bottom separate analysis. Possible discrepancies due to the limited number of
calibration positions are covered by the uncertainty discussed in 7.).
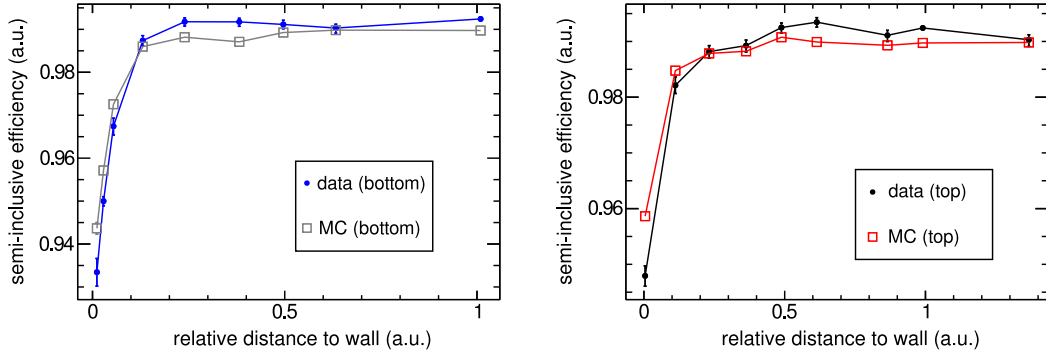
(a) Semi-inclusive bottom ($z_{calib} \leq 0$) shape. The data results are given by the blue bullets, the MC simulation values by the gray open boxes.

(b) Semi-inclusive top ($z_{calib} \geq 0$) shape. The data results are given by the black bullets, the MC simulation values by the red open boxes.

Figure 5.14: Semi-inclusive efficiency shapes as a function of the relative distance to wall for the ^{252}Cf first calibration campaign data. The z-axis top ($z_{calib} \geq 0$) and bottom ($z_{calib} \leq 0$) data is plotted separately, the MC simulation values are multiplied with $c_v = 0.9984$. The uncertainties are statistical, a position dependent uncertainty is not included.

6.) Efficiency definitions

Two sets of cuts are applied to selected the events in the enumerator and denominator of the efficiency estimate as given in Eq. (5.3). The cuts in the enumerator are defined by the selection criteria of the neutrino candidates, whereas the cuts in the denominator are chosen with the intention to cover the full accessible parameter space. The influence of these cuts is hence studied by variation of the selection windows:

- Neutrino selection cut dependent (enumerator sample)

  - Lower energy cut $E_{cut,low}$: $4\,\text{MeV} \rightarrow 3.5\,\text{MeV}$, $4.5\,\text{MeV}$
  - Lower correlation time cut ΔT_{min}: $0.5\,\mu\text{s} \rightarrow 1\,\mu\text{s}$, $2\,\mu\text{s}$
  - Upper correlation time cut ΔT_{max}: $150\,\mu\text{s} \rightarrow 125\,\mu\text{s}$, $175\,\mu\text{s}$
  - Correlation distance cut ΔR_{max}: $100\,\text{cm} \rightarrow 80\,\text{cm}$, $120\,\text{cm}$

- Efficiency definition dependent (denominator sample)

  - Lower energy threshold E_{th}: $3.5\,\text{MeV} \rightarrow 3\,\text{MeV}$
  - Upper time window cut t_{upper}: $1000\,\mu\text{s} \rightarrow 600\,\mu\text{s}$

The selection cut variations are for almost all results shown in Table 5.12 larger than the uncertainties on the respective observables. The largest discrepancies to the value from default efficiency definition are of $\sim 0.2\,\%$, and are caused by either a tighter ΔT_{max} or ΔR_{max} cut. The other discrepancies are smaller than $0.1\,\%$. It is therefore concluded that the exact choice of the enumerator as well as denominator cuts has negligible impact on the c_v result, as long as the variations of the threshold values are small (a few percent) with respect to the default set of cuts.

Table 5.12: Volume-wide correction factor for different cuts in the efficiency definition. The first eight results correspond to neutrino selection cut dependent variations and affect the enumerator sample. The lower two results are obtained from the change of denominator sample cuts. In the last column the discrepancy to the default result $c_{\mathrm{v}} = (1.0003 \pm 0.0007)$ is given.

varied cut	c_{v}	discrepancy [%]
$\Delta T_{\min} = 1\,\mu\mathrm{s}$	1.0007 ± 0.0008	0.03
$\Delta T_{\min} = 2\,\mu\mathrm{s}$	1.0013 ± 0.0010	0.1
$\Delta T_{\max} = 125\,\mu\mathrm{s}$	0.9986 ± 0.0009	0.18
$\Delta T_{\max} = 175\,\mu\mathrm{s}$	1.0011 ± 0.0007	0.07
$E_{\mathrm{cut}} = 3.5\,\mathrm{MeV}$	1.0005 ± 0.0007	0.02
$E_{\mathrm{cut}} = 4.5\,\mathrm{MeV}$	1.0000 ± 0.0008	0.03
$\Delta R_{\mathrm{cut}} = 0.8\,\mathrm{m}$	1.0023 ± 0.0009	0.2
$\Delta R_{\mathrm{cut}} = 1.2\,\mathrm{m}$	0.9997 ± 0.0007	0.07
$t_{\mathrm{upper}} = 600\,\mu\mathrm{s}$	1.0004 ± 0.0007	< 0.01
$E_{\mathrm{th}} = 3\,\mathrm{MeV}$	1.0011 ± 0.0008	0.08

7.) Volume-wide efficiency estimation

In this paragraph the contribution of the efficiency estimation method to the systematic uncertainty of the MC correction is studied. The method dependent uncertainty should therefore be a measure for how accurate the full volume efficiency can be reproduced by having point-wise information along the z-axis. In Section 5.3.1 it was shown that the full volume efficiency could be replicated with a discrepancy of $(0.17 \pm 0.07)\%$. This result is gained if all the MC data points of the graph in Fig. 5.15a are used. In order to imitate a scenario which meets the ^{252}Cf analysis conditions, the number of data points has to be reduced. The volume-wide efficiency estimate is therefore recomputed with MC data points randomly removed, whereas the number of data points kept in a certain region was fixed to the values given in Table 5.13. In Fig. 5.15a these regions are illustrated by gray bands, while the plot in Fig. 5.15b shows one example of a data set with reduced points. In total the mean relative discrepancy to the full volume efficiency from 5000 draws of reduced data sets was estimated to be 0.221%. As both the data and MC ^{252}Cf set of points is limited to the same number of deployment positions, the relative systematic uncertainty on the cut dependent MC correction amounts to

$$\frac{\Delta c_{\mathrm{v}}}{c_{\mathrm{v}}} = \sqrt{\left(\frac{\Delta \varepsilon_{\mathrm{v}}^{\mathrm{Data}}}{\varepsilon_{\mathrm{v}}^{\mathrm{Data}}}\right)^2 + \left(\frac{\Delta \varepsilon_{\mathrm{v}}^{\mathrm{MC}}}{\varepsilon_{\mathrm{v}}^{\mathrm{MC}}}\right)^2} = \sqrt{2 \cdot (0.221\,\%)^2} = 0.313\,\% \, .$$

Table 5.13: Number of allowed data points at a certain relative distance to Target wall for systematic uncertainty estimation (see also Fig. 5.15a.

relative distance to wall	number of data points
-0.01 − 0.15	5
0.15 − 0.199	0
0.199 − 0.3	2
0.3 − 0.5	4
> 0.5	10
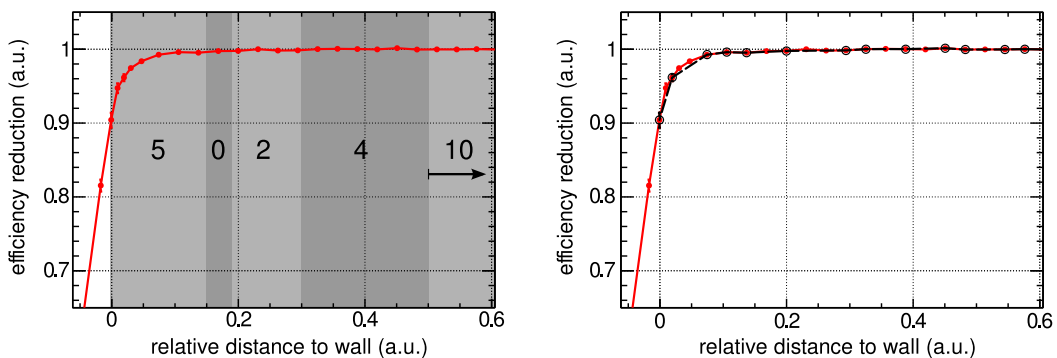
(a) Number of allowed data points at a certain relative distance to Target wall (see also Table 5.13).

(b) The red bullets (connected with a solid line) show the full set of MC points, the black empty points and dashed line is an example for a randomly chosen sample of reduced points.

Figure 5.15: Reduction of data points in the semi-inclusive efficiency shape for systematic uncertainty estimation.

Impact of a global efficiency correction on the prompt spectrum shape

The introduction of a volume-wide MC correction factor is supposed to eliminate data to MC discrepancies in the detection efficiency. The uncertainty on this correction represents a relative uncertainty on the neutrino rate and is treated as energy independent, as seen in Eq. (5.2). Owing to energy loss occurring close to the acrylic walls, the prompt visible energy spectrum exhibits a slightly different shape depending on the location of the IBD reaction. In case the MC correction would locally differ from the global value of c_v, the prompt MC spectrum could be distorted by the application of a global correction factor. Most of the local MC corrections factors computed with ^{252}Cf calibration data (Fig. 5.16) deviate from the global DC-III MC correction within less than 0.5 %. However, it is not straightforward to distinguish between statistical fluctuations and possible systematic local deviations or their impact on the prompt spectral shape.

In order to evaluate the degree of potential spectral distortions induced by a global correction factor, a MC-based study was performed. Since the prompt spectrum shape changes with respect to the distance from the Target center, the neutrino candidate MC sample was split in two sub-samples contained in an inner cylinder and its anti-
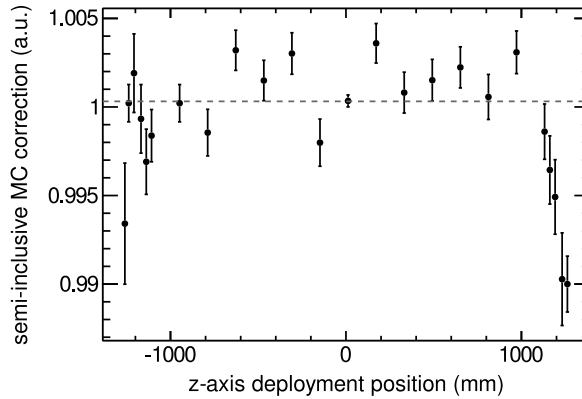
121

Figure 5.16: Local MC correction factors from ^{252}Cf calibration data as a function of the z-axis deployment position. The DC-III global $cv = 1.0003$ is marked by the gray dashed line.

selection (Fig. 5.17). The inner cylinder's dimensions are given by $|z| < z_{\text{limit}}$ and $\rho < (z_{\text{limit}} \cdot r_{\text{Target}} / \frac{1}{2} h_{\text{Target}})$, and the cuts were applied to the true IBD position. The choice of volume cut allows to compute an inner volume MC correction c_{inner} as well as the inner volume efficiencies $\varepsilon^{\text{x}}_{\text{inner}}$ (x = Data or MC) using the ^{252}Cf deployment points with $|z_{\text{calib}}| < z_{\text{limit}}$. The outer volume MC correction $\varepsilon^{\text{x}}_{\text{outer}}$ (x = Data or MC) is then given by

$$\varepsilon^{\text{x}}_{\text{outer}} = \frac{\varepsilon^{\text{x}}_{\text{v}} - \varepsilon^{\text{x}}_{\text{inner}} \cdot w_{\text{inner}}}{w_{\text{outer}}} \, , \tag{5.50}$$

with the volume proportion weighting factors $w_{\text{inner,outer}}$, with $w_{\text{inner}} + w_{\text{outer}} = 1$. The outer volume MC correction c_{outer} is consequently computed via $c_{\text{outer}} = \varepsilon^{\text{Data}}_{\text{outer}} / \varepsilon^{\text{MC}}_{\text{outer}}$. The globally corrected prompt spectrum $S(E)$ is then compared to the locally corrected one in each bin i, while the corrections $c_{\text{inner,outer}}$ are fluctuated within their uncertainties, which were assumed to be Gaussian distributed. For the relative discrepancy we yield

$$D_i = \frac{S^{\text{global}}_i - (S^{\text{inner}}_i \cdot c_{\text{inner}} + S^{\text{outer}}_i \cdot c_{\text{outer}})}{S^{\text{global}}_i} \, . \tag{5.51}$$

The discrepancy between the locally and the globally corrected spectra is well below 0.1 % over a wide energy range (cf. Fig. 5.18a-5.18d). For prompt energies smaller than 1 MeV the discrepancies are ~ 0.5 %. In this energy region the statistical uncertainty of the IBD candidate spectrum is on the level of several percent, making this deviation negligible. Above 1 MeV the average discrepancies are at (0.03 ± 0.12) % or lower and are therefore not taken into account in the final error budget.

Conclusion

The MC correction factor systematic uncertainty of the cut related neutron detection efficiency was studied taking into account contributions which could lead to possible biases of the corrected MC candidate rate and prompt spectral shape. The influence of a bias in the Gd-concentration on the neutron simulation modeling does not constitute a problem, as any discrepancy in the detection efficiency caused by it would be included in the MC correction computation and therefore calibrated out. The results
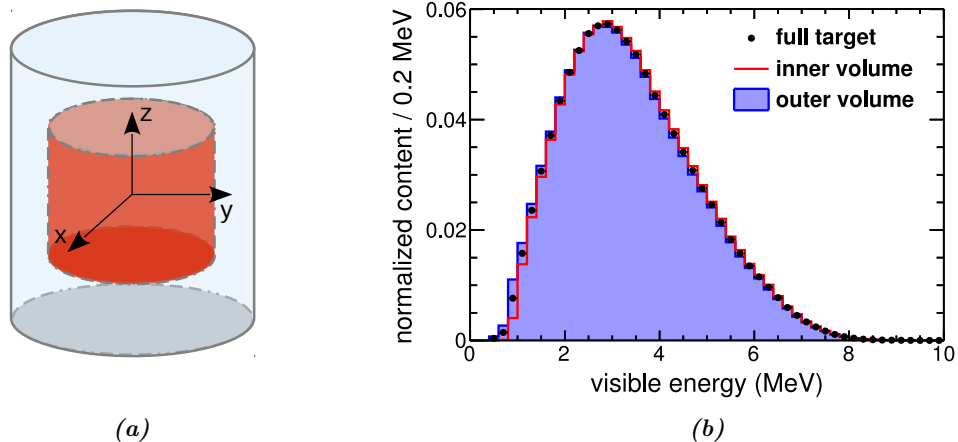
(a)   (b)

Figure 5.17: Neutrino candidate MC data set division in two sub-samples. **a)** Illustration of
the inner sub-sample. **b)** Prompt MC spectra for the cut $z_{\mathrm{limit}} = 1000\,\mathrm{mm}$. The black bullets
show the histogram of the full Gd-channel MC spectrum, the red line represents the inner
volume data, while the blue filled histogram shows the outer volume spectrum. All spectra
have the same normalization.

from a MC-MC comparison using Tripoli-4 code with a more realistic neutron modeling
are in very good agreement with the ^{252}Cf calibration MC corrections.

A position dependent contribution to the systematic uncertainty was assumed to be
negligible, as well as the MC correction is considered to be stable over the DC-III time
period. Furthermore the impact of the data selection and background subtraction on
the MC correction was found to be negligible. Also, it was shown that a change in the
efficiency definition cuts would leave the correction factor result unchanged. Minimal
variations in the selection cuts were concluded to not alter the MC correction signif-
icantly. Moreover, the analysis of possible prompt spectral distortions, introduced by
the application of a global correction factor, yields negligibly small discrepancies com-
pared to the locally corrected spectra. This effect is therefore not included in the c_{v}
systematic uncertainty.

The largest contribution to the total cut dependent correction uncertainty is intro-
duced by the volume-wide efficiency estimation method. Due to the limited number of
data points in z-axis calibration and the conversion of the $f(z)$ efficiency shape function
to the full volume, the mean relative discrepancy to the actual Target wide efficiency
was computed to be $0.221\,\%$. This results in a relative uncertainty on the MC correction
of $0.314\,\%$. Besides this contribution, the statistical uncertainty is added quadratically.
The cut dependent MC correction factor estimated using ^{252}Cf calibrations data is
hence given by

$$c_{\mathrm{v}}^{\mathrm{cut}} = 1.0003 \pm 0.0032 \;(\mathrm{stat+syst})\,.$$

Possible influences of the difference in neutron kinetic energy between ^{252}Cf and IBD
neutrons were expected to be negligible. An uncertainty contribution was therefore not

(a) $|z| < 700$ mm and $\rho < 631.6$ mm, 17.6%.

(b) $|z| < 1000$ mm and $\rho < 902.3$ mm, 51.2%.

(c) $|z| < 1100$ mm and $\rho < 992.5$ mm, 67.9%.

(d) $|z| < 1150$ mm and $\rho < 1037.6$ mm, 77.5%.
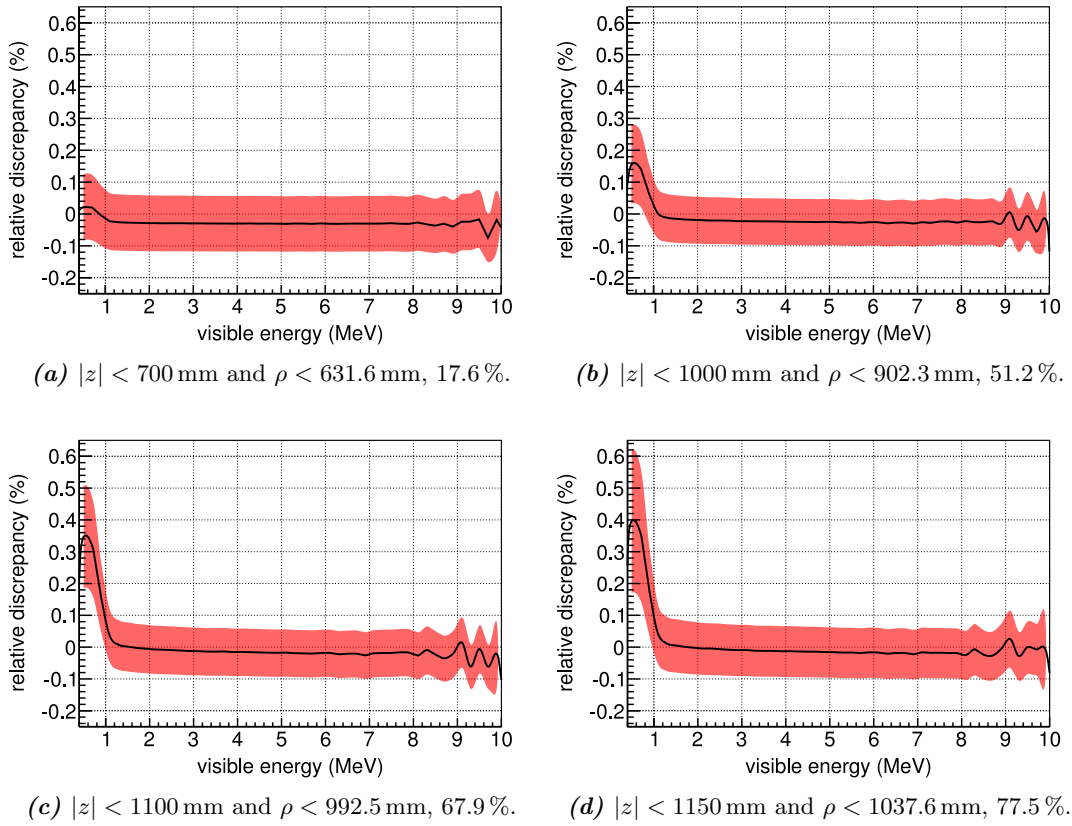
Figure 5.18: Discrepancy of the globally and locally corrected IBD prompt event MC spectra for different volume separations. The colored band represents the uncertainty range from variation of c_{inner} and c_{outer}. The inner volume cuts along with the inner sample percentage size are given below each figure.

included in the systematic error budget of this result. The additional measurement of $c_{\mathrm{v}}^{\mathrm{cut}}$ using IBD neutrons provides the possibility of an independent crosscheck, as briefly summarized in the following section.

5.3.4 IBD neutron results

Besides the $c_{\mathrm{v}}^{\mathrm{cut}}$ estimation by means of ^{252}Cf calibration data, neutrons produced by the IBD reaction of antineutrinos were used to obtain an independent measurement. In the following subsection the results retrieved by J. I. Crespo Anadón [89] are summarized. The IBD values can on one hand be used to validate the ^{252}Cf values, on the other hand they will be combined with the ^{252}Cf estimate to derive the final result and uncertainty on $c_{\mathrm{v}}^{\mathrm{cut}}$. Neutrons originating from IBD reactions of reactor antineutrinos constitute the signal sought for in the oscillation analysis. As their mean kinetic energy deviates from the average energy of the ^{252}Cf fission neutrons by two orders of magnitude, the IBD neutron based MC correction analysis is an essential crosscheck. Moreover IBD reactions are assumed to occur homogeneously distributed in the detector, allowing for a direct measurement of the volume-wide detection efficiencies.

(a) Projection on z-axis with $\rho < 470$ mm.

(b) Projection in ρ^2 from $|z| < 637.5$ mm.

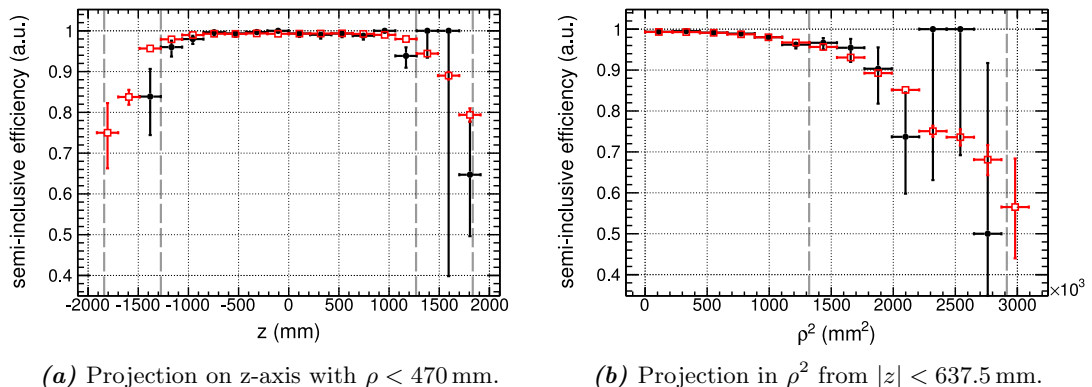***Figure 5.19:*** Semi-inclusive efficiency map projections onto z- and ρ^2-axis. The data (black bullets) was accidental background subtracted, MC efficiencies are shown by the red empty boxes. **(a)** Projection on z-axis with $\rho < 470$ mm. The inner pair of dashed lines mark the Target wall, whereas the outer pair shows the gamma catcher acrylics location. **(b)** Projection in ρ^2 from $|z| < 637.5$ mm. The inner dashed line represents the Target wall, while the outer line marks the gamma catcher border.

Data used in the IBD efficiency analysis is given by the official θ_{13} analysis run list. The event selection cuts are the same as for the candidate selection (see Chapter 3.3.1), except for an upper prompt energy cut of 8 MeV and the set of loosened cuts for the denominator sample (which can be read off from Eq. (5.52)). The semi-inclusive efficiency definition

$$\varepsilon_{\text{semi}} = \frac{N(4 < E_{\text{delayed}} < 10\,\text{MeV} \ \cap \ \Delta R < 1\,\text{m} \ \cap \ 0.5 < \Delta T < 150\,\text{µs})}{N(3.5 < E_{\text{delayed}} < 10\,\text{MeV} \ \cap \ \Delta R < 1.7\,\text{m} \ \cap \ 0.25 < \Delta T < 200\,\text{µs})} \quad (5.52)$$

differs in the denominator cuts from the ^{252}Cf one given in Eq. (5.46), as the IBD selection had to comply with the candidate isolation cut and optimize the signal to background ratio. Only events which do not consist of a neutron capture as delayed event and a prompt event marking the creation of the free neutron are background in this analysis. The two classes of background events encountered are therefore stopping muons and accidental coincidences. The latter were subtracted using an off-time window method.

In Fig. 5.19 the projected semi-inclusive efficiencies on the z- and ρ^2-axis are given. From the IBD neutrons data and MC samples inside Target volume excluding the chimney region [89], the volume-wide cut dependent MC correction was estimated:

$$c_{\text{v}}^{\text{cut}} = 0.9996 \pm 0.0021 \ (\text{stat+syst}) \,. \quad (5.53)$$

The systematic uncertainty is retrieved from the difference of $c_{\text{v}}^{\text{cut}}$ to the value obtained using only data in the bottom half of the Target. In this way the influence of stopping muons is accounted for, which happen to occur mainly in the upper part of the Target, accumulated below the chimney. Stability of the result with respect to changing vertex cuts to limit the selection to the Target region has been proven [88]. Furthermore, it was shown that the $c_{\text{v}}^{\text{cut}}$ value does not vary significantly in case the selection or efficiency definition cuts are altered. Removal of the ^{9}Li+^{8}He likelihood cut as well as the IV-veto cut tested the impact of decay neutrons and fast neutrons.

Table 5.14: Target-wide MC correction c_v for the semi-inclusive and the different cut efficiencies. The exclusive efficiencies were computed using the isolated efficiency definitions. The IBD neutron values are from [89].

	$c_\mathrm{v}(^{252}\mathrm{Cf})$	$c_\mathrm{v}(\mathrm{IBD})$
semi-inclusive	$1.0003 \pm 0.0007\,(\mathrm{stat})$	$0.9996 \pm 0.0021\ (0.0010\,(\mathrm{stat}) \pm 0.0019\,(\mathrm{syst}))$
exclusive	$1.0000 \pm 0.0007\,(\mathrm{stat})$	$0.9996 \pm 0.0013\ (0.0010\,(\mathrm{stat}) \pm 0.0008\,(\mathrm{syst}))$
E_delayed	$1.0005 \pm 0.0003\,(\mathrm{stat})$	$0.9994 \pm 0.0008\ (0.0007(\mathrm{stat}) \pm 0.0004(\mathrm{syst}))$
ΔR	$1.0009 \pm 0.0003\,(\mathrm{stat})$	$1.0013 \pm 0.0003\ (0.0003(\mathrm{stat}) \pm 0.00003(\mathrm{syst}))$
ΔT	$0.9986 \pm 0.0006\,(\mathrm{stat})$	$0.9989 \pm 0.0010\ (0.0007(\mathrm{stat}) \pm 0.0007(\mathrm{syst}))$

In Table 5.14 the c_v values of both the ^{252}Cf and IBD neutron analysis are given for the semi-inclusive as well as the exclusive efficiencies. The exclusive values were computed using the isolated efficiency definition. The IBD exclusive result is observed to be in good agreement with the semi-inclusive value, while the systematic uncertainty differs by more than a factor two. A general accordance of the ^{252}Cf and IBD results is given not only in the total $c_\mathrm{v}^\mathrm{cut}$ values from exclusive and semi-inclusive efficiency estimation, but also for the MC corrections of each cut separately. Both the ^{252}Cf and IBD results, estimated using the semi-inclusive definitions, will be combined to yield the detection systematic uncertainty in the oscillation analysis (see Section 5.6).

5.4 Gd-fraction correction: ^{252}Cf fission neutron analysis

In the following the determination of the intrinsic, cut independent part of the MC correction factor will be discussed. In Section 4.3.2 Gd-fraction values for different ^{252}Cf multiplicity and prompt energy selections are given in Table 4.2. From comparison of the data and MC simulation values, a discrepancy of about 2.5 % became evident. Gd-fraction analyses using different neutron sources, such as IBD or spallation neutrons, have confirmed this observation and will be discussed later in this section.

In order to calibrate the IBD detection rate in the MC simulation with respect to this detector inherent discrepancy, the MC correction factor c_{Gd} was introduced in Section 5.2.3. Unlike the cut dependent correction c_v (also c_{cut}) which is evaluated using the volume-wide detection efficiencies, c_{Gd} is measured at the Target center as described in Eq. (5.36). This definition follows the concept that the Gd-fraction is to the first order constant over the full Target volume. At the same time the inclusion of spill-out events in the measurement is avoided.

The Gd-fraction is estimated in data and MC using the same method, given in Eq. (5.4) (referred to as *method 1*). There, the delayed energy spectrum between 0.5 and 10 MeV is subdivided in an energy region (from 3.5 to 10 MeV) attributed to neutron captures on gadolinium nuclei and an energy interval assigned to hydrogen captures (below 3.5 MeV). Multiple captures, mainly two neutron captures on gadolinium and hydrogen or twice on gadolinium, detected within one ADC window are excluded from the analysis, having negligible impact on the Gd-fraction results. The exclusion of the events below the analysis threshold of 0.5 MeV is considered to have no influence.

The Gd-fraction estimation is hence given by the ratio of events capturing on gadolinium and all neutron captures. As more than 99.9 % of the neutron captures in the Target liquid occur on hydrogen and gadolinium nuclei, the Gd-fraction can be expressed as

$$f_{Gd} = \frac{N_{Gd}}{N_H + N_{Gd}} \,. \tag{5.54}$$

The choice of the energy regions used to select the neutron captures on a certain nucleus can change the Gd-fraction result. A variation of the selection cuts can thus be used to estimate the systematic uncertainty. Two additional methods are introduced to evaluate the Gd-fraction correction. Also applied to both data as well as MC to estimate the Gd-fraction, *method 2* only takes into account events with visible energies in the capture peak regions. A modified version of *method 1* is given by *method 3*, which excludes the events below a variable analysis threshold $E_{th} = [0.4, 1.5]$ MeV, removing different parts of the energy spectrum where the relative data to MC discrepancies are largest. The maximum threshold of 1.5 MeV was chosen such that energy scale related data to MC discrepancies by cutting too close to the hydrogen capture peak are not included. The Gd-fraction estimation methods are summarized in Table 5.15.

Table 5.15: Gd-fraction estimation methods: neutron capture selection cuts.

	H selection	Gd selection
method 1	$0.5 < E_{delayed} < 3.5$ MeV	$3.5 < E_{delayed} < 10$ MeV
method 2	$1.5 < E_{delayed} < 3$ MeV	$6.5 < E_{delayed} < 9.5$ MeV
method 3	$E_{th} < E_{delayed} < 3.5$ MeV	$3.5 < E_{delayed} < 10$ MeV

Results and systematic uncertainty estimation

The results of the Gd-fraction correction factor c_{Gd} were evaluated using Eq. (5.54)
along with the three methods for Gd-fraction estimation given in Table 5.15. Ta-
ble 5.16 summarizes all results, ranging from 0.975 to 0.979, as four different energy
thresholds were applied with *method 3*. The data to MC discrepancy in the Gd-fraction
with increasing energy threshold, which can be seen by the larger MC correction factors.

Systematic uncertainties in the estimation of c_{Gd} could have mainly two origins: either
from discrepancies arising from the use of ^{252}Cf fission neutrons (such as backgrounds
or neutron kinetic energy) or due to the Gd-fraction estimation methods. The MC
simulation model itself does not represent a source of systematic uncertainty. The
simulated Gd-fraction strongly depends on the neutron physics modeling such as the
Gd-concentration, neutron scattering and capture cross sections as well as the gamma
spectrum of the radiative neutron captures. However, any bias in one of these pa-
rameters would be present in the oscillation data as well, and therefore "calibrated
out" by the Gd-fraction correction. The influence of the neutron kinetic energy can
be investigated by means of MC simulation data. In Table 5.17 the Gd-fractions com-
puted with *method 1* for simulated IBD neutrons produced within a sphere of radius
$R = \sqrt{x_{\mathrm{IBD}}^2 + y_{\mathrm{IBD}}^2 + z_{\mathrm{IBD}}^2}$ located at the Target center are given. The Gd-fraction
of the simulated ^{252}Cf neutrons for a deployment at the Target center amounts to
$f_{\mathrm{Gd}}^{\mathrm{Cf-MC}} = 0.8749 \pm 0.0004$ and is in excellent agreement with the IBD MC results. Pos-
sible discrepancies could still exist and might not be observed due to lack of statistics.
Nevertheless, we can conclude that they are certainly smaller than 0.1 %. Although no
systematic bias can be found from comparison of the simulated values for f_{Gd}, it does
not guarantee that no discrepancy will be observed in the data either. Therefore, the
measurement of c_{Gd} using IBD neutrons is an essential crosscheck and will be discussed
later in this section.

In order to check the robustness of the Gd-fraction correction with respect to the
lower energy threshold, the Gd-fraction estimation is performed using *method 3*. The
application of this method also tests for a change in the correction in case the events for
visible energies smaller than the hydrogen peak in the data spectrum are not caused by
neutron captures on hydrogen. Moreover, the influence of the accidental background
subtraction is studied by variation of the prompt energy cut of the ^{252}Cf fission gammas.
Lowering the prompt cut to 0.5 MeV yields $c_{\mathrm{Gd}}^{0.5\,\mathrm{MeV}} = 0.9749 \pm 0.0010$ for *method 1*,
which is in accordance with the result based on the default 4 MeV cut.

The definition of the methods to estimate f_{Gd} can have an effect on the MC cor-
rection value. Since the exact same method is applied to the data sample as well as
the MC simulation events, the only source of systematic uncertainty would be related
to discrepancies in the spectral shape of the radiative neutron capture gammas. This
consideration is mostly covered by the comparison of the results from application of
the three different methods. Additionally the energy window for neutron captures on
gadolinium is altered from 3.5 MeV to 3 MeV in *method 1*, which slightly changes the
Gd-fraction correction to 0.9744 ± 0.0011, but changes the total MC correction includ-
ing the semi-inclusive by only 0.01 %.

Table 5.16: Gd-fraction correction factor c_{Gd} using three methods for Gd-fraction estimation. Uncertainties are statistical.

analysis method	E_{th} [MeV]	c_{Gd}
method 1	–	0.9750 ± 0.0011
method 2	–	0.9781 ± 0.0011
method 3	$0.4\,\mathrm{MeV}$	0.9750 ± 0.0011
method 3	$0.7\,\mathrm{MeV}$	0.9753 ± 0.0011
method 3	$1.0\,\mathrm{MeV}$	0.9762 ± 0.0011
method 3	$1.5\,\mathrm{MeV}$	0.9790 ± 0.0011

Table 5.17: Gd-fraction f_{Gd} evaluated with *method 1* for IBD neutrons simulated within a sphere of radius R located at the Target center. Uncertainties are statistical.

R [mm]	400	500	600
f_{Gd}	0.87493 ± 0.00099	0.87500 ± 0.00071	0.87497 ± 0.00054

As by default the full energy range from 0.5 to $10\,\mathrm{MeV}$ is used to not reject parts of the signal, the standard method for the estimation of f_{Gd} is represented by *method 1*, also providing the central value of the Gd-fraction correction.

As suggested by the results discussed above is the main source of systematic uncertainty caused by the application of different Gd-fraction estimation methods, while the largest discrepancy is found between *method 1* and *method 3*. This discrepancy is taken as systematic uncertainty. Together with the statistical uncertainty we get for the Gd-fraction correction

$$\Delta c_{\mathrm{Gd}} = 0.0042 \ \ (0.0011\,(\mathrm{stat}) \pm 0.0041\,(\mathrm{syst}))\,. \tag{5.55}$$

The statistical uncertainty is limited by the amount of ^{252}Cf data taken in the second calibration campaign, whereas the systematic uncertainty is dominated by the estimation method and possible backgrounds.

Furthermore another estimate of c_{Gd} exists, extracted by means of the improved MC simulation code **TRIPOLI-4**. In a study performed by A. Collin [74] the Gd-fractions in both the DC-III default MC and the **TRIPOLI-4** simulation code was evaluated for IBD neutrons. With the DC-III code a Gd-fraction of 0.8800 ± 0.0012 was found, whereas for the Gd-fraction from the **TRIPOLI-4** simulation a lower value of 0.8565 ± 0.0013 was estimated. Assuming the **TRIPOLI-4** code to reproduce the neutron physics more realistic, a capture fraction related correction factor for the DC-III MC can be computed to be

$$\Delta c_{\mathrm{Gd}}^{\mathrm{T4}} = 0.9733 \pm 0.0020\,. \tag{5.56}$$

In contrast to the analysis methods presented with respect to the ^{252}Cf data analysis, these results are gained from true MC information, telling on which nucleus the neutron was actually caught. This approach is therefore expected to yield slightly different results for the Gd-fractions as well as the correction factor, as it does not take into account possible discrepancies in the neutron capture gamma spectra. Despite this limitation in comparison of the **TRIPOLI-4** and the ^{252}Cf results, this observation is a

strong hint for the DC-III MC neutron scattering and capture cross-section modeling
as source of the data to MC discrepancy in the Gd-capture fraction.

Comparison to the first calibration campaign data

As stability crosscheck c_{Gd} is evaluated using data from the first calibration campaign,
which had been conducted one year earlier than the second campaign. The result of
0.9784 ± 0.0017 computed with *method 1* is consistent with the second campaign's
value within the statistical uncertainty. For the total MC correction related to neutron
detection, including the volume-wide semi-inclusive correction, a value of 0.9768 ± 0.0019
is measured in the first campaign. This result agrees with the second campaign within
0.0015 ± 0.0023.

Third calibration campaign data

One year after second calibration deployment of the ^{252}Cf source along the Target sym-
metry axis, a third stability calibration was conducted, which is not part of the official
DC-III dataset. This campaign used a newly produced ^{252}Cf source with the Double
Chooz code Cf-252-12, as the activity of the previously used source[9] had further de-
creased over the past year due to the ^{252}Cf life-time of 3.8 years.

The results discussed in this paragraph should be considered as preliminary numbers
and are supposed to serve as rough crosscheck, rather than a precise measurement. At
the time of the analysis the energy time stability correction was not yet extended up to
the runs of the third campaign, furthermore no corresponding MC simulation runs had
been produced yet. Therefore MC runs of the 2nd campaign generated at the matching
positions were used to compute a MC correction factor estimate via

$$c_{\mathrm{Gd}} = \frac{(f_{\mathrm{Gd}})^{\mathrm{Data,3rd}}}{(f_{\mathrm{Gd}})^{\mathrm{MC,2nd}}} \tag{5.57}$$

As the trigger rate was higher in this time period caused by an increased occurrence of
light noise events (cf. Section 3.3), the trigger threshold was raised during calibration
to $E_{\mathrm{trigger}} > 1\,\mathrm{MeV}$. Therefore the Gd-fraction estimation method with an increased
analysis threshold $E_{\mathrm{th}} > 1.5\,\mathrm{MeV}$ was used to retrieve the inputs to Eq. (5.57). Roughly
half an hour of detector data was collected with the source placed at the Target cen-
ter, hence additional runs located at about $\pm 320\,\mathrm{mm}$ and $\pm 640\,\mathrm{mm}$ were included in
the analysis to enhance the statistics (see Table 5.18). Runs simulated at the same
positions were chosen and their live times (i.e. number of events) adjusted in order to
guarantee that each deployment position contributes with the same statistical weight in
data and MC simulation. The same adjustment was made for the result of the second
campaign using runs within $|z| < 652\,\mathrm{mm}$, given in Table 5.19 in bold.
Table 5.19 summarizes the MC correction values of the third calibration deployment as
well as the results of the first and second campaign computed with the same analysis
threshold at the Target center or within $|z| < 652\,\mathrm{mm}$ (bold numbers).

The comparison between the third and second campaign results, measured either at the
Target center with higher statistics or for the same run configuration within $|z| < 652\,\mathrm{mm}$,

---

[9]The Double Chooz source code of the other two campaigns is Cf-252-4.

Table 5.18: Deployment positions and corresponding runs of the third ^{252}Cf calibration campaign [100]. The MC simulation runs used for data to MC comparison were produced at the same positions.

z position [mm]	Data, 3rd campaign	MC, 2nd campaign
652	67081	45048
332	67080	45076
12	67071, 67086	43705, 45042
-308	67072	45077
-628	67074	45047

Table 5.19: Gd-fraction related MC correction c_{Gd} for a lower analysis threshold of $E_{th} > 1.5$ MeV. The MC corrections are computed using the runs within the z-region given in the first column. The last column contains the discrepancy to the second calibration campaign result at the Target center ($z = 0$). The numbers in bold were retrieved analyzing the same z-region.

z positions [mm]	campaign	MC correction	discr. to 2nd campaign ($z=0$) [%]
-628 to 652	3rd	**0.9797 ± 0.0014**	0.07
0	2nd	0.9790 ± 0.0011	–
-628 to 652	2nd	**0.9810 ± 0.0016**	0.20
0	1st	0.9825 ± 0.0017	0.36

yields good agreement, for the first case within (0.07 ± 0.18) % and for the latter within (0.13 ± 0.22) %. The results for the Gd-fraction MC correction of all three campaigns agree within less than 0.4 %, while the observed discrepancies are covered by the statistical uncertainties.

Further background reduction crosschecks

Additional background studies have been performed with the goal to better understand the data to MC discrepancy in the delayed energy spectrum for energies smaller than the hydrogen capture peak.

For energies $E_{delayed} < 1.9$ MeV the correlation time spectrum of ^{252}Cf fissions in data with more than one delayed event ($m > 1$) were plotted (Fig. 5.20). In case these low energy events are related to the Compton tail of neutron captures on hydrogen, we would expect to observe an exponential distribution of the correlation times with a decay constant of $\tau \approx 30$ µs. A component with these properties can be detected, however, correlated events following distributions with shorter decay constants are found as well. From a fit

$$N(t) = \sum_{i=1}^{3} N_i \cdot e^{t/\tau_i} \tag{5.58}$$

with three time constants, sufficiently parametrizing the time spectrum, the capture or decay constants $\tau_1 = (30.6 \pm 2.8)$ µs, $\tau_2 = (5.2 \pm 1.2)$ µs and $\tau_3 = (625 \pm 85)$ ns were extracted (see Fig. 5.20). While the energy depositions of events related to τ_1 are most

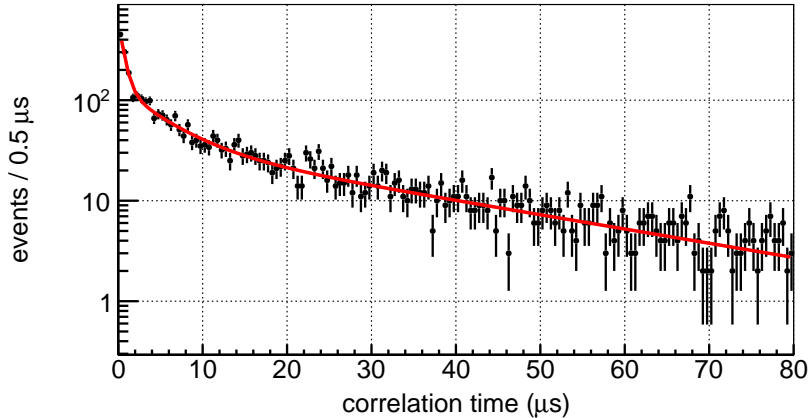**Figure 5.20:** Correlation time spectrum for energies $E_{\text{delayed}} < 1.9\,\text{MeV}$ of the twelve ^{252}Cf second calibration campaign deployment runs at the Target center $|z| < 600\,\text{mm}$.

probably caused by neutron captures on hydrogen, the events occurring with shorter mean correlation time might be due to correlated background. As the events following short τ are present in the spectra for neutron multiplicities $m > 1$, these correlated events occur along with a number of neutrons. Therefore radioactive/secondary decays of the ^{252}Cf fission fragments would come into consideration.

Since we would like to study the impact of the low energy events on the Gd-fraction correction, different approaches have been pursued. As the short τ correlated events can be removed by requiring a minimum Δt_{min}, the Gd-fraction correction c_{Gd} is studied as a function of the minimum correlation time Δt_{min}. In Fig. 5.21a the results of c_{Gd} are given for different analysis thresholds E_{th} applied with *method 3*. The graph shows that with increasing minimum correlation time, the value of c_{Gd} drops. This behavior can be understood by taking into account the correlation time distributions[10] of H- and Gd-captures in data and MC simulation as given in Fig. 5.21b. The decrease in c_{Gd} can be explained by the difference in shape in the H-capture correlation time. The simulated distribution possesses a faster component in the first 30 µs compared to data. Therefore a larger fraction in H-capture events is removed from the MC spectrum by an increasing Δt_{min}, which in turn further enlarges the data to MC discrepancy in the Gd-fraction and thus leads to a reduction in c_{Gd}. Once the cut of $\Delta t_{\text{min}} = 30\,\mu\text{s}$ is passed, the MC correction should remain constant, as the correlation times in Fig. 5.21b show a good agreement for larger Δt. For $E_{\text{th}} = 0.5\,\text{MeV}$ the values of c_{Gd} are affected by correlated background events, both with short and long correlation times. For $E_{\text{th}} = 1.5\,\text{MeV}$ or $1.7\,\text{MeV}$ the background contributions are strongly reduced.

We can see that the contribution of correlated background can be weakened or even removed by application of an energy cut. The correlated events with small τ can be removed by a correlation time threshold Δt_{min}, but due to a difference in the Δt related selection efficiency of the H-capture events, the values of c_{Gd} are biased.

---

[10]The correlation time of neutron captures on hydrogen are selected by requiring the energy to satisfy $2 < E_{\text{delayed}} < 2.8\,\text{MeV}$ whereas the Gd-capture events are selected via $7 < E_{\text{delayed}} < 9.5\,\text{MeV}$.
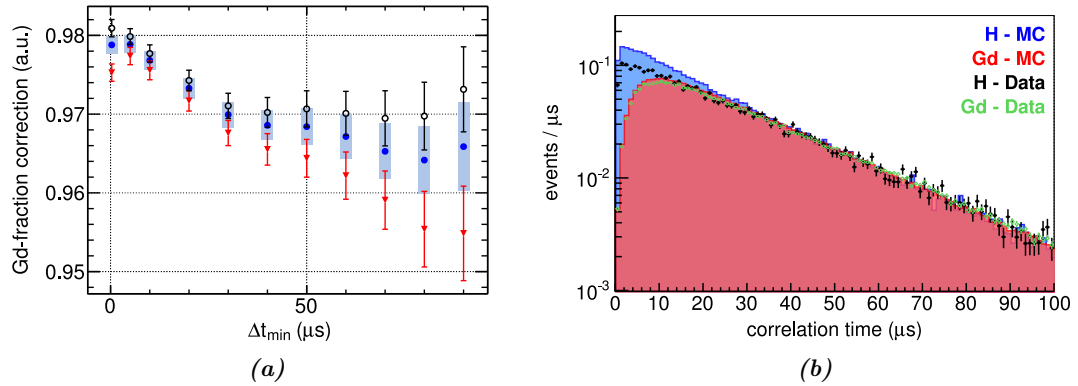
Figure 5.21: Evolution of the Gd-fraction correction c_{Gd} with respect to the prompt-delayed correlation time. **a)** c_{Gd} as a function of the minimum correlation time Δt_{min} for *method 3* with different analysis thresholds: $E_{\mathrm{th}} = 0.5\,\mathrm{MeV}$ corresponding to the standard *method 1* (red), $E_{\mathrm{th}} = 1.5\,\mathrm{MeV}$ (blue), $E_{\mathrm{th}} = 1.7\,\mathrm{MeV}$ (black). **b)** Correlation times of neutron captures in ^{252}Cf data and MC: H-captures (black points) and Gd-captures (green open circles) in data (black points), H-captures (blue filled histogram) and Gd-captures (red filled histogram) in MC simulation.
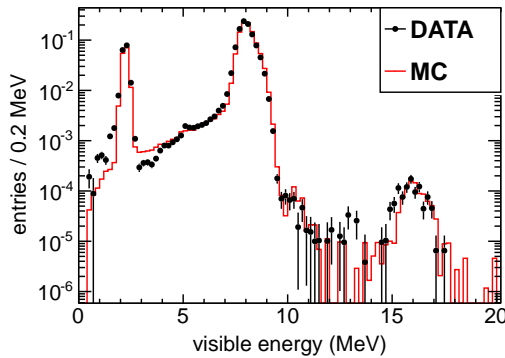

Figure 5.22: Merged data and MC simulation delayed energy spectra of the six ^{252}Cf second calibration campaign deployment runs at the Target center $(x,y,z) = (0,0,12)\,\mathrm{mm}$. The accidental background was subtracted and the neutron multiplicity is $m > 1$. Additionally, events with $E_{\mathrm{delayed}} < 1.7\,\mathrm{MeV}$ and correlation times $\Delta t < 20\,\mu\mathrm{s}$ are removed.

In Fig. 5.22 the delayed energy spectra of the ^{252}Cf deployment at the Target center is shown, along with an additional cut: events with energies smaller than $1.7\,\mathrm{MeV}$ and simultaneously correlation times $\Delta t < 20\,\mu\mathrm{s}$ were removed. The data and MC spectra show an improved agreement for low energies, the MC correction factor with this additional cut is $c_{\mathrm{Gd}} = (0.9795 \pm 0.0011\,(\mathrm{stat}))$.

As a last crosscheck, the Gd-fraction correction can be analyzed by estimation of the amount of correlated events with short τ in the region of $0.5 < E_{\mathrm{delayed}} < 3\,\mathrm{MeV}$ with a Δt fit. Removing these events from the MC correction computation yields $c_{\mathrm{Gd}} = 0.9792 \pm 0.0011$. For $2 < E_{\mathrm{delayed}} < 3\,\mathrm{MeV}$ no short τ component is observed in the Δt spectra.

The background reduced data samples obtained in these studies – either with a modified ^{252}Cf event selection or varied analysis thresholds as shown in Fig. 5.21a – yield results consistent within less than $1.5\,\sigma$ uncertainty with the Gd-III correction factor of the Gd-fraction, which was estimated to be $c_{\mathrm{Gd}} = (0.9750 \pm 0.0042\,(\mathrm{stat} + \mathrm{syst}))$.

Crosscheck using IBD events

The IBD neutron kinetic energy is with $\sim 15\,\mathrm{keV}$ significantly lower than the kinetic energy of $^{252}\mathrm{Cf}$ fission neutrons. Hence the analysis of the Gd-fraction correction using IBD neutron samples constitutes an important crosscheck. In a study performed by J. I. Crespo Anadón [89], the correction factor was computed to be $c_{\mathrm{Gd}}^{\mathrm{IBD}} = 0.9794 \pm 0.0059\,(0.0040\,(\mathrm{stat.}) \pm 0.0044\,(\mathrm{syst.}))$. As the IBD data sample contained correlated background events from Bi-Po decays, the analysis had to use an energy threshold of $E_{\mathrm{delayed}} < 1.6\,\mathrm{MeV}$. This result should therefore be compared to the $^{252}\mathrm{Cf}$ value using *method 3*, providing very good agreement.

## 5.5 Gd-fraction crosscheck: cosmic spallation neutron analysis

Cosmic ray muons and physics events caused by these muons are in general background sources in the search of the reactor antineutrino signal. Hence, events passing the muon energy threshold in either the IV or ID as well as any subsequent trigger within 1 ms after the muon are removed from the set of valid triggers. Muons passing through the detector and surrounding rock can produce neutrons and other hadrons as well as cosmogenic isotopes. The process of neutron production is often referred to as *cosmic muon spallation*, the different channels of neutron production are however complex and often include secondary neutron production processes involving other muon-induced particles [206].

Usually removed by the 1 ms muon veto, spallation neutrons do not only constitute background, but can also be used as calibration source e.g. for the extraction of correction maps [6, 12], which are used to provide spatial uniformity of the visible energy. In the following spallation neutrons will be used with the intension to independently crosscheck the Gd-fraction correction result obtained from $^{252}\mathrm{Cf}$ source analysis.

5.5.1 Spallation neutron data

Since muon-induced neutrons are produced over the full detector volume, they appear to be a suitable source to study the cut related neutron detection efficiency in the full Target volume. Owing to baseline fluctuations after a high energy event such as a muon, the spallation event selection can however only start 50 µs after the muon event [181]. As we assume the neutron production to be a fast process, the information about neutron moderation is not accessible, making it impossible to study the efficiency of the correlation time cut. Another complication is the lack of knowledge of the actual position of neutron origin due to the absence of a nearby prompt. Therefore the neutron displacement and the related cut efficiency cannot be investigated. Despite these limitations of the spallation data, we can use the energy information of the neutron captures, e.g. to study the Gd-fraction and its correction factor. Just as the IBD neutron sample, spallation neutron events are present throughout the DC-III data sample, making it possible to obtain an average MC correction factor c_{Gd} representing the full data taking period.

In principle no dedicated MC simulation of spallation neutrons was available. Here the minimum after-muon time of 50 µs is of advantage: muon-induced neutrons in the
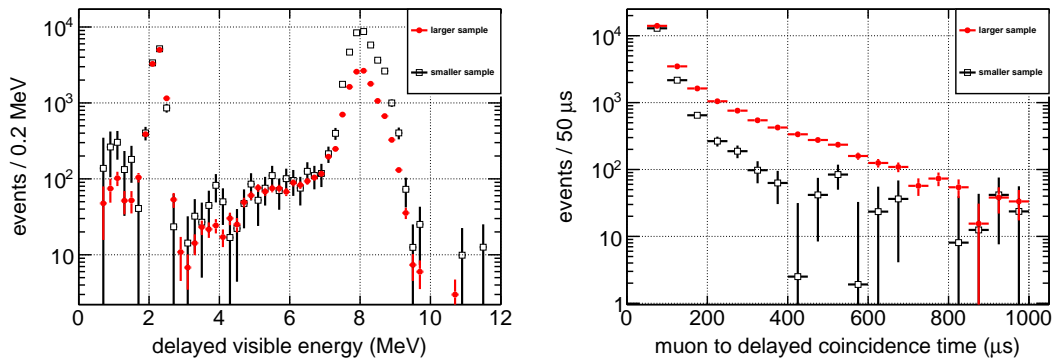
(a) Delayed visible energy. Normalized with respect to the events below the hydrogen peak.

(b) Muon to delayed correlation time. Normalized with respect to the events below the gadolinium peak of Fig 5.23a.

Figure 5.23: Delayed visible energy spectra and muon to delayed correlation time spectra of the after muon events. The histograms show the spectra for two different sample sizes gained from differently sized fiducial volumes. The red bullets show the spectra of the larger sample selected with $\rho_{\text{delayed}} < 1\,\text{m}$. The black open boxes represent the data sample from the cut $\rho_{\text{delayed}} < 0.5\,\text{m}$.

DC detector are expected to have high kinetic energies of $\sim 20\,\text{MeV}$ on average [39], however after $50\,\mu\text{s}$ most of them should have lost the largest fraction of their energy. Therefore the spallation neutrons will be treated as thermal neutrons ($E_{\text{kin}} \approx 0.025\,\text{eV}$) and their Gd-fraction can hence be compared to the one obtained from IBD neutron MC code.

Spallation neutrons occur with higher event multiplicities $m > 1$, which enables to suppress background via multiplicity cut. Accidental background is measured and subtracted using the off-time window technique (as done for ^{252}Cf data in Section 4.3.1). Correlated backgrounds owing to decaying cosmogenic isotopes will be present in the neutron sample, as the off-time method can subtract such contributions only partially.

Data selection

In a first step all events after a muon satisfying $E_\mu > 50\,\text{MeV}$ in the ID were selected while the muon to delayed correlation time had to fulfill $\Delta t_{\mu\text{-d}} = [50; 5000]\,\mu\text{s}$. The standard DC-III LN and FV cuts were applied, but no ^9Li cut was used in the selection. The muon was isolated in time, no other muon[11] was allowed $\pm 5\,\text{ms}$ around the $> 50\,\text{MeV}$ muon. An additional short event veto ($100\,\mu\text{s}$) on any trigger was applied before the prompt muon. The off-time window method (the number of multiple windows was six, the time offset between the windows $7\,\text{ms}$) was used to measure and subtract accidental background. The same isolation, veto and selection criteria as for the on-time window were applied to the off-time measurements. Details on the data labels used to select the spallation neutrons and the sample of simulated IBD events can be found in Appendix A.1.

---

[11]A muon is identified as such in case the visible energy in the ID is larger than $20\,\text{MeV}$ or if the energy deposition in the IV exceeds $30\,\text{kDUQ}$.
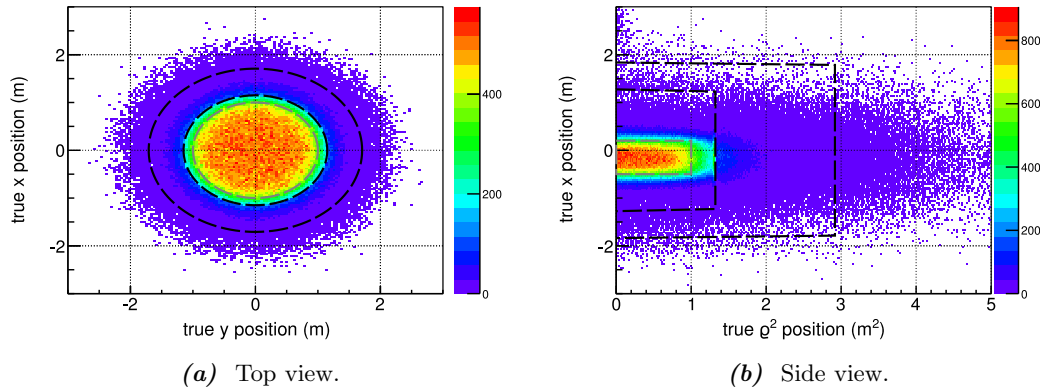
(a) Top view. *(b)* Side view.

Figure 5.24: True neutron capture locations of simulated IBD neutron events with reconstructed vertices inside a cylindrical fiducial volume with $-0.5 < z_{\text{reco}} < 0.2\,\text{m}$ and $\rho_{\text{reco}} < 1\,\text{m}$. The outer and inner black dashed lines mark the Gamma Catcher and Target acrylics, respectively. The gray dashed line represents the fiducial volume limits.

Additional cuts had to be applied to make a Gd-fraction analysis possible. For the spallation neutron sample only events belonging to a group of at least two neutron candidates (i.e. $m > 1$) were used. In order to guarantee, that the neutron origin is located in the Target center, events inside a fiducial volume would be selected by means of their prompt event position. In the case of spallation neutrons, the event selection can only be performed by cutting on the delayed event vertices i.e. the neutron capture positions, as the prompt event is given by the muon and the location of neutron production is not known. The boundaries of the cylindrical fiducial volume are determined such that the vertices need to fulfill $-0.5 < z_{\text{delayed}} < 0.2\,\text{m}$ in z-direction, while the radius ρ_{max} is kept variable. The bottom half of the detector is selected as it is expected to be the region in the Target with the lowest background contributions, since stopping muons enter the detector through the chimney and are concentrated at the Target top (see Section 3.3.4).

In Fig. 5.23 (a) and (b) the spectra of the delayed visible energy and the muon to delayed correlation time are given for two different volume selections, respectively. The larger data sample has the additional cut of $\rho_{\text{delayed}} < 1\,\text{m}$, while the smaller sample features the cut $\rho_{\text{delayed}} < 0.5\,\text{m}$. From Fig. 5.23 (a) we can conclude that the larger volume sample contains an increased fraction of hydrogen capture events. Fig. 5.23 (b) shows that this excess of events consists mainly of hydrogen captures actually occurring in the Gamma Catcher volume, as seen by the increased portion of events following the neutron capture time constant $\tau_{\text{GC}} \approx 200\,\mu\text{s}$. A possible explanation for this observation is given in the following paragraph.

Vertex cuts and Gd-fraction

Since neutron captures on hydrogen nuclei yield a single $2.2\,\text{MeV}$ gamma, the reconstructed vertex position and the true neutron capture location are not necessarily in agreement. The reconstructed position can be biased by the distance the gamma travels before it deposits the main fraction of its energy. This effect might also be present
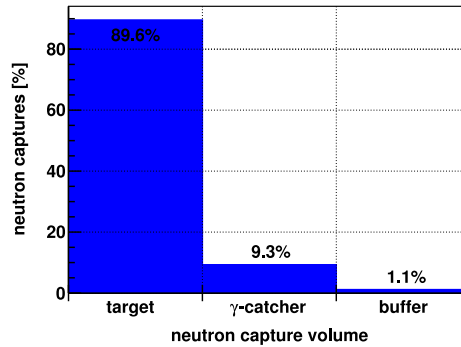
Figure 5.25: Actual neutron capture locations of simulated IBD neutron events with reconstructed vertices inside a cylindrical fiducial volume with $-0.5 < z_{\mathrm{reco}} < 0.2\,\mathrm{m}$ and $\rho_{\mathrm{reco}} < 1\,\mathrm{m}$, while no cut is applied to the correlation time between prompt and delayed event.

for the Gd-capture events, though it is expected to be less pronounced as the radiative neutron capture on Gd produces multiple gammas. Due to geometrical reasons a larger portion of hydrogen capture events actually occurring outside the fiducial volume will be included in the selection compared to the amount of captures occurring inside but being reconstructed outside the volume (see Fig. 5.24). These misplaced events will be present in the MC simulation as well, but data to MC discrepancies in the vertex reconstruction can be misinterpreted as mismatch in the Gd-fractions. Spatial inhomogeneities in the spallation neutron selection can enhance these discrepancies.

A study performed with simulated IBD neutrons showed that almost $10\,\%$ of the neutron capture events with a reconstructed vertex satisfying $-0.5 < z_{\mathrm{reco}} < 0.2\,\mathrm{m}$ and $\rho_{\mathrm{reco}} < 1\,\mathrm{m}$ were actually caught in the Gamma Catcher (cf. Fig. 5.25), while no cut was applied to the prompt-to-delayed correlation time. For a minimum correlation time of $50\,\mu\mathrm{s}$ the fraction of Gamma Catcher events will increase to roughly $30\,\%$, since a large proportion of Target events is not detected due to the constraint on the coincidence time.

By restricting the vertex and maximum correlation time cuts, it is possible to reduce the amount of gamma catcher neutrons in a Target sample. With a tightened vertex cut $\rho_{\mathrm{reco}} < 0.5\,\mathrm{m}$ and a correlation time of $\Delta t < 150\,\mu\mathrm{s}$, the contribution of neutron captures outside the Target to the sample is lowered to $5.4\,\%$.

5.5.2 Gd-fraction correction results

For Gd-fraction analysis of the spallation neutron sample, correlation time and distance cuts were applied: the muon-delayed correlation time had to be in the range of $50\,\mu\mathrm{s}$ to Δt_{max} and the delayed reconstructed vertex had to satisfy $0.2 < z_{\mathrm{reco}} < -0.5\,\mathrm{m}$ and $\rho_{\mathrm{reco}} < \rho_{\mathrm{max}}$. The same vertex and Δt cuts as for the spallation neutron data were applied to the simulated IBD neutron sample.

Two different methods were used for the Gd-fraction estimation. The full energy range from 0.5 to $10\,\mathrm{MeV}$ was taken into account with *method 1* (see Eq. (5.4)), while *method 3* with an $1.5\,\mathrm{MeV}$ energy threshold (see Eq. (5.54) and Table. 5.15) reduces the influence of irregularities in the low energy region. An excess of low energy events can either be remaining correlated background or caused by baseline fluctuations after a muon. Correlated background contributions at higher energies are expected to be small, but cannot be excluded.
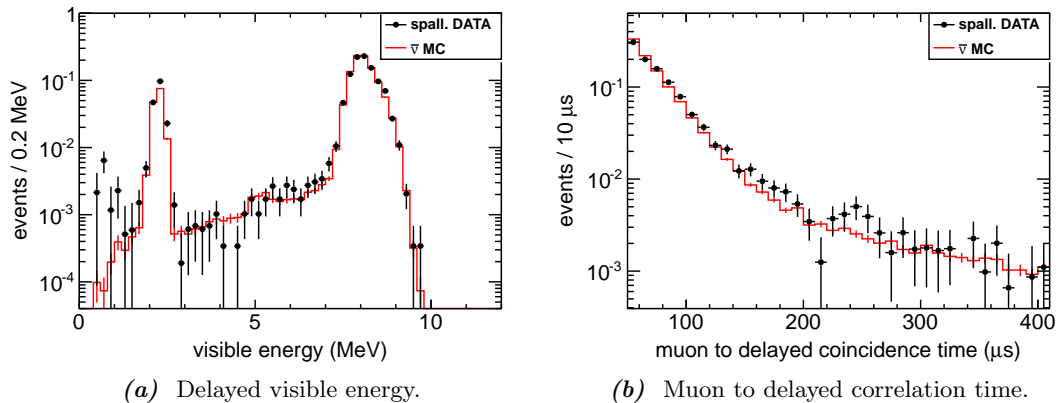
(a) Delayed visible energy.

(b) Muon to delayed correlation time.

Figure 5.26: Delayed energy spectra and muon to delayed correlation time spectra of an after muon event selection (black bullets) and simulated IBD neutrons (red histogram). Both data and MC samples were selected with a cut on the delayed reconstructed vertex of $0.2 < z < -0.5\,\mathrm{m}$ and $\rho < 0.5\,\mathrm{m}$. The delayed energy spectra were normalized in the region of 7 to $10\,\mathrm{MeV}$, the time spectra were normalized from 50 to $150\,\mathrm{\mu s}$.

In Fig. 5.26 the spallation neutron spectra are shown along with the spectra retrieved from the MC simulation of IBD neutrons. The hydrogen peak of the spallation data contains more events than the simulation spectrum. Hence, the data to MC discrepancy in the Gd-fraction is also observed with the muon-induced neutron sample. The Gd-fraction MC correction is in this context defined as the ratio of the Gd-fraction measured with spallation neutrons and the Gd-fraction from IBD simulation:

$$c_{\mathrm{Gd}} = \frac{(f_{\mathrm{Gd}})^{\mathrm{spall\text{-}n}}}{(f_{\mathrm{Gd}})^{\mathrm{IBD\text{-}MC}}} \qquad (5.59)$$

The evolution of the Gd-fraction correction with respect to changing radii $\rho_{\max}$ are given in Fig. 5.27 for fixed maximum correlation times $\Delta t_{\max}$. We can see that either the hydrogen event "contamination" from Gamma Catcher events or other event distribution inhomogeneities reduce the correction factor for larger vertex cuts. The influence of these events seems to decrease for the values of *method 3* in case the vertex cut is tightened.

Fig. 5.28 shows the Gd-fraction correction as a function of $\Delta t_{\max}$ whereas the fiducial volume radius $\rho_{\max}$ is kept fixed. For a fixed volume limit $\rho_{\max}$, the MC correction values are stable with respect to changing $\Delta t_{\max}$.

The values computed from *method 1* are in general found to be lower than the results we obtain with *method 3*. For tighter vertex cuts $\rho_{\max} < 0.5\,\mathrm{m}$ the discrepancy between the two methods increases. The source of this offset is unknown, but could be caused by background. In Fig. 5.27 and 5.28 corresponding ^{252}Cf source result is given for each of the two methods, while a correlation time cut of $50 < \Delta t < 150\,\mathrm{\mu s}$ was applied.

With a maximum vertex cut of $\rho_{\max} \le 0.5\,\mathrm{m}$ the c_{Gd} results appear to be in good agreement, however, they require a careful interpretation. The results presented in Fig. 5.27 and 5.28 are only representative of a Gd-fraction correction in case the same proportion of hydrogen event "contamination" from the Gamma Catcher is present in
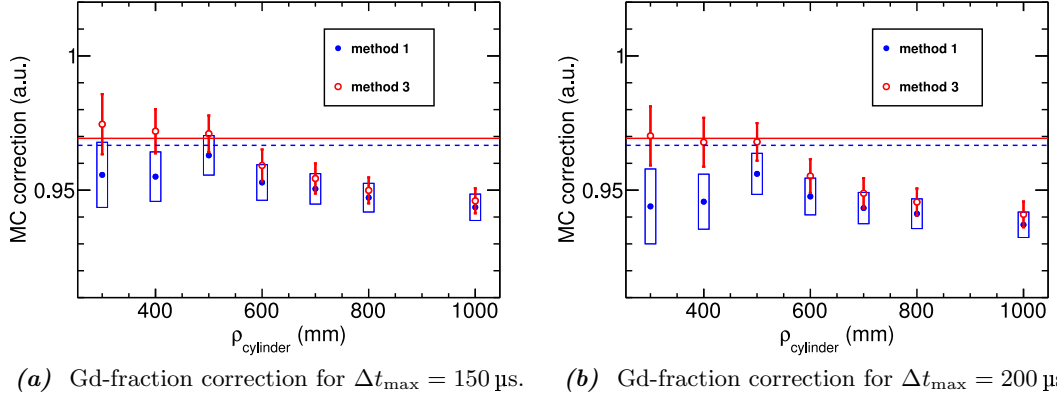
(a) Gd-fraction correction for $\Delta t_{\max} = 150\,\mu s$.   **(b)** Gd-fraction correction for $\Delta t_{\max} = 200\,\mu s$.

Figure 5.27: Gd-fraction correction as a function of the fiducial volume limit $\rho_{\max}$ for fixed maximum correlation times $\Delta t_{\max}$ computed with *method 1* (blue points) and *method 3* (red empty points). The blue dashed line (red solid line) corresponds to the ^{252}Cf result for *method 1* (*method 3*) analyzed with a correlation time cut of $50 < \Delta t < 150\,\mu s$.

(a) Gd-fraction correction for $\rho_{\max} = 500\,mm$.   **(b)** Gd-fraction correction for $\rho_{\max} = 400\,mm$.

Figure 5.28: Gd-fraction correction as a function of the maximum correlation times $\Delta t_{\max}$ for a fixed fiducial volume limit $\rho_{\max}$. The blue dashed line (red solid line) corresponds to the ^{252}Cf result for *method 1* (*method 3*) analyzed with a correlation time cut of $50 < \Delta t < 150\,\mu s$.
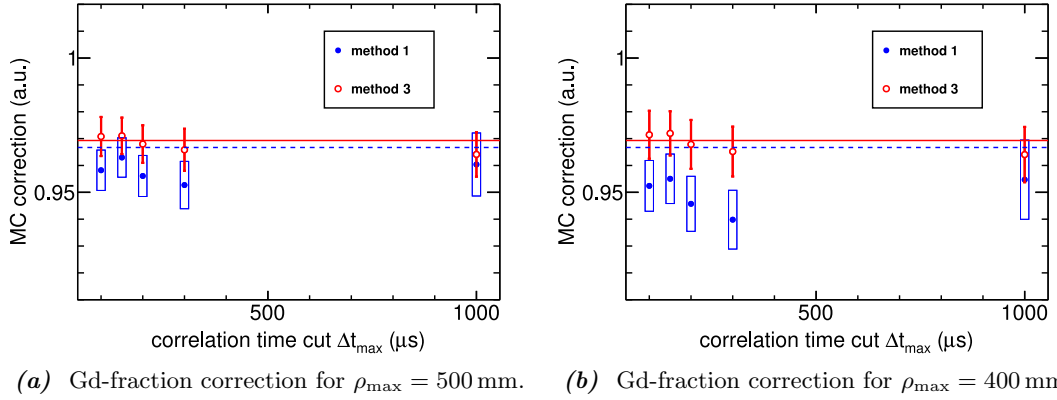
both the spallation data and MC sample. Furthermore, the Gd-capture and H-capture events should be uniformly distributed in the analyzed sub-volume of data and MC, to avoid biases due to discrepancies in the spatial event distributions. In Fig. 5.29 we can see that for $\rho_{\max} \leq 0.5\,m$ the spatial event distributions are approximatively flat, which would support the assumption that the Gd-fractions are reliably measured. The hydrogen event distributions, however, also contain the misreconstructed GC events.

Concerning the contribution of hydrogen events from the GC, a scaling factor could be applied to the MC correction result, in case the fraction of these hydrogen events $s_H = (N_{GC}/N_T)$ (with the GC events N_{GC} and the actual Target events N_T) is known. Since only the denominator of the Gd-fractions f_{Gd} are affected by the hydrogen contamination, the actual MC correction value would be given by

$$c_{Gd}^{corr} = \frac{(f_{Gd})^{spall-n}}{(f_{Gd})^{IBD-MC}} \times \frac{1 + s_{H,spall}}{1 + s_{H,MC}} \, . \qquad (5.60)$$
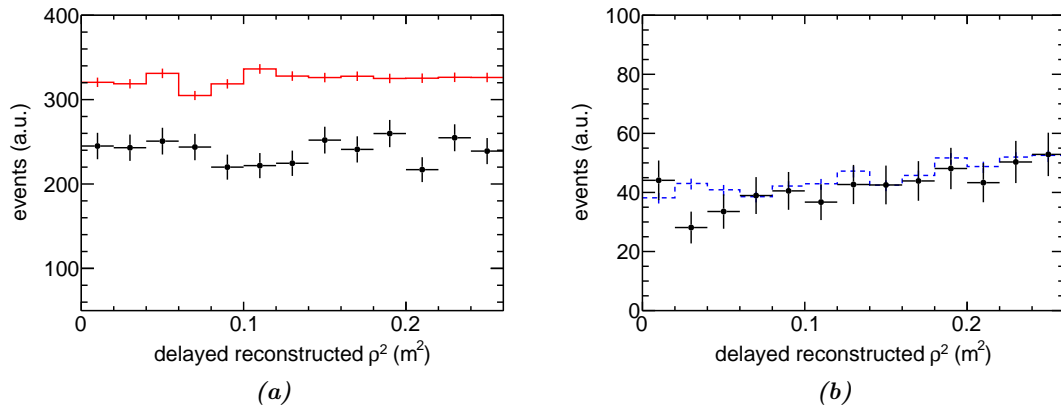
139

Figure 5.29: Reconstructed positions of spallation neutrons and simulated IBD neutron captures with reconstructed vertices inside a cylindrical fiducial volume with $-0.5 < z_{\mathrm{reco}} < 0.2\,\mathrm{m}$ and $\rho_{\mathrm{reco}} < 0.5\,\mathrm{m}$. The plots shows the reconstructed locations as a function of ρ_{reco}^2 for the maximum correlation times $\Delta t_{\mathrm{max}} = 150\,\mu\mathrm{s}$. ***a)*** for spallation neutrons (black circles) and IBD MC (red solid line) neutron captures on gadolinium ($4 < E_{\mathrm{vis}} < 10\,\mathrm{MeV}$), ***b)*** for spallation (black points) and IBD MC (blue dashed line) neutron captures on hydrogen ($1.5 < E_{\mathrm{vis}} < 3\,\mathrm{MeV}$).

The fraction of H-captures can be estimated from a fit of two exponential distributions to the correlation time spectra as e.g. shown in Fig 5.26b. Independently from the reconstructed vertex, the capture times will reveal in which scintillator liquid the neutron energy loss, and probably also the neutron capture, has occurred. If we neglect the influence of any border effects with intermediate capture times close to the acrylic walls, the fit function will be described by

$$f(\Delta t) = A \cdot e^{-\Delta t/\tau_{\mathrm{T}}} + B \cdot e^{-\Delta t/\tau_{\mathrm{GC}}} + C \,, \tag{5.61}$$

with the Target and GC capture time constants τ_{T} and τ_{GC} and the three parameters A, B and C. As a result a fraction of $s_{\mathrm{H,MC}} = (0.127 \pm 0.001)$ is found in the IBD MC and $s_{\mathrm{H,spall}} = (0.110 \pm 0.017)$ with spallation neutrons, for the samples with $\rho_{\mathrm{max}} = 0.5\,\mathrm{m}$ and $\Delta t_{\mathrm{max}} = 1000\,\mu\mathrm{s}$. The uncertainties were obtained from variation of the fit ranges. Hence, the MC correction factor with inclusion of the scaling factor via Eq. (5.60) yields $c_{\mathrm{Gd}}^{\mathrm{corr}} = (0.9460 \pm 0.0190)$, in agreement with the corresponding $^{252}\mathrm{Cf}$ result of $c_{\mathrm{Gd}} = (0.9667 \pm 0.0024\,(\mathrm{stat}))$ for $\Delta t > 50\,\mu\mathrm{s}$.

Concluding this section we have seen that it can be a difficult task to perform a reliable measurement of the Gd-fraction and its correction factor in case the neutron origin is unknown. Careful interpretation of results retrieved from samples selected with vertex cuts on the neutron capture location is necessary, as we try to detect $\sim 3\,\%$ discrepancies in the amount of H-captures. This necessitates to make sure that a discrepancy in data and MC is not induced by reconstruction biases or the event selection. As we can see from the results obtained in this section, good agreement to the $^{252}\mathrm{Cf}$ values is achieved, however, further studies are required to improve the spallation neutron selection in terms of statistics and to investigate the spatial event distributions proving the unbiasedness of the Gd-fraction measurements. One consequence of the spallation neutron study has therefore been the inclusion of a vertex cut on the IBD prompt event in the crosscheck analysis of the Gd-fraction correction using an antineutrino sample (see for results Section 5.4).

5.6 Combination of the efficiency correction results

Two neutron detection related MC normalization corrections were computed for the Gd-III oscillation analysis. One factor is related to the neutron capture fraction on Gd (c_{Gd}), the second factor depends on the delayed event selection criteria (c_{v}). Different neutron samples haven been used to calculate the latter, which is given by the ratio of the volume-wide estimates of the semi-inclusive efficiency obtained from data and MC simulation. From the two datasets of ^{252}Cf fission neutrons and neutrons created in the IBD reaction we yield for the volume-wide correction c_{v}

- $c_{\mathrm{v}}^{\mathrm{IBD}} = 0.9996 \pm 0.0021$ (stat+sys) (study by J. I. Crespo Anadón [89]), and

- $c_{\mathrm{v}}^{\mathrm{Cf\text{-}252}} = 1.0003 \pm 0.0032$ (stat+sys) (Section 5.3.3).

Since these values were obtained from independent analyses, utilizing different data samples and hence also different volume-integrating techniques, the results themselves are considered as independent. The uncertainties of both numbers are dominated by statistical and method dependent contributions of different origin and are therefore uncorrelated.

Both, the ^{252}Cf and the IBD result measure a MC normalization correction consistent with unity, i.e. accurate agreement between the data and MC semi-inclusive efficiencies. As a consequence, no correction factor is applied in the Gd-II analysis in terms of delayed event selection criteria. The ^{252}Cf and IBD neutron results can be combined by calculation of their error weight mean to $c_{\mathrm{v}}^{\mathrm{comb}} = 0.9998 \pm 0.0018$. In order to cover the correction values in the 68 % C.L. interval of the combined result $c_{\mathrm{v}}^{\mathrm{comb}}$, the Gd-III MC normalization correction of the cut dependent neutron detection efficiency is set to[12]:

$$c_{\mathrm{cut}}^{\mathrm{Gd\text{-}III}} = c_{\mathrm{v}}^{\mathrm{Gd\text{-}III}} = 1.0000 \pm 0.0019 \, (\mathrm{stat} + \mathrm{syst}) \,.$$

Together with the Gd-fracton correction factor of

$$c_{\mathrm{Gd}} = 0.9750 \pm 0.0011 \, (\mathrm{stat}) + 0.0041 \, (\mathrm{syst}) \,,$$

and the remaining detection efficiency contributions summarized in Table 5.1, a total correction factor of

$$c_{\mathrm{MC}} = 0.9150 \pm 0.0058 \, (\mathrm{stat} + \mathrm{syst}) \,,$$

is found. This correction factor and its relative uncertainty of

$$\sigma_{\mathrm{det}} = 0.63 \, \% \,,$$

are given as input to the θ_{13} oscillation fit, as pointed out in Eq. (5.1) and Eq. (5.2).

---

[12]Both the $c_{\mathrm{v}}^{\mathrm{comb}}$ and the $c_{\mathrm{cut}}^{\mathrm{Gd\text{-}III}}$ uncertainties are considered to be normal distributed.

5.7 Conclusion and outlook

In this chapter the neutron detection efficiency, the MC normalization correction and
the estimation of related systematic uncertainties were discussed.
Three influences, all considered as independent, contribute to the neutron detection un-
certainty: the fraction of neutrons captured on Gd nuclei, the delayed neutron candidate
selection cuts and border effects at the Target walls caused by neutron migration. This
chapter focused on the first two aspects, the latter is separately addressed in Chapter 7.

In order to handle data to MC discrepancies, MC normalization corrections were in-
troduced. The intrinsic Gd-capture efficiency, the Gd-fraction, is uniform and stable
throughout the fiducial volume and is measured with high precision at the Target center
to avoid the inclusion of border effects induced by Compton scattering related energy
loss. The cut dependent efficiency, on the contrary, depends on the IBD position, which
required the computation of a volume-averaged value. Hence an analysis strategy was
developed rendering possible to estimate the Target-wide efficiency with 0.22 % uncer-
tainty by the use of ^{252}Cf z-axis calibration data solely. In particular the Gd-captures
in the energy range from 3.5 to 10 MeV can be analyzed using the ^{252}Cf source se-
lection presented in Chapter 4 with low background contamination, enabling accurate
efficiency measurements.

A discrepancy of ~ 2.2 % was found in the Gd-fractions of ^{252}Cf data and MC code.
From comparison of an IBD neutron sample to DC-III MC code (Section 5.4 and [89])
a similar discrepancy in the Gd-fraction is observed. A third crosscheck confirmed the
^{252}Cf and IBD neutron results: instead of real data a MC sample of neutrons from
IBD, produced with simulation code featuring an improved neutron modeling called
TRIPOLI4, is used to compute the Gd-fraction and compare it to the predicted fraction
in DC-III MC code [74]. Similar results were obtained in all three independent cases,
consistent within uncertainties.
The MC correction of the Gd-fraction obtained with ^{252}Cf data is in agreement with
the result gained using spallation neutrons. However, the interpretation of the these
values was shown to be difficult, due to the low resolution of the vertex reconstruction
when selecting the neutrons in combination with a minimum time difference of 50 μs to
the last muon required by a spallation neutron analysis.
From data taken with a ^{252}Cf calibration source deployed at the Target center a
Gd-fraction of $(85.30 \pm 0.09\,(\text{stat}))$ % was measured, while it was estimated to be
$(87.49 \pm 0.05\,(\text{stat}))$ % with corresponding simulation code. The MC normalization
correction related to the Gd-fraction discrepancy was hence computed to be $0.9750 \pm 0.0011\,(\text{stat}) \pm 0.0041\,(\text{syst})$.

In past Gd-channel analyses[13] were data to MC discrepancies covered by the systematic
uncertainties without MC normalization correction [98]. The accuracy of the Gd-III
MC correction was anticipated to improve compared to previous Gd-channel analyses
as the factor c_{cut}, correcting systematic discrepancies in the cut dependent efficiencies,
was added to the analysis. Owing to modified Gd-III selection criteria, the correction
c_{cut} of the Gd-III efficiency approach was measured to be consistent with unity, which

---

[13]The method presented in this chapter would yield for the Gd-II selection criteria a cut dependent
correction of $c_{\text{cut}}^{\text{Gd-II}} = 0.9882 \pm 0.0015\,(\text{stat})$ [126].

demonstrates an excellent agreement between the data and MC cut efficiencies. Careful studies of the robustness of the MC correction c_{cut} have been carried out with respect to e.g. the position dependency of the deployment locations, spatial inhomogeneity, the ^{252}Cf event selection and backgrounds, time stability, the efficiency definitions and the computation method itself due to the limitation of the calibration positions available for volume-integration. As a result the systematic uncertainty of c_{cut} was shown to be dominated by the uncertainty on the computation method. Furthermore, the volume-wide correction and the correction calculated at the Target center were found to agree remarkably well. Nevertheless, discrepancies of a few per mil to locally computed correction factors were observed. This triggered an additional study which could prove that the application of a global correction, neglecting local variations in the MC corrections, has negligible impact on the IBD prompt spectral shape.

Besides the ^{252}Cf source also IBD reaction products [89] and hence neutrons of different origin were used to compute c_{cut}. As both results showed a remarkable agreement in the exclusive corrections of the ΔT and ΔR efficiencies, an energy dependent bias of the ^{252}Cf data is not observed. Furthermore, no correlation is found between the MC correction of each individual selection cut. This conclusion could be drawn as the nested exclusive and the isolated exclusive efficiency definitions yield the same correction results. Also, no significant discrepancies are found between the volume-wide corrections based on either the exclusive and the semi-inclusive efficiency definition. Thus the correction result does not depend on whether the volume-integration is performed on each cut efficiency exclusively or on the combined semi-inclusive efficiency. The semi-inclusive approach, however, allows to compute the method dependent systematics at once.

With a near and far detector running, the focus will switch from the comparison of the efficiencies in data and MC to the comparison of efficiency measurements performed in both detectors. The Target liquids of the ND and FD originate from the same batch and both detectors are almost identical concerning the inner volumes' geometry. As the ID materials are alike, neutron and gamma propagation and energy loss are anticipated to be the same in both detectors. Both, near and far, datasets will be calibrated in the energy scale for uniformity and stability. The vertex reconstruction in the two detectors is expected to behave analogous, as much as their optical properties and timing of the scintillators are similar. Hence a cut dependent efficiency correction might no longer be necessary, most probable independent of the choice of the selection ranges. Besides the identicalness of the two detectors will calibration campaigns be conducted with the exact same source in both the near and far detector. Thus, uncertainties due to possible background contaminations will be strongly reduced. Calibration of the two detectors close in time will ensure the source to be in the same condition.
As a consequence, the systematic uncertainties of the neutron detection efficiencies of a ND+FD oscillation analysis will be limited by the detector-to-detector uncorrelated precision the efficiencies can be measured with. Hence, the method dependent systematic uncertainty will dominate the MC correction uncertainty. Concerning the ^{252}Cf volume-wide method, the calibration campaigns should be tailored in their deployment schedule to minimize the volume-integration uncertainty. Long calibration runs at the Target center are favored to keep the Gd-fraction statistical uncertainty low. The systematic uncertainty of the Gd-fraction is expected to be low, in case the same neutron

source is used. As of current knowledge from the amount and location of the points
tested in MC studies, a cut dependent uncertainty down to $0.32\,\%$ can be reached using
^{252}Cf alone. Further studies could optimize this value, e.g. by adding more calibration
points, especially within less than $20\,\mathrm{cm}$ distance to the Target acrylic walls.

Altogether yield the uncertainties on the semi-inclusive efficiency, the Gd-fraction, the
spill-in/out effect, the proton number and further contributions listed in Table 5.1 a
total detection systematic uncertainty of $0.6\,\%$ in the Gd-III analysis based on one
detector. This result is almost a factor two lower compared to the detection efficiency
uncertainty of the last Gd-channel analysis, Gd-II.

In the upcoming ND+FD phase the deficit in neutrino rate and its spectral shape
deformation will be gained from a relative measurement of the two detectors. Any sys-
tematic uncertainty which is correlated between the ND and FD will therefore cancel
out in the θ_{13} analysis. As the proton number uncertainty as well as most of the spill-
in/out uncertainty are anticipated to be fully correlated between the two detectors,
the neutron detection efficiencies will be the dominant source of the detection related
systematic uncertainty. The Gd-III cut dependent MC correction computed with ^{252}Cf
combined with the value obtained from IBD neutrons yields a remarkably low uncer-
tainty of $0.2\,\%$ at present. The upper argumentation indicates that this uncertainty
could be representative for an upcoming ND+FD Gd-channel analysis, and could even
be reduced due to improved calibration techniques. The proposed goal of $0.25\,\%$ on
the cut dependent uncertainty [39] is thus likely to be achieved by the current strategy
of the efficiency analysis. In case that the neutron detection uncertainty will amount
to $0.2\,\%$, in combination with a $0.1\,\%$ uncorrelated uncertainty on the reactor flux and
background uncertainties as in Gd-III scaled from FD to ND, a precision of 0.015 on
$\sin^2 2\theta_{13}$ could be reached after 3 years by a ND+FD measurement (cf. Fig. 3.19).

Chapter 6

Neutron detection efficiency in the H-channel analysis

Based on preliminary selection cuts of an updated H-channel analysis a method was developed using ^{252}Cf fission neutrons to estimate the neutron detection correction integrated over the fiducial volume created by the ν-target (Target) and Gamma Catcher liquid scintillators. In Section 6.1 an introduction to efficiency analysis of neutron captures on H is given. Prior to the ^{252}Cf data analysis the efficiency behavior in the enlarged fiducial volume is studied by means of MC simulation code in Section 6.2. In Section 6.3 the methods used by the ^{252}Cf analysis strategy are presented and first results given in Section 6.4. The optimization of the H-channel selection cuts with respect to the neutron detection uncertainty is discussed in Section 6.5.

6.1 Efficiency analysis of neutron captures on H

The analysis of the H-III detection efficiency follows the same principle as the methods described for the Gd-III detection efficiency in Chapter 5. As for the H-channel oscillation analysis the fiducial volume is expanded from the Target to the Gamma Catcher and beyond[1], the analysis techniques to estimate the volume-wide selection correction $c_{\mathrm{cut,v}}$ have to be extended accordingly. In this chapter two integration strategies are described to estimate the H-III MC normalization correction related to the detection efficiency using ^{252}Cf calibration data. Both methods are set up so that the more complex geometry of the Gamma Catcher volume is taken into account.

6.1.1 Efficiency definitions

For a preliminary set of selection cuts given in Table 6.1, the efficiency definitions can be constructed, following Eq. (5.3) in Section 5.2.2. The prompt event energy had to satisfy $0.5 < E_{\mathrm{p}} < 30\,\mathrm{MeV}$. Just as for the Gd-III analysis the neutron capture efficiency can be separated in a detector inherent efficiency and a cut related efficiency. Both efficiencies depend on the liquid scintillator composition, whereas only the latter can be adjusted by the choice of the neutron selection criteria.

---

[1]IBD reactions in the Buffer liquid and the Gamma Catcher acrylics can contribute to the detected signal, e.g. in case the prompt gammas, the neutron or the neutron capture gammas cross the Buffer boundary and create a coincidence signal in the scintillator liquids.

Table 6.1: Preliminary delayed event selection criteria of the H-III analysis. ΔT corresponds
to the correlation time and ΔR to the correlation distance between the prompt and delayed
event of the coincidence signal. E_d represents the delayed visible energy.

Cut variable	Selection range
Delayed energy	$1.8 < E_\mathrm{d} < 2.6\,\mathrm{MeV}$
Corr. time	$0.5 < \Delta T < 600\,\mathrm{\mu s}$
Corr. distance	$\Delta R < 60\,\mathrm{cm}$

The intrinsic efficiency of the H-channel analysis is given by the H-fraction, which is
directly linked to the Gd-fraction f_Gd (described in Section 5.2.2):

$$f_\mathrm{H} = \frac{N(0.5 < E_\mathrm{delayed} < 3.5\,\mathrm{MeV})}{N(0.5 < E_\mathrm{delayed} < 10\,\mathrm{MeV})} = 1 - f_\mathrm{Gd}\,, \tag{6.1}$$

The H-fraction f_H specifies which fraction of neutron captures occur on hydrogen nuclei.
Selecting subsamples of the delayed neutron captures according to their visible energy
E_delayed, the size of f_H can be estimated as suggested by Eq. (6.1). As the capture
fraction is affected by the nuclear abundances of the relevant capturing isotopes as well
as the related cross sections, the H-fractions in the Target and the Gamma Catcher
liquid will differ greatly.
The cut dependent efficiency can be computed as described in Section 5.2.2 in *exclusive*
and *inclusive* ways, either computing the efficiency related to each selection cut one by
one or combined in a single efficiency definition. Utilizing the *nested exclusive* efficiency
definitions the cut efficiency of the delayed visible energy E_d can be expressed by

$$\varepsilon_{E_\mathrm{d}} = \frac{N(1.8 < E_\mathrm{delayed} < 2.6\,\mathrm{MeV} \ \cap \ 0.25 < \Delta T < 1000\,\mathrm{\mu s})}{N(0.5 < E_\mathrm{delayed} < 3.5\,\mathrm{MeV} \ \cap \ 0.25 < \Delta T < 1000\,\mathrm{\mu s})}\,. \tag{6.2}$$

The cut efficiency on the correlation distance ΔR between the prompt and delayed
events writes

$$\varepsilon_{\Delta R} = \frac{N(1.8 < E_\mathrm{delayed} < 2.6\,\mathrm{MeV} \ \cap \ \Delta R < 0.6\,\mathrm{m} \ \cap \ 0.25 < \Delta T < 1000\,\mathrm{\mu s})}{N(1.8 < E_\mathrm{delayed} < 2.6\,\mathrm{MeV} \ \cap \ 0.25 < \Delta T < 1000\,\mathrm{\mu s})}\,; \tag{6.3}$$

consequently the selection efficiency of the correlation time cut ΔT is given by

$$\varepsilon_{\Delta T} = \frac{N(1.8 < E_\mathrm{delayed} < 2.6\,\mathrm{MeV} \ \cap \ \Delta R < 0.6\,\mathrm{m} \ \cap \ 0.5 < \Delta T < 600\,\mathrm{\mu s})}{N(1.8 < E_\mathrm{delayed} < 2.6\,\mathrm{MeV} \ \cap \ \Delta R < 0.6\,\mathrm{m} \ \cap \ 0.25 < \Delta T < 1000\,\mathrm{\mu s})}\,. \tag{6.4}$$

The *semi-inclusive efficiency*, incorporating the contribution of all selection cuts at the
same time is computed via

$$\varepsilon_\mathrm{semi} = \frac{N(1.8 < E_\mathrm{delayed} < 2.6\,\mathrm{MeV} \ \cap \ \Delta R < 0.6\,\mathrm{m} \ \cap \ 0.5 < \Delta T < 600\,\mathrm{\mu s})}{N(0.5 < E_\mathrm{delayed} < 3.5\,\mathrm{MeV} \ \cap \ 0.25 < \Delta T < 1000\,\mathrm{\mu s})}\,, \tag{6.5}$$

while the *inclusive efficiency* is given by

$$\varepsilon_\mathrm{semi} = \frac{N(1.8 < E_\mathrm{delayed} < 2.6\,\mathrm{MeV} \ \cap \ \Delta R < 0.6\,\mathrm{m} \ \cap \ 0.5 < \Delta T < 600\,\mathrm{\mu s})}{N(0.5 < E_\mathrm{delayed} < 10\,\mathrm{MeV} \ \cap \ 0.25 < \Delta T < 1000\,\mathrm{\mu s})}\,. \tag{6.6}$$

### 6.1.2 Efficiency correction analysis with ^{252}Cf source data

With the ^{252}Cf calibration data estimates of the detection efficiency, corrections for the inner two volumes, the Target and the Gamma Catcher (GC), can be derived. Consequently the Target and GC volume-wide efficiencies are corrected separately. The detection efficiency is considered as a quantity connected to the IBD position, hence the volume-wide efficiencies are gained from weighting the calibration data with respect to the source location.

In contrast to the Gd-channel efficiency analysis[2], neutrons which change the volume are included in the samples of the H-channel efficiency studies. Deployment data recorded with the z-axis system (cf. Section 2.1.4) corresponds to test points of the detection efficiency in the Target. Besides the efficiency of neutrons originating and captured in Target, a detection efficiency measurement will also include the efficiency of spill-out events (see Chapter 7) into the GC or Target acrylics. Likewise, the Guide-Tube (see Section 2.1.4) ^{252}Cf data samples the efficiency in the GC volume. With the Guide-Tube data, the efficiency of neutrons created and captured in the GC as well as the spill-out efficiency into Target and Buffer are measured at the same time. Inaccessible to the ^{252}Cf calibration data is the efficiency of neutrons created in the Buffer liquid as well as in the acrylic vessels and support structures, which will roughly make up 1-2 % of all events. Such border effects need to be studied using MC simulation code and will be incorporated in the final systematic uncertainty on the spill-in/out effect if necessary.

As the 22.5 m^3 GC liquid mainly contains organic molecules composed of hydrogen and carbon at a ratio of 2:1, roughly 99 % of all neutron captures will occur on hydrogen nuclei in the GC scintillator. The Gd-loading of the 10.3 m^3 Target scintillator reduces the relative amount of neutron captures on H to roughly 14 % for neutron captures inside the Target. As both the GC and Target liquid have a similar proton density and neglecting border effects, we would expect that about 6 % of the neutrino signal in the H-channel analysis will arise from IBD reactions in the Target. The main contribution is with ~ 94 % of the signal ascribed to the GC. Hence the detection efficiency corrections in the H-capture analysis will be dominated by the efficiency characteristics of the GC volume, building the main focus of the following analyses. As we will later see, the geometry of the GC volume is more challenging compared to the cylindrical Target vessel. In order to obtain an overview of the efficiency behavior in the GC, simulation studies were conducted, similar to the ones present in Section 5.3.1 of the Gd-III analysis.

Calibration data is available in the upper half of the GC volume at various positions along the deployment tube as shown in Fig. 4.8a. In Fig. 6.1 the prompt and delayed visible energy spectra, as well as the correlation time and distance spectra are shown for data and simulation of all merged Guide-Tube calibration runs.

---

[2]In the Gd-channel analysis it is possible to explicitly study the efficiency of Target events. A cut on the delayed energy isolates the neutrons which are caught on Gd from the H-captures, excluding at the same time neutrons which leave the Target volume and are caught outside.
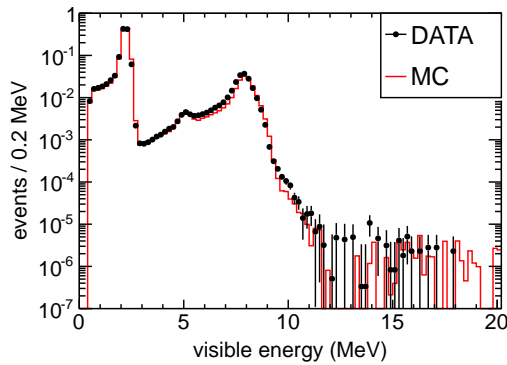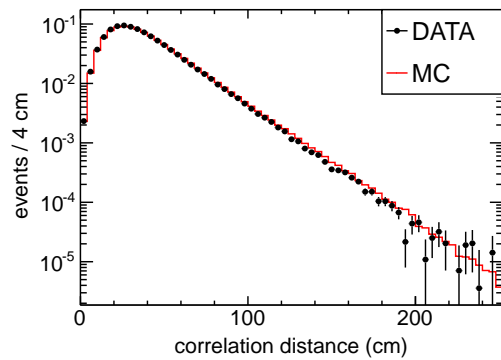
(a) Delayed visible energy. Spectra normalized to the same integral in the region from 1.8 to 2.6 MeV.
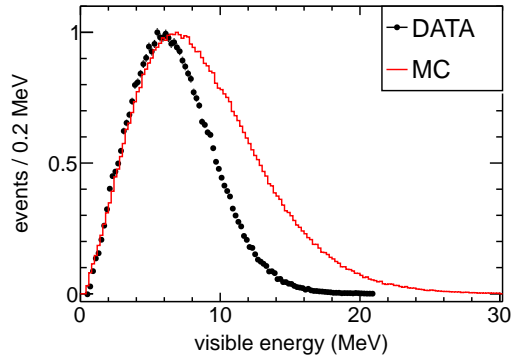
(b) Prompt visible energy.
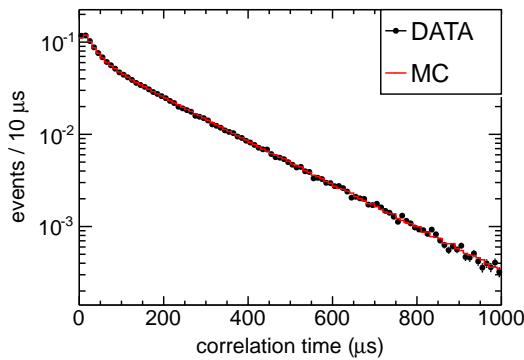
(c) Correlation time. Spectra normalized to the same integral in the region from 20–250 µs.

(d) Correlation distance. Spectra normalized to the same integral in the region from 0–5 m

Figure 6.1: ^{252}Cf spectra of all 38 Guide-Tube deployment runs of the second calibration campaign for deployment data (black points) and MC simulation (red line). The selections of Fig. 6.1a, 6.1c and 6.1d were obtained for a prompt energy cut $E_\mathrm{p} > 4\,\mathrm{MeV}$, whereas for Fig. 6.1b the cut has been $E_\mathrm{p} > 0.5\,\mathrm{MeV}$. The discrepancy in the prompt visible energy is caused by an imperfect gamma spectrum modeling in the MC, but is expected to have no significant influence on the efficiency analyses.

6.2   Volume-wide neutron detection efficiency strategy

In this section we will first discuss the neutron detection efficiency on hydrogen observed in both the Target and GC volumes. To gain knowledge on the efficiency behavior throughout the fiducial volume, a high statistics MC simulation sample is analyzed. Along with the ^{252}Cf deployment positions and values, an analysis strategy is developed to estimate the volume-wide MC correction of the H-channel detection efficiency.

The ^{252}Cf data obtained from calibration with the z-axis and Guide-Tube systems (see Section 2.1.4) will be used to estimate separate MC correction factors for the Target and the GC volumes.

6.2.1 Monte Carlo efficiency studies

Using the same simulated IBD sample as the studies in Chapter 5, the Target and GC efficiency behavior with respect to the preliminary selection cuts presented in Table 6.1 is investigated. Similar to the Gd-channel efficiency studies, the evolution of the detection efficiency is evaluated in z and ρ-direction to meet the cylindrical geometry of the DC detector. Sub-volumes are selected and the local efficiencies computed, in addition the IBD events had to fulfill the following criteria

- the prompt energy E_p has to satisfy $0.5 > E_\mathrm{p} > 20\,\mathrm{MeV}$

- the IBD reaction has to occur inside the sub-volume

- the neutron capture position can occur in any volume

The efficiencies ε_z and ε_ρ are then computed as shown in Fig. 6.2. Since the presence of the chimney on top of the Target affects the results for $\rho = 0$ in the GC, the efficiency is studied inside a hollow cylinder above and below the Target volume, avoiding the chimney region. The efficiencies computed in each sub-volume cell are then treated as local efficiencies at the center of mass positions z_CM and ρ_CM of each sub-volume. For the efficiency ε_z^T inside the Target, we analyze slices with height $z_\mathrm{up} - z_\mathrm{low}$ of a cylinder which is aligned with the detector symmetry axis and has a radius of $300\,\mathrm{mm}$.

$$\varepsilon_z^\mathrm{T}(z_\mathrm{CM}) = \varepsilon(\rho_\mathrm{IBD} < 300\,\mathrm{mm} \ \cap \ z_\mathrm{low} < |z_\mathrm{IBD}| < z_\mathrm{up}) \,. \tag{6.7}$$

The GC efficiencies $\varepsilon_z^\mathrm{GC}$ are studied inside a hollow cylinder with $550\,\mathrm{mm}$ inner and $650\,\mathrm{mm}$ outer radius:

$$\varepsilon_z^\mathrm{GC}(z_\mathrm{CM}) = \varepsilon(550\,\mathrm{mm} < \rho_\mathrm{IBD} < 650\,\mathrm{mm} \ \cap \ z_\mathrm{low} < |z_\mathrm{IBD}| < z_\mathrm{up}) \,. \tag{6.8}$$

The center of mass position in z-direction is given by $z_\mathrm{CM} = \frac{1}{2} \cdot (z_\mathrm{up} - z_\mathrm{low})$. As the Target height and diameter differ only slightly and the GC thickness at the top and the side of the GC vessel are almost similar, normalized distances relative to the Target wall $\hat{d}$ are computed taking the top and bottom slopes of the acrylic vessels into account. These distances represent the shortest perpendicular distance to the acrylic surfaces[3] and are calculated such, that

- $\hat{d} = -1$ corresponds to the Target center,

- $\hat{d} = 0$ represents the Target wall,

- $\hat{d} = 1$ corresponds to the Gamma Catcher wall.

Note that the distance variable inside the Target is of opposite sign than for the Gd-channel studies in Section 5.3.1. The efficiency ε_ρ is given by

$$\varepsilon_\rho(\rho_\mathrm{CM}) = \varepsilon_z(r_\mathrm{inner} < \rho_\mathrm{IBD} < r_\mathrm{outer} \ \cap \ |z_\mathrm{IBD}| < 150\,\mathrm{mm}) \,, \tag{6.9}$$

where r_inner refers to the inner radius and r_outer to the outer radius of the sub-volume selection. The center of mass in ρ-direction is given by $\rho_\mathrm{CM}^2 = \frac{1}{2} \cdot (r_\mathrm{inner}^2 + r_\mathrm{outer}^2)$. In

---

[3]Outside the Target the shortest perpendicular distance to the Target acrylic wall or corner is computed.
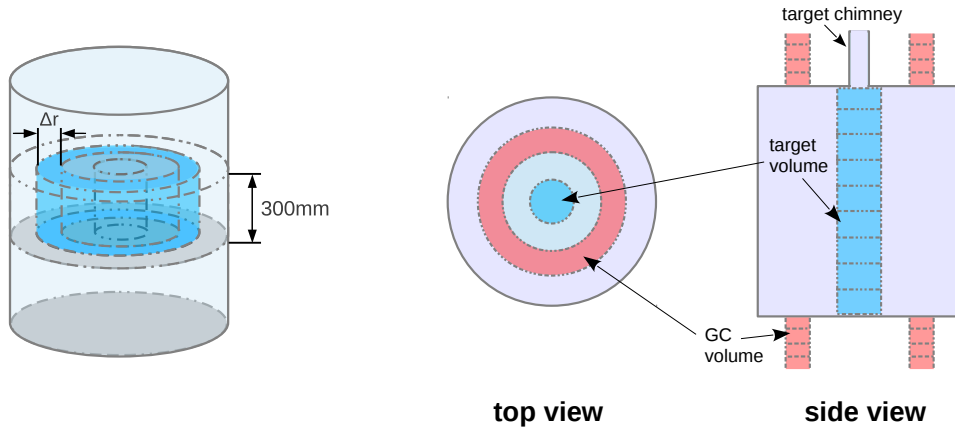
(a) Division into hollow cylinders to investigate the efficiency evolution $\varepsilon(\rho)$.

(b) Division into volume segments to study $\varepsilon(z)$. The sub-samples inside the Target are sub-volumes (light blue) of a cylinder along the z-axis, the sub-volumes inside the GC are contained in a hollow cylinder (light pink) on top and below the Target. **Left:** Top view. **Right:** Side view.

Figure 6.2: Sketch of the sub-sample selection to study the efficiencies ε_z and ε_ρ in Target and Gamma Catcher.

Fig. 6.3 the inclusive efficiency as defined in Eq. (6.6) is shown. Qualitatively, the z and ρ-behaviors are in good agreement, the efficiency is about $\sim 10\,\%$ in the Target and remains stable over a wide volume range when approaching the acrylic wall. Due to spill-out of neutrons, the efficiency sharply rises close to the Target wall. Inside the GC the detection efficiency reaches its maximum value of almost $75\,\%$ at about $10\,\mathrm{cm}$ from the Target wall and slowly drops to $\sim 60\,\%$ at the GC boundary. The efficiency in ρ-direction tends to be 2-3 % larger than in the z-direction at the top and bottom of the GC volume. On one hand, it is possible that detection efficiency observed in z-direction is lower due to the off-axis location of the sub-samples of Eq. (6.8) inside a hollow cylinder. Furthermore could this condition be enhanced by the tightness of particular selection cuts or the detection mechanisms themselves.

In order to investigate this observation further, the efficiency variation of the hydrogen capture fraction and of each cut dependent efficiency is shown in Fig. 6.4 and 6.5. The H-fraction and the efficiency of the correlation time cut are both expected to possess a position dependency which is dominated by the neutron movement. Both efficiencies appear to be constant in Target and GC and the Target and GC efficiencies are connected by a rather steep slope at the Target wall. Owing to the presence of Gd in the Target scintillator the ΔT efficiency in the Target is close to $100\,\%$, whereas the H-fraction is about $12\,\%$. Moreover, a good agreement is found between the ε_z and ε_ρ. In contrast to this, the delayed energy and the correlation distance efficiency show a less constant behavior, especially in the GC volume. Discrepancies are visible in the efficiencies in z and ρ-directions, which could be explained by the fact that both efficiencies are rather influenced by the gamma detection process than by the neutron physics. As a single $2.2\,\mathrm{MeV}$ gamma is produced upon H-capture, the related efficiencies might be affected by the gamma energy depositions to happen within several few $10\,\mathrm{cm}$
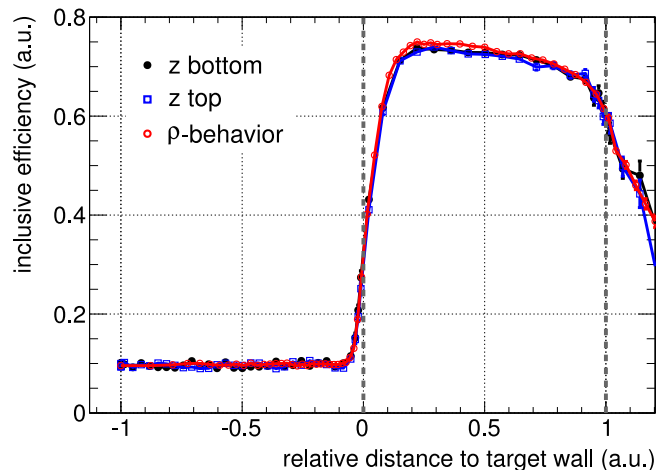
Figure 6.3: Inclusive efficiency in the Target and GC volume. The efficiency behavior in ρ-direction (red), and for the z-direction at the Target top (blue) and bottom (black) are given separately.

of travel distance in liquid scintillators, causing energy loss in the acrylics, gamma spill-out[4] as well as a stronger bias of the vertex reconstruction compared to a multiple-gamma event. Discrepancies between GC top and bottom could be introduced by the influence of the acrylic feet at the bottom of the Target vessel on the light detection and vertex reconstruction. Nevertheless, the detection efficiency shapes shown in Fig. 6.5 are dependent on the selection cuts. Wider open selection criteria would modify and could even flatten the efficiency evolution with respect to the spatial position. The delayed energy efficiency decreases as the Target and GC acrylic walls are approached. This behavior is most likely the result of non-scintillating energy loss in the acrylic structures. At the GC walls, the gamma can escape into the insensitive Buffer volume. The gain in energy containment of the delayed neutron detection at the GC inner border, however, can be explained by the increase in neutron spill-out to the GC volume. In the two bottom graphs of Fig. 6.5 the efficiency of the correlation distance cut is shown. It is observed to monotonically increase from the Target center to the GC outer boundary, where it begins to drop off. As the linear distance between neutron production location and neutron detection is known to be similar in MC simulation for Target and GC (see Section 7.5.1), this rising trend might be caused by the enhanced efficiency of light detection in the GC in combination with a reconstructional bias towards the Target center [187].

6.2.2 Target volume-wide efficiency

The volume-wide efficiency in the Target will be estimated following the technique described in Section 5.3.2. Calibration data taken with the z-axis system is used to infer the efficiency reduction shape along the z-direction. The z-shape is used to estimate the full Target efficiency with ^{252}Cf fission neutrons of both calibration data and simulation code (cf. Fig. 5.11). From these results a Target related MC correction factor of the

---

[4]The gamma might leave the sensitive detector volume before depositing its full energy.
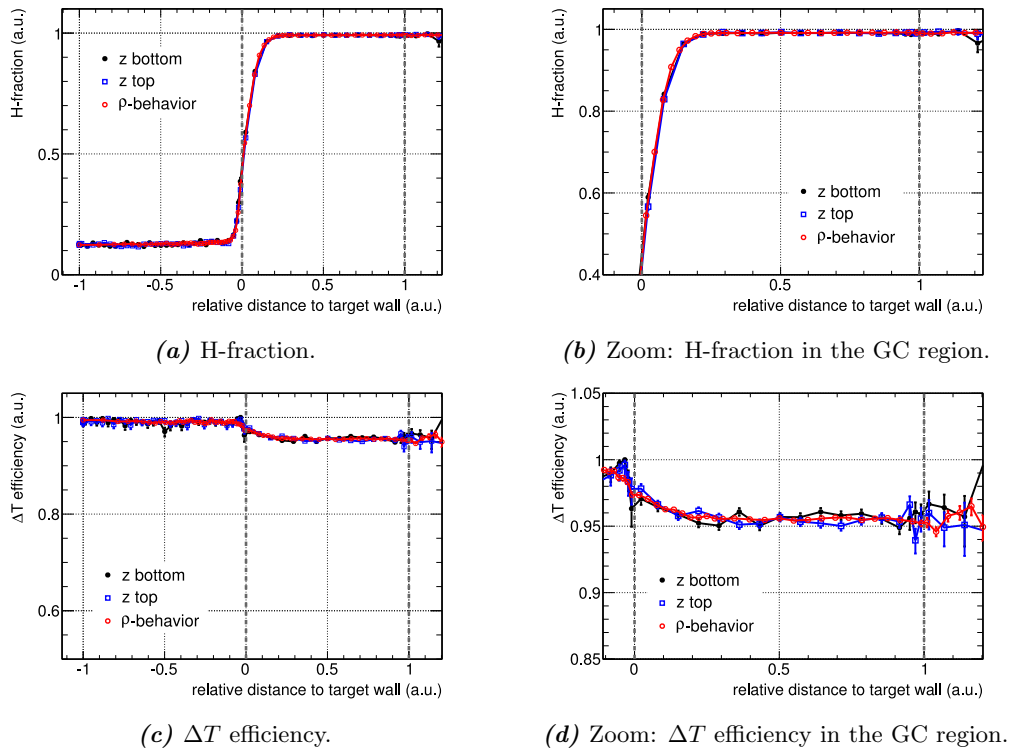
(a) H-fraction.

(b) Zoom: H-fraction in the GC region.

(c) ΔT efficiency.

(d) Zoom: ΔT efficiency in the GC region.

Figure 6.4: Neutron physics dominated efficiencies.

(a) Delayed energy efficiency.

(b) Zoom: Delayed energy efficiency in the GC.

(c) ΔR efficiency.

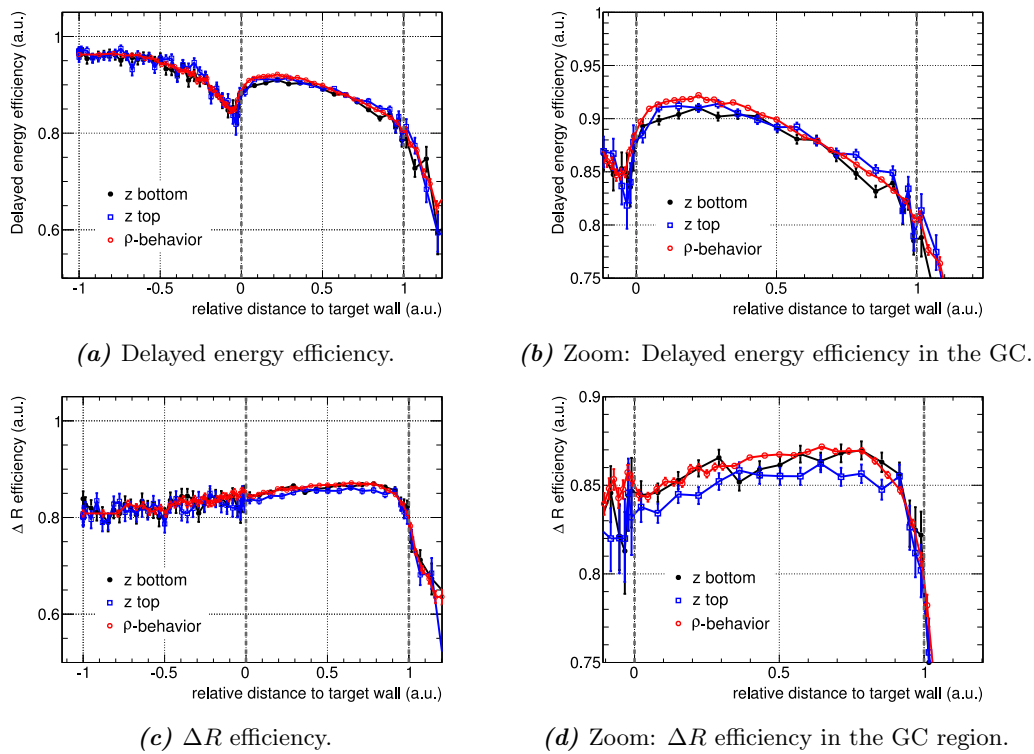*(d)* Zoom: ΔR efficiency in the GC region.

Figure 6.5: Gamma physics and vertex reconstruction influenced efficiencies.

detection efficiency in the H-channel analysis can be computed and at a later stage combined with the correction factor of the GC volume.

6.2.3 Efficiency analysis in the Gamma Catcher volume

The development of a method to estimate the volume-wide MC normalization corrections of the detection efficiency strongly depends on the data set available for analysis. In the case of calibration data, the deployment positions are of particular relevance. Just as for the Gd-III efficiency analysis, the deployment runs of the second calibration campaign are used to compute the central value of the H-III correction of the MC detection efficiency. The calibration positions of the second campaign are shown in Fig. 6.6a. Two black encircled data points have been excluded in the analysis, as they do not fit in the two chosen parametrizations presented in the following.
In order to obtain a clearer arrangement of the data points, the Guide-Tube sample is divided corresponding to three subregions in the GC volume (Fig. 6.6b):

- a top (bottom) region right above (below) the Target vessel;

- a side region next to the Target vessel for $\rho > r_{\text{Target}}$ (with $r_{\text{Target}} = 1150\,\text{cm}$), limited in z-direction by the Target dimensions;

- the GC edge, which has no boundary adjacent to the Target volume expect for the Target corner.

For these three subgroups the ^{252}Cf semi-inclusive efficiency is plotted as a function of the deployed distance to Target center R ($R = \sqrt{x^2 + y^2 + z^2}$ for the source deployment coordinates (x, y, z)) in Fig. 6.7a and the shortest deployed distance perpendicular to the Target wall or corner d in Fig. 6.7b. Runs which agree either in R or d were merged on the event basis before efficiency analysis, the MC statistics at these points was adjusted according to the variations in runlength of the data. We can see that for both parametrizations efficiency patters within each subgroup can be found. Whereas the runs at the edge and side of the GC plotted with respect to R exhibit at intermediate R an abrupt change in the efficiency and appear more scattered for large R, the efficiencies follow as a function of d a smooth trend. Differences are observed for the calibration runs taken at the GC top compared to data points in the other sub-volumes. Furthermore, the top points show a steady trend for the R-parametrization, which could be a consequence of a rather spherical spatial dependence of the gamma influenced efficiencies. How smooth an efficiency trend is described by a certain parametrization is hence determined by how well the parametrization reflects the geometrical efficiency dependence at the particular calibration positions. The difference in spatial dependency of the neutron dominated and gamma influence efficiencies is visualized when the exclusive efficiencies are plotted as a function of d and R as in Appendix D.3.
Overall a good agreement in the efficiency trend is observed for data and MC simulation.

Based on these two parametrizations methods to compute the volume-wide efficiencies and correction factors can be derived. Both methods weight the calibration results with respect to the chosen volume representation relative to R or d and will be presented in the next section.

(a) Guide-Tube ^{252}Cf calibration positions of the second campaign in the (z, ρ) plane. The black marked data points were excluded.

(b) Subdivision of the Gamma Catcher volume into top (red), edge (blue) and side (green) region.
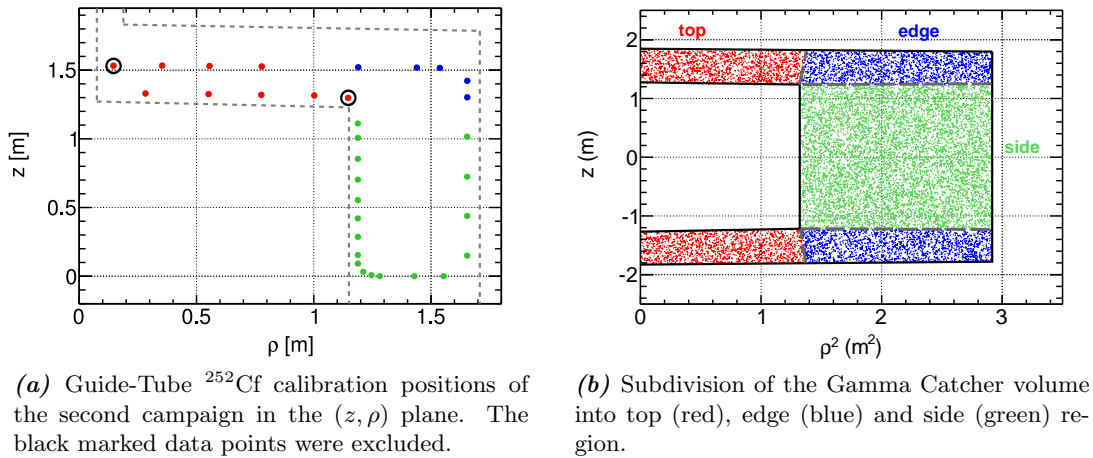
Figure 6.6: Guide-Tube calibration data in the Gamma Catcher volume and subdivision of the Gamma Catcher data into top (red), edge (blue) and side (green) data.
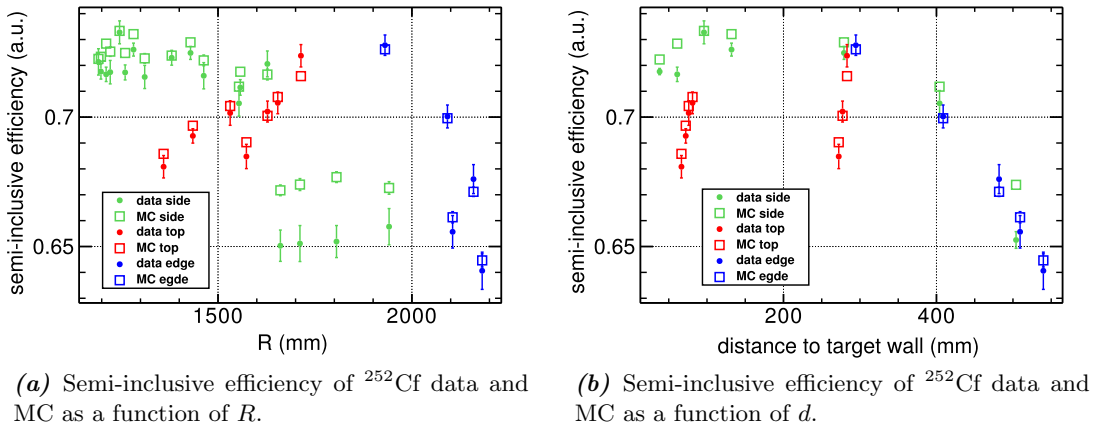

(a) Semi-inclusive efficiency of ^{252}Cf data and MC as a function of R.

(b) Semi-inclusive efficiency of ^{252}Cf data and MC as a function of d.

Figure 6.7: Guide-Tube ^{252}Cf calibration data and simulation, seperated in top (red), edge (blue) and side (green) region data points.

6.3 H-channel volume-wide efficiency correction

In this section the methods applied for a computation of the cut efficiency dependent volume-wide MC correction in the GC volume will be presented. Furthermore, the systematic uncertainties associated with the volume-wide integration approaches are discussed. The combination with the Target results and the H-fraction corrections will be addressed at the end of this section.

The GC results are calculated using ^{252}Cf calibration runs of the second campaign, taken with the Guide-Tube system (see Fig. 6.6a). Two data points (marked in Fig. 6.6a by black circles) were removed, as they are not representative for a volume-wide weighting using a parametrization in the variable d (cf. Section 6.3.2). One removed data point is located close to the Target chimney, the other one at the Target top corner[5].

---

[5]The computation of the variable d does not take into account the presence of the Target chimney and the data point close to the Target corner will yield a low value for d, but is mainly surrounded by GC liquid, which is different for most of the other values with low d.

Since the Guide-Tube deployment samples the GC volume locally at particular positions, data points representing a larger sub-volume of the GC should be weighted accordingly. A volume-wide estimate of the cut dependent efficiency is obtained from weighted integration of the interpolated local calibration results, taking into account the geometrical dimensions of the GC volume. Therefore weighting functions are used in the integration, which are computed according to the spatial parametrization utilized to obtain the interpolated efficiency curves. The two volume-wide efficiency approaches presented in this section are parametrized with respect to

- the deployed distance to Target center $R = \sqrt{x^2 + y^2 + z^2}$ (for the calibration coordinates (x, y, z)),

- the shortest deployed distance perpendicular to Target wall or corner d.

As discrepancies in the efficiencies of the top and side sub-volume of the GC have been observed with ^{252}Cf data (Fig. 6.7), the Guide-Tube dataset is divided in two subsamples and the volume-wide estimates computed for comparison. The GC is split into the "GC top/bottom" and the "GC side" volume (see also Fig. 6.8a), dividing the total GC volume in two nearly equally sized sub-volumes. Separation of the dataset in calibration positions at the top and side of the GC yields two subsets which cover respectively almost the full parameter range in d and R. In addition, a separation of the dataset provides smoother interpolation curves for each subset.

With the methods presented in the next subsections, volume-wide estimates of the GC efficiency is computed for data ($\varepsilon_{\text{data}}^{\text{GC}}$) and MC ($\varepsilon_{\text{MC}}^{\text{GC}}$). The volume-wide MC normalization correction is then similar to Eq. (5.35) given by the ratio:

$$c_{\text{v}}^{\text{GC}} = \frac{\varepsilon_{\text{data}}^{\text{GC}}}{\varepsilon_{\text{MC}}^{\text{GC}}} \ . \tag{6.10}$$

6.3.1 R-weighted volume-wide efficiency correction

The R-weighted estimation of the volume-wide efficiency correction was inspired by the method used to compute the MC correction in the H-II analysis [198]. There, the weighted integration was performed on the local MC correction factors of the first calibration campaign's dataset. In contrast to this, global efficiency estimates will be calculated first in the analysis presented here. In a second step, MC correction factors related to the cut dependent neutron detection can be computed. The analysis can be done using either the full set of calibration runs or subsamples, divided in deployment positions at the GC top or side. From the comparison of the MC corrections obtained using different data subsets and from comparison to values obtained with another spatial parametrization (see Section 6.3.2), a method dependent systematic uncertainty can be evaluated (discussed in Section 6.3.3).

The weighting functions $w(R)$ (Fig. 6.8b) are determined by counting the number of simulated IBD reactions enclosed by spherical shells, either in the full GC volume, the GC top part or the GC side (Fig. 6.8a). Taking into account the minimum and maximum value of R reached by the calibration locations, 91.6 % of the GC volume is technically covered by the interpolation of the ^{252}Cf deployment positions (Fig. 6.8c).

The volume-wide correction factors can then be calculated in two different ways. The first one utilizes top/side separated datasets $\varepsilon_x^{\text{top}}(R)$ and $\varepsilon_x^{\text{side}}(R)$ (with $x = $ data, MC)
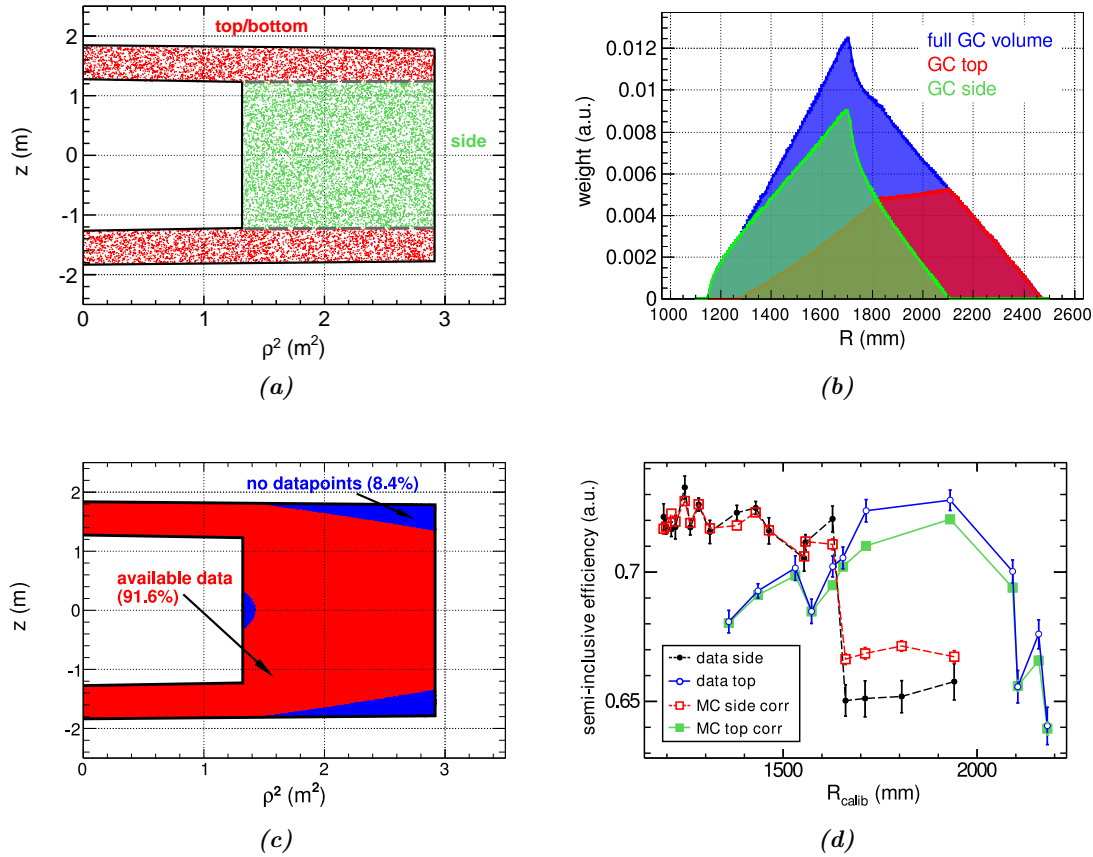
Figure 6.8: *R*-weighted volume-wide efficiency method. ***a)*** Gamma-catcher sub-volumes.
b) Weighting functions $w(R)$. ***c)*** *R*-weighting volume coverage. ***d)*** Top/side separated ^{252}Cf
deployment points with respect to the calibration position R_{calib}: The semi-inclusive efficiency
is plotted for data and MC runs taken at the GC side and top. The MC values were corrected
using c_{v} from Eq. (6.13).

(Fig. 6.8d) and weighting functions $w_{\text{top}}(R)$ and $w_{\text{side}}(R)$ to compute the two MC
normalization corrections

$$c_{\text{v}}^{\text{top}} = \frac{\int \varepsilon_{\text{data}}^{\text{top}}(R) \cdot w_{\text{top}}(R) \, \mathrm{d}R}{\int \varepsilon_{\text{MC}}^{\text{top}}(R) \cdot w_{\text{top}}(R) \, \mathrm{d}R} \,, \tag{6.11}$$

and

$$c_{\text{v}}^{\text{side}} = \frac{\int \varepsilon_{\text{data}}^{\text{side}}(R) \cdot w_{\text{side}}(R) \, \mathrm{d}R}{\int \varepsilon_{\text{MC}}^{\text{side}}(R) \cdot w_{\text{side}}(R) \, \mathrm{d}R} \,. \tag{6.12}$$

The two MC correction factors are then combined to one volume-wide correction

$$c_{\text{v}}^{\text{GC}} = s_{\text{top}} \cdot c_{\text{v}}^{\text{top}} + s_{\text{side}} \cdot c_{\text{v}}^{\text{side}} \,, \tag{6.13}$$

using the sub-volume weights $s_{\text{top}} + s_{\text{side}} = 1$.
The second integration strategy uses all data points in the full GC volume by one
integration:

$$c_{\text{v}}^{\text{GC}} = \frac{\int \varepsilon_{\text{data}}(R) \cdot w(R) \, \mathrm{d}R}{\int \varepsilon_{\text{MC}}(R) \cdot w(R) \, \mathrm{d}R} \,, \tag{6.14}$$

where $w(R) = w_{\text{top}}(R) + w_{\text{side}}(R)$, as represented by the blue function in Fig. 6.8b.

6.3.2 d-weighted volume-wide efficiency correction

The second method to estimate the volume-wide efficiency and MC normalization correction uses a spatial parametrization with respect to the shortest distance d from the deployment position perpendicular to the Target wall or corner. The weighting functions $w(d)$ are determined by counting the number of IBD reactions in MC simulation for which $d \in [d, d+\Delta d]$. Similar to the R-weighted integration (Section 6.3.1 were the $w(d)$ computed for either the full GC volume, the GC top and the GC side sub-volumes (see Fig. 6.9a and 6.9b). In total 85 % of the GC volume is technically covered by the ^{252}Cf deployment sample, ranging from the lowest value of d to the maximum d reached by the calibration positions (Fig. 6.9c).

The volume-wide correction factors can then be calculated by using all or only subsamples of the data. The first strategy, splitting into top and side data points $\varepsilon_x^{\text{top}}(d)$ and $\varepsilon_x^{\text{side}}(d)$ (with $x = $ data, MC) (Fig. 6.9d) and weighting functions $w_{\text{top}}(d)$ and $w_{\text{side}}(d)$, to compute two separate MC normalization corrections

$$c_{\text{v}}^{\text{top}} = \frac{\int \varepsilon_{\text{data}}^{\text{top}}(d) \cdot w_{\text{top}}(d)\,\mathrm{d}d}{\int \varepsilon_{\text{MC}}^{\text{top}}(d) \cdot w_{\text{top}}(d)\,\mathrm{d}d}, \tag{6.15}$$

and

$$c_{\text{v}}^{\text{side}} = \frac{\int \varepsilon_{\text{data}}^{\text{side}}(d) \cdot w_{\text{side}}(d)\,\mathrm{d}d}{\int \varepsilon_{\text{MC}}^{\text{side}}(d) \cdot w_{\text{side}}(d)\,\mathrm{d}d}. \tag{6.16}$$

The top and side MC correction factors are then combined to one volume-wide correction

$$c_{\text{v}}^{\text{GC}} = s_{\text{top}} \cdot c_{\text{v}}^{\text{top}} + s_{\text{side}} \cdot c_{\text{v}}^{\text{side}}, \tag{6.17}$$

with sub-volume weights $s_{\text{top}} + s_{\text{side}} = 1$.

Another integration strategy uses the full ^{252}Cf calibration dataset in a single full volume integration via

$$c_{\text{v}}^{\text{GC}} = \frac{\int \varepsilon_{\text{data}}(d) \cdot w(d)\,\mathrm{d}d}{\int \varepsilon_{\text{MC}}(d) \cdot w(d)\,\mathrm{d}d}, \tag{6.18}$$

with $w(d) = w_{\text{top}}(d) + w_{\text{side}}(d)$. Likewise we can only use the top data and weight the efficiency values with respect to the full volume weighting function $w(d)$:

$$c_{\text{v}}^{\text{GC}} = \frac{\int \varepsilon_{\text{data}}^{\text{top}}(d) \cdot w(d)\,\mathrm{d}d}{\int \varepsilon_{\text{MC}}^{\text{top}}(d) \cdot w(d)\,\mathrm{d}d}. \tag{6.19}$$

Or use the side data solely weighted by the volume weighting function $w(d)$:

$$c_{\text{v}}^{\text{GC}} = \frac{\int \varepsilon_{\text{data}}^{\text{side}}(d) \cdot w(d)\,\mathrm{d}d}{\int \varepsilon_{\text{MC}}^{\text{side}}(d) \cdot w(d)\,\mathrm{d}d}. \tag{6.20}$$

The first integration presented in Eq. (6.17) will be used as default d-weighted volume-wide method. The systematic uncertainty estimation will be discussed in the next paragraph, followed by a subsection dealing with the combination of the Target and GC results.
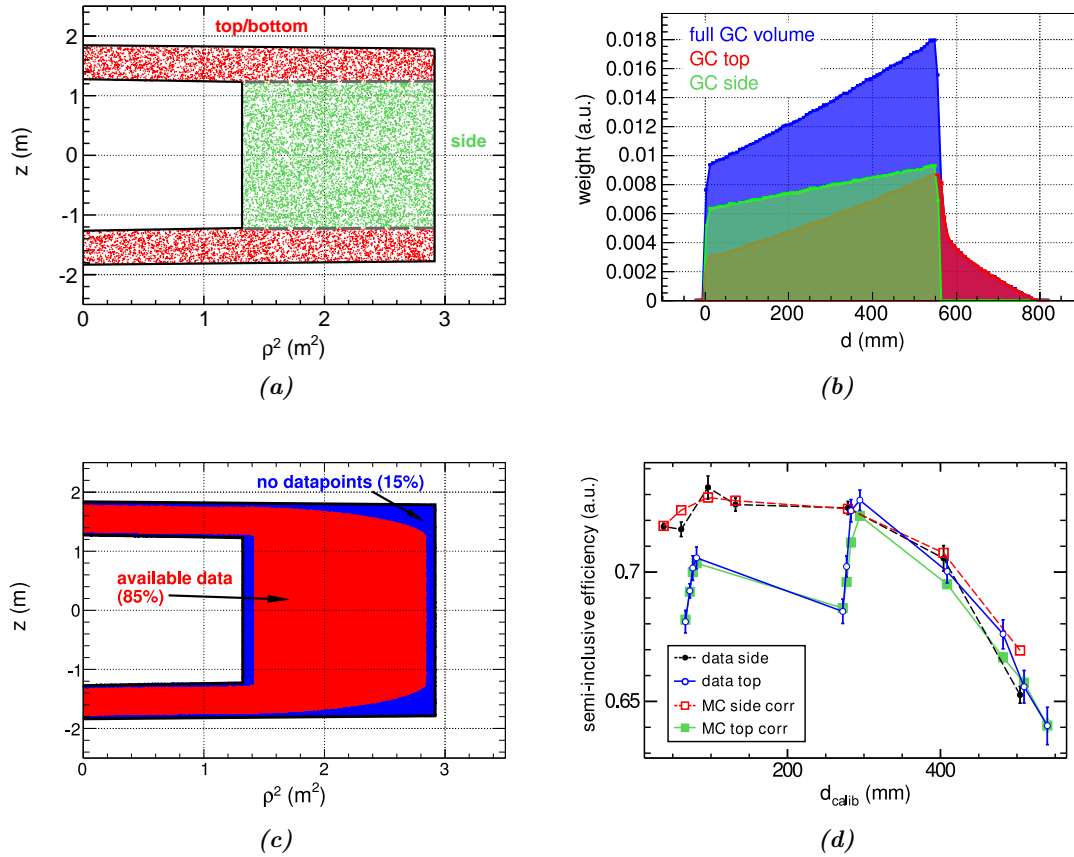
Figure 6.9: d-weighted volume-wide efficiency method. *a)* Gamma-catcher sub-volumes.
b) Weighting functions $w(d)$. *c)* d-weighting volume coverage. *d)* Top/side separated ^{252}Cf
deployment points with respect to the calibration position d_{calib}: The semi-inclusive efficiency
is plotted for data and MC runs taken at the GC side and top. The MC values were corrected
using c_{v} from Eq. (6.17).

6.3.3 Systematic uncertainty estimation

The volume theoretically covered by the d-weighted method is $6.6\,\%$ lower than for
the R-weighted method. However, the parametrization with respect to d is geometri-
cally stronger motivated. Especially the data points at the GC side and edge exhibit a
smooth trend in the semi-inclusive efficiency. Hence, the d-weighted integration method
of Eq. (6.17) is used to compute the central value of the MC normalization correction.
As we will later see, wider open cuts will lead to a smoothening of the efficiency inter-
polation at the GC top, evaluated with respect to the variable d.

In order to cover the correction factors obtained by any of the other calculation strate-
gies in Eq. (6.13), (6.14), (6.18), (6.19) and (6.20), the largest discrepancy between the
central value and the other results will be assigned as $68\,\%$ C.L. systematic uncertainty.
Other contributions to the systematic uncertainty are

- cut dependent: variation of the selection cuts might not only change the efficien-
  cies but also impact the MC corrections.

- background dependent: using different prompt energy cuts changes the amount of backgrounds in the ^{252}Cf data. The low energy correlated background discussed at the end of Section 5.4 is subject to the H-III ^{252}Cf data. Since the H-fraction is about $14\,\%$ in the Target, the Target results might be stronger affected by this background, which amounts to about $0.4\,\%$ of the total ^{252}Cf neutron sample. In contrast to the Target is the background contribution, because of the high H-fraction, on the few per mil level in the GC. As the Target results constitute only $\sim 6\,\%$ of the total MC correction, possible biases of the Target values will affect the combined result only slightly. In total a maximum uncertainty of $0.55\,\%$ on the overall preliminary MC corrections is estimated. In the final analysis these backgrounds can be removed by more sophisticated efficiency definitions (e.g. use of the exclusive efficiency definition and inclusion of a Δt cut in the delayed energy efficiency, along with a test of non-correlation of the exclusive efficiencies).

- stability dependent: the first calibration campaign results can be used to cross-check the stability of the H-III MC correction.

- neutron data dependent: the volume-wide correction factor has to be compared to the result obtained with an IBD neutron sample.

The method dependent uncertainty of the Target efficiency amounts to $0.94\,\%$ and was estimated as done for 5) in Section 5.3.3.

6.3.4 Detector-wide H-capture efficiency: combination of Target and Gamma Catcher correction

The total efficiency in the H-channel analysis is in principle represented by the product of the cut dependent efficiency and the H-fraction (similar to Eq. (5.13) in the Gd-channel analysis). Furthermore, the global MC normalization correction of the neutron detection efficiency would be given by the product of a cut dependent and a H-fraction related MC correction factor (as for Gd-III in Eq. (5.15)). Since the fiducial volume of the H-channel analysis includes the Target and the GC, the global MC correction has to incorporate the correction factor results of both sub-volumes. In the case of the cut dependent efficiency correction, the combination of c_v^T and c_v^{GC} is computed by

$$c_v = c_v^T \cdot 0.062 + c_v^{GC} \cdot 0.938 \,. \tag{6.21}$$

The Target and GC weights in Eq. (6.21) were computed using MC simulation and represents the fraction of events with IBD in the particular sub-volume and the neutron being captured on a hydrogen nucleus in any volume.

Since a global MC correction can introduce a systematic bias of the prompt energy spectral shape (see also Section 5.3.3), a dedicated study was performed by A. Collin [76], using MC data along with the preliminary normalization corrections presented in this thesis. The study showed that with a global factor correcting both H-fraction and cut dependent efficiency discrepancies, in the low energy bins around $\sim 1\,\mathrm{MeV}$ deviations of up to $1\,\%$ could be observed between the locally and globally corrected prompt spectra. In the higher energy bins differences of about $-0.5\,\%$ were detected. This effect could be reduced to a $\pm 0.05\,\%$ discrepancy, in case the Target and the GC spectra were separately corrected with their corresponding H-fraction correction factor. The Target
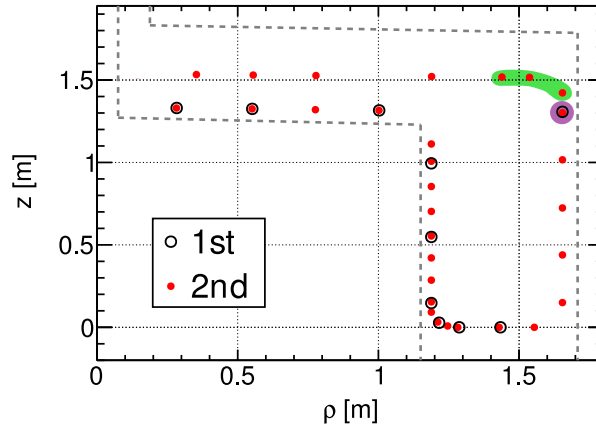
Figure 6.10: GuideTube ^{252}Cf deployment positions of the first (black circles) and second (red bullets) calibration campaign in the (z, ρ) plane, used for MC correction computation in the Gamma Catcher volume. The runs used to calculate the H-fraction correction are highlighted for the first campaign in purple and for the second campaign in green.

spectrum is given by the event with IBD reaction and neutron capture inside the Target volume, whereas the GC spectrum is represented by any other prompt-delayed event configuration.

As a result, separate MC correction factors of the H-fraction will be applied to the MC predicted Target and GC spectra. The cut dependent MC correction will, however, be applied globally, as computed via Eq. (6.21).

6.4   Monte Carlo normalization correction results

This section will deal with the result of the MC normalization correction, removing global discrepancies in the neutron detection efficiencies observed with ^{252}Cf calibration data and simulation code. The results of the cut dependent correction term is based on preliminary H-channel selection criteria, as presented in Table 6.1. Furthermore, the semi-inclusive efficiency of Eq. (6.5) is used as default efficiency definition. The statistical uncertainty is propagated to the final result according to the technique discussed in Section 5.3.2.
In Fig. 6.10 the GuideTube ^{252}Cf deployment positions used to compute the GC cut dependent and H-fraction MC correction factors are given. The corresponding run numbers and lengths are listed in Appendix B. The calibration runs used to compute the Target MC correction are the same as in the Gd-III efficiency analysis (Fig. 5.5 in Section 5.3).

6.4.1   H-fraction Monte Carlo normalization

As suggested in Section 6.3.4, the Target and Gamma Catcher IBD prompt event normalizations are separately corrected for discrepancies in the H-fraction. The Target
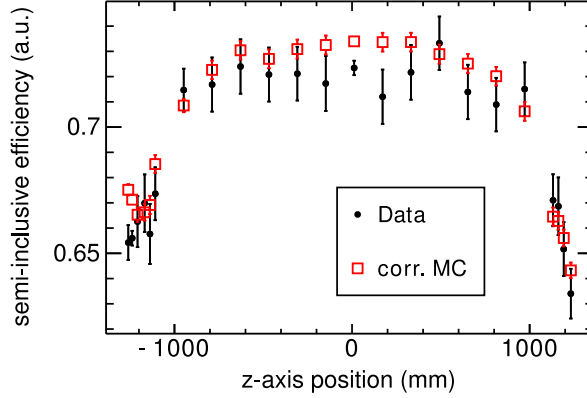
Figure 6.11: Data and MC semi-inclusive efficiency from ^{252}Cf calibration as a function of the theoretical deployed z-coordinate z_{calib}. The black bullets show the efficiency results of the ^{252}Cf data runs, the red open boxes the values from ^{252}Cf MC simulation. All uncertainties are statistical, a position dependent uncertainty is not included.

value can be derived from the Gd-fraction results of Section 5.4 according to

$$c_{\mathrm{H}}^{\mathrm{T}} = \frac{(1 - f_{\mathrm{Gd}}^{\mathrm{Data}})|_{(x,y,z)=(0,0,0)}}{(1 - f_{\mathrm{Gd}}^{\mathrm{MC}})|_{(x,y,z)=(0,0,0)}} \,, \tag{6.22}$$

The Gd-fraction results translate into a Target correction of $c_{\mathrm{H}}^{\mathrm{T}} = (1.1750 \pm 0.0078 \,(\mathrm{stat}))$. In contrast to this, the GC correction evaluated from the ^{252}Cf deployments at the GC edge

$$c_{\mathrm{H}}^{\mathrm{GC}} = \frac{(f_{\mathrm{H}}^{\mathrm{Data}})|_{\mathrm{edge}}}{(f_{\mathrm{H}}^{\mathrm{MC}})|_{\mathrm{edge}}} = 1.0020 \pm 0.0007 \,(\mathrm{stat}) \,, \tag{6.23}$$

is in agreement with unity. In accordance with the DC-III Gd-fraction analysis (see Section 5.4), the H-fraction correction systematic uncertainty was evaluated by variation of the computational method. A second H-fraction definition excludes the events below $1.5\,\mathrm{MeV}$ to include method and background dependent effects. The total H-fraction related systematic uncertainty was estimated from the discrepancy between the results obtained from different methods and amounts to $0.19\,\%$.

The results of the first campaign were found to be $c_{\mathrm{H,1st}}^{\mathrm{T}} = (1.1497 \pm 0.0120 \,(\mathrm{stat}))$ and $c_{\mathrm{H,1st}}^{\mathrm{GC}} = (1.0023 \pm 0.0005 \,(\mathrm{stat}))$, in agreement with the second campaign's values.

6.4.2 Target volume-wide efficiency correction

A value of $c_{\mathrm{v}}^{\mathrm{T}} = (0.9806 \pm 0.0083 \,(\mathrm{stat}))$ is found for the volume-wide efficiency correction in the Target. The semi-inclusive efficiencies estimated at the different calibration positions are shown in Fig. 6.11 for data and the $c_{\mathrm{v}}^{\mathrm{T}}$-corrected MC simulation. Accordingly to the Target geometry, data points at the Target borders are stronger weighted by the volume-wide efficiency method. Hence a better data to MC agreement is obtained after correction for calibration positions close to the Target wall.

6.4.3 Gamma-catcher volume-wide and combined efficiency correction

For the cut related term of the GC volume-wide correction computed with the d-weighted method (described in Eq. (6.17)) a value of $c_{\mathrm{v}}^{\mathrm{GC}} = (0.9939 \pm 0.0019\,\text{(stat)})$ was found. A discrepancy of $0.47\,\%$ to the R-integration without top/bottom separation (as in Eq. (6.14)) and a discrepancy of $-0.48\,\%$ is discovered in comparison to the result computed using solely data points at the GC top weighted with the d-method (as in Eq. (6.19)). Hence, a method dependent systematic uncertainty of $0.5\,\%$ is assigned. The semi-inclusive efficiencies found with the ^{252}Cf data runs as well as the corrected MC efficiencies are given for the R- and d-parametrization in Fig. 6.8d and Fig. 6.9d. The Target and GC correction can be combined to $c_{\mathrm{v}} = (0.9930 \pm 0.0018\,\text{(stat)})$. To find a discrepancy of less than $0.05\,\%$ to the result using the exclusive efficiencies suggests an independence of the detection efficiency corrections with respect to volume integration. From variation of the energy cut on the ^{252}Cf prompt event, an additional systematic uncertainty on the combined result of $0.15\,\%$ is estimated.
Using calibration data of the first ^{252}Cf campaign, the MC correction is estimated to $c_{\mathrm{v}}^{\mathrm{1st}} = (0.9926 \pm 0.0020\,\text{(stat)})$, in agreement with the second calibration campaign.

6.5 H-channel neutron selection optimization

The volume-integration methods to estimate c_{v} described above, can furthermore be used to optimize the neutron selection cuts with respect to the detection systematics. Dedicated studies can help to identify the selection criteria which minimize the efficiency systematics. For each of the delayed event cuts three different cut configurations were tested. In each step only one of the cut values was varied, whereas for all other cuts the default value was kept. The semi-inclusive efficiency is then given by

$$\varepsilon_{\mathrm{semi}} = \frac{N(E_{\min} < E_{\mathrm{delayed}} < 2.6\,\text{MeV} \ \cap \ \Delta R < \Delta R_{\max} \ \cap \ 0.5\,\mu\text{s} < \Delta T < \Delta T_{\max})}{N(0.5 < E_{\mathrm{delayed}} < 3.5\,\text{MeV} \ \cap \ 0.25 < \Delta T < 1000\,\mu\text{s})},$$
(6.24)

with the different cut values

- $\Delta T_{\max} = [300, \ 450, \ \mathbf{600}]\,\mu\text{s}$,

- $\Delta R_{\max} = [\mathbf{0.6}, \ 0.8, \ 1.0]\,\text{m}$,

- $E_{\min} = [1.6, \ 1.7, \ \mathbf{1.8}]\,\text{MeV}$.

The numbers highlighted in bold are the default cut values. The combined correction factors c_{v} for the three sets of cuts are summarized in Table 6.2a-6.2c, in Appendix D.4 the values are given for Target and GC separately. As the GC corrections are weighted by almost a factor 16 relative to the Target values, the combined c_{v} are dominated by the GC results, deviating by $0.1\,\%$ at most. The method dependent systematic uncertainty is for the GC result given by the largest discrepancy between the correction values of the default and any of the alternative integration methods. An estimate for the cut dependent systematic uncertainty is given by the discrepancy between the correction results of two neighboring selection cut values, assuming c_{v} to change monotonically in case one cut is changed individually.

Table 6.2: MC correction factor results for changing selection cuts. The combined correction factor c_v is given along with the statistical as well as the method and cut dependent systematic uncertainties. The last column contains the discrepancy to the MC correction computed with the exclusive efficiency definitions. Cut values preferred by the ^{252}Cf study are highlighted in bold.

(a) MC correction factor results for varying ΔT cuts.

Δt_{max}	c_v	$\Delta c_{v,stat}$	method dep. $\Delta c_{v,sys}$	cut dependent discrepancy	discrepancy to exclusive
300 µs	0.9912	0.0024	0.0066	0.0020	0.0004
450 µs	0.9932	0.0020	0.0053	0.0020	0.0005
600 µs	0.9930	0.0019	0.0045	0.0002	0.0005

(b) MC correction factor results for varying ΔR cuts.

ΔR_{max}	c_v	$\Delta c_{v,stat}$	method dep. $\Delta c_{v,sys}$	cut dependent discrepancy	discrepancy to exclusive
60 cm	0.9930	0.0018	0.0045	0.0032	0.0005
80 cm	0.9899	0.0015	0.0045	0.0032	0.0004
100 cm	0.9885	0.0014	0.0046	0.0013	0.0004

(c) MC correction factor results for varying delayed energy cuts.

E_{min}	c_v	$\Delta c_{v,stat}$	method dep. $\Delta c_{v,sys}$	cut dependent discrepancy	discrepancy to exclusive
1.6 MeV	0.9950	0.0017	0.0038	0.0006	0.0004
1.7 MeV	0.9944	0.0018	0.0046	0.0014	0.0005
1.8 MeV	0.9930	0.0019	0.0045	0.0014	0.0005

In case the cut limit ΔT_{max} is raised from 300 µs to 600 µs, the central value of c_v is slightly increased, whereas the method dependent systematic uncertainty decreases from 0.67 % to 0.45 % and the cut dependent discrepancy becomes negligible (see Table 6.2a). In contrary, loosening the upper cut value ΔR_{max} diminishes the data and MC agreement in the efficiency, inducing a significant change in c_v. The method dependent systematic uncertainty, however, remains stable and the cut dependent discrepancy reduces by a factor two, thus slightly favoring the wide ΔR cut of 1 m (see Table 6.2b). A change in the delayed energy cut from 1.8 MeV to 1.6 MeV only slightly improves the data and MC efficiency agreement. The wider cut range starting from 1.6 MeV is preferred, as the method dependent systematic uncertainty slightly decreases and the cut dependent discrepancy lowered by more than a factor two (Table 6.2c). In addition is the statistical uncertainty on c_v reduced for loosened cuts due to an increase of the detection efficiency values.

Loosening all cuts and thus widening the selection ranges for each delayed detection cut yields a MC correction of $c_v = (0.9906 \pm 0.0013\,(\text{stat}) \pm 0.0040\,(\text{syst}))$, in which the method dependent uncertainty is quoted as systematic uncertainty. With tight selection cuts the MC correction changes to $c_v = (0.9912 \pm 0.0024\,(\text{stat}) \pm 0.0066\,(\text{syst}))$, again taking only the method dependent systematic uncertainty into account. Hence a relaxation of all selection criteria compared to the tightest set of cuts would lead to a
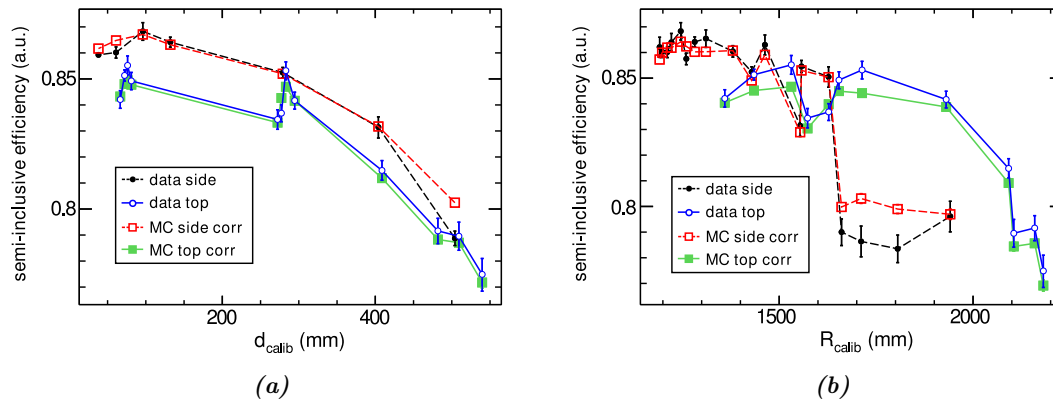
Figure 6.12: Top/side separated ^{252}Cf deployment points with respect to the calibration
position d_{calib} and R_{calib}: The semi-inclusive efficiency for the loosened cut values ($E_{delayed} >$
1.6 MeV, $\Delta R < 100$ cm, $\Delta T < 100$ µs) is plotted for data and MC runs taken at the GC side
and top. ***a)*** Semi-inclusive efficiency as a function of d_{calib}, the MC values were corrected using
c_v from Eq. (6.17). ***b)*** Semi-inclusive efficiency as a function of R_{calib}, the MC values were
corrected using c_v from Eq. (6.13).

factor 1.7 reduction in the total[6] uncertainty on c_v, keeping the correction central value
nearly unchanged. From the results in Table 6.2c we can see that a loose delayed energy
and ΔT cut yields a comparably low total uncertainty (0.38 %) as the case with all cut
loosened. The results suggest, however, that the cut dependent uncertainty might be
lower for the latter case.

In Fig. 6.12 the semi-inclusive efficiency with loose cuts is plotted for the ^{252}Cf data
points and MC simulation. Owing to the wider selection windows, the efficiency curves
smoothen compared to Fig. 6.8d and 6.9d. Especially relaxation of the ΔR cut has an
effect on the position dependence of the detection efficiency.

6.6 Conclusion

In this chapter studies performed to investigate the H-channel neutron detection effi-
ciency and to estimate the corresponding MC correction were presented. Using ^{252}Cf
calibration data the mean value of the cut efficiency dependent MC correction c_v is
computed separately for Target and GC and combined afterwards. While the Target
correction is estimated using the technique discussed in Chapter 5, two different volume
integration strategies were presented to compute the GC volume-wide correction factor.
These strategies depend on the spatial parametrization applied to weight the ^{252}Cf data
points, with a default shortest distance to Target wall "d-weighting" and a distance to
Target center "R-weighting" method. In contrast to the cut efficiency correction c_v, the
H-fraction corrections are independently applied to the Target and GC prompt spectra,
in order to avoid spectral distortions which would be induced by a global correction.
The Target H-fraction correction amounts to $c_H^T = (1.1748 \pm 0.0078\,(\text{stat}))$, whereas

---

[6]Here, "total uncertainty" refers to the combination of statistical and method dependent systematic
uncertainty.

the GC correction is $c_{\mathrm{H}}^{\mathrm{GC}} = (1.0020 \pm 0.0007\,(\mathrm{stat}))$. For the combined statistical and systematic uncertainty a value of $0.19\,\%$ was estimated.

The efficiency values at the GC top and side volume show discrepancies of 2-3 %, especially when plotted with respect to the distance to the Target wall d. These discrepancies are possibly related to the spatial dependence of the delayed energy and ΔR efficiencies, which is influenced by the detection process of the H-capture single gamma and the vertex reconstruction. As a consequence the MC correction in the GC volume $c_{\mathrm{v}}^{\mathrm{GC}}$ is the combination of the separately estimated correction factors using Guide-Tube top and side calibration runs.

The H-channel neutron selection criteria were varied in order to find the preferred set of cuts minimizing the detection efficiency systematics. The $^{252}\mathrm{Cf}$ analysis favors loosened selection cuts of $E_{\mathrm{delayed}} > 1.6\,\mathrm{MeV}$, $\Delta R < 100\,\mathrm{cm}$ and $\Delta T < 100\,\upmu\mathrm{s}$. With these cuts a MC correction of $c_{\mathrm{v}} = (0.9906 \pm 0.0013\,(\mathrm{stat}) \pm 0.0040\,(\mathrm{syst}))$ is computed, where the systematic uncertainty is given by the integration method dependent uncertainty.

Assuming a $0.2\,\%$ cut dependent uncertainty, the total uncertainty including method ($0.4\,\%$), background ($0.55\,\%$) and statistical ($0.13\,\%$) contributions and the H-fraction contribution ($0.19\,\%$) would amount to $0.75\,\%$. Hence, we can expect to obtain a total neutron detection uncertainty of less than $1\,\%$ in the upcoming H-channel oscillation analysis, not taking spill-in border effects and the proton number uncertainty into account. In case of further studies, e.g. reducing background uncertainties, and in combination with results from an efficiency analysis with an IBD neutron sample, the uncertainty could be further reduced.

Chapter 7

Spill-in/out systematic uncertainty

In this chapter the spill-in/out systematic uncertainty estimation for the Gd-I and Gd-II analyses will be described. A general introduction to the spill-in/out phenomenology in the context of a Gd-channel neutrino detection will be given in the first section. The second section will specify the variables used to describe the effect in a Monte Carlo analysis. Details on the different neutron scattering models used to produce the MC samples involved in the studies on spill-in/out systematic effects are given in Section 7.3. The fourth section deals with the uncertainty determination for Gd-I, while Section 7.5 explains how the uncertainty estimation was developed further for the Gd-II analysis. In Section 7.6 the Gd-III result will be briefly discussed.

The spill-in/out effect cannot be measured with detector data. But since the full DC geometry is implemented in the Double Chooz simulation framework DCGLG4sim, its size and robustness with respect to changing detector parameters can be evaluated by Monte Carlo studies. Hence, all plots and numbers shown in this chapter were obtained from Monte Carlo simulation code, if not stated differently.

7.1 Spill-in/out definition

The coincidence signal of an antineutrino undergoing inverse beta decay (IBD) in the DC detector consists of a prompt positron energy deposition and a delayed neutron capture event (cf. Section 1.3.2). The three basic cuts to select neutrino events in both Gd-based analyses of the first and second publication are cuts on the prompt and delayed energy respectively, while a third cut ensures that both energy depositions occur within a certain time window (see Section 3.3.1).

Only events with neutron captures on gadolinium (Gd) contribute to the signal in the neutrino selection of the standard Gd-channel analysis. As the ν-target vessel is the only volume filled with Gd-doped scintillator, it technically forms the fiducial volume.
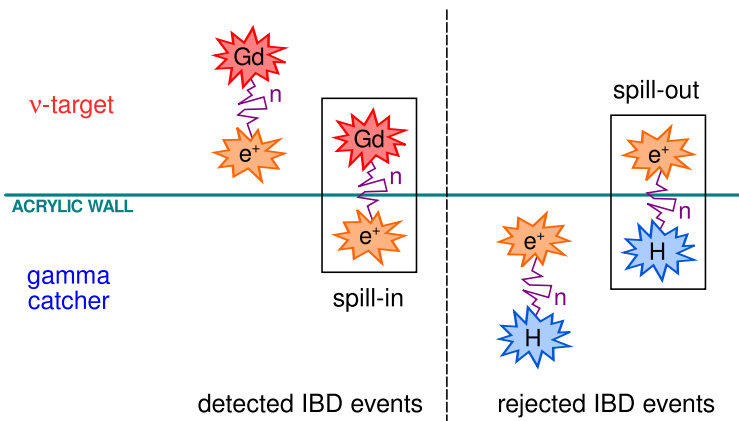
Figure 7.1: Illustration of the spill-in/out border effect.

However, due to neutron migration[1] the borders of the fiducial volume are softened and the expected number of detected neutrino events changed. There are two contributions to the effect summarized as *"spill-in/out"*:

Spill-in: If a neutrino interaction occurs inside the Gamma Catcher volume, most of the events will not pass the neutrino selection cuts, as almost all neutrons are captured on hydrogen. But for IBD close to the ν-target wall or inside the ν-target acrylics it is also possible that the neutron travels into the ν-target volume, where it can be captured on a gadolinium nucleus. This special class of events is referred to as *"spill-in"* events, as IBD events outside the ν-target leak *into* the neutrino sample by having the required event signature[2].

Spill-out: Contrary to the spill-in, an IBD inside the ν-target where the neutron *leaves* the Gd-doped scintillator volume and hence the detection channel on Gd, is called *"spill-out"* event. Such an event is missed by the neutrino selection cuts even though the neutrino interaction happened in the fiducial volume.

Both effects counteract but due to several reasons they do not eliminate each other. First of all, the presence of Gd in the ν-target scintillator shortens the travel distance of neutrons compared to the travel distance in an undoped liquid, such as the Gamma Catcher scintillator. Another reason follows from a geometrical argument: The Gamma Catcher volume surrounds the ν-target and thus the volume of a hollow cylinder in the Gamma Catcher is larger (and can contain more IBD and possible spill-in events) than the volume of a hollow cylinder of same thickness inside the ν-target. Consequently the amount of spill-in neutrons is larger than the number of spill-out neutrons resulting in a net spill-in event excess. The probability of IBD resulting in spill-in or spill-out events are shown in Fig. 7.2a and 7.2b as function of the prompt event position. As described above, they occur close to the ν-target wall.

---

[1]The mean track length – which corresponds to the total distance traveled by the neutron – observed in MC simulations of IBD neutrons is $10-30$ cm depending on the neutron scattering model and scintillator composition.

[2]More precisely we would refer to the type of events introduced here as "neutron spill-in", in contrast to the "gamma spill-in" where a neutron is caught on a nucleus *outside* the ν-target but emitting gammas in the energy window relevant for delayed event selection. In the case of the Gd-I and Gd-II analyses the class of the gamma spill-in events can be neglected and is not discussed further.
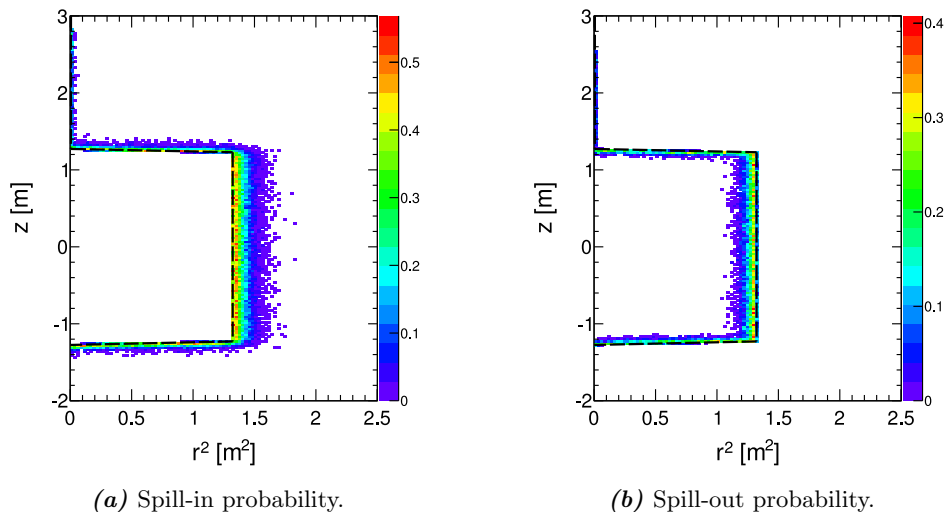
(a) Spill-in probability.

(b) Spill-out probability.

Figure 7.2: Spill-in/out probability as a function of the IBD position. The black dashed line marks the ν-target acrylic wall.

The spill-in/out effect can also be understood as a leakage of neutron detection efficiency into the Gamma Catcher, which is shown in Fig. 7.3 as a function of the distance d between the IBD position and the nearest ν-target acrylic wall.

Impact on the analysis of θ_{13}

In the oscillation analysis the predicted antineutrino rate and spectrum are calculated using the DC detector response modeled within MC (Section 3.1), which does also include the spill-in/out effect. Therefore there should be, at least in general, no need to adapt the normalization of the neutrino prediction to account for the presence of spill-in/out events in the data. What enters the θ_{13} fit is the systematic uncertainty on the spill-in/out effect (for description see Section 7.2) in form of an effective uncertainty contribution on the neutron detection efficiency (cf. Section 5.2). As it is not possible to perform a reliable measurement of the global spill-in/out effect, the systematic uncertainty determination is based on MC simulation studies, aiming to estimate to which extend the MC normalization could be affected by inaccuracies in the net spill-in/out effect due to imperfections in the MC modeling.

In the CHOOZ experiment the spill-in/out MC analysis led to a $\sim 1\%$ uncertainty on the total number of antineutrino events [39]. In the three Gd-based Double Chooz analyses this systematic uncertainty was reduced by more than a factor two and will become even smaller as soon as the measurement period with two detectors will commence. In the two detector scenario the remaining systematics will be the relative uncertainty between the near and far detector net spill-in/out effects, which will be most likely dominated by discrepancies in the detector geometry and material composition, in particular the Gamma Catcher scintillator constituents. Deviations in these quantities are however expected to be small.
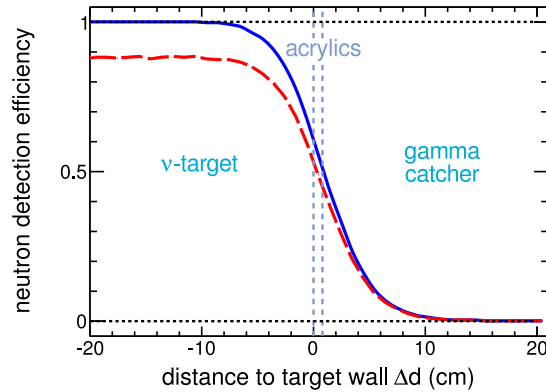
Figure 7.3: Neutron detection efficiency leakage due to spill-in/out as a function of the distance Δd between the IBD position and the nearest ν-target acrylic wall. The proportion of neutrons detectable in and outside the ν-target due to neutron migration is given for both cases, with (red dashed line) and without (blue solid line) taking into account the Gd-fraction (Section 5.2.2). Note, that the graphs do not include the detection efficiency introduced by selection cuts.

7.2   Spill-in/out Monte Carlo analysis

The Double Chooz Geant4-based simulation framework DCGLG4sim [130] supports the full DC geometry and chemical compositions of the detector components. This enables to observe and study the spill-in/out effect's magnitude and characteristics using MC simulation code.

7.2.1   True spill-in/out fractions

For an elementary spill-in/out analysis the position of the IBD and the neutron capture can be retrieved from the MC simulation. The true number of spill-in and spill-out events – i.e. without any selection cuts on the neutrino coincidence time, correlation distance or energy – can be determined in a straight-forward way:

1) spill-in selection criteria:

- IBD occurred outside the ν-target

- neutron capture in the ν-target liquid

2) spill-out selection criteria:

- IBD occurred inside ν-target

- neutron capture outside the ν-target liquid

The ν-target acrylics inner border limits the ν-target region, e.g. the acrylics itself is part of the region outside the ν-target volume. We define N_ν^0 to be the number of "true" IBD events, i.e. the number of neutrino events if there were no spill-in/out effect and all IBD inside the ν-target could be detected as being such. The size of the spill-in

effect can now be described by the *spill-in fraction* f_{SI}, which is the number of spill-in events N_{SI} divided by N_ν^0:

$$f_{\mathrm{SI}} = \frac{N_{\mathrm{SI}}}{N_\nu^0} \,. \qquad (7.1)$$

All forthcoming variables will be normalized with respect to N_ν^0 as this provides the possibility to compare results gained using different MC models. We derive N_ν^0 from the number of regular ν-target events N_{T} (number of IBD events inside the ν-target followed by a neutron capture inside the ν-target) plus the amount of lost events due to spill-out:

$$N_\nu^0 = N_{\mathrm{T}} + N_{\mathrm{SO}} \,. \qquad (7.2)$$

Likewise, for the *spill-out fraction* we write

$$f_{\mathrm{SO}} = \frac{N_{\mathrm{SO}}}{N_\nu^0} \,. \qquad (7.3)$$

As discussed before, the spill-in/out effect leads to an increase of the total number of true measurable neutrino events N_ν^{fid} inside the ν-target, forming the fiducial volume. The *net spill-in ratio* ϕ_{SI} is thus given by

$$\phi_{\mathrm{SI}} = \frac{(N_{\mathrm{SI}} - N_{\mathrm{SO}})}{N_\nu^0} = f_{\mathrm{SI}} - f_{\mathrm{SO}} \,, \qquad (7.4)$$

and hence

$$N_\nu^{\mathrm{fid}} = N_\nu^0 \cdot (1 + \phi_{\mathrm{SI}}) \,. \qquad (7.5)$$

7.2.2 Detected spill-in/out fractions

The Gd-I and Gd-II neutrino cuts relevant for the spill-in/out MC analysis are on the visible energy and correlation time ($\Delta t_{\mathrm{p-d}} \equiv t_{\mathrm{delayed}} - t_{\mathrm{prompt}}$) of the two coincident signals:

- $0.7\,\mathrm{MeV} < E_{\mathrm{prompt}} < 12.2\,\mathrm{MeV}$

- $6\,\mathrm{MeV} < E_{\mathrm{delayed}} < 12\,\mathrm{MeV}$

- $2\,\mu\mathrm{s} < \Delta t_{\mathrm{p-d}} < 100\,\mu\mathrm{s}$

From Fig. 7.4 we can see that the coincidence time is larger for spill-in/out events than for regular ν-target events. This means the size of the net spill-in ratio will depend on the selection cuts performed in the neutrino analysis. In order to obtain the spill-in excess of neutrino events after cuts it appears sufficient to apply the selection criteria on the quantities given in Eq. (7.1)–(7.5). However, this does not work in the case of spill-out events, as these originate from neutrons leaving the ν-target and therefore miss the delayed energy cut. To estimate the number of true neutrino events after selection

$$N_\nu^{0,\mathrm{det}} = N_{\mathrm{T}}^{\mathrm{det}} + N_{\mathrm{SO}}^{\mathrm{det}} \,, \qquad (7.6)$$

the number of lost events due to spill-out has to be multiplied by the detection efficiency of regular ν-target events ε_{T}. The factor ε_{T} is calculated from the fraction of ν-target
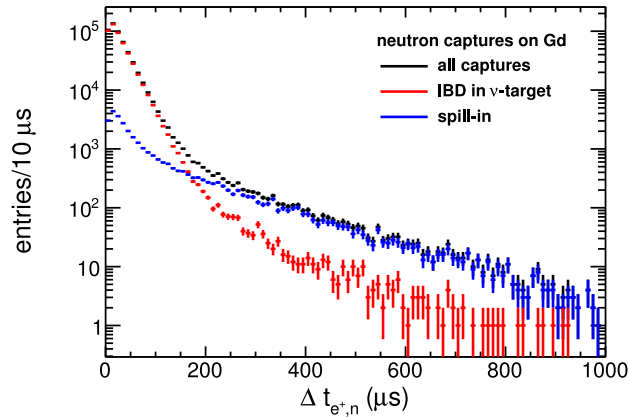
Figure 7.4: Coincidence time $\Delta t_{e^+,n}$ of simulated IBD events with neutron capture on Gd using NeutronTh code (further information on NeutronTh is given in Section 7.3). The Coincidence time with neutron capture on Gd is shown for: all IBD events (black), IBD event in the ν-target scintillator (red) and spill-in events (blue).

events gathered with and without cuts, and for the effectively lost amount of spill-out events we yield

$$N_{\text{SO}}^{\text{det}} = N_{\text{SO}} \cdot \varepsilon_{\text{T}} = N_{\text{SO}} \cdot \frac{N_{\text{T}}^{\text{det}}}{N_{\text{T}}} \,. \tag{7.7}$$

Since the spill-out fraction is defined as

$$f_{\text{SO}}^{\text{det}} = \frac{N_{\text{SO}}^{\text{det}}}{N_{\nu}^{0,\text{det}}} = \frac{N_{\text{SO}} \cdot \varepsilon_{\text{T}}}{N_{\text{T}}^{\text{det}} + N_{\text{SO}} \cdot \varepsilon_{\text{T}}} = \frac{N_{\text{SO}}}{N_{\text{T}} + N_{\text{SO}}} = f_{\text{SO}} \,, \tag{7.8}$$

both the true and the detected spill-out fraction are of same size. The net spill-in ratio and the number of measured neutrino events N_{ν}^{m} are now given by

$$\phi_{\text{SI}}^{\text{det}} = \frac{(N_{\text{SI}}^{\text{det}} - N_{\text{SO}}^{\text{det}})}{N_{\nu}^{0,\text{det}}} = f_{\text{SI}}^{\text{det}} - f_{\text{SO}} \,, \tag{7.9}$$

and

$$N_{\nu}^{\text{m}} = N_{\nu}^{0,\text{det}} \cdot (1 + \phi_{\text{SI}}^{\text{det}}) \,. \tag{7.10}$$

7.3   Neutron scattering and Monte Carlo models

Neutrons are slowed down in an organic liquid scintillator (LS) mainly by elastic scattering with hydrogen atoms, which is the dominant interaction for neutron energies in the range of 100 MeV down to 10 keV [191]. Below these energies the elastic cross section is constant over a wide range (at about 20.3 b) and the neutron capture processes gain in importance, as the neutron capture cross-sections increase with decreasing neutron kinetic energy (Fig. 7.5). In particular for captures on a Gd isotope the cross-sections sharply rise for $E_n < 0.1$ eV. Since the proton and neutron masses are of similar size and at energies at which the hydrogen nucleus can be considered as free proton at rest, the hydrogen-rich liquid scintillator is an effective moderator, and the neutron loses on average half of its energy in a neutron-proton collision [146]. As a result the neutron
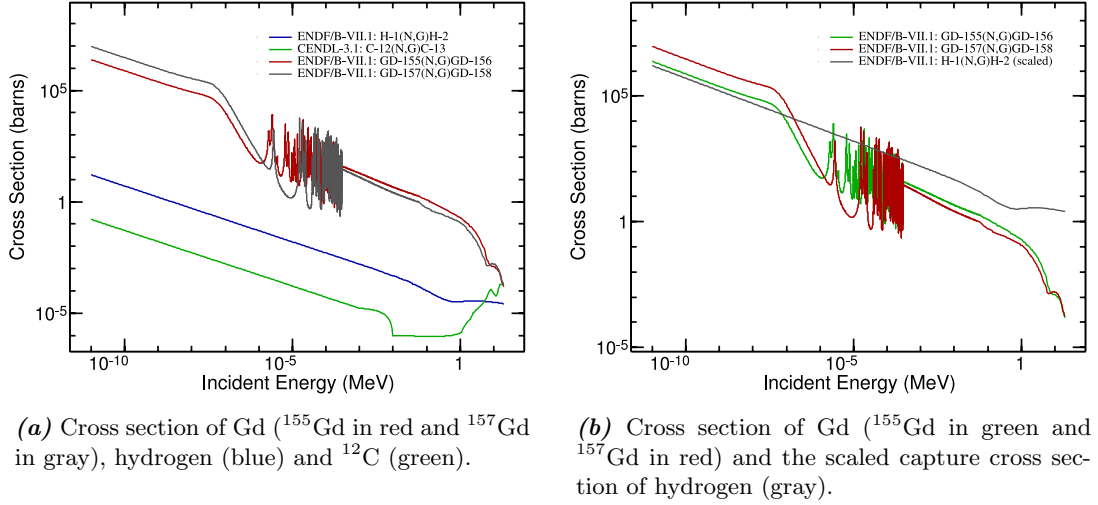
(a) Cross section of Gd (^{155}Gd in red and ^{157}Gd in gray), hydrogen (blue) and ^{12}C (green).

(b) Cross section of Gd (^{155}Gd in green and ^{157}Gd in red) and the scaled capture cross section of hydrogen (gray).

Figure 7.5: Neutron capture cross sections (from [167]).

loses energy in subsequent collisions until it is in thermal equilibrium with the detector liquid, which corresponds to a kinetic energy of $\sim 0.025 \, \mathrm{eV}$. The slowing down of the neutron is hence often called *thermalization*, while neutron scattering at thermal energies is referred to as *diffusion*.

The combination of the capture cross section of a scintillator component together with its abundance or rather its density defines the neutron capture probability. The number of hydrogen nuclei compared to gadolinium in a unit volume of ν-target scintillator [60] is for H/^{155}Gd $\approx$ H/^{157}Gd $\approx 10^5$ and H/^{12}C ≈ 2, the capture cross sections are given in Fig. 7.5. Neutrons created in the IBD reactions will reach only after several scatterings the energy range at which the neutron capture on Gd nuclei become relevant at the given abundance in the LS. In other words: the neutron requires to be slowed down before Gd-captures will occur with sufficiently large probability to outperform the rate of H-captures. Since H has a low capture cross section ($0.33 \, \mathrm{b}$ at thermal neutron energies) compared to its elastic scattering cross section, the majority of the neutrons will reach thermal energies and are captured on Gd. The neutron capture time spectra are characterized by a rising part and an exponentially decreasing part (see Fig. 7.6), which can be described by a simplified time correlation model given in Ref. [132]. It assigns for each of the two processes a characteristic time[3], the "thermalization time" τ_{th} and the "capture time" τ_{cap}. The distribution of the coincidence time $\Delta t_{\mathrm{e^+,n}}$ between positron annihilation and neutron capture is then given by a convolution of two exponential processes with the two introduced characteristic times as time constants:

$$
\begin{aligned}
P(t) &= \frac{1}{\tau_{\mathrm{th}}} \cdot e^{-t/\tau_{\mathrm{th}}} \otimes \frac{1}{\tau_{\mathrm{cap}}} \cdot e^{-t/\tau_{\mathrm{cap}}} \\
&= \frac{1}{\tau_{\mathrm{cap}} - \tau_{\mathrm{th}}} \cdot e^{-t/\tau_{\mathrm{cap}}} \cdot \left(1 - e^{-T \cdot t}\right), \\
&\quad \text{with} \quad T = \frac{\tau_{\mathrm{cap}} - \tau_{\mathrm{th}}}{\tau_{\mathrm{cap}} \cdot \tau_{\mathrm{th}}} \, .
\end{aligned}
\tag{7.11}
$$

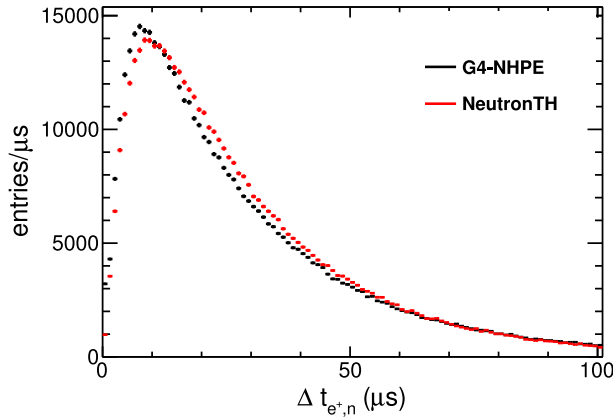[3]The characteristic times of course depend on the scintillator composition.

Figure 7.6: Coincidence time $\Delta t_{\mathrm{e^+,n}}$ of simulated antineutrino events using G4-NHPE and NeutronTh code (description in the text below).

The rising part in the time spectrum until it reaches its maximum is dominated by τ_{th}, whereas the declining part follows an exponential decay with time constant τ_{cap}. The thermalization is in general a fast process (few µs), while the capture time is $\sim 30\,$µs. Owing to the large relative abundance of hydrogen atoms compared to Gd nuclei, the capture cross-section of H is larger in the keV range than for Gd. Thus IBD neutrons do not need to be significantly slowed down to observe a neutron capture on H, and no rising part is seen for the DC capture time spectra (cf. Fig 5.21b in Section 5.4). From the capture cross sections and the relative abundances of the nuclei present in the ν-target scintillator we can see that the largest fraction of captures will occur on H and Gd nuclei with a mean capture time of 31 µs. In the GC liquid more than 99 % of the captures are on H, due to the lower cross-section at thermal energies the capture time is with about 200 µs lower compared to the ν-target.

However, the scatter processes are in fact more complicated when the neutron upon slowing down reaches energies comparable to the binding energy of a hydrogen atom in the scintillator molecules of a few eV. Below this energy the neutron has no longer enough energy to free the hydrogen nucleus in a collision or transfer energy to the molecular vibration. In this case the neutron will scatter with a target that rather has the mass of the whole molecule instead of a single proton. As a consequence it becomes harder for the neutron to lose energy. On the other hand, the scattering cross-section rises compared to the one of free protons, as the reduced mass of the neutron and target particle system increases. For further details the reader is referred to Ref. [191].

The different MC simulations used to estimate the spill-in/out systematic uncertainty involve different modelings of neutron scattering. The modelings taken into account by this study based on three simulation codes are discussed in the following.

Geant4 NeutronHPElastic

The Gd-I Monte Carlo framework DCGLG4sim used a standard Geant4 package called "NeutronHPElastic"[4] to describe neutron elastic scattering in the region of $0 < E_n < 20\,\text{MeV}$ (E_n = neutron kinetic energy) [132]. It models the neutron energy loss by assuming the scintillator nuclei to be an ideal gas. Thus, neutron scattering on H is at any neutron energy relevant for DC simulations treated as collision with a free proton. In the following we will refer to the NeutronHPElastic Geant4 simulations as "G4-NHPE".

NeutronTh patch for Geant4

The "NeutronTh" patch, developed by A. Etenko, provides an improved radiative capture model for neutron energies $E_n < 300\,\text{eV}$ and takes into account hydrogen molecular bonds in neutron elastic scattering for $E_n < 4\,\text{eV}$ [104, 105]. The patch is an extension of the DCGLG4sim code, replacing NeutronHPElastic for $E_n < 4\,\text{eV}$. It was adopted for the DC-II and successive simulations.

Neutron scattering cross section on hydrogen is for NeutronTh based on an analytical model effectively describing neutron scattering at low energies [118]. NeutronTh alters the scattering of neutrons with any hydrogen nucleus as if the hydrogen atom was bound in Dodecane ($C_{12}H_{26}$) [106]. The ν-target liquid scintillator consists to $80\,\%$ of dodecane molecules. The molecular structures of the liquid oil molecules in the Gamma Catcher are similar to dodecane, however, the exact proportion of a certain molecular structure and its isomers in the admixture are not exactly known. Nevertheless, dodecane and dodecane-like molecules make up the largest fraction in the DC scintillators and do thus dominate the neutron elastic scattering physics.

Introduction of an effective mass which changes with neutron energy lowers the energy loss per collision. It applies corrections to the scattering modeling of a free proton taking into account inelastic energy exchange to internal degrees of freedom of the hydrogen-containing molecule, corresponding to vibrational or rotational motions. As a result, the scattering cross section is enhanced at low neutron energies. Also, the angular distribution of the scattered neutrons is changed. Whereas the scattering angle is on average peaked forward for collisions with free protons, it is almost isotropic for low neutron energy scatterings in NeutronTh (Fig. 7.7a). Hence, the slowing down of neutrons and their diffusion process is modified. This can have an effect on the neutron thermalization and capture time constants, the distance traveled by a neutron relative to its origin and the capture fraction on Gd.

A study performed by A. Hourlier had shown that the data to MC agreement of the capture time on short timescales, the thermalization part of the spectrum, is enhanced for neutron captures on Gd when NeutronTh is applied [132, 131]. On the contrary, the capture time constant remained unchanged. The studies arrived at this conclusion using ^{252}Cf neutron capture events on Gd.

The gamma emission spectra of radiative neutron captures on Gd nuclei tend to be energy dependent. Furthermore, resonances are present between 1 and $300\,\text{eV}$ in the

---

[4]NeutronHPElastic stands for "Neutron High Precision Elastic".
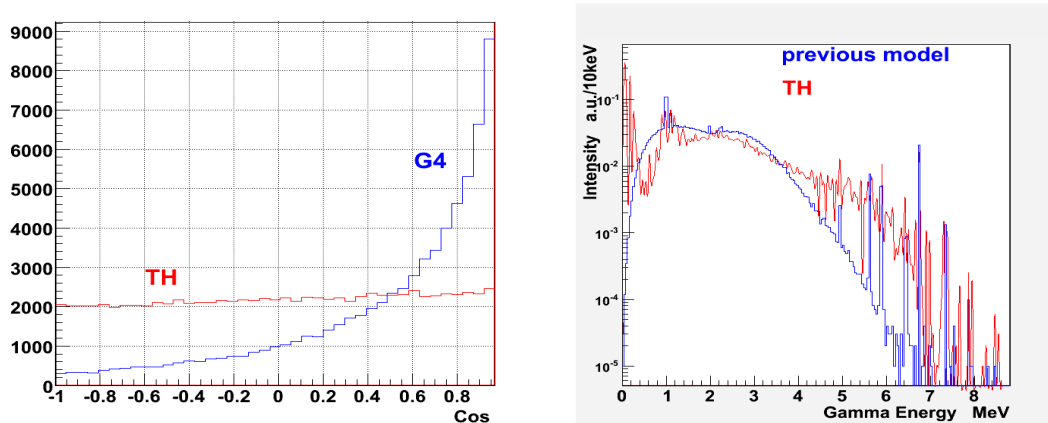
(a) Angular distribution of scattered thermal neutrons.

(b) Gamma emission spectra of radiative neutron captures on gadolinium.

Figure 7.7: Comparison of G4-NHPE and NeutronTh (from [104]).

neutron capture cross sections of the Gd isotopes. These correspond to different nuclear excitation states, which should yield differences in the gamma radiation. NeutronTh accounts for this effectively by replacing the gamma emission probabilities for neutron captures below 300 eV with a spectrum retrieved from experimental data [105, 78] (see also Fig. 7.7b).

TRIPOLI4

The simulation code TRIPOLI4 [201] was developed at Saclay, France, in order to describe neutron processes in the context of reactor physics. It is suited to describe neutron physics at low energies and models neutron propagation in a medium based on experimental data. TRIPOLI4 is not embedded in the DC simulation framework DCGLG4sim and therefore ran independently. The code features different modelings of neutron scattering with hydrogen atoms, either treating them in a free proton gas hypothesis or a molecular bond model mode. The first of the two approaches is thought to be comparable to the G4-NHPE neutron physics.

In the course of the Gd-III analysis, MC-MC comparisons were carried out between TRIPOLI4 and the Gd-III MC framework which includes NeutronTh. The two simulation codes were used to evaluate the ΔT cut efficiencies and the Gd-fractions with IBD neutrons. The discrepancies in the studied observables were of similar amplitude and had the same sign as the differences between these quantities in ^{252}Cf fission neutron data and the corresponding source simulation (see Section 5.3.3 and Section 5.4). This similarity in deviation from the DC simulation code suggests that TRIPOLI4 proves to model low energy neutron physics more accurately than NeutronTh.

7.4 Gd-I systematic uncertainty

The Gd-I Monte Carlo was based on the G4-NHPE simulation package, which was known to model the elastic scattering of low energy neutrons (E_n of a few eV and less) inaccurately. A study of T. Mueller [162] had shown that the application of a

Table 7.1: True spill-in and spill-out fractions (evaluated without selection cuts) gained using different neutron physics simulation models (from [162]).

	G4-NHPE	TRIPOLI4 free gas	TRIPOLI4 bond model
spill-in f_{SI}	8.06 %	8.34 %	6.54 %
spill-out f_{SO}	2.62 %	2.30 %	2.34 %

more realistic neutron scattering model led to differing results. He investigated the spill-in/out effect using the neutron simulation package TRIPOLI4 in a free proton gas hypothesis and a molecular bond model mode. For the latter, hydrogen atoms were treated as bound in $-CH_2$ groups. In comparison to other C-H bonds, such as benzene rings (C_6H_{12}), consistent results were found. The values of T. Mueller's study using neutrons with a fixed energy of 20 keV and a simplified DC detector geometry are given in Table 7.1. The work on the spill-in/out fractions for the Gd-I analysis was prepared by C. Langbrandtner [122]. Together we determined the systematic uncertainty of the spill-in/out effect as described in the next subsection, using a bond model correction factor derived from T. Mueller's work.

7.4.1 Analysis strategy in Gd-I

From the results in Table 7.1 it is possible to see that both the TRIPOLI4 free proton gas hypothesis and the G4-NHPE code overestimate the net spill-in ratio. Hence, the spill-in ratio is overestimated by the Double Chooz Gd-I MC model, yielding an overestimated neutrino flux in the MC simulation. As it is known that the Gd-I MC neutron physics model is not complete, corrections of the spill-in/out fractions are introduced. Based on the corrected spill fractions, a global MC normalization correction is computed in a second step. The spill-in/out correction factors were determined by comparison of the TRIPOLI4 free gas and the TRIPOLI4 bond model results of Ref. [162].

Bond model correction

The spill-in and spill-out fractions were corrected separately. The bond model corrected spill-out fraction is given by

$$f_{SO,CH_2}^{det} = f_{SO}^{det} \cdot \alpha_{SO} \,, \tag{7.12}$$

while the corrected spill-in fraction is dependent on two correction factors:

$$f_{SI,CH_2}^{det} = f_{SI}^{det} \cdot \alpha_{SI} \cdot \beta_{\Delta t} \,. \tag{7.13}$$

In both Eq. (7.12) and (7.13) we find a factor α_x, which is the bond correction factor for spill-out and spill-in respectively. The second correction factor $\beta_{\Delta t}$ in Eq. (7.13) is a time cut correction. In his document T. Mueller states that a time cut of $0 < \Delta t < 100\,\mu s$ will be passed by 66.2 % of the spill-in events using TRIPOLI4's bond model code compared to 61.4 % in the TRIPOLI4 free gas hypothesis. The contribution of the cut at the lower end $\Delta t > 2\,\mu s$ was assumed to be negligible. Figure 7.8 shows the detected
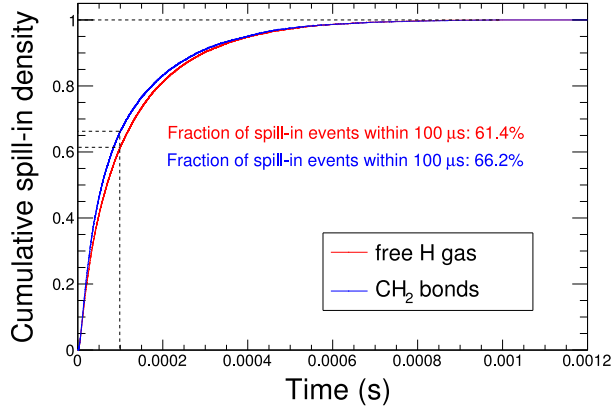
Figure 7.8: Spill-in fraction within time interval $[0; t]\,\mu$s for the bond model and the free gas mode using TRIPOLI4 (taken from [161], modified).

Table 7.2: Spill-in and spill-out results. The last column shows the Gd-I results, which are the bond model corrected values of the detected spill fractions obtained with G4-NHPE.

	G4-NHPE true values	G4-NHPE detected values	**Gd-I** detected values
N_{T}	174779	132126	-
N_{SI}	16006	5987	-
N_{SO}	4168	3151	-
f_{SI}	8.94 %	4.43 %	**3.74 %**
f_{SO}	2.33 %	2.33 %	**2.37 %**
ϕ_{SI}	6.62 %	2.10 %	**1.37 %**

spill-in fraction as a function of the time interval $[0; t]\,\mu$s for the two different TRIPOLI4 modes. The correction factors applied to the Gd-I values of the spill fractions are:

$$
\begin{aligned}
\alpha_{\mathrm{SO}} &= (2.34/2.30) = 1.017\,, \\
\alpha_{\mathrm{SI}} &= (6.54/8.34) = 0.784\,, \\
\beta_{\Delta t} &= (0.662/0.614) = 1.078\,.
\end{aligned}
$$

For the bond model corrected net spill-in ratio we now yield

$$
\phi_{\mathrm{SI,CH_2}}^{\mathrm{det}} = f_{\mathrm{SO,CH_2}}^{\mathrm{det}} - f_{\mathrm{SI,CH_2}}^{\mathrm{det}} = 1.37\,\%\,. \tag{7.14}
$$

The corrected net spill-in ratio reduces from 2.10 % to 1.37 %; the results of the different analysis steps – real fractions without cuts, detected fractions with cuts and bond model corrected values – are summarized in Table 7.2.

Monte Carlo live time correction factor

The correction factor of the MC simulation event rate can either be done by reducing the number of events or by an increase of the MC live time. For the Gd-I MC live time

correction factor related to the spill-in/out effect we find using Eq. (7.10)

$$
\begin{aligned}
c_{\mathrm{SI}} &= \frac{N_{\nu,\mathrm{CH}_2}^{\mathrm{m}}}{N_\nu^{\mathrm{m}}} = \frac{1 + \phi_{\mathrm{SI},\mathrm{CH}_2}^{\mathrm{det}}}{1 + \phi_{\mathrm{SI}}^{\mathrm{det}}} \\
&= \frac{1 + 0.0137}{1 + 0.0210} = 1.0072 \,.
\end{aligned}
\tag{7.15}
$$

7.4.2 Systematic uncertainty estimation

As the model dependency of the spill-in ratio was expected to be by far the largest uncertainty in the spill-in determination, it was concluded to derive the systematic uncertainty from the size of the bond model correction. Therefore the difference between the spill-in ratio gained from G4-NHPE simulation (2.10%) and the bond model corrected value (1.37%) were used for uncertainty estimation. There was no complete MC simulation including the correct neutron physics as well as the accurate DC detector properties available, which led to the decision to not totally exclude the G4-NHPE result. Consequently, the difference of 0.73% between the two results was taken to be a 2σ systematic uncertainty.

The MC live time correction c_{SI} and the combined statistical and systematic uncertainty on the spill-in ratio are inputs to the oscillation analysis:

$$
c_{\mathrm{SI}} = \mathbf{1.0072} \,,
\tag{7.16}
$$

$$
\begin{aligned}
\phi_{\mathrm{SI},\mathrm{CH}_2}^{\mathrm{det}} &= (1.37 \pm 0.06\,(\mathrm{stat}) \pm 0.37\,(\mathrm{syst}))\,\% \\
&= (1.37 \pm \mathbf{0.38})\,\% \,.
\end{aligned}
\tag{7.17}
$$

7.5 Gd-II systematic uncertainty

After the Gd-I analysis, enhancements in the low energy neutron physics MC modeling had been introduced by the implementation of the NeutronTh package in the Double Chooz MC framework. A study had shown that the data to MC agreement in the neutron capture time at short time scales was improved by the NeutronTh code [132, 131]. Hence it was concluded that the neutron thermalization process simulated with the NeutronTh code was enhanced due to the refined neutron elastic scattering modeling. As NeutronTh apparently modeled neutron physics more realistically than the former used G4-NHPE package, the bond model correction on the spill-in ratio was abandoned. From the Gd-II analysis onwards, no MC live time correction related to the spill-in/out effect was applied in the oscillation analysis.

The main focus of the spill-in/out work for the Gd-II analysis was to gain a more detailed knowledge about the robustness of the spill-in/out fractions provided by the simulation code for different MC configurations. Therefore the systematic uncertainty estimation was done by variation of parameters which impact the spill-in/out fractions.

In the next section the influence of the NeutronTh package on neutron physics and thus on the spill-in ratio will be discussed. The subsequent section will describe the analysis strategy and MC samples used. Finally the Gd-II spill-in ratio will be given along with its uncertainties. In the last subsection the method applied to yield a symmetric systematic uncertainty is explained.

7.5.1 Influence of **NeutronTh** on the neutron migration

The study with TRIPOLI4 showed that in a MC simulation with molecular bonds implemented, the thermalization time of the neutron would become larger and the linear distance between the prompt and delayed event shorter [161]. From the results given in Table 7.1 we can conclude that the scattering model has a strong influence on the spill-in/out fractions.

The average results of parameters characterizing the neutron migration of NeutronTh and G4-NHPE are given in Table D.6 of Appendix D.5.
Testing the properties of NeutronTh shows that below $E_n = 4\,\mathrm{eV}$ we observe a larger number of neutron interactions. These occur since the elastic scattering cross section of neutrons on hydrogen atoms rises as the influence of hydrogen molecular bonds come into effect. Moreover, the energy loss per proton collision decreases since the neutron – due to an increase in the effective mass of the target – does rather interact with the whole molecule than a single hydrogen atom, which is reflected in the enlarged capture times (see Fig. 7.6). The thermalization time for neutron captures on gadolinium $\tau_{\mathrm{th,Gd}}$ becomes larger than in G4-NHPE and as a consequence the total capture time in the ν-target volume does increase. The effect on the Gd-fraction, however, is small and changes it from 88.2 % to 88.0 % by only $-0.2\,\%$. The capture time in the Gamma Catcher scintillator does change slightly if we use NeutronTh instead of the G4-NHPE code.

Furthermore, the enhanced scattering cross section and restrained energy loss result not only in a larger number of neutron interactions but also a decreasing average mean free path between the collisions. As a consequence, together with the flat distribution in scattering angles, the linear distance between IBD event and neutron capture location ΔR decreases. Figure 7.9 shows the ΔR distributions obtained with G4-NHPE and NeutronTh for the ν-target and the Gamma Catcher volume. If we compare both plots 7.9a and 7.9b, we see that the relative decrease of ΔR from $8.8\,\mathrm{cm}$ to $6\,\mathrm{cm}$ on average due to the improved MC model NeutronTh is with about $-40\,\%$ considerably larger for the Gamma Catcher liquid. An explanation could be the long neutron capture time in the Gamma Catcher in combination with the increased number of collisions, the smaller neutron mean free path and the change in angular distribution of the scattered neutrons. This aspect will finally have an influence on the spill-in/out fractions. As the distance ΔR in the ν-target does not change to a large extent, the effect on the number of spill-out events is expected to be small. The decrease in the mean linear distance is larger in the Gamma Catcher, which should lead to a reduced number of spill-in events. This effect can also be demonstrated by plotting the "skin-depth" Δd, which is the distance of a spill-in or spill-out IBD event to the nearest ν-target acrylics wall or ν-target edge. In Fig. 7.10a and 7.10b this quantity is shown for spill-in and spill-out events, respectively. The average spill-out skin-depth reduces only slightly from $2.3\,\mathrm{cm}$ to $2\,\mathrm{cm}$ by applying the more realistic thermalization model. In contrast to this, the mean spill-in skin-depth shrinks by factor 1.6 from $4.2\,\mathrm{cm}$ to $2.6\,\mathrm{cm}$ as NeutronTh is utilized.
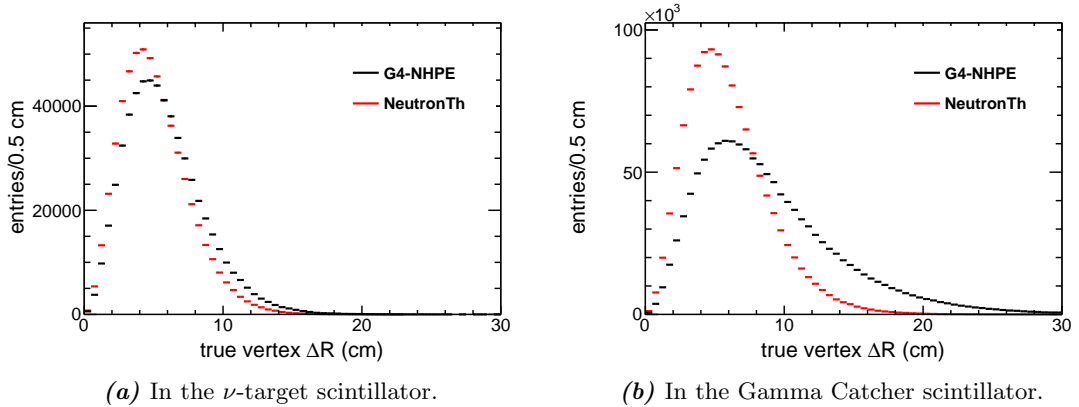
(a) In the ν-target scintillator.

(b) In the Gamma Catcher scintillator.

Figure 7.9: Neutron capture distance ΔR (linear distance between IBD position and neutron capture).

(a) Δd for spill-in events.

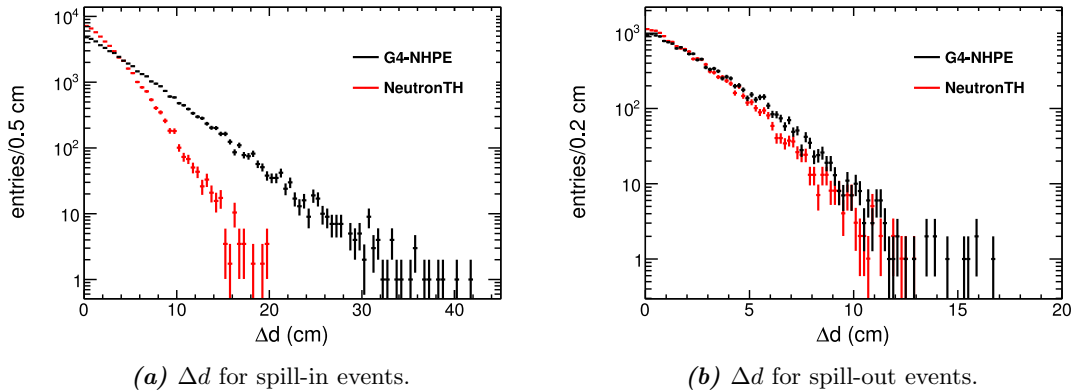

(b) Δd for spill-out events.

Figure 7.10: Distance Δd to nearest ν-target acrylics wall of the position of IBD events, which either produce a spill-in neutron *(a)*, or a spill-out neutron *(b)*.

7.5.2 Analysis strategy

While in the Gd-I analysis the spill-in/out uncertainty was considered to be dominated by the influence of the neutron physics model, the Gd-II analysis incorporated an enhanced low energy modeling. The analysis approach was hence extended to further investigate the robustness of the spill effect with respect to other parameters influencing the simulation of the neutron migration. Parameters mainly affecting spill-in/out fraction estimation in the MC are

1. the neutron scattering model,

2. the neutron capture cross sections,

3. the chemical composition of the scintillator liquids,

To test the stability and reliability of the spill-in ratio value of the Gd-II Monte Carlo, these parameters had to be modified within their known tolerance. Consequently different MC simulation samples were produced and the influence of changing these on the spill-in/out effect analyzed.

To investigate the impact of the neutron thermalization model on the spill-in results, the following two MC modelings were used: G4-NHPE and the Double Chooz custom code NeutronTh. The spill-in ratio gained using G4-NHPE was bond model corrected (as done for Gd-I, see Section 7.4.1) before comparing it to the NeutronTh result.

The capture cross sections were effectively changed by altering the Gd concentration of the ν-target scintillator and the H concentration in the Gamma Catcher liquid. Owing to the high precision of the weight measurement used to determine the amount of Gd dissolved in the ν-target liquid, the uncertainty on the Gd concentration is small [59]. Nevertheless, a discrepancy is found in the neutron capture fraction on Gd evaluated with calibration data and the predicted value from MC simulation (see Section 5.4). Furthermore, it was unknown whether the scattering cross section or a deviation in the capture cross section leads to the Gd-fraction discrepancies. Hence, three additional Gd concentrations used for the spill studies were constructed to meet in the ideal case the lower Gd-fraction seen in data[5] compared to MC. Only values below the default Gd concentration were hence considered. Additional MC simulation samples with 0.121, 0.110 and 0.100 wt. % gadolinium were generated, whereas the default Gd concentration amounts to 0.123 wt. %.

Furthermore, the hydrogen concentration in the Gamma Catcher was varied with respect to the default value of 14.6 wt. % to be 14.4 and 14.8 wt. % in two additional samples. These values were estimated based on the 0.2 wt. % uncertainty on the hydrogen concentration [59]. The influence of the acrylic ν-target vessel geometry and thickness is expected to be a small effect and was therefore not studied further.

Monte Carlo samples

In Table A.1 of Appendix A the MC simulation samples used and the particular MC configurations are listed. Each additional sample was produced differing in only one parameter compared to the standard configuration. All of the data samples contain 1.8×10^6 to 2×10^6 neutrinos in ν-target plus Gamma Catcher. The hydrogen concentration in the Gamma Catcher scintillator was altered by changing the hydrogen fraction of the medicinal white oil Ondina909, which constitutes the largest part of the liquid. The hydrogen and carbon abundances are altered in the MC code by changing the relative nuclear abundances n_x (x = H, C) and was for each sample with changed H content adjusted to match

$$n_H + n_C = 1.$$

7.5.3 Results and systematic uncertainty estimation

For each of the configurations given in Table A.1 of Appendix A a MC sample was produced and analyzed. The results of the two samples with varied hydrogen concentration in the Gamma Catcher liquid and the standard Gd-II sample were compatible within less than $1.9\,\sigma$ of the negligibly small statistical uncertainty. Hence the contribution of the hydrogen concentration uncertainty to the spill-in systematic uncertainty was considered to be negligible.

---

[5]The Gd-fraction in the Gd-II data of the first calibration campaign is with $(86.5 \pm 0.5)\,\%$ about 1.5 % lower than the fraction observed using MC simulation [98].

Table 7.3: Gd-fractions for the four different Gd concentrations. The default Gd concentration is highlighted in bold.

Gd concentration		Gd-fraction (%)
0.123 wt. %	**988 mg/l**	**87.98 ± 0.05**
0.121 wt. %	972 mg/l	87.75 ± 0.05
0.110 wt. %	884 mg/l	87.00 ± 0.05
0.100 wt. %	804 mg/l	86.13 ± 0.05

Table 7.4: Detected spill-in and spill-out fractions for the Gd-II analysis. The NeutronTh results highlighted in bold correspond to the Gd-II default MC results, the sample with a Gd-concentration of 804 mg/l was produced with NeutronTh applied.

	G4-NHPE	G4-NHPE bond model corr.	**NeutronTh**	NeutronTh 804 mg/l Gd
N_T^{det}	465355	-	**463392**	378039
N_{SI}^{det}	23617	-	**17432**	13889
N_{SO}^{det}	11223	-	**11043**	9710
f_{SI}^{det}	$(4.96 \pm 0.04)\,\%$	$(4.19 \pm 0.03)\,\%$	$\mathbf{(3.67 \pm 0.03)\,\%}$	$(3.58 \pm 0.04)\,\%$
f_{SO}^{det}	$(2.35 \pm 0.03)\,\%$	$(2.40 \pm 0.03)\,\%$	$\mathbf{(2.33 \pm 0.03)\,\%}$	$(2.50 \pm 0.03)\,\%$
ϕ_{SI}^{det}	$(2.60 \pm 0.04)\,\%$	$(1.79 \pm 0.04)\,\%$	$\mathbf{(1.35 \pm 0.04)\,\%}$	$(1.08 \pm 0.04)\,\%$

In Table 7.3 the Gd-fractions obtained for the four different Gd concentrations are shown. Here, the Gd-fractions were computed using truth information about the capture nucleus provided by the MC simulation. The Gd capture fraction is then given by the fraction of neutron captures on Gd out of IBD reactions in the ν-target volume followed by a neutron capture inside the ν-target. We can see that the value of 86.5 % gained with ^{252}Cf calibration data lies between the two lower Gd concentrations of 884 mg/l and 804 mg/l. As the uncertainty on the Gd-fraction measurement from data is 0.5 % in the Gd-II analysis [98], the MC simulation sample with the lowest Gd loading was used for the spill-in/out systematics determination.

Reducing the Gd concentration to 804 mg/l leads to a decrease in the spill-in ratio. Since the neutron capture time constant is enlarged if the Gd abundance is lowered, a larger amount of neutrons originating from IBDs in the ν-target can escape the ν-target volume, thus increasing the spill-out fraction. Likewise, potential spill-in neutrons have an increased probability to leave the ν-target again before being captured in it as well as a reduced selection efficiency inside the ν-target, the change in the spill-in fraction is however not significant.

The decrease of the spill-in ratio can be seen in the case of the MC sample with 804 mg/l Gd in Table 7.4 relative to the results using G4-NHPE as well as NeutronTh. As predicted in Section 7.5.1, the spill-in fraction reduces compared to the hydrogen free gas modeling of G4-NHPE if NeutronTh is applied; the spill-out fraction on the other hand does not change significantly.

The NeutronTh spill-in value of $1.35\,\%$ represents the central value of the spill-in ratio observed in the Gd-II simulation. The discrepancy between the default Gd and the low $(804\,\mathrm{mg/l})$ Gd spill-in ratio was used as asymmetric uncertainty component induced by discrepancies in the Gd concentration or effective neutron capture cross section. The discrepancy of $0.27\,\%$ is taken as asymmetric uncertainty towards lower spill-in ratios in accordance with the Gd-fraction measurement, which yields a lower value than observed with MC simulation. Since we cannot ensure that the spill-in ratio lower limit is given by the NeutronTh result, the uncertainty component introduced by the MC neutron scattering model was considered to be symmetric. The uncertainty component itself was estimated from the deviation between the NeutronTh value and the arithmetic mean of the NeutronTh and the G4-NHPE bond model corrected value to be $0.224\,\%$. The combination of all systematic uncertainty components leads to a total asymmetric uncertainty of

$$\phi_{\mathrm{SI}}^{\mathrm{det}} = \left(1.347\,^{+\mathbf{0.224}}_{-\mathbf{0.350}}\,(\mathrm{syst}) \pm 0.035\,(\mathrm{stat})\right)\%\,, \tag{7.18}$$

where the two negative uncertainties were combined in quadrature.

Uncertainty symmetrization

As the Gd-II θ_{13} fit required symmetric uncertainties it was necessary to symmetrize the spill-in ratio systematic uncertainty. To describe both the positive and negative uncertainty contributions of the spill-in ratio, we start with Gaussian distributions of the form

$$f_i(x) = \frac{1}{\sigma_i\sqrt{2\pi}} \cdot e^{-\frac{1}{2}\left(\frac{x-\phi}{\sigma_i}\right)^2} \quad \text{with } i = 1, 2\,, \tag{7.19}$$

where ϕ denotes the spill-in ratio and $\sigma_{1,2}$ the negative and positive uncertainties given in Eq. (7.18) respectively. From these, an asymmetric continuous and normalized Gaussian probability density function is built:

$$\rho(x) = A \cdot \Bigg(\Theta(x - \phi)\, f_1(x)$$

$$+ \frac{\sigma_2}{\sigma_1}\, \Theta(x + \phi)\, f_2(x) \Bigg)\,, \tag{7.20}$$

with the normalization factor

$$A = \frac{2\sigma_1}{(\sigma_1 + \sigma_2)}\,,$$

and the Heaviside step function

$$\Theta(x) = \begin{cases} 1 & \text{if } x \geq 0\,, \\ 0 & \text{if } x < 0\,. \end{cases}$$

It is constructed in such a way, that the integral from σ_1 to σ_2 yields $68.27\,\%$ of the total area. To obtain a symmetric uncertainty the $68.27\,\%$ C. L. needs to be shifted so that $\sigma_1 = \sigma_2$. In order to do this, the probability density function in Eq. (7.20) is first integrated and in a second step the point of intersection $\hat{x}$ of the integral and 0.6827 is
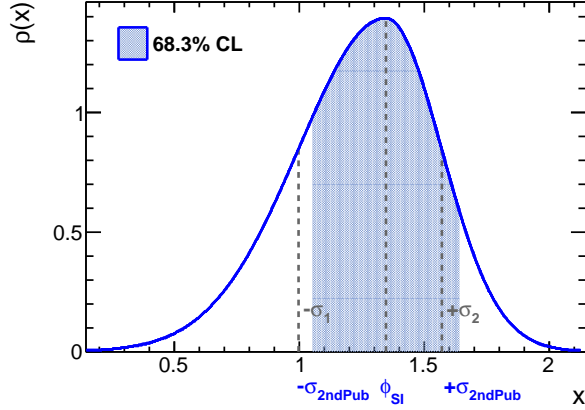
Figure 7.11: Asymmetric Gaussian distribution used for uncertainty symmetrization. In blue the Gd-II systematic uncertainty is shown, the blue shaded area represents the 68.3 % C. L..

calculated (see Fig. 7.11):

$$0.6827 = \frac{\sigma_1}{\sigma_1 + \sigma_2} \cdot \left(\mathrm{erf}\left(\frac{\hat{x} - \phi}{\sigma_1 \sqrt{2}} \right) + \frac{\sigma_2}{\sigma_1} \mathrm{erf}\left(\frac{\hat{x} - \phi}{\sigma_2 \sqrt{2}} \right) \right) . \tag{7.21}$$

The symmetrized uncertainty is then $\sigma_{\mathrm{2ndPub}} = \hat{x} - \phi$. For the spill-in/out result of Gd-II we finally obtain

$$
\begin{aligned}
\phi_{\mathrm{SI}}^{\mathrm{det}} &= (1.347 \pm \mathbf{0.295} \, (\mathrm{syst}) \pm 0.035 \, (\mathrm{stat})) \, \% \\
&= (1.35 \pm \mathbf{0.30}) \, \% .
\end{aligned}
\tag{7.22}
$$

7.6 Gd-III systematic uncertainty

The systematic uncertainty estimation of the Gd-III spill-in/out effect was performed by A. Collin [77]. He accomplished to implement the full DC detector structure in a TRIPOLI4-based framework, rendering possible to perform direct MC-MC comparison to the Gd-III simulation code. The modeling of hydrogen bonds in TRIPOLI4 was realized in form of CH_2 groups. A response map was used to transfer the spatial dependence of the energy cut efficiency on the Gd capture peak from Gd-III simulation to TRIPOLI4. The Gd-III net spill-in ratio evaluated with the standard NeutronTh code was computed to be 2.08 %, whereas a higher value of 2.36 % was obtained using the TRIPOLI4 code. The systematic uncertainty on the spill-in ratio computed from the difference of the two results was found to be 0.27 % [12]. Owing to the modified neutrino selection cuts (see Table 3.2 in Section 3.3.1) the spill-in ratio had changed compared to the Gd-I and Gd-II analyses.

7.7 Attempt to measure the spill-in effect

In Ref. [149] the possibility to measure the spill-in effect is discussed and was studied using simulation code. A technique to distinguish spill-in events from regular IBD reactions in the ν-target liquid has to be able to identify in which scintillator liquid the positron events deposited the main fraction of their energy. One promising approach was therefore to focus on the pulseshapes of the prompt positron events. The pulseshape of the photon emission process in a liquid scintillator can be described as the sum of exponential de-excitations with time constants τ_i and weight factors q_i:

$$p(t) = \sum_i \frac{q_i}{\tau_i} e^{-t/\tau_i} . \tag{7.23}$$

The parameters determining the pulseshape depend on the mass and charge of the ionizing particle, as well as on the scintillator components. Due to different scintillator composition the time constants τ_i are shorter in the ν-target compared to the Gamma Catcher. Hence, light emission in the ν-target is faster than in the Gamma Catcher. Based on these concepts it might be possible to distinguish energy depositions occurring in the ν-target and the Gamma Catcher liquid.

The scintillation pulseshapes used in the studies presented in the following were extracted from the hit times of the PMTs. Each hit time was corrected for the time of flight of the scintillation photons using the reconstructed event position and the PMT location. A histogram was filled with the start times of the first occurring pulse of each PMT.
The variable used to characterize the pulseshape is the *Late Light Ratio (LLR)* [149]: the ratio of the fraction of scintillation light in the tail of the pulseshape and the total pulseshape is computed. Hence, a large LLR corresponds to a slow scintillation pulse.

Since the LLR technique was thought to be applied on positrons produced in the IBD reaction, ^{60}Co source data was analyzed to optimize the LLR definition. As discussed in Section 2.1.4 provides the ^{60}Co source data an energy deposition of $\sim 2.5\,\mathrm{MeV}$, which is comparable to the peak of the prompt visible energy at $\sim 3\,\mathrm{MeV}$.
Averaged scintillation pulseshapes were formed using the deployment data taken at the ν-target center and in the Gamma Catcher volume. As desired, the ν-target scintillation light emission was observed to occur faster than the one in the Gamma Catcher. However, reflections accumulating at $\sim 30\,\mathrm{ns}$ after the first PMT hit time in the ν-target pulseshape worsened the discrimination power [123]. The observed reflections were found to be consistent with the Buffer dimensions. As a consequence, the LLR method was optimized to yield the best ν-target to GC difference in the LLR variable. The largest discrimination power should hence be obtained when only the interval of largest discrepancy in the pulseshapes is taken into account. Various LLR definitions were tested on scintillation pulseshapes of ^{60}Co events and the best performance was found in case the time interval $t = [10, 26]\,\mathrm{ns}$ after the start time of the scintillation pulse was used to compute the LLR variable. In Fig. 7.12a the LLR variable for the ^{60}Co source deployment at the ν-target center and in the Gamma Catcher volume are given, showing two separate LLR populations. The energy depositions in the ν-target indeed exhibit a lower LLR value and with respect to the peak positions the discrimination power is satisfying. The peak-to-valley ratio, however, is not as large as for the
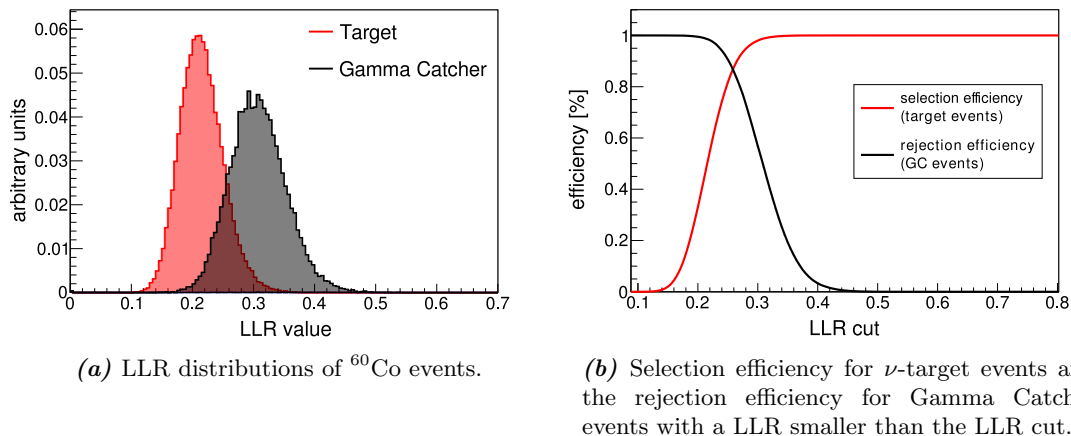
(a) LLR distributions of ^{60}Co events.

(b) Selection efficiency for ν-target events and the rejection efficiency for Gamma Catcher events with a LLR smaller than the LLR cut.

Figure 7.12: LLR results for ^{60}Co data at the ν-target center and in the Gamma Catcher volume.

simulation results reported by Ref. [149]. The discrimination power on the event basis will not be sufficiently large enough to measure the spill-in effect with a fit of the LLR distribution of IBD candidates with two Gaussian distributions. Fig. 7.12b shows the selection efficiency for ν-target events and the rejection efficiency for Gamma Catcher events having LLR values smaller than a particular LLR cut.

7.8 Conclusion

In this chapter the spill-in/out systematic uncertainty estimations for the Gd-I and Gd-II analyses were described, induced by border effects at the ν-target acrylic wall due to neutron migration. Neutrons from IBD reactions outside the ν-target scintillator can enter the ν-target volume, whereas neutrons produced in IBD reactions inside the ν-target can leave the Gd-doped liquid. Each effect enhances or reduces the amount of detected neutrino events - they counterbalance but do not cancel. A net excess of events migrating into the ν-target is observed, which is sensitive to a variation in the parameters changing the slowing down of a neutron.

As the Gd-I MC could not model the low energy neutron physics with sufficient accuracy, the spill-in ratio was overestimated. Therefore a MC live time correction factor of 1.0072 was introduced. The systematic uncertainty was estimated based on the size of the bond model correction. Dominated by the systematic uncertainty, the total uncertainty including both the statistical and systematic contributions was 0.38 %.

For the Gd-II analysis the neutron physics package NeutronTh was implemented in the DC Monte Carlo. Since NeutronTh describes the neutron thermalisation process better than the former used free proton approach, a MC live time correction was no longer considered as necessary. The systematic uncertainty was estimated by variation of parameters on which the spill-in ratio is expected to depend on. Several MC samples were produced and analyzed. The contributions to the uncertainty came from variation of the Gd concentration in the ν-target scintillator and application of different neutron

MC models. For the combined uncertainty for Gd-II 0.30 % was obtained.

In comparison to the preceding CHOOZ experiment, where the spill-in/out effect contributed a $\sim 1\,\%$ uncertainty on the antineutrino rate, the systematic uncertainty in Gd-II is reduced by a factor three. Since the effect cannot be measured with detector data, MC simulation studies were performed to estimate the impact of different MC configurations on the net spill-in ratio. In the two detector analysis the uncertainty will mainly depend on deviations in the detector geometry and material compositions between the near and far detector. Possible discrepancies in these parameters are expected to be small and since most of the other factors affecting the spill-in ratio are correlated between the two detectors, the spill-in/out systematic uncertainty should be further reduced.

Summary

As the current Double Chooz analyses are accomplished with data from a single detector measurement, the neutrino oscillation parameter θ_{13} is obtained from a relative comparison to a Monte Carlo (MC) prediction of the reactor neutrino rate and spectral shape. One focus of the analysis is therefore on calibration of the detector data and MC simulation as well as studies of the data to MC consistency and the evaluation of corresponding systematic uncertainties.

This thesis discussed the systematic uncertainties associated with the neutrino signal detection in the Double Chooz experiment. In particular systematic influences related to the neutron detection have been studied, which constitute the dominant component of the total signal detection uncertainty. Distinguishing between three different contributions to the neutron detection uncertainty, each of them has been addressed: the neutron capture fraction on the isotopes of a particular element, the efficiency introduced by the choice of the neutron selection cuts and an effect related to neutron migration altering the fiducial volume size.

The latter is also known as *spill-in/out effect* and occurs in the standard neutrino analysis at the boundary of the innermost detector vessel. Neutrons created by inverse beta decays (IBD) outside the fiducial volume cross the vessel border and are detected via radiative captures on gadolinium (Gd). Likewise, events can escape the detection if the neutron leaves the Gd-doped scintillator. Both opposed neutron event fluxes do not cancel, as the spill-in exceeds the spill-out effect. The absolute uncertainty on the net effect directly propagates as relative uncertainty to the neutrino normalization of the θ_{13} analysis. Since the net effect cannot be measured, the systematic uncertainty estimation is not straightforward. Consequently the net spill-in currents evaluated for different MC configurations were taken into consideration, estimating the impact of parameter modifications and neutron scattering modelings on this quantity. In the Gd-I analysis the computed neutrino flux expectation included an incomplete low energy neutron model. To account for this, the net spill-in current was corrected based on results obtained from simulation code designed to model neutron processes at low energies. The impact on the total neutrino rate was evaluated and a correction factor along with a systematic uncertainty were assigned. The enhanced neutron modeling in the Gd-II MC code made a similar correction unnecessary and yields a net spill-in current of 1.4 %. By changing parameters which impact the spill-in current within their tolerances, the systematic uncertainty was estimated to be 0.3 %. Main contributions to this result came from modification of the neutron scattering physics at low energies and the Gd concentration in the scintillator liquid. In addition, the presented studies could improve the knowledge on the low-energy neutron processes in the DC Monte Carlo framework.

A correction factor adjusts the MC normalization to systematic discrepancies in the signal detection efficiencies between detector data and MC prediction. This correction factor in combination with a systematic uncertainty is given as input to the θ_{13} fit. Contributions from neutron related detection efficiencies were studied using ^{252}Cf source data coupled with dedicated simulation code. Emission of prompt gamma rays accompanying the release of multiple neutrons allowed to tag the occurrence of a ^{252}Cf fission event and select fission neutrons by searching for a prompt-delayed coincidence pattern. As a consequence, it was possible to measure timing, peak energy containment and spatial displacement of the neutron capture events with high statistics. Separating into accidental and correlated background contributions selected along with fission events, intense background studies ensured that background reduction techniques minimized systematic effects on the measurements, while at the same time not biasing the results by the background-reduced selection. Consistency checks with calibration data recorded in source deployment campaigns at intervals of almost a year allowed to prove the stability of the liquid scintillators with respect to the neutron capture fractions. The capture fractions represent a neutron detection efficiency inherent to the particular detector liquid and are to the first order predetermined by its chemical composition and constant throughout the respective volume. A $\sim 2\,\%$ discrepancy was discovered in the capture fraction on Gd nuclei comparing the value gained with calibration data to the fraction predicted by simulation code. Comparison with the results from a neutron sample from IBD reactions [89] confirmed the observation and excluded a dependency on neutron kinetic energy. Furthermore, the same inconsistency in the capture fraction was encountered in a MC-MC comparison of the Double Chooz simulation with a MC code known to incorporate a more realistic neutron physics modeling [74]. A MC normalization correction related to the discrepancy in the neutron capture fraction on Gd was retrieved from ^{252}Cf data and simulation. The associated evaluation of the systematic uncertainty of $0.4\,\%$ was based on the variation of the applied capture fraction definitions used to compute the correction and accounted for possible remaining background contributions.

Usually rejected as background in the neutrino analysis, neutrons originating from cosmic muon spallation were selected to crosscheck the ^{252}Cf result. The result obtained from spallation neutrons was found to be consistent with the ^{252}Cf value within uncertainties. However, due to limitations of the vertex reconstruction and the ignorance of the position of neutron creation, the interpretation of the results was shown to be difficult. Nevertheless it had proven the necessity of knowledge on the neutron emission location in an efficiency study.

Neutrino interactions in a liquid scintillator detector produce a distinct twofold coincidence signal: a prompt energy deposition by a positron and the delayed radiative neutron capture. The selection criteria of the neutron events include cuts on the visible energy, the coincidence time and the correlation distance. Each cut introduces a signal detection efficiency depending on the IBD position. Different definitions were proposed to estimate the efficiency, taking into account different subsets of the accessible parameter space. The *exclusive* definition evaluates the neutron detection efficiency for each selection cut individually, whereas the *semi-inclusive* efficiency definition incorporates every neutron detection efficiency except for the capture fraction.

In order to account for the spatial dependence of the detection efficiency and the increasing number of IBD reactions in the radial direction of the volumes, a global MC

correction has to be computed from volume-integrated efficiency estimates. In the standard analysis, the ν-target forms the fiducial volume. Since it is calibrated along the central symmetry axis, a volume-integration method was proposed, extrapolating the efficiencies measured with the limited set of calibration points to the full volume. Validation of the method was rendered with simulation data, which demonstrated that the Target-wide semi-inclusive efficiency can be reproduced with 0.23 % accuracy.

The Target-wide efficiencies and global MC corrections were evaluated for the exclusive and semi-inclusive efficiency definition giving consistent results and thus proving the absence of correlations between the cut efficiencies which might impact the MC correction computation. The global cut dependent correction was computed to be consistent with unity, which implies excellent agreement between data and simulation in the selection cut efficiency. A series of robustness tests was conducted to estimate the systematic uncertainty, including tests of the computational methods, time stability, fission event selection, position inaccuracy of the calibration and spatial inhomogeneity. The effect of a global MC correction on the prompt spectral shape of IBD events was studied and found to be negligible. Dominated by the uncertainty on the volume-integration method, the systematic uncertainty of the cut dependent global MC correction was estimated to be 0.32 % in an analysis with ^{252}Cf calibration data. In combination with the result obtained using neutrons created by IBD reactions [89] a global MC correction of $1.000 \pm 0.002\,(\text{stat} + \text{syst})$ was estimated.

The work prepared on the global efficiency MC correction of an alternative θ_{13} analysis based on neutron captures on hydrogen (H) nuclei was presented. In these studies the volume-integration technique had to be extended to the Gamma Catcher volume, which features a more complex geometry than the ν-target. Spatial parametrization of the calibration measurements with respect to the distance to the acrylic wall of the ν-target or the distance to the detector center enabled to compute volume-averaged efficiency corrections. From the comparison of results obtained with the different integration methods and subdivided datasets, the systematic uncertainty of the volume-integration could be estimated. A set of proposed cuts was tested to find the combination of selection criteria which yields the lowest systematic uncertainty on the efficiency related MC correction. The results retrieved using ^{252}Cf source neutrons tend to prefer loosened selection cuts in any variable. Furthermore, the capture fraction of neutrons on hydrogen in calibration data was observed to be in agreement with the simulated value.

In the Gd-III analysis the total systematic uncertainty of the signal detection efficiency amounts to 0.6 %, representing a reduction by almost a factor two compared to previous analyses. Currently dominated by the reactor flux uncertainty the DC experiment will soon enter the two detector phase. From then on, the detection efficiency uncertainty and in particular the neutron detection systematics will become one of the main contributions to the total systematic uncertainty on θ_{13}. Systematic uncertainties which are correlated between both detectors will cancel out. Therefore uncertainty contributions from spill-in/out effect or the neutron capture fraction will be strongly reduced. As demonstrated by the Gd-III cut dependent detection systematics, an uncertainty of 0.2 % can be achieved. Along with this result a sensitivity of $\sigma(\sin^2 2\theta_{13}) = 0.015$ could be reached after three years of data taking [12]. With regard to the systematic uncertainty studies, which have been aided by the work put forward in this thesis, it was shown that this field of the data analysis is well-prepared for a near and far detector phase.

Appendix A

Data labels and production tags

A.1 ^{252}Cf analysis: detection efficiency uncertainty

Monte Carlo detection efficiency studies

The two IBD event labels used for MC simulation studies MC_DC3rdPub_ANTINU_v3 and MC_DC3rdPub_ANTINU_v4 were produced with the CommonTrunk version CTv5 and energy scale ESv5. The IBD reactions were created in the full DC detector based on proton density maps.

The data labels MC_DC3rdPub_ANTINU_v3 and MC_DC3rdPub_ANTINU_v4 are used in this analysis, produced with the common trunk version CTv5 and featuring the energy scale kESv5.

Target-wide detection efficiency

The ^{252}Cf selection was performed on runs with the label EUppCf252Production_v4r7p0 in the case of real detector data, while the MC simulation can be found under the label MC_DC3rdPub_ZAXIS_CF252_v6. Both data sets were produced with the common trunk version CTv5, along with the official DC-III energy scale kESv5.

Gamma catcher-wide detection efficiency

The data used for analysis were for the first campaign all runs of Appendix B and the label EUppCf252Production_v4r7p0. For the MC simulation the label was MC_DC3rdPub_GUIDE_TUBE_CF252_v6 for the Guide-Tube runs and MC_DC3rdPub_ZAXIS_CF252_v6 for the z-axis. All data sets were produced with the common trunk version CTv5, along with the official DC-III energy scale kESv5. The MC runs were cut in length, such that the relative run lengths of different positions agreed with the relative run lengths of the data runs.

Spallation neutron analysis

The spallation neutron selection was made using the physics runs of the official DC-III run list TAGGED_DC3rdPub_CTv5_ALL_v1. As MC input the IBD neutron simulations with labels MC_DC3rdPub_ANTINU_v3 + v4 were used.

A.2 Spill-in/out analysis

Spill-in/out in the Gd-I analysis

The MC simulation labels utilized were produced with the CommonTrunk version CTv2 and energy scale ESv1:

CommonMCDC1stPub_AntiNuReduceGd_RLv3_10days
CommonMCDC1stPub_AntiNuReduceGd_RLv3_10days_v2
CommonMCDC1stPubIter3_AntiNuReduceGd_RLv3_10days
CommonMCDC1stPubIter3_AntiNuReduceGd_RLv3_10days_v2

Spill-in/out in the Gd-II analysis

The MC samples produced for the spill-in/out studies of the Gd-II analysis are summarized in Table A.1. All of the samples were produced with the CommonTrunk version CTv3 and energy scale ESv2.
The standard antineutrino MC sample used was MC_Gd-II_ANTINU_v1.

Table A.1: Table of the spill-in/out Gd-II MC simulation samples with varied parameters. $H(O_{909})$ is the hydrogen fraction of the medicinal white oil Ondina909. It differs from the total hydrogen fraction in the gamma-catcher, as several other scintillator components have to be taken into account as well.

MC simulation sample	NeutronTh	Gd in T		H in GC	
		[wt.%]	[g/l]	[wt.%]	$H(O_{909})$
MC_Gd-II_ANTINU_v1	✓	0.123	0.988	14.6	0.147
MC_Gd-II_ANTINU_NEUTRONTH_OFF_v1	—	0.123	0.988	14.6	0.147
MC_Gd-II_ANTINU_GD_972mg	✓	0.121	0.972	14.6	0.147
MC_Gd-II_ANTINU_GD_884mg	✓	0.110	0.884	14.6	0.147
MC_Gd-II_ANTINU_GD_804mg	✓	0.100	0.804	14.6	0.147
MC_Gd-II_ANTINU_C26H52	✓	0.123	0.988	14.5	0.144
MC_Gd-II_ANTINU_C26H54	✓	0.123	0.988	14.7	0.148

Appendix B

^{252}Cf deployment runs

The run lists of the first calibration campaign was retrieved from Ref. [96], the run list from the second campaign from Ref. [97].

B.0.1 First calibration campaign ^{252}Cf deployments

z-axis deployment

Table B.1: Run information for ^{252}Cf source deployed at z-axis. The Double Chooz source code is Cf-252-4.

| run number	x [mm]	y [mm]	z [mm]	run length [s]
23981	0	0	0	3600
23986	0	0	-1250	3600
24405	0	0	1257	900
24406	0	0	967	900
24407	0	0	640	900
24408	0	0	0	900
24409	0	0	-654	900
24410	0	0	-981	900
24411	0	0	-1250	900
25067	0	0	1257	900
25068	0	0	1120	860
25069	0	0	800	900
25070	0	0	480	900
25075	0	0	160	900
25076	0	0	-160	900
25077	0	0	-480	900
25078	0	0	-800	900
25079	0	0	-1120	900
25080	0	0	-1217	900
25081	0	0	-1272	900
25082	0	0	-1250	900
25083	0	0	0	2760

Guide-Tube deployment

Table B.2: Run information for ^{252}Cf source deployed in the Guide-Tube. The Double Chooz source code is Cf-252-4.

run number	x [mm]	y [mm]	z [mm]	run length [s]
22775	12.6	282.8	1330.4	180
22776	12.6	282.8	1330.4	1200
22777	12.6	282.8	1330.4	1200
22778	12.6	551.6	1325	1200
22779	12.6	551.6	1325	1200
22780	12.6	1002.6	1315.8	1200
22781	12.6	1002.6	1315.8	1200
22811	12.6	1188	994.5	1200
22812	12.6	1188	994.5	1200
22813	12.6	1188	548.1	1200
22814	12.6	1188	548.1	1200
22815	12.6	1188	147.2	1200
22816	12.6	1188	147.2	1200
22817	12.6	1215.8	27.8	1200
22818	12.6	1215.8	27.8	1200
22819	12.6	1287.2	0	1200
22820	12.6	1287.2	0	1200
22821	12.6	1433.8	0	1200
22822	12.6	1433.8	0	1200
22823	12.6	1654	1307.1	1200
22824	12.6	1654	1307.1	1200
22825	12.6	1654	1307.1	1200
22826	12.6	1654	1307.1	1200
22827	12.6	1654	1307.1	1200
22828	12.6	1654	1307.1	1200
22829	12.6	1654	1307.1	1200
22830	12.6	1654	1307.1	1200

B.0.2 Second calibration campaign ^{252}Cf deployments

z-axis deployment

Table B.3: Run information for ^{252}Cf source deployed at z-axis. The Double Chooz source code is Cf-252-4.

run number	x [mm]	y [mm]	z [mm]	run length [s]	run start time
43705	0	0	0	3600	2012-05-15 16:38:07
43706	0	0	-1250	1200	2012-05-15 17:47:45
44236	0	0	0	3600	2012-05-22 16:46:34
44656	0	0	0	3600	2012-05-28 11:10:07
44657	0	0	-1250	3600	2012-05-28 12:38:11
44658	0	0	-960	1200	2012-05-28 13:46:48
45042	0	0	0	3600	2012-06-06 12:56:50
45044	0	0	-1250	3600	2012-06-06 15:05:08
45047	0	0	-640	1200	2012-06-06 16:28:36
45048	0	0	640	1200	2012-06-06 16:54:32
45049	0	0	1250	1200	2012-06-06 17:18:20
45050	0	0	1250	1200	2012-06-06 17:39:21
45051	0	0	1250	1200	2012-06-06 18:00:24
45075	0	0	960	1200	2012-06-07 10:41:27
45076	0	0	320	1200	2012-06-07 11:06:30
45077	0	0	-320	1200	2012-06-07 11:30:02
45078	0	0	-960	1200	2012-06-07 11:53:30
45079	0	0	-1120	1200	2012-06-07 12:16:01
45080	0	0	-800	1200	2012-06-07 12:39:16
45081	0	0	-480	1200	2012-06-07 13:02:25
45082	0	0	-160	1200	2012-06-07 13:25:29
45083	0	0	160	1200	2012-06-07 13:48:00
45084	0	0	480	1200	2012-06-07 14:11:25
45085	0	0	800	1200	2012-06-07 14:34:17
45086	0	0	1120	1200	2012-06-07 14:57:09
45087	0	0	1150	900	2012-06-07 15:19:21
45089	0	0	1180	900	2012-06-07 15:39:39
45090	0	0	1220	900	2012-06-07 15:57:04
45091	0	0	1280	900	2012-06-07 16:14:10
45092	0	0	-1150	900	2012-06-07 16:38:16
45093	0	0	-1180	900	2012-06-07 16:55:33
45094	0	0	-1220	900	2012-06-07 17:12:49
45095	0	0	-1272	1200	2012-06-07 17:31:54
45700	0	0	0	1800	2012-06-15 17:28:07
45701	0	0	0	1800	2012-06-15 17:59:00

Guide-Tube deployment

Table B.4: Run information for ^{252}Cf source deployed in the Guide-Tube. The Double Chooz source code is Cf-252-4.

run number	x [mm]	y [mm]	z [mm]	run length [s]	run start time
46030	0	145	1532	1200	2012-06-18 16:11:19
46031	0	282	1330	1500	2012-06-18 16:35:27
46032	0	551	1325	1800	2012-06-18 17:03:12
46033	0	551	1325	1800	2012-06-18 17:35:53
46034	0	776	1320	1200	2012-06-18 18:08:46
46035	0	1002	1316	1500	2012-06-18 18:31:08
46036	0	1146	1298	1200	2012-06-18 18:57:33
46065	0	1188	1112	1200	2012-06-19 08:45:24
46066	0	1188	1007	1800	2012-06-19 09:09:26
46067	0	1188	1007	1800	2012-06-19 09:41:06
46068	0	1188	854	1200	2012-06-19 10:16:14
46069	0	1188	703	1800	2012-06-19 10:40:17
46070	0	1188	703	1800	2012-06-19 11:11:49
46071	0	1188	554	1500	2012-06-19 11:45:26
46072	0	1188	421	1800	2012-06-19 12:13:17
46073	0	1188	421	1800	2012-06-19 12:44:42
46074	0	1188	286	1500	2012-06-19 13:17:58
46075	0	1188	154	1800	2012-06-19 13:46:21
46077	0	1188	154	1800	2012-06-19 14:24:56
46078	0	1188	92	1200	2012-06-19 14:56:33
46079	0	1211	32	1800	2012-06-19 15:19:13
46080	0	1211	32	1800	2012-06-19 15:50:48
46081	0	1246	8	1200	2012-06-19 16:23:00
46082	0	1282	0	1800	2012-06-19 16:46:12
46083	0	1282	0	1800	2012-06-19 17:17:18
46084	0	1429	0	1800	2012-06-19 17:49:01
46085	0	1429	0	1800	2012-06-19 18:23:26
46108	0	1554	0	1200	2012-06-20 09:28:24
46109	0	1654	150	1500	2012-06-20 09:50:01
46110	0	1654	439	1200	2012-06-20 10:16:34
46111	0	1654	724	1500	2012-06-20 10:39:51
46112	0	1654	1016	1200	2012-06-20 11:06:42
46113	0	1654	1302	1500	2012-06-20 11:29:16
46114	0	1654	1422	1200	2012-06-20 11:57:36
46115	0	1537	1516	1200	2012-06-20 12:19:57
46116	0	1439	1518	1500	2012-06-20 12:42:35
46117	0	1189	1521	1500	2012-06-20 13:09:51
46118	0	778	1527	1200	2012-06-20 13:37:28
46119	0	555	1530	1500	2012-06-20 13:59:58
46120	0	353	1533	1200	2012-06-20 14:26:51

Appendix C

^{252}Cf fission spectra for different multiplicities
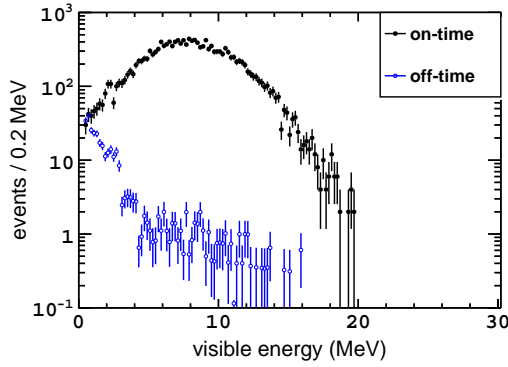
(a) Data prompt visible energy, $m=2$.
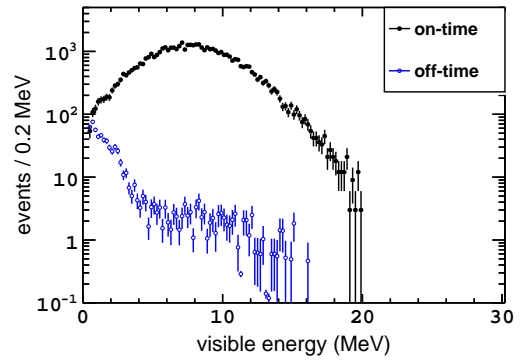
(b) Data prompt visible energy, $m=3$.
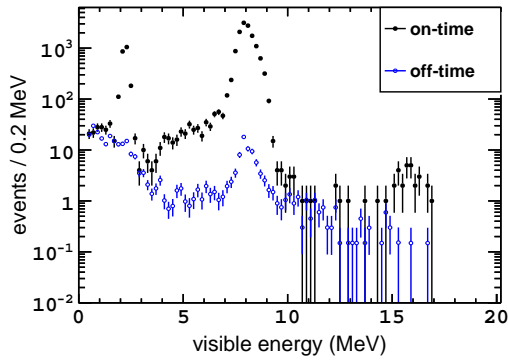
(c) Data delayed visible energy, $m=2$.
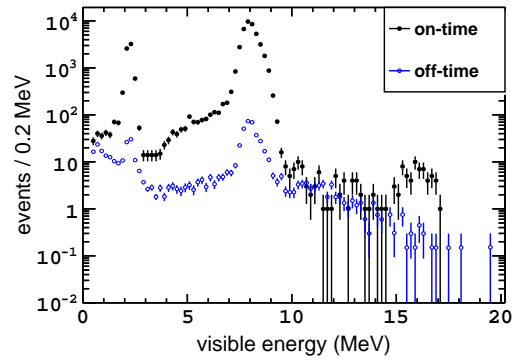
(d) Data delayed visible energy, $m=3$.

Figure C.1: Merged data spectra for multiplicities $m = 2, 3$ of the 6 ^{252}Cf 2nd calibration campaign deployment runs at the target center (x,y,z)=(0,0,12) mm. Prompt energy cut $E_{\mathrm{prompt}} > 0.5$ MeV and a maximal selected prompt-delayed correlation time of 1 ms. The blue points show the on-time delayed events, the black points the off-time (accidental background) delayed events. The red data points are the accidental background subtracted spectra.
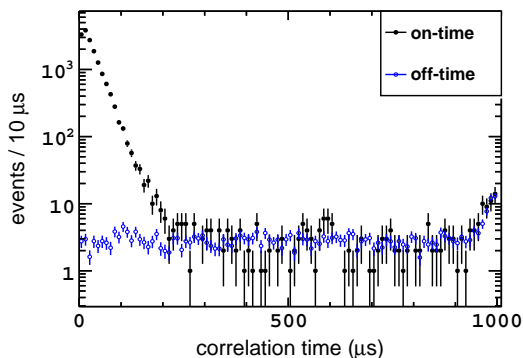
(a) Data prompt-delayed correlation time, $m\!=\!2$.
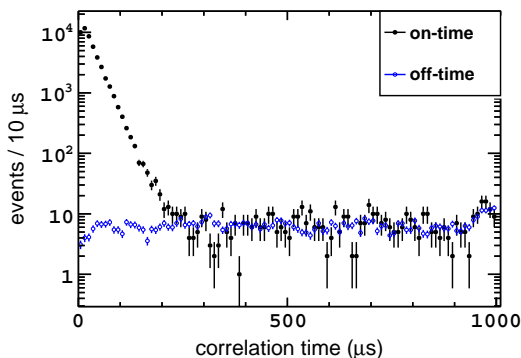
(b) Data prompt-delayed correlation time, $m\!=\!3$.
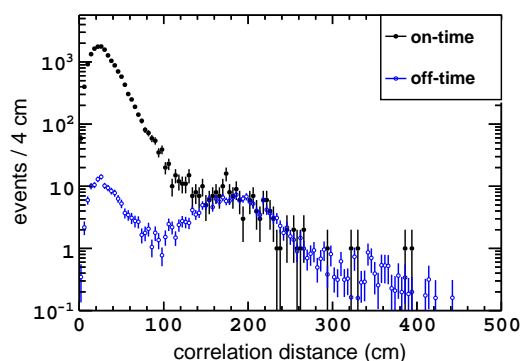
(c) Data prompt-delayed correlation distance, $m\!=\!2$.
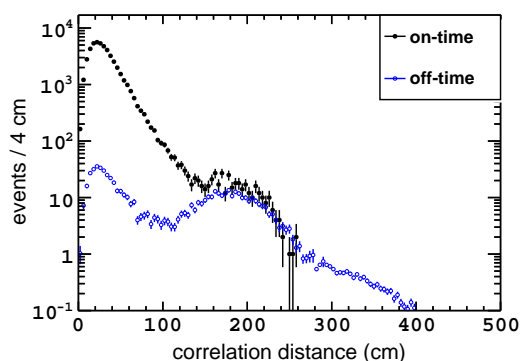
(d) Data prompt-delayed corr. distance, $m\!=\!3$.

Figure C.2: Merged data spectra for multiplicities $m = 2, 3$ of the 6 ^{252}Cf 2nd calibration campaign deployment runs at the target center (x,y,z)=(0,0,12) mm. Prompt energy cut $E_{\mathrm{prompt}} > 0.5\,\mathrm{MeV}$ and a maximal selected prompt-delayed correlation time of 1 ms. The blue points show the on-time delayed events, the black points the off-time (accidental background) delayed events. The red data points are the accidental background subtracted spectra.

The drop-off at short correlation times Δt and the rise at higher Δt is caused by the prompt event identification veto (see section 4.1.2) and the limited measurement range of the measurement window[1], respectively.

---

[1]Also fissions with higher multiplicities $l > n$ can contribute, in case $l - n$ events possess a too large correlation time. They occur outside the measurement window and are therefore not measured.

Appendix D

Detection efficiency results

D.1 Antineutrino MC efficiency reduction shapes

(a)

(b) Zoom of figure (a).
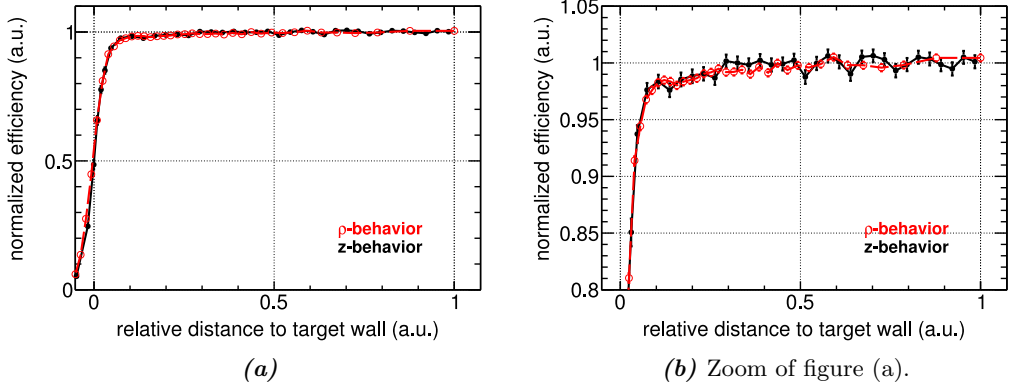
Figure D.1: Efficiency reduction shapes $f_1(\hat{z})$ and $f_2(\hat{\rho})$ of the inclusive efficiency. The top and bottom z data was combined in one shape. The red open circles connected by the dashed red lines represent the ρ-shape $f_2(\hat{\rho})$. The black bullets show the z-shape $f_1(\hat{z})$.
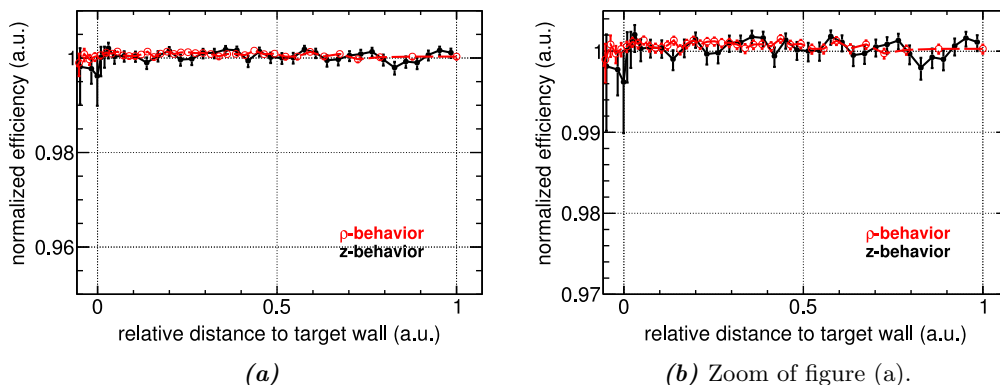

(a)

(b) Zoom of figure (a).
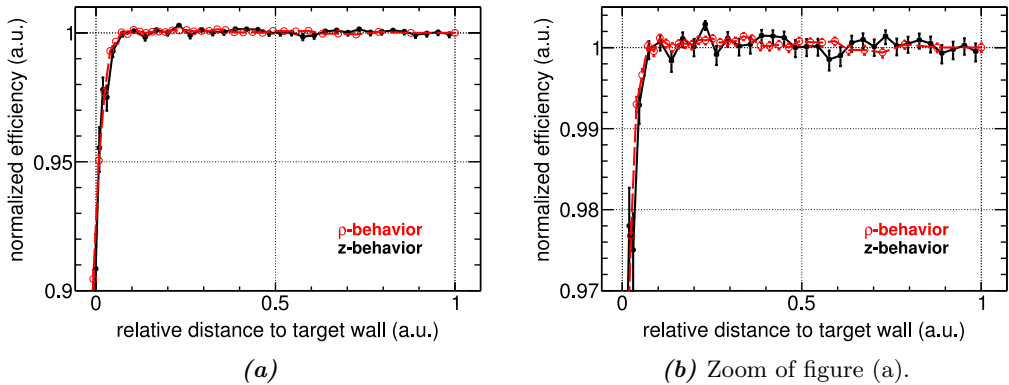
Figure D.2: Efficiency reduction shapes $f_1(\hat{z})$ and $f_2(\hat{\rho})$ of the ΔT efficiency. The top and bottom z data was combined in one shape. The red open circles connected by the dashed red lines represent the ρ-shape $f_2(\hat{\rho})$. The black bullets show the z-shape $f_1(\hat{z})$.

(a)

(b) Zoom of figure (a).
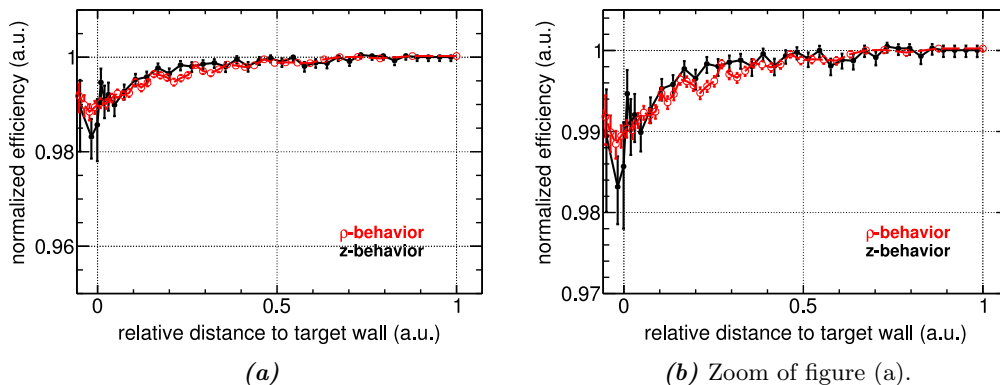
Figure D.3: Efficiency reduction shapes $f_1(\hat{z})$ and $f_2(\hat{\rho})$ of the E_{delayed} efficiency. The top and bottom z data was combined in one shape. The red open circles connected by the dashed red lines represent the ρ-shape $f_2(\hat{\rho})$. The black bullets show the z-shape $f_1(\hat{z})$.

(a)

(b) Zoom of figure (a).

Figure D.4: Efficiency reduction shapes $f_1(\hat{z})$ and $f_2(\hat{\rho})$ of the ΔR efficiency. The top and bottom z data was combined in one shape. The red open circles connected by the dashed red lines represent the ρ-shape $f_2(\hat{\rho})$. The black bullets show the z-shape $f_1(\hat{z})$.

D.2   Gd-III detection efficiency results and MC corrections from ^{252}Cf data

The results shown were calculated by means of the definitions given in section 5.3.2.

Table D.1: Table of the ^{252}Cf 2nd calibration campaign detection efficiencies at target center and the corresponding MC correction c_0 at the target center. Uncertainties are statistical only.

efficiency	$\varepsilon_0^{\text{Data}}$	$\varepsilon_0^{\text{MC}}$	c_0
inclusive	0.84562 ± 0.00088	0.86690 ± 0.00044	0.9755 ± 0.0012
semi-inclusive	0.99115 ± 0.00030	0.99081 ± 0.00017	1.00034 ± 0.00035
exclusive	0.99111 ± 0.00030	0.99080 ± 0.00017	1.00031 ± 0.00034
E_{delayed}	0.99880 ± 0.00010	0.99815 ± 0.00006	1.00065 ± 0.00011
ΔR	0.99710 ± 0.00014	0.99576 ± 0.00009	1.00134 ± 0.00017
ΔT	0.99519 ± 0.00025	0.99687 ± 0.00013	0.99831 ± 0.00028

Table D.2: Table of the ^{252}Cf 2nd calibration campaign target-wide detection efficiencies and the corresponding target-wide MC correction c_{v}. The last column shows the c_0 to c_{v} discrepancy. All uncertainties are statistical only.

efficiency	$\varepsilon_{\mathrm{v}}^{\mathrm{Data}}$	$\varepsilon_{\mathrm{v}}^{\mathrm{MC}}$	c_{v}	discrepancy $(c_0 - c_{\mathrm{v}})$ [%]
inclusive	0.8021 ± 0.0017	0.82504 ± 0.00063	0.9722 ± 0.0022	0.33 ± 0.29
semi-inclusive	0.98288 ± 0.00062	0.98257 ± 0.00025	1.00032 ± 0.00069	0.0026 ± 0.0010
exclusive	0.98247 ± 0.00062	0.98253 ± 0.00025	0.99994 ± 0.00068	0.04 ± 0.08
E_{delayed}	0.99407 ± 0.00024	0.99361 ± 0.00012	1.00047 ± 0.00029	0.02 ± 0.04
ΔR	0.99685 ± 0.00027	0.99594 ± 0.00013	1.00092 ± 0.00030	0.04 ± 0.04
ΔT	0.99145 ± 0.00050	0.99288 ± 0.00019	0.99856 ± 0.00054	-0.03 ± 0.07

D.3 H-III exclusive detection efficiencies
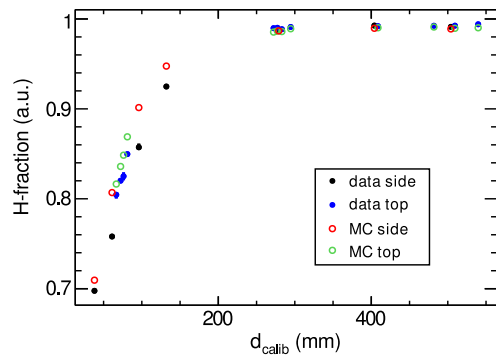
(a) H-fraction as function of d_{calib}.
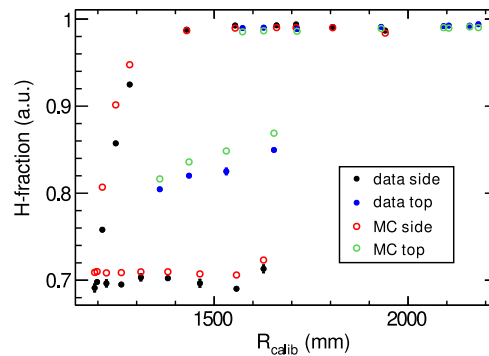
(b) H-fraction as function of R_{calib}.
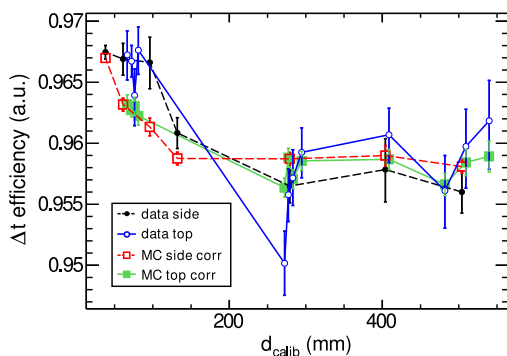
(c) ΔT efficiency as function of d_{calib}.
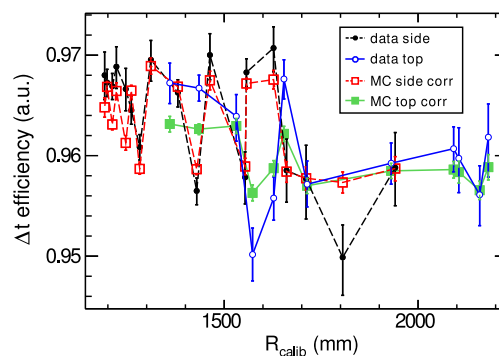
(d) ΔT efficiency as function of R_{calib}.

Figure D.5: Top/side separated ^{252}Cf deployment points with respect to the calibration position d_{calib} and R_{calib}: The exclusive efficiencies are plotted for data and MC runs taken at the GC side and top. In case the MC values are corrected, the correction is computed via Eq. (6.13) and Eq. (6.17).
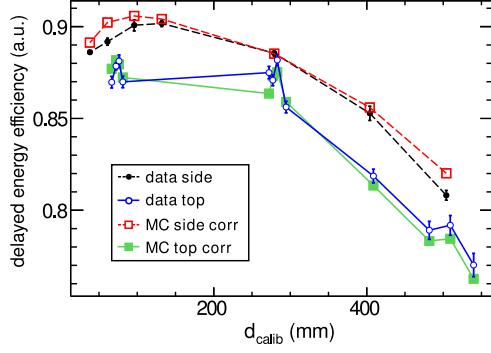
(a) Delayed energy efficiency wrt. d_{calib}.
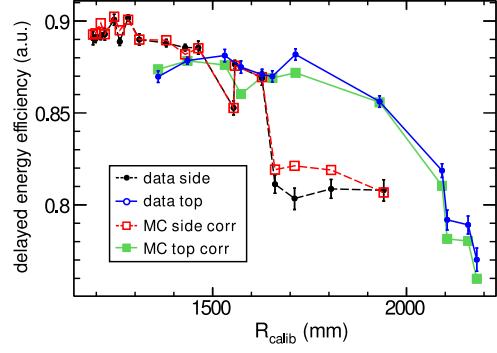
(b) Delayed energy efficiency wrt. R_{calib}.
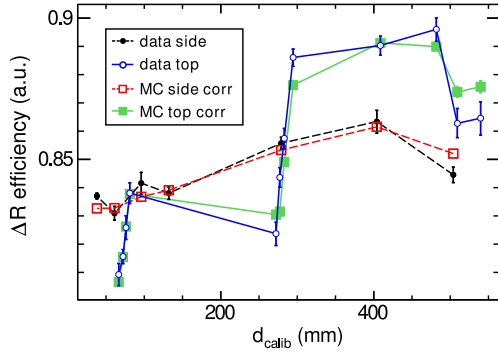
(c) ΔR efficiency as function of d_{calib}.
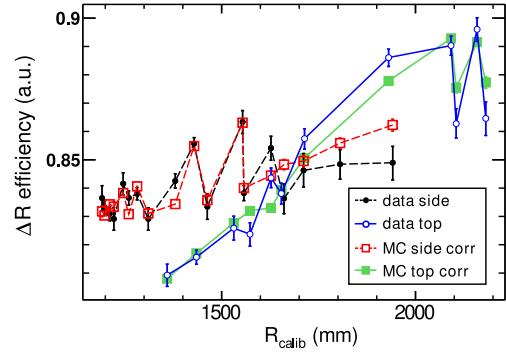
(d) ΔR efficiency as function of R_{calib}.

Figure D.6: Top/side separated ^{252}Cf deployment points with respect to the calibration position d_{calib} and R_{calib}: The exclusive efficiencies are plotted for data and MC runs taken at the GC side and top. In case the MC values are corrected, the correction is computed via Eq. (6.13) and Eq. (6.17).

D.4 Preliminary H-III detection MC corrections from ^{252}Cf data

Table D.3: MC correction factor results for changing Δt cuts. The target and GC corrections and corresponding uncertainties are listed separately.

$\Delta t_{\max}$	c_{v}	$\Delta c_{\mathrm{v,stat}}$	method dep. $\Delta c_{\mathrm{v,sys}}$	cut dependent discrepancy
300 µs	0.9912	0.0024	0.0066	0.0020
450 µs	0.9932	0.0020	0.0053	0.0020
600 µs	0.9930	0.0019	0.0045	0.0002

<div align="center">target $c_{\mathrm{v}}^{\mathrm{T}}$</div>

300 µs	0.9830	0.0083	0.0094	0.0018
450 µs	0.9813	0.0083	0.0094	0.0018
600 µs	0.9806	0.0083	0.0094	0.0007

<div align="center">gamma catcher $c_{\mathrm{v}}^{\mathrm{GC}}$</div>

300 µs	0.9917	0.0025	0.0070	0.0023
450 µs	0.9940	0.0021	0.0056	0.0023
600 µs	0.9939	0.0019	0.0048	0.0001

Table D.4: MC correction factor results for changing ΔR cuts. The target and GC corrections and corresponding uncertainties are listed separately.

$\Delta R_{\max}$	c_{v}	$\Delta c_{\mathrm{v,stat}}$	method dep. $\Delta c_{\mathrm{v,sys}}$	cut dependent discrepancy
60 cm	0.9930	0.0018	0.0045	0.0032
80 cm	0.9899	0.0015	0.0045	0.0032
100 cm	0.9885	0.0014	0.0046	0.0013

<div align="center">target c_{v}</div>

60 cm	0.9806	0.0083	0.0094	0.0062
80 cm	0.9744	0.0063	0.0094	0.0062
100 cm	0.9748	0.0054	0.0094	0.0004

<div align="center">gamma catcher c_{v}</div>

60 cm	0.9939	0.0019	0.0048	0.0030
80 cm	0.9909	0.0016	0.0048	0.0030
100 cm	0.9894	0.0014	0.0049	0.0015

Table D.5: MC correction factor results for changing delayed energy cuts. The target and GC corrections and corresponding uncertainties are listed separately.

$E_{\min}$	c_{v}	$\Delta c_{\mathrm{v,stat}}$	method dep. $\Delta c_{\mathrm{v,sys}}$	cut dependent discrepancy
1.6 MeV	0.9950	0.0017	0.0040	0.0006
1.7 MeV	0.9944	0.0018	0.0046	0.0014
1.8 MeV	0.9930	0.0019	0.0045	0.0014

<div align="center">target $c_{\mathbf{v}}$</div>

1.6 MeV	0.9924	0.0081	0.0094	0.0076
1.7 MeV	0.9848	0.0082	0.0094	0.0076
1.8 MeV	0.9806	0.0083	0.0094	0.0042

<div align="center">gamma catcher $c_{\mathbf{v}}$</div>

1.6 MeV	0.9952	0.0018	0.0040	0.0001
1.7 MeV	0.9951	0.0018	0.0048	0.0012
1.8 MeV	0.9939	0.0019	0.0048	0.0012

D.5 MC studies with **NeutronTh** and **G4-NHPE**

Table D.6: Average results of parameters characterizing the neutron migration of IBD neutrons analyzed with NeutronTh and G4-NHPE. ΔT represents the prompt-delayed correlation time. ΔR is the prompt-delayed correlation distance (linear distance traveled by the neutron). The total traveled distance of the neutron is given ΔL, whereas $\lambda = \left\langle \frac{L}{\# \text{collisions}} \right\rangle$ is an estimate of the average distance traveled by the neutron per collision (mean free path). Δd is the spill-in/out skin-depth (cf. Section 7.5.1).

mean value	ν-target		gamma-catcher	
	G4-NHPE	NeutronTh	G4-NHPE	NeutronTh
ΔT	$(29.40 \pm 0.04)\,\mu s$	$(29.40 \pm 0.04)\,\mu s$	$(179.3 \pm 0.2)\,\mu s$	$(184.0 \pm 0.2)\,\mu s$
ΔR	$(57.85 \pm 0.04)\,mm$	$(51.20 \pm 0.04)\,mm$	$(88.33 \pm 0.05)\,mm$	$(60.03 \pm 0.03)\,mm$
# collisions	27.43 ± 0.02	37.91 ± 0.03	109.0 ± 0.1	170.7 ± 0.2
ΔL	$(15.70 \pm 0.01)\,cm$	$(16.15 \pm 0.01)\,cm$	$(51.73 \pm 0.04)\,cm$	$(47.31 \pm 0.04)\,cm$
λ	$(6.081 \pm 0.002)\,mm$	$(4.789 \pm 0.002)\,mm$	$(5.060 \pm 0.001)\,mm$	$(3.233 \pm 0.001)\,mm$
Δd	$(4.24 \pm 0.02)\,cm$	$(2.55 \pm 0.02)\,cm$	$(2.26 \pm 0.02)\,cm$	$(1.96 \pm 0.02)\,cm$
Gd-fraction	$(88.19 \pm 0.05)\,\%$	$(87.98 \pm 0.05)\,\%$	–	–

Acknowledgements

Bibliography

[1] J. N. Abdurashitov et al. [SAGE Collaboration] : *Results from SAGE (The Russian-American gallium solar neutrino experiment)*, Phys. Lett. B **328**, 234-248, (1994).

[2] S. Abe et al. [KamLAND Collaboration] : *Production of Radioactive Isotopes through Cosmic Muon Spallation in KamLAND*, Phys. Rev. C **81**, 025807, (2010).

[3] K. Abe et al. [T2K Collaboration] : *Indication of Electron Neutrino Appearance from an Accelerator-Produced Off-Axis Muon Neutrino Beam*, Phys. Rev. Lett. **107**, 041801, (2011).

[4] K. Abe et al. : *Letter of Intent: The Hyper-Kamiokande Experiment — Detector Design and Physics Potential —*, arXiv:1109.3262v1, (2011).

[5] Y. Abe et al. [Double Chooz Collaboration] : *Indication of Reactor $\bar{\nu}_e$ Disappearance in the Double Chooz Experiment*, Phys. Rev. Lett. **108**, 131801, (2012).

[6] Y. Abe et al. [Double Chooz Collaboration] : *Reactor $\bar{\nu}_e$ disappearance in the Double Chooz experiment*, Phys. Rev. **D86**, 052008, (2012).

[7] Y. Abe, A .Cabrera and M. Ishitsuka : *Linearized-PE calibration tech-note*, Double Chooz Internal Document, DC-doc-4114-v2, (2012).

[8] Y. Abe et al. [Double Chooz Collaboration] : *First Measurement of θ_{13} from Delayed Neutron Capture on Hydrogen in the Double Chooz Experiment*, Phys. Lett. **B723** 66-70, (2013).

[9] Y. Abe et al. [Double Chooz Collaboration] : *Direct Measurement of Backgrounds using Reactor-Off Data in Double Chooz*, Phys. Rev. D **87**, 011102(R), (2013).

[10] K. Abe et al. [T2K Collaboration] : *Observation of Electron Neutrino Appearance in a Muon Neutrino Beam*, Phys. Rev. Lett. **112**, 061802, (2014).

[11] K. Abe et al. [T2K Collaboration] : *Precise Measurement of the Neutrino Mixing Parameter θ_{23} from Muon Neutrino Disappearance in an Off-axis Beam*, Phys. Rev. Lett. **112**, 181801, (2014).

[12] Y. Abe et al. [Double Chooz Collaboration] : *Improved measurements of the neutrino mixing angle θ_{13} with the Double Chooz detector*, JHEP **10**, 086, (2014).

[13] Y. Abe et al. [Double Chooz Collaboration] : *Internal note of DC-III neutrino oscillation analyses using energy spectrum*, Double Chooz Internal Document, DC-doc-5162-v23, (2014).

[14] Y. Abe et al. [Double Chooz Collaboration] : *Background-independent measurement of θ_{13} in Double Chooz*, Phys. Lett. **B735**, 51-56, (2014).

[15] Y. Abe et al. [Double Chooz Collaboration] : *Precision Muon Reconstruction in Double Chooz*, Nucl. Instrum. Methods Phys. Res., Sect. A **764**, 330, (2014).

[16] C. Aberle, C. Buck, F.X. Hartmann and S. Schönert : *Light yield and energy transfer in a new Gd-loaded liquid scintillator*, Chem. Phys. Lett. **516**, 257, (2011).

[17] C. Aberle : *Optimization, simulation and analysis of the scintillation signals in the Double Chooz experiment*, Ph.D. Thesis, Universität Heidelberg, (2011).

[18] C. Aberle, C. Buck, F.X. Hartmann, S. Schönert and S. Wagner : *Light output of Double Chooz scintillators for low energy electrons*, JINST **6**, P11006, (2011).

[19] C. Aberle, C. Buck, B. Gramlich, F.X. Hartmann, M. Lindner, S. Schönert, U. Schwan, S. Wagner and H. Watanabe : *Large scale Gd-beta-diketonate based organic liquid scintillator production for antineutrino detection*, JINST **7**, P06008 (2012).

[20] C. Adams et al. [LBNE Collaboration] : *The Long-Baseline Neutrino Experiment: Exploring Fundamental Symmetries of the Universe*, BNL-101354-2014-JA, FERMILAB-PUB-14-022, LA-UR-14-20881, arXiv:1307.7335v3, (2013).

[21] P. Adamson et al. [MINOS Collaboration] : *Measurement of the Neutrino Mass Splitting and Flavor Mixing by MINOS*, Phys. Rev. Lett. **106**, 181801, (2011).

[22] P. Adamson et al. [MINOS Collaboration] : *Improved Search for Muon-Neutrino to Electron-Neutrino Oscillations in MINOS*, Phys. Rev. Lett. **107**, 181802, (2012).

[23] P. Adamson et al. [MINOS Collaboration] : *Combined Analysis of ν_μ Disappearance and $\nu_\mu \to \nu_e$ Appearance in MINOS Using Accelerator and Atmospheric Neutrinos*, Phys. Rev. Lett. **112**, 191801, (2014).

[24] P. A. R. Ade [Planck Collaboration] : *Planck 2013 results. XVI. Cosmological parameters*, Astronomy & Astrophysics, Volume **571**, (2013).

[25] S. K. Agarwalla et al. [LAGUNA-LBNO Collaboration] : *The mass-hierarchy and CP-violation discovery reach of the LBNO long-baseline neutrino experiment*, arXiv:1312.6520v3, (2013).

[26] S. Agostinelli et al. : *Geant4 – a simulation toolkit*, Nucl. Instrum. Methods Phys. Res., Sect. A **506**, 250 (2003).

[27] B. Aharmim et al. [SNO Collaboration] : *Electron Energy Spectra, Fluxes, and Day-Night Asymmetries of ^8B Solar Neutrinos from the 391-Day Salt Phase SNO Data Set*, Phys. Rev. C **72**, 055502, (2005).

[28] Q. R. Ahmad et al. [SNO Collaboration] : *Measurement of the Rate of $\nu_e + d \to p + p + e^-$ Interactions Produced by ^8B Solar Neutrinos at the Sudbury Neutrino Observatory*, Phys. Rev. Lett. **87**, 071301, (2001).

[29] M. H. Ahn et al. [K2K Collaboration] : *Measurement of neutrino oscillation by the K2K experiment*, Phys. Rev. D **74**, 072003, (2006).

[30] J. K. Ahn et al. [RENO Collaboration] : *Observation of Reactor Electron Antineutrinos Disappearance in the RENO Experiment*, Phys. Rev. Lett. **108**, 191802, (2012).

[31] T. Akiri : *Test des Flash-ADCs, optimisation de la conception du détecteur et développement d'un nouveau concept de reconstruction spatiale dans l'expérience d'oscillation de neutrinos Double Chooz* , Ph.D. thesis, Universite Paris-Diderot, (2010).

[32] The ALEPH, DELPHI, L3, OPAL, SLD Collaborations and the LEP Electroweak Working Group and the SLD electroweak, heavy flavour groups : *Precision Electroweak Measurements on the Z Resonance*, Phys. Rept. **427**, 257-454, (2006).

[33] J. Allison et al. : *Geant4 developments and applications*, EEE Trans. Nucl. Sci. **53** No. 1, 270 (2006).

[34] F. P. An et al. [Daya Bay Collaboration] : *Observation of electron-antineutrino disappearance at Daya Bay*, Phys. Rev. Lett. **108**, 171803, (2012).

[35] F. P. An et al. [Daya Bay Collaboration] : *Spectral measurement of electron antineutrino oscillation amplitude and frequency at Daya Bay*, Phys. Rev. Lett. **112**, 061801, (2014).

[36] P. Anselmann et al. [GALLEX Collaboration] : *Solar neutrinos observed by GALLEX at Gran Sasso*, Phys.Lett. B **285**, 376-389, (1992).

[37] M. Apollonio et al. [CHOOZ Collaboration] : *Initial Results from the CHOOZ Long Baseline Reactor Neutrino Oscillation Experiment*, Phys. Lett. **B420** (1998) 397, hep-ex/9711002.

[38] M. Apollonio et al. [CHOOZ Collaboration] : *Search for neutrino oscillations on a long base-line at the CHOOZ nuclear power station*, Eur. Phys. J. **C27** (2003) 331, hep-ex/0301017.

[39] F. Ardellier *et al.*: *Double Chooz: A Search for the Neutrino Mixing Angle θ_{13}*, hep-ex/0606025v4 (2006).

[40] D. Ayres, et al. [Noν Collaboration] : *Proposal to Build a 30 Kiloton Off-Axis Detector to Study $\nu_\mu \to \nu_e$ Oscillations in the NuMI Beamline*, Fermilab-Proposal-0929, arXiv:hep-ex/0503053v1, (2005).

[41] C. Bauer et al. : *Qualification tests of 474 photomultiplier tubes for the inner detector of the Double Chooz experiment*, JINST **6**, P06008 (2011).

[42] F. Beissel et al. : *The Trigger and Timing System of the Double Chooz Experiment*, JINST **8**, T01003 (2013).

[43] G. Bellini et al. [Borexino Collaboration] : *Precision Measurement of the ^7Be Solar Neutrino Interaction Rate in Borexino*, Phys. Rev. Lett. **107**, 141302, (2011).

[44] G. Bellini et al. [Borexino Collaboration] : *SOX: Short distance neutrino Oscillations with BoreXino*, arXiv:1304.7721, (2013).

[45] C. Bemporad , G. Gratta , P. Vogel : *Reactor-based Neutrino Oscillation Experiments*, Rev. Mod. Phys. **74**, 297, (2012).

[46] D. Benchekroun et al. : *Proposal of a search for sterile neutrinos at ILL: the STEREO experiment*, `uphe.fsac.ac.ma/Neutrino_ILL_experiment/STEREO/Stereo_Proposal.pdf`, (2012).

[47] J. Beringer et al. (Particle Data Group), Phys. Rev. D **86**, 010001 (2012) and 2013 partial update for the 2014 edition.

[48] J. B. Birks : *Scintillations from Organic Crystals: Specific Fluorescence and Relative Response to Different Radiations*, Proc. Phys. Soc. London Sect. A **64**, 874 (1951).

[49] J. B. Birks and F. A. Black : *Deterioration of Anthracene under α-Particle Irradiation*, Proc. Phys. Soc. London Sect. A **64**, 511 (1951).

[50] E. Blucher et al. : *Outer Veto Documentation*, Double Chooz Internal Document, DC-doc-1400-v3, (2010).

[51] E. Blucher et al. : *Two OV photos*, Double Chooz Internal Document, DC-doc-2634-v1, (2011).

[52] F. Boehm et al. : *Search for Neutrino Oscillations at the Palo Verde Nuclear Reactors*, Phys. Rev. Lett. **84**, 3764-3767, (2000).

[53] F. Boehm et al. : *Final results from the Palo Verde Neutrino Oscillation Experiment*, Phys. Rev. D **64**, 112001, (2001).

[54] J. W. Boldeman, M. G. Hines : *Prompt Neutron Emission Probabilities Following Spontaneous and Thermal Neutron Fission*, Nucl. Sci. Eng. **91**, 114, (1985).

[55] H. R. Bowman et al. : *Further Studies of the Prompt Neutrons from the Spontaneous Fission of ^{252}Cf*, Phys. Rev. **129**, 2133, (1963).

[56] L. D. Brown, T. T. Cai and A. DasGupta : *Interval Estimation for a Binomial Proportion*, Statistical Science Vol. **16**, No. 2, 101-117, (2001).

[57] G. Brunson : *Multiplicity and correlated energy of gamma rays emitted in the spontaneous fission of Californium-252*, LA-9408-T, Los Alamos National Laboratory, (1982).

[58] R. Brun and F. Rademakers : *ROOT - An Object Oriented Data Analysis Framework*, Proceedings AIHENP'96 Workshop, Lausanne, Sep. 1996, Nucl. Inst. & Meth. in Phys. Res. A **389** (1997) 81-86. See also `http://root.cern.ch/`.

[59] C. Buck : *Target proton number*, Double Chooz Internal Document, DC-doc-3236-v1, (2011).

[60] C. Buck and B. Reinhold : *Proton Number Tech Note*, Double Chooz Internal Document, DC-doc-4211-v7, (2012).

216

[61] C. Buck, private communication (2013).

[62] C. Buck, private communication (2014).

[63] J. Busenitz et al. : *Plan for deployment of radioactive sources*, Double Chooz Internal Document, DC-doc-2049-v2, (2010).

[64] J. Busenitz : *Measuring the neutron detection efficiency with a Cf-252 source*, Double Chooz Internal Document, DC-doc-3097-v2, (2012).

[65] A. Cabrera, J. I. Crespo Anadon, K. Terao : *Inclusive Efficiency Estimation*, Double Chooz Internal Document, DC-doc-4489-v1, (2012).

[66] A. Cabrera et al. : *Gd-III All VETOES Plots*, Double Chooz Internal Document, DC-doc-5588-v3, (2014).

[67] E. Calvo, M. Cerrada, C. Fernández-Bedoya, I. Gil-Botella, C. Palomares, I. Rodríguez, F. Toral and A. Verdugo : *Characterization of large-area photo-multipliers under low magnetic fields: Design and performance of the magnetic shielding for the Double Chooz neutrino experiment*, Nucl. Instrum. Methods Phys. Res., Sect. A **621**, 222 (2010).

[68] R. Carr and K. Crum : *Gd-III Rate+Shape results - blessed*, Double Chooz Internal Document, DC-doc-5610-v14, (2014).

[69] R. Carr : *Future precision plot*, Double Chooz Internal Document, DC-doc-5651-v1, (2014).

[70] R. Carr, private communication (2014).

[71] D. Casadei : *Estimating the selection efficiency*, JINST **7** P08021, (2012).

[72] E. Chauveau : Draft slides for TYL/FJPPL workshop, Double Chooz Internal Document, DC-doc-5643-v4, (2014).

[73] C. J. Clopper, E. S. Pearson : *The Use of Confidence or Fiducial Limits Illustrated in the Case of the Binomial*, Biometrika, Vol. **26**, No. 4., 404-413, (1934).

[74] A. Collin : *Spill in/out Studies for Gd and Hydrogen Analyses*, Double Chooz Internal Document, DC-doc-4930-v1, (2013).

[75] A. Collin : *Impact of the ΔT cut values on spill-in/out systematics*, Double Chooz Internal Document, DC-doc-5078-v5, (2013).

[76] A. Collin, J. Haser : *Effect of a Global Efficiency Correction on the Prompt Spectrum Shape*, Double Chooz Internal Document, DC-doc-5669-v1, (2014).

[77] A. Collin : *Étude des antineutrinos de réacteurs : mesure de l'angle de mélange leptonique θ_{13} et recherche d'éventuels neutrinos stériles*, Ph.D. thesis, Université Paris Sud, (2014).

[78] A. Collin, private communication (2014).

[79] E. Conover : *9Li Likelihood Technote*, Double Chooz Internal Document, DC-doc-5160-v2, (2013).

[80] E. Conover : *IBD inefficiency due to OV veto and 9Li veto*, Double Chooz Internal Document, DC-doc-5177-v1, (2013).

[81] E. Conover : *Updates to Li likelihood results and OV veto deadtime*, Double Chooz Internal Document, DC-doc-5254-v2, (2013).

[82] E. Conover : *Li/He plots to be blessed*, Double Chooz Internal Document, DC-doc-5459-v6, (2014).

[83] E. Conover : *Muon-Induced Backgrounds in the Double Chooz Neutrino Oscillation Experiment*, Ph.D. thesis, University of Chicago, (2014).

[84] R. D. Cousins, K. E. Hymes, J. Tucker : *Frequentist evaluation of intervals estimated for a binomial parameter and for the ratio of Poisson means*, Nucl. Instrum. Methods Phys. Res., Sect. A **612**, 388-398, (2010).

[85] C. L. Cowan Jr. et al. : *Detection of the free neutrino: a confirmation*, Science, Volume **124**, pp. 103-104, (1956).

[86] G. Cowan : *Error analysis for efficiency*, `http://www.pp.rhul.ac.uk/~cowan/stat/notes/efferr.pdf`, (2008).

[87] L. Cranberg, G. Frye, N. Nereson and L. Rosen : *Fission Neutron Spectrum of ^{235}U*, Phys. Rev. **103**, 662, (1956).

[88] J. I. Crespo Anadon, Inés Gil-Botella : *DC3rdPub n-Gd Detection Efficiency Estimation with IBD Candidates*, Double Chooz Internal Document, DC-doc-5291-v1, (2013).

[89] J. I. Crespo Anadon : *DC3rdPub n-Gd detection efficiency estimation with IBD candidates: Results for blessing*, Double Chooz Internal Document, DC-doc-5454-v6, (2014).

[90] M. D'Agostino et al. : *Z-axis Deployment System IRR*, Double Chooz Internal Document, DC-doc-2419-v2, (2011).

[91] M. Danilov : *Sensitivity of the DANSS detector to short range neutrino oscillations*, proceedings of ICHEP 2014 talk, arXiv:1412.0817, (2014).

[92] R. Davis Jr., D. S. Harmer and K. C. Hoffman : *Search for Neutrinos from the Sun*, Phys. Rev. Lett. **20**, 1205, (1968).

[93] Y. Declais et al. : *Study of reactor antineutrino interaction with proton at Bugey nuclear power plant*, Phys. Lett. B **338**, 383 (1994).

[94] H. De Kerret : Talk at "LowNu11" conference, Seoul National University, November 2011 (unpublished).

[95] D. Dietrich et al. : *Monte Carlo aided design of the Inner Muon Veto detectors for the Double Chooz experiment*, JINST **7** P08012, (2012).

[96] Z. Djurcic and J. Reichenbacher : *Deployed Radioactive Calibration Source Info*, Double Chooz Internal Document, DC-doc-3202-v3, (2011).

[97] Z. Djurcic *et al.* : *Second Calibration Source Data Info (May - June 2012)*, Double Chooz Internal Document, DC-doc-4129-v3, (2012).

[98] Z. Djurcic *et al.* : *Detection Systematics For 2nd Oscillation Analysis*, Double Chooz Internal Document, DC-doc-4023-v1, (2012).

[99] Z. Djurcic : *Cf-252 Calibration Source Analysis and Efficiency Studies*, Double Chooz Internal Document, DC-doc-4758-v2, (2013).

[100] Double Chooz Calibration Group : *Calibration Campaign Three Data Information*, Double Chooz Internal Document, DC-doc-4967-v2, (2013).

[101] M. Dracos and L. Kalousis : *The Inner Veto Light Injection System*, Double Chooz Internal Document, DC-doc-1772-v3, (2010).

[102] K. Eguchi et al. [KamLAND Collaboration] : *First Results from KamLAND: Evidence for Reactor Antineutrino Disappearance*, Phys. Rev. Lett. **90**, 021802, (2003).

[103] M. Elnimr : *The Li9 MC generator*, Double Chooz Internal Document, DC-doc-4402-v1, (2012).

[104] A. Etenko : *Slow Neutrons Modelling*, Double Chooz Internal Document, DC-doc-1264-v1, (2009).

[105] A. Etenko : *Slow Neutrons Modelling – NeutronTH*, Double Chooz Internal Document, DC-doc-1430-v1, (2010).

[106] A. Etenko, private communication (2012).

[107] M. Fallot, A. Onillon : *Reactor plots*, Double Chooz Internal Document, DC-doc-3377-v1, (2011).

[108] F. von Feilitzsch, A. A. Hahn, and K. Schreckenbach : *Experimental beta-spectra from ^{239}Pu and ^{235}U thermal neutron fission products and their correlated antineutrino spectra*, Phys. Lett. **118B**, 162 (1982).

[109] G. J. Feldman and R. D. Cousins : *Unified approach to the classical statistical analysis of small signals*, Phys. Rev. D **57**, 3873 (1998).

[110] S. Fernandez and J. Hartnell : *Buffer Light Injection System*, Double Chooz Internal Document, DC-doc-595-v1, (2009).

[111] D. V. Forero, M. Tortola, J. W. F. Valle : *Neutrino oscillations refitted*, Phys. Rev. D **90**, 093006, (2014).

[112] A. J. Franke : *Searching for Reactor Antineutrino Flavor Oscillations with the Double Chooz Far Detector*, Ph.D. thesis, Columbia University, (2012).

[113] Y. Fukuda et al. [Super-Kamiokande Collaboration] : *Evidence for Oscillation of Atmospheric Neutrinos*, Phys. Rev. Lett. **81**, 1562, (1998).

[114] S. Fukuda et al. [Super-Kamiokande Collaboration] : *Solar ^8B and hep Neutrino Measurements from 1258 Days of Super-Kamiokande Data*, Phys. Rev. Lett. **86**, 5651, (2001).

[115] A. Gando et al. [KamLAND Collaboration] : *Constraints on θ_{13} from a three-flavor oscillation analysis of reactor antineutrinos at KamLAND*, Phys. Rev. D **83**, 052002, (2011).

[116] M. Goldhaber, L. Grodzins and A. W. Sunyar : *Helicity of Neutrinos*, Phys. Rev. **109**, 1015, (1958).

[117] J. Goon : *UV laser-ball technote*, Double Chooz Internal Document, DC-doc-2412-v2, (2011).

[118] J. R. Granada : *Slow-neutron scattering by molecular gases: A synthetic scattering function*, Phys. Rev. B31, 4167 (1985).

[119] N. Haag et al. : *Experimental Determination of the Antineutrino Spectrum of the Fission Products of ^{238}U*, Phys. Rev. Lett. 112, 122501 (2014).

[120] T. Hagner, R. von Hentig, B. Heisinger, L. Oberauer, S. Schönert, F. von Feilitzsch, and E. Nolte : *Muon-induced production of radioactive isotopes in scintillation detectors*, Astropart. Phys. **14**, 33 (2000).

[121] A. Hahn, K. Schreckenbach, W. Gelletly, F. von Feilitzsch, G. Colvin, and B. Krusche : *Antineutrino spectra from ^{241}Pu and ^{239}Pu thermal neutron fission products*, Phys. Lett. B **218**, 365 (1989).

[122] J. Haser, C. Langbrandtner : *Spill in/out Update*, Double Chooz Internal Document, DC-doc-3445-v3, (2011).

[123] J. Haser : *Update on spill-in/out and late light studies*, Double Chooz Internal Document, DC-doc-3669-v1, (2012).

[124] J. Haser : *Status of Gd inclusive detection efficiency analysis*, Double Chooz Internal Document, DC-doc-4598-v2, (2013).

[125] J. Haser : *Volume wide detection efficiency proposal*, Double Chooz Internal Document, DC-doc-5058-v3, (2013).

[126] J. Haser : *n-Gd Neutron Detection Efficiency – DC2ndPub Cuts*, Double Chooz Internal Document, DC-doc-5349-v1, (2013).

[127] J. Heinrich et al. : *Interval estimation in the presence of nuisance parameters. 1. Bayesian approach.*, arXiv:physics/0409129v1, (2004).

[128] K. S. Hirata et al. : *Observation of ^8B solar neutrinos in the Kamiokande-II detector*, Phys. Rev. Lett. **63**, 16, (1989).

[129] M. Hofmann : *Liquid Scintillators and Liquefied Rare Gases for Particle Detectors*, Ph.D. Thesis, Technische Universität München, (2012).

[130] G. Horton-Smith : *Glg4sim: a generic liquid-scintillator antineutrino detector ("genericland") geant4 simulation*, `http://neutrino.phys.ksu.edu/GLG4sim/`, (2005).

[131] A. Hourlier : *Neutron Thermalization in the Neutrino Target*, Double Chooz Internal Document, DC-doc-3673-v1, (2012).

[132] A. Hourlier *et al.* : *TechNote – Neutron Capture in the Far Detector Target*, Double Chooz Internal Document, DC-doc-4028-v1, (2012).

[133] P. Huber, T. Schwetz : *Precision spectroscopy with reactor anti-neutrinos*, Phys. Rev. D **70**, 053011, (2004).

[134] P. Huber : *Determination of antineutrino spectra from nuclear reactors*, Phys. Rev. C **84**, 024617 (2011).

[135] IAEA [International Atomic Energy Agency] : *Database of Prompt Gamma Rays from Slow Neutron Capture for Elemental Analysis*, `http://www-pub.iaea.org/books/`, STI/PUB/1263 (ISBN:92-0-101306-X), (2007).

[136] The IceCube-PINGU Collaboration : *Letter of Intent: The Precision IceCube Next Generation Upgrade (PINGU)*, arXiv:1401.2046, (2014).

[137] Image from `http://www.nobelprize.org/educational/physics/energy/fission_2.html`

[138] S. A. E. Johansson : *Gamma de-excitation of fission fragments: (II). Delayed radiation*, Nucl. Phys. **64**, 147-160, (1965).

[139] C. Jones : *Prediction of the Reactor Antineutrino Flux for the Double Chooz Experiment*, Ph.D. thesis, Massachusetts Institute of Technology, (2012).

[140] F. Kaether et al. : *Reanalysis of the GALLEX solar neutrino flux and source experiments*, Phys. Lett. B **685**, 47, (2010).

[141] Y. A. Karelin et al. : *Californium-252 Neutron Sources*, Appl. Radiat. Isot. **48**, 1563-1566, (1997).

[142] T. Kawasaki and M. Kitazawa : *Validation of Corr. BG rate*, Double Chooz Internal Document, DC-doc-5321-v1, (2013).

[143] M. Kitazawa et al. : *Correlated BG plots to be Blessed*, Double Chooz Internal Document, DC-doc-5461-v14, (2014).

[144] M. Komatsu : *Latest results on $\nu_\mu \to \nu_\tau$ oscillations from the OPERA experiment*, talk at ICHEP 2014, Valencia, (2014).

[145] T. Konno : Talk at "Moriond Cosmology 2012" conference, La Thuile, (2012).

[146] Landolt-Börnstein New Book Series : *Subvolume A1 – Low Energy Neutrons and their Interaction with Nuclei and Matter. Part 1: 3. Neutron-matter interactions*, Volume: 16A1, ISBN: 978-3-540-60857-8, Springer-Verlag, (2000), `http://www.springermaterials.com/docs/bookshelf.html`

[147] Landolt-Börnstein New Book Series : *Subvolume A1 – Low Energy Neutrons and their Interaction with Nuclei and Matter. Part 1: 9. Nuclear fisson, 9.3 Fisson neutrons*, Volume: 16A1, ISBN: 978-3-540-60857-8, Springer-Verlag, (2000), `http://www.springermaterials.com/docs/bookshelf.html`

[148] Landolt-Börnstein New Book Series : *Subvolume A1 – Low Energy Neutrons and their Interaction with Nuclei and Matter. Part 1: 9. Nuclear fisson, 9.4 Fisson gamma-rays*, Volume: 16A1, ISBN: 978-3-540-60857-8, Springer-Verlag, (2000), `http://www.springermaterials.com/docs/bookshelf.html`

[149] C. Langbrandtner : *Background, Sensitivity and Directionality Studies for the Double Chooz Experiment*, Ph.D. Thesis, Universität Heidelberg, (2011).

[150] D. Lhuillier : *Reactor plots and macros*, Double Chooz Internal Document, DC-doc-3373-v4, (2011).

[151] Y.-F. Li, J. Cao, Y. Wang, L. Zhan : *Unambiguous Determination of the Neutrino Mass Hierarchy Using Reactor Neutrinos*, Phys.Rev. D **88**, 013008,s (2013).

[152] J. M. Lopez : *Update on Acc BG rate uncertainty and new blessed plots*, Double Chooz Internal Document, DC-doc-5607-v1, (2014).

[153] X. B. Ma et al. : *Improved Calculation of the Energy Release in Neutron Induced Fission*, Phys. Rev. C **88**, 014605, (2013).

[154] Z. Maki, M. Nakagawa and S. Sakata : *Remarks on the Unified Model of Elementary Particles*, Prog. Theor. Phys. **28**, 870, (1962).

[155] G. Marleau et al. : *DRAGON: A Collision Probability Transport Code for Cell and Supercell Calculations*, Report No. IGE-157, (1994).

[156] R. C. Martin, J. B. Knauer, P. A. Balo : *Production, distribution and applications of californium-252 neutron sources*, Appl. Radiat. Isot. **53**, 785-792, (2000).

[157] T. Matsubara et al. : *Evaluation of 400 low background 10-in. photo-multiplier tubes for the Double Chooz experiment*, Nucl. Instrum. Methods Phys. Res., Sect. A **661**, 16 (2011).

[158] G. Mention, M. Fechner, Th. Lasserre, Th. A. Mueller, D. Lhuillier, M. Cribier, and A. Letourneau : *Reactor antineutrino anomaly*, Phys. Rev. D **83**, 073006 (2011).

[159] O. Meplan et al., in ENC 2005: European Nuclear Conference; Nuclear power for the XXIst century: from basic research to high-tech industry, (2005).

[160] S. P. Mikheyev and A. Yu. Smirnov : *Resonance enhancement of oscillations in matter and solar neutrino spectroscopy*, Sov. J. Nucl. Phys. **42**, 913, (1985).

[161] Th. A. Mueller et al. : *Improved predictions of reactor antineutrino spectra*, Phys. Rev. C **83**, 054615 (2011).

[162] Th. A. Mueller : *Spill-in/out studies and other interesting stuff about neutron physics*, DC-doc-3031-v1, (2011).

[163] NEA-1845/01, documentation for MURE, (2009).

[164] K. Nakajima : *Cluster Noise Events and ^{214}Bi-Po Increase*, Double Chooz Internal Document, DC-doc-4104-v2, (2012).

[165] E. Nardi, A. Gavron and Z. Fraenkel : *Total Energy Associated with Prompt γ-Ray Emission in the Spontaneous Fission of* ^{252}Cf, Phys. Rev. C **8**, 2293, (1973).

[166] The National Nuclear Data Center (NNDC), nuclear physics database, Brookhaven National Laboratory, `http://www.nndc.bnl.gov/`.

[167] These plots were retrieved from the National Nuclear Data Center `http://www.nndc.bnl.gov/exfor/endf00.jsp` using the databases ENDF/B-VII.1 and CENDL-3.1.

[168] J. Neyman. Philos. Trans. R Soc. London Sect. A **236**, 333 (1937), reprinted in A selection of Early Statistical Papers on J. Neyman University of California, Berkeley, 1967, p. 250.

[169] H. Nifenecker et al. : *Gamma-neutron competition in the de-excitation mechanism of the fission fragments of* ^{252}Cf, Nucl. Phys. A **189**, 209, (1972).

[170] P. Novella, C. Palomares and A. Cabrera : *RecoPulse*, Double Chooz Internal Document, DC-doc-649-v2, (2009).

[171] P. Novella : *DOGS Analysis Framework*, Double Chooz Internal Document, DC-doc-1870-v1, (2010).

[172] P. Novella : *DCIII nGd Candidates: Blessed Plots*, Double Chooz Internal Document, DC-doc-5608-v4, (2014).

[173] P. Novella : *DCIII nGd RRM: blessed plots*, Double Chooz Internal Document, DC-doc-5622-v3, (2014).

[174] K. A. Olive et al. (Particle Data Group), Chin. Phys. C, **38**, 090001 (2014).

[175] I. Ostrovsky : *Guide tube IRR*, Double Chooz Internal Document, DC-doc-887-v1, (2009).

[176] M. Paterno : *Calculating Efficiencies and Their Uncertainties*, `http://home.fnal.gov/~paterno/images/effic.pdf`, (2003).

[177] W. Pauli : *Dear radioactive ladies and gentlemen*, Phys. Today 31N9 (1978) 27

[178] P. Pfahler : *Realization of the low background neutrino detector Double Chooz*, Technische Universität München, Ph.D. Thesis, (2012).

[179] A. Pichlmaier, V. Varlamov, K. Schreckenbach, P. Geltenbort : *Neutron lifetime measurement with the UCN trap-in-trap MAMBO II*, Phys. Lett. B **693**, 221 (2010).

[180] B. Pontecorvo : *Inverse beta processes and nonconservation of lepton charge*, Sov. Phys. JETP **7**, 172, (1958).

[181] G. Pronost, B. Reinhold : *3rdPub Energy Scale Maps - Status*, Double Chooz Internal Document, DC-doc-5142-v1, (2013).

[182] J. Reichenbacher : *Update on work on untagged sources*, Double Chooz Internal Document, DC-doc-2275-v2, (2011).

[183] J. Reichenbacher : *Precision Energy Scale Note*, Double Chooz Internal Document, DC-doc-3810-v1, (2012).

[184] B. Reinhold : *Energy scale status and plans*, Double Chooz Internal Document, EU++ Analysis Group Meeting, (2012).

[185] B. Reinhold et al. : *DCIII Energy Blessing candidates (ESv5)*, Double Chooz Internal Document, DC-doc-5603-v29, (2014).

[186] A. Remoto : *Correlated background and impact on the measurement of θ_{13} with the Double Chooz detector*, Ph.D. thesis, Université de Nantes, (2012).

[187] R. Roncin : *Position reconstruction correction*, Double Chooz Internal Document, DC-doc-5425-v3, (2014).

[188] ROOT Data Analysis Framework, `http://root.cern.ch/root/html/TEfficiency.html#TEfficiency:ClopperPearson`.

[189] ROOT Data Analysis Framework, `http://root.cern.ch/root/html/ROOT__Math.html#ROOT__Math:beta_quantile`.

[190] K. Schreckenbach, G. Colvin, W. Gelletly, and F. von Feilitzsch : *Determination of the antineutrino spectrum from ^{235}U thermal neutron fission products up to $9.5\,MeV$*, Phys. Lett. **160B**, 325 (1985).

[191] E. Segrè : *Nuclei and Particles*, W. A. Benjamin, Inc., (1964).

[192] A. P. Serebrov et al. : *On possibility of realization NEUTRINO-4 experiment on search for oscillations of the reactor antineutrino into a sterile state*, arXiv:1310.5521, (2013).

[193] K. Skarsvåg : *Differential angular distribution of prompt gamma rays from spontaneous fission of ^{252}Cf*, Phys. Rev. C **22**, 638, (1980).

[194] A. B. Smith, P. R. Fields and A. M. Friedman : *Prompt Gamma Rays Accompanying the Spontaneous Fission of ^{252}Cf*, Phys. Rev. **104**, 699, (1956).

[195] M. Strait : *Which delta m squared?*, Double Chooz Internal Document, DC-doc-3689-v2, (2012).

[196] D. A. Stüken : *Estimation of the systematic uncertainties of the measurement of the weak mixing angle θ_{13} related to the trigger system of the Double Chooz Experiment*, Ph.D. thesis, Rheinisch-Westfälische Technische Hochschule Aachen, (2013).

[197] D. Stump, J. Pumplin, R. Brock, D. Casey, J. Huston, J. Kalk, H. L. Lai, and W. K. Tung : *Uncertainties of predictions from parton distribution functions. I. The Lagrange multiplier method*, Phys. Rev. D **65**, 014012 (2001), Appendix B.

[198] K. Terao, R. Carr, K. Crum, S. Lucht, J. Maeda, K. Nakajima and B. Reinhold : *Memo for $\bar{\nu}_e$ Analysis With Neutron Capture on Hydrogen*, Double Chooz Internal Document, DC-doc-4156-v30, (2013).

[199] K. Terao et al. : *nH Analysis Technote, Blessed Plots So Far*, Double Chooz Internal Document, DC-doc-4156-v30, (2013).

[200] J. A. Thomas, P. L. Vahle: *Neutrino Oscillations – Present Status and Future Plans*, World Scientific, (2008).

[201] TRIPOLI-4, NEA-1716/07, `http://www.oecd-nea.org/tools/abstract/detail/nea-1716`, (2013).

[202] T. Ullrich and Z. Xu : *Treatment of Errors in Efficiency Calculations*, arXiv:physics/0701199v2, (2008).

[203] V. V. Verbinski, H. Weber and R. E. Sund : *Prompt Gamma Rays from $^{235}U(n, f)$, $^{239}P(n, f)$, and Spontaneous Fission of ^{252}Cf*, Phys. Rev. C **7**, 1173, (1973).

[204] P. Vogel and J. F. Beacom : *Angular distribution of neutron inverse beta decay, $\bar{\nu}_e + p \rightarrow e^+ + n$*, Phys. Rev. D **60**, 053003 (1999).

[205] C. Walck : *Hand-book on statistical distributions for experimentalists*, `http://www.fysik.su.se/~walck/suf9601.pdf`, (2007).

[206] Y.-F. Wang, V. Balic, G. Gratta, A. Fassò , S. Roesler, and A. Ferrari : *Predicting neutron production from cosmic-ray muons*, Phys. Rev. D **64**, 013012 (2001).

[207] B. E. Watt : *Energy Spectrum of Neutrons from Thermal Fission of ^{235}U*, Phys. Rev. **87**, 1037, (1952).

[208] J. B. Wilhelmy et al. : *Angular Momentum of Primary Products Formed in the Spontaneous Fission of ^{252}Cf*, Phys. Rev. C **5**, 2041, (1972).

[209] L. Wolfenstein : *Neutrino oscillations in matter*, Phys. Rev. D **17**, 2369, (1978).

[210] M. Worchester, private communication (2014).

[211] C. S. Wu, E. Ambler, R. W. Hayward, D. D. Hoppes and R. P. Hudson : *Experimental Test of Parity Conservation in Beta Decay*, Phys. Rev. **105**, 1413, (1957).

[212] M. Wurm : *Muon ID and tracking summary talk*, Double Chooz Internal Document, DC-doc-3826-v1, (2012).

[213] M. Wurm : *Li rate estimate*, Double Chooz Internal Document, DC-doc-5253-v1, (2013).

[214] M. Wurm : *DC3rdPub Li/He rate from dt-fits*, Double Chooz Internal Document, DC-doc-5458-v6, (2014).

[215] F. Yermia : *SoLid: Search for Oscillations with Lithium-6 Detector at the SCK·CEN BR2 reactor*, poster at ICHEP 2014, Valencia, (2014).

[216] V. Zimmer : *Measurements of Proton Quenching Factors and PSD-Parameters for the DC IV Scintillator*, Double Chooz Internal Document, DC-doc-4052-v1, (2012).